Measurement of Deformation in Varying Stress Fields

Thesis

Faculty of Science, Technology, Engineering and Mathematics

Department of Engineering and Innovation

Measurement of Deformation in Varying Stress Fields

By

Ellies Muyupa

January 2018

A THESIS SUBMITTED TO THE DEPARTMENT OF ENGINEERING AND INNOVATION OF THE OPEN UNIVERSITY FOR THE DEGREE OF DOCTOR OF PHILOSOPHY

AUTHOR'S DECLARATION

This thesis is submitted for the degree of Doctor of Philosophy of the Open University, United Kingdom. The work described in this thesis was performed in the department of Engineering and Innovation, Faculty of Science, Technology, Engineering and Mathematics, between October 2012 and January 2018, under the supervision of Professor John Bouchard and Dr Salih Gungor.

It is entirely the work of the author except where clearly referenced. None of this work has been submitted for a degree or other qualification at this or any other university.

Ellies Muyupa

January 2018

ACKNOWLEDGEMENTS

This PhD project was funded by EDF Energy within the High Temperature Research centre at the Open University, sincere acknowledgements goes to EDF Energy and the Open University for funding the project.

I would like to express my sincere gratitude to my supervisors Prof John Bouchard and Dr Salih Gungor for their constant support, guidance, encouragements and patience. I would like to thank Dr Shirley Northover for the encouragements and proof reading of this work, and Dr Alex Forsey for helping with DIC analysis and for supplying useful discussions on DIC which have been helpful during the course of this study. I wish to thank Dr Amir Shirzadi for helping with diffusion bonding and encouraging support.

I am also indebted to Dr Yuki Sakanashi, Stan Hiller, Peter Ledgard, Gordon Imlach and Damian Flack for their help in specimen preparations, metallography and mechanical tests.

Furthermore, I would like to acknowledge all the students in the Materials Engineering group for their friendship and support during the course of this study.

Finally, I would like to thank my wife (Nanyangwe) for her support and encouragements, not forgetting Mwinji and Chengo for being there too.

Ellies Muyupa

January 2018.

ABSTRACT

Welding is one of the most widely used joining techniques for manufacturing complex engineering components. However, due to transient temperature cycles in the adjacent materials being joined, the local microstructure is altered and plastic strain in the surrounding materials is introduced resulting in a variation of mechanical properties across the weldment. When an extracted cross-weld test specimen is subjected to an external uniaxial load, there is interaction between the various constituents of the weld (such as the weld fused zone, heat affected zone and parent metal) resulting in development of constraint in the weaker material due to the adjacent stronger material. This affects the distribution of stress along and within the test specimen. The level of constraint developed is dependent on the strength mismatch between adjacent materials which may be graded across the heat affected zone and the specimen cross-sectional geometry.

With development of digital image correlation (DIC) and its application to measuring deformation of solids, it has become feasible to measure local stress-strain properties of cross-weld samples and also specimens of variable geometry at both room and high temperature. Local deformation measured by DIC is correlated with nominal stress based on an iso-stress assumption, where it is assumed that the various regions of the weld are arranged in series and that the stress is uniform over the cross-section area at any given location in the specimen. Thus, local mechanical properties are inferred by mapping the measured local strain against the global stress. In this context the effect of constraint is important because it introduces a local stress distribution that will differ from the global net section stress and can therefore introduce errors in determination of local stress-strain properties.

The influence of these factors raises questions concerning the interpretation of apparent local mechanical properties of cross-welds measured using DIC. Specifically, there is uncertainty as to whether the measured variation in local strain versus average cross-sectional stress (average global stress) represents the local mechanical properties of the material with negligible error. The severity of potential constraint errors will be influenced by the specimen geometry (particularly the tensile specimen thickness to width ratio for 2D DIC strain measurements) and the gradient of material property inhomogeneity along the specimen gauge length.

In the current study, measurement of deformation in varying stress fields using DIC was carried out. Two distinct methods of introducing varying stress fields were employed: in the first case, the stress field was varied by designing an hour-glass shaped specimen with the specimen width varying as a function of the gauge length. In the second case, stress fields were varied due to a change in the specimen thickness in mismatched dissimilar metal joints. To reduce the complexity in the developed stress fields in the region near the interface, two materials were joined using solid state diffusion bonding giving a step change in the material properties across a planar interface. Test specimens spanning the interface were studied by finite element modelling and experimental tests with DIC deformation monitoring.

Using DIC and a single hour-glass shaped specimen, multiple creep curves at different stress levels along the specimen gauge length have been successfully extracted for a test temperature of 525^{o}C. The creep data obtained at 525^{o}C from the hour-glass specimen test have been fitted to RCC-MR, Garofalo and Graham-Walles creep deformation models. A better correlation is achieved between the experimental data and the RCC-MR model predicted values when the local deformations from the single specimen are plotted as a function of time and true stress at the end of the specimen's initial loading.

From both elastic-plastic FE models and experimental local stress-strain curves extracted from DIC measurements, it can be concluded that a thin (1mm thick or less) 6mm wide test specimen should be used to extract the local mechanical properties from tensile specimens that have varying material properties along the gauge length, such as found in cross-weld test specimens. This is because the thinner specimen reduces the size of the strain concentration region adjacent to the interface where errors in measured local mechanical properties can occur. As a 'rule of thumb', the intrinsic stress-strain properties of the material should not be inferred from regions within 1mm of the interface for these 1mm thick samples because of concentration errors.

The results obtained demonstrate the capability of DIC as a measurement technique for characterising the local deformation of specimens with varying stress fields. The findings also highlight some aspects of the technique which need to be considered when interpreting data from DIC measurements of local deformation from specimens with varying stress fields.

TABLE OF CONTENTS

NOMENCLATURE

T	*Temperature*
T_m	*Melting temperature*
K	*Kelvin*
^oC	*degrees centigrade*
E	*Young's modulus (GPa)*
σ	*stress (MPa)*
ε	*strain*
Δε	*change in strain*
έ	*strain rate*
t	*time*
Δt	*change in time*
t_r	*creep rupture time*
ε_{tot}	*total creep strain*
ε_p	*primary creep strain*
ε_s	*secondary creep strain*
ε_t	*tertiary creep strain*
B	*creep coefficient*
n_1	*creep stress exponent*
n	*power law stress exponent*
n_3	*RCC-MR model - stress exponent at the end of primary creep*
m	*creep time exponent*
$\dot{\varepsilon}_s$	*steady state creep strain rate*
A	*power law stress coefficient*
A_1	*hyperbolic function stress coefficient*
C_1	*RCCM-MR model coefficient*
C_2	*RCC-MR model – time coefficient*
C_3	*RCC-MR model stress coefficient at the end of primary creep*
C_i	*stress coefficient for Graham-Walles model*

$\dot{\varepsilon}_{min}$	*minimum or steady state creep rate*
θ	*creep test temperature*
θ_1	*maximum primary creep strain*
θ_2	*material hardening exponent (Theta projection model)*
θ_3	*creep ductility*
θ_4	*material damage exponent*
θ_m	*steady state creep strain rate applied in the theta projection model*
t_{fp}	*time at the end of primary creep regime*
ε_{tp}	*maximum primary creep*
r	*primary creep hardening exponent*
α	*hyperbolic function – stress multiplication factor*
α_i	*stress exponent for the Graham-Walles model*
β_i	*time exponent for the Graham-Walles model*
u	*modified Garofalo model – time exponent*
a_i, b_i, c_i and d_i	*theta projection model – material constants*
Q	*activation energy*
R	*universal gas constant*
M	*weld strength mismatch*

CHAPTER ONE

1. Introduction

In high thermal efficiency power generation plants, pressure vessels and piping components can be subjected to high stresses at high operational temperatures, making them susceptible to creep deformation and degradation (cavitation damage, creep cracking and potential rupture). Such components are usually manufactured from materials which exhibit high creep resistance, good ductility and high fracture toughness. However, complex shaped components such as steam boilers (composed of headers, pipes and tubes) are be joined to other components by welding. Welding is an aggressive process that alters the local mechanical properties of the engineering components being joined. Sections of material in the vicinity of the weld are subjected to transient temperature cycles which change the local microstructure and introduce plastic strain that results in a variation of mechanical properties across the weldment. The variation in material properties adjacent to welds affects the mechanical performance of the weld joints. Assessments of the lifetime and structural integrity of safety critical components, and especially those operating at high temperature, requires accurate knowledge of the mechanical properties of the weldment. This is especially important for the operator of the UK's fleet of Advanced Cooled Gas Reactors (AGR), EDF Energy, which has to prepare life extension safety cases for its nuclear reactors in order to maintain UK power supply until the next generation of power plants are built.

1.1 Uniaxial tensile deformation of cross-weld test samples

Generally, power plant components are joined by fusion welding processes which expose adjacent parent material to high transient temperatures producing a heat affected zone (HAZ) varying microstructure and mechanical properties. To improve the homogeneity of the weldments, weld filler materials having superior mechanical properties compared to the parent metal are chosen such that an over-matched weld is produced (that is the weld has a higher yield and ultimate tensile strength compared to the parent material).

When a uniaxial load is applied to a tensile test specimen that spans a weld joint (i.e. a cross-weld specimen) at room temperature, initial yielding occurs in the weakest material within the specimen gauge length. However, the subsequent deformation depends not only on the mechanical behaviour of the weaker material but also on the geometry of the specimen (width and thickness) and the variation in elastic and plastic stress-strain material properties along

the specimen gauge section which can be severe especially at the fusion boundary. For under-matched welds, early experimental research carried out on welded steel plates by Satoh et al [1, 2] noted an apparent increase in the weld strength due to the presence of a stronger parent material. The increase in the apparent strength of the under-matched weld was explained based on the constraining effects of the stronger material.

At the onset of plastic deformation of an under-matched weld, constraint is developed at the interface between the weld and the adjacent stronger parent material still controlled by elastic deformation. This tends to inhibit strain in the transverse direction and the weld develops a hydrostatic stress component (triaxial stresses). The developed triaxial stress state completely modifies the overall load-displacement response of the weld joint by introducing a significant apparent local hardening in the weaker material. As a result, a larger tensile stress is required to induce further plastic deformation of the weld. The apparent increase in strength of the weld was found to be dependent on the material mismatch and specimen geometry; such that, for a given specimen width and thickness, the global strength of the weld joint increases (approaching that of the base material) with decrease in the length scale of the weld (weld length) [1, 2]. An increase in specimen thickness (for a given weld length) also results in an increase in the apparent weld strength, however the increase in specimen width was found to have limited influence on the weld strength. Similar conclusion has been reached for under-matched HAZ (heat affected zone) from both experimental test results and finite element (FE) analysis [3-5].

1.2 Uniaxial tensile creep deformation behaviour of cross-weld samples

At high temperature, deformation of cross-welds is even more complex owing to creep (time dependent deformation) in addition to plastic and elastic deformations. In ferritic steel welds, experimental work and FE (finite element) analyses have shown that the creep deformation of cross-welds is highly influenced by constraint which can result in an increase in the creep life of the weldments [6-8]. In these cases, it has been concluded that the presence of a creep soft HAZ may not be a source of worry in the performance of high temperature ferritic steel components as the creep properties of this region can be enhanced by the induced constraint due to the presence of an adjacent creep hard material (that is providing the soft region is very narrow compared to the thickness of the component). Despite this conclusion, service failure of most ferritic steel weldments operating at high temperature has been associated with the creep damage in creep-soft HAZ adjacent to creep-hard parent material. This type of

failure is mostly referred to as Type IV cracking in creep-resistant steel weldments, and is associated with increased creep void formation in the fine grained HAZ adjacent to the parent material [9].

To understand the causes of Type IV cracking in ferritic steel welds, a substantial amount of experimental and numerical work has been carried out. A major challenge facing researchers has been how to characterise the local mechanical properties of the narrow region HAZ associated with Type IV cracking as there are limited strain measurement techniques that can be applied to measure the local deformation in this region at high temperature. Instead it has become common practice to use simulated HAZ properties obtained from parent materials subjected to similar heat treatment as the local HAZ region in the cross-weld. Although, the microstructure and hardness obtained is similar to the local HAZ in a cross-weld, the creep results obtained from simulated HAZ are somehow different [10, 11].

Studies of cross-welds to date have been hampered by lack of practical strain measurement techniques capable of measuring local creep deformation properties at high temperature. Parker *et al* [12] measured local strain deformation in ferritic steel cross-welds using a micro-hardness grid on the surface of the specimen; their results showed an increase in creep deformation concentrated in the HAZ region of the weld compared to other regions of the specimen. Further, using a two sensor extensometer to improve the accuracy of measured local creep strain in ferritic steel transition welds, it was found that the local deformation within the HAZ accounted for about 70% of the total deformation of these welds [13]. These local strain measurements, although not very accurate, showed that at high temperature, there is a high local strain concentration within the creep soft HAZ adjacent to the parent material in ferritic steel welds. These experimental results seemingly contrasted the conclusions made in [6, 7] based on observations that during creep deformation, there is little constraint developed due to the presence of the creep hard material as the creep soft material tends to creep more easily [14].

On the other hand, the creep deformation of austenitic stainless steel weldments differ from that observed in ferritic steel welds. Measurement of local deformation of stainless steel cross-welds shows that creep strain and creep rates are higher in the weld and the parent material compared to the HAZ [15, 16]. For instance, detailed time and spatially resolved creep strains have been measured by DIC in cross-weld specimens extracted from different locations through the thickness of a large section stainless steel multi-pass weld [16]. The

creep properties were found to vary not only along each cross-weld specimen (weld, HAZ, and base metal) but also with location (near weld root, mid-section and near weld cap) from which the specimen had been extracted from the weldment. Similarly, the rupture points of the cross-weld specimens were dependent on the position from which the specimens were extracted from weldment [16]. These spatially and time resolved creep results highlight the complexity of the creep behaviour of thick section austenitic stainless steel weldments.

The mechanical deformation observations summarised above relating to both ferritic and austenitic stainless steel weldments illustrate how geometric and materials homogeneity factors can affect the creep deformation behaviour of weldments in a complex way.

1.3 Application of Digital Image Correlation (DIC) in characterising local deformation across weldments

In the past, measurement of local deformation of cross-welds at both room and high temperature has been challenging. However, development and availability of full-field displacement measurement techniques such as Digital Image Correlation (DIC) is opening new opportunities for measuring local mechanical properties of material [17]. DIC was first applied by Reynolds *et al* [18] to measure spatially resolved mechanical properties of cross-weld specimens at room temperature. Detailed weld characterization results using DIC where parameters have been optimised for room temperature tensile testing have been published [19-21]. Over the past 10 years, DIC has become an established technique for characterising the mechanical behaviour of cross-welds at room temperature.

DIC has also been extended to high temperature characterisation of creep properties of engineering materials [22]. Recently, application of DIC at high temperature to measure both time and spatially resolved creep properties of austenitic stainless steel cross-welds has been successfully carried out [16, 23]. Full-field strain measurements across the weld at high temperature and for extended periods of time present challenges such as (1) image distortion caused by the convection currents between the furnace window and the camera, (2) change in the test specimen due to oxidation at high temperature, and (3) appropriate illumination of the test sample surface. But these factors have been successfully addressed [24, 25].

Despite recent advances there remains a need to understand the fundamental effects of geometric and material property constraint on the local uniaxial tensile and creep properties of cross-welds determined using DIC.

For instance, at both room and high temperature, it has been shown that when a cross-weld is subjected to an external uniaxial load, there is interaction between the various constituents of the weld (weld, HAZ and parent metal) resulting in development of a constraint in the weaker material due to the adjacent stronger material [2, 3, 7, 16, 26, 27]. The level of constraint developed is dependent on the strength mismatch of the materials, the specimen geometry and the HAZ geometry. The effects of constraint on local deformation of cross-welds is particularly important especially when 2D DIC is used to observe flat specimens placed perpendicular to the optical path of the camera.

Since DIC only measures the local deformation, characterisation of local mechanical properties is based on the iso-stress assumption, which implies that the various regions of the weld are arranged in series and that the cross section area at any given location in the specimen is homogenous [18, 28]. Therefore, local mechanical properties are extracted by mapping the measured local strain against the global stress. The validity of the iso-stres assumption has been checked by comparing DIC measured local deformation to the ones obtained from 2D and 3D FE analysis and to some extent a good correlation between the two sets of data has been observed. [28].

However, there remains a need to understand the fundamental effects of geometric and material property variation constraints on the local deformation of cross-weld tensile specimens subjected to uniaxial loads. The influence of these factors raises questions concerning the interpretation of local mechanical properties of cross-welds measured using DIC and other full field techniques. Specifically, there is uncertainty as to whether the measured variation in local strain versus average cross-sectional stress represents the local mechanical properties of the material with negligible error. The severity of potential constraint errors will be influenced by the specimen geometry (particularly the tensile specimen thickness to width ratio for 2D DIC strain measurements) and the gradient of material property inhomogeneity along the specimen gauge length [4, 29]. Therefore, two questions need to be addressed, what level of inhomogeneity gradient introduces significant error and how is this error distributed within the test specimen (along the length, across the width and through the thickness) and secondly how is the local deformation affected by the test specimen geometry. From a DIC application point of view, guidance is required on what specimen thickness is best to use for determining the actual local mechanical properties of cross-weld specimens.

On the other hand, the ability to measure time and spatially resolved creep strain at high temperature using DIC makes it an invaluable technique. This is especially important when it comes to characterisation of new high temperature materials and component life assessment. Generally, transient and steady-state creep properties are required for design and undertaking remaining life assessments of safety critical components in power plants, operating under load at high temperature. To characterise these material properties as a function of stress and temperature, many uniaxial creep tests must be carried out. But given the full field monitoring capability of DIC at high temperature, it is of high practical relevance to consider whether a test specimen can be designed to measure creep deformation properties simultaneously at multiple stress levels.

1.4 Aims of the Thesis

The objective of this thesis is to study the effects of geometric and material property gradient constraint on the local deformation of cross-weld tensile and creep test specimens measured using DIC at both room and high temperature. Owing to the multiplicity of factors affecting such deformation, a simplified weld geometry was chosen. This simplified weld geometry was achieved by solid state diffusion bonding of AISI Type 316H stainless steel billets to Esshete1250 stainless steel billets. In the diffusion bonding process, a joint between two adjacent parent materials is produced by applying a moderate stress and temperature to cause plastic collapse of the contacting asperities [30]. This results in formation of a planar array of interfacial voids. The diffusion bonding temperature applied allows the atoms from the two adjacent parent materials to diffuse into the voids, whereas the applied load facilitates the creep deformation at the interface resulting in complete removal of voids and an atom to atom bonding of the interface [31, 32]. Due to its capability to produce joints with a very thin interface and no HAZ, the diffusion bonding processing was chosen as a process for producing simplified joint interface. Thus, the test specimens extracted from diffusion bonded billets were ideal for studying the effects of constraint due to a step change in material deformation properties (elastic, plastic and creep) at the joint interface and the effect of specimen geometry (thickness to width ratio).

This thesis also exploits the potential of DIC monitored mechanical testing at elevated temperature through developing a novel method for extracting multiple creep deformation curves at different stress levels along the gauge section of a single hour-glass shaped design of test specimen. The specimen design is supported by finite element analysis and the results

are validated by creep deformation data acquired from an independent conventional creep test. It is illustrated how common creep models can be fitted to the multiple stress creep deformation data produced. Use of a single specimen reduces the aggregated testing time several fold and is therefore a very promising cost-effective technique which may revolutionise creep testing methods.

1.5 Thesis outline

The thesis is outlined as follows;

Chapter 1 is the thesis introduction and includes the objectives of the current study

Chapter 2 presents basic concepts of creep deformation and some commonly used creep models are discussed. Fundamentals of room temperature and creep deformation of cross-welds have been critically reviewed. The literature on principles of digital image correlation (DIC) and its capability have been discussed and reviewed.

In chapter 3, materials characterisation techniques used in the current study have been described. The chapter also includes the description of the solid-state diffusion bonding process applied and the parameters used in manufacturing the diffusion bonded specimens.

Chapter 4 presents results on extraction of multiple creep deformation curves from a single hour-glass shaped specimen. The chapter includes a brief description of the design of the hour-glass specimen. Results from a single hour-glass shaped specimen have been compared to results obtained from testing conventional creep specimens. Three different creep models were fitted to the multiple creep deformation curves extracted from a single specimen to characters the creep properties of the material.

In Chapter 5, results on the effects of specimen geometry and material gradient constraint on local mechanical properties measured using DIC have been presented. The first section the chapter presents results from elastic and elastic-plastic FE analyses. The second part presents results from both DIC-tensile and DIC-creep tests of diffusion bonded specimens with varying aspect ratio (specimen thickness to width ratio). The magnitude of errors and the size of the region from the interface within which errors in measured local mechanical properties can occur owing to assumption of iso-stress and constraint effects are presented.

Chapter 6 presents a discussion of the results obtained from chapter 4 and chapter 5, and how the finds from the current study can be applied.

Finally, the overall conclusions drawn and suggestions for future work are outlined in chapter 7.

1.6 REFERENCES

1. Satoh, K. and M. Toyoda, *Static strength of welded plates including soft interlayer under tension across a weld line.* Transactions of the Japan Welding Society, 1970. **1**(2): p. 10-17.
2. Satoh, K. and M. Toyada, *Joint Strength of Heavy Plates With Lower Strength Weld Metals.* Welding journal, 1975. **54**(9): p. 311.
3. Dexter, R.J., *Significance of strength undermatching of welds in structural behaviour.* in: K.H. Schwalbe, M. Koçak (Eds.), Mismatching of Interfaces and Welds, GKSS Research Center Publications, 1997: p. 55–73.
4. Kim, Y.-J. and C.-S. Oh, *Finite element limit analyses of under-matched tensile specimens.* Engineering Fracture Mechanics, 2006. **73**(10): p. 1362-1378.
5. Rodrigues, D.M., et al., *Numerical study of the plastic behaviour in tension of welds in high strength steels.* International Journal of Plasticity, 2004. **20**(1): p. 1-18.
6. Iwadate, T., Prager, M., and Humphries, M. J., *Reliability of New and Old Chrome-Moly Steels for Hydrogen Processing Vessels: Part II: Enhanced Perfomance.* In New Alloys for Pressure Vessels and Piping, ASME, New York, 1990: p. 38 - 47.
7. Storesund, J. and S.T. Tu, *Geometrical effect on creep in cross weld specimens.* International Journal of Pressure Vessels and Piping, 1995. **62**(2): p. 179-193.
8. Hyde, T., et al., *Effect of weld angle and axial load on the creep failure behaviour of an internally pressurised thick walled CrMoV pipe weld.* International Journal of Pressure Vessels and Piping, 2001. **78**(5): p. 365-372.
9. Shüller, H., L. Hagn, and A. Woitscheck, *Cracks in the weld area of formed parts in superheated steam lines—material analysis.* Der Maschinenschaden, 1974. **1**: p. 1-13.
10. Abe, F. and M. Tabuchi, *Microstructure and creep strength of welds in advanced ferritic power plant steels.* Science and technology of welding and joining, 2004. **9**(1): p. 22-30.
11. Matsui, M., et al., *Degradation of creep strength in welded joint of 9% Cr steel.* ISIJ international, 2001. **41**(Suppl): p. S126-S130.

12. Parker, J.D. and A.W.J. Parsons, *High temperature deformation and fracture processes in 214Cr1Mo-12Cr12Mo14V weldments.* International Journal of Pressure Vessels and Piping, 1995. **63**(1): p. 45-54.
13. Parker, J., *Creep and fracture behaviour of English Electric Mark III transition welds:(a) New weldments.* International journal of pressure vessels and piping, 1998. **75**(2): p. 83-94.
14. Kimmins, S. and D. Smith, *On the relaxation of interface stresses during creep of ferritic steel weldments.* The Journal of Strain Analysis for Engineering Design, 1998. **33**(3): p. 195-206.
15. Hongo, H., et al., *Creep deformation behavior of weld metal and heat affected zone on 316FR steel thick plate welded joint.* Zairyo, 1999. **48**(2): p. 116-121.
16. Sakanashi, Y., et al., *Measurement of Creep Deformation across Welds in 316H Stainless Steel Using Digital Image Correlation.* Experimental Mechanics, 2017. **57**(2): p. 231-244.
17. LaVision, *StrainMaster DaVis 8.1 Digital Image Correlation Software*. 2013.
18. Reynolds, A. and F. Duvall, *Digital image correlation for determination of weld and base metal constitutive behavior.* WELDING JOURNAL-NEW YORK-, 1999. **78**: p. 355-s.
19. Acar, M., et al., *Effect of prior cold work on the mechanical properties of weldments,* in *Proceedings of the 2010 SEM Annual Conference and Exposition on Experimental and Applied Mechanics*. 2010: Indianapolis, Indiana, USA.
20. Acar, M., et al., *Variation of mechanical properties in a multi-pass weld measured using digital image correlation,* in *Society of Experimental Mechanics Annual Conference on Experimental and Applied Mechanics 2009,* K.B. Zimmerman, Editor. 2009, Society for Experimental Mechanics Inc.: Albuquerque, New Mexico, USA. p. 288-293.
21. Molak, R.M., et al., *Use of micro tensile test samples in determining the remnant life of pressure vessel steels.* Applied Mechanics and Materials, 2007. **7-8**: p. 187-194.
22. Lyons, J., J. Liu, and M. Sutton, *High-temperature deformation measurements using digital-image correlation.* Experimental Mechanics, 1996. **36**(1): p. 64-70.
23. Sakanashi, Y., S. Gungor, and P.J. Bouchard, *Measurement of Creep Deformation in Stainless Steel Welded Joints*, in *Proceedings of the 2011 Annual Conference on Experimental and Applied Mechanics; Volume 5 Optical Measurements, Modeling, and Metrology*. 2011: Uncasville, CT, USA.

24. Sakanashi, Y., *Measurement of Creep Deformation in Weldments.* PhD Thesis, The Open University, 2013.
25. Morris, A., Maharaj, C., Puri, A., Kourmpetis, M., Dear, J., *Recent Developments in Methods to Study Creep Strain Variations in Power Station Steam Plant.* Proceedings of the ASME Pressure Vessels and Piping Conference, 2009. **7**: p. 529-536
26. Chellapandi, P. and S. Chetal, *Influence of mis-match of weld and base material creep properties on elevated temperature design of pressure vessels and piping.* Nuclear Engineering and Design, 2000. **195**(2): p. 189-196.
27. Hyde, T.H., et al., *Effect of weld angle and axial load on the creep failure behaviour of an internally pressurised thick walled CrMoV pipe weld.* International Journal of Pressure Vessels and Piping, 2001. **78**(5): p. 365-372.
28. Lockwood, W. and A. Reynolds, *Simulation of the global response of a friction stir weld using local constitutive behavior.* Materials Science and Engineering: A, 2003. **339**(1): p. 35-42.
29. Rodrigues, D., et al., *Numerical study of the plastic behaviour in tension of welds in high strength steels.* International Journal of Plasticity, 2004. **20**(1): p. 1-18.
30. Mahoney, M.W. and C.C. Bampton, *Fundamentals of Diffusion Bonding[1],* in *Welding, Brazing and Soldering,* D.L. Olson, et al., Editors. 1993, ASM International. p. 0.
31. Ridley, N., M.T. Salehi, and J. Pilling, *Isostatic diffusion bonding of microduplex stainless steel.* Materials Science and Technology, 1992. **8**(9): p. 791-795.
32. Kurt, B. and A. Çalik, *Interface structure of diffusion bonded duplex stainless steel and medium carbon steel couple.* Materials Characterization, 2009. **60**(9): p. 1035-1040.

CHAPTER TWO

2 Literature Review

2.1 Creep Deformation

Creep can be defined as time-dependent inelastic deformation under sustained load at high temperature. In contrast to tensile testing, in creep testing the plastic strain is time dependent and can occur at stresses which in an ordinary tensile test would be below the yield stress. If creep occurs for a sufficiently long time, excessive deflection (creep-failure) or fracture (creep-fracture) occurs. The combined effects of load, temperature and time produce creep and possibly creep-failure or creep-fracture of a component (or test specimen) depending on the material and the environment.

Generally, for polycrystalline materials creep mechanisms are classified into two main categories, dislocation creep (also referred to as power law creep) and diffusion creep [1, 2]. Based on the temperatures and stress applied in the current work, dislocation creep is the predominant mechanism. In this mechanism, dislocation motion is by glide and climb. Dislocations motion by gliding is hindered by internal structures of the material, however further dislocation glide is facilitated by dislocation climb which serves as mechanism for unlock dislocations from obstacles. Detailed discussion of the various creep deformation mechanisms are given in [2, 3].

For a given material, a creep mechanism may be predominant at a given temperature and stress. Creep mechanisms are summarized on deformation maps which indicate the governing creep mechanism at a given temperature and stress, Figure 2.1 [4]. From creep deformation maps, the dominant mechanism is identified as a function of homologous stress (stress normalised by Young's modulus) and homologous temperature which the ratio of the absolute temperature, T, to the absolute melting temperature, T_m.

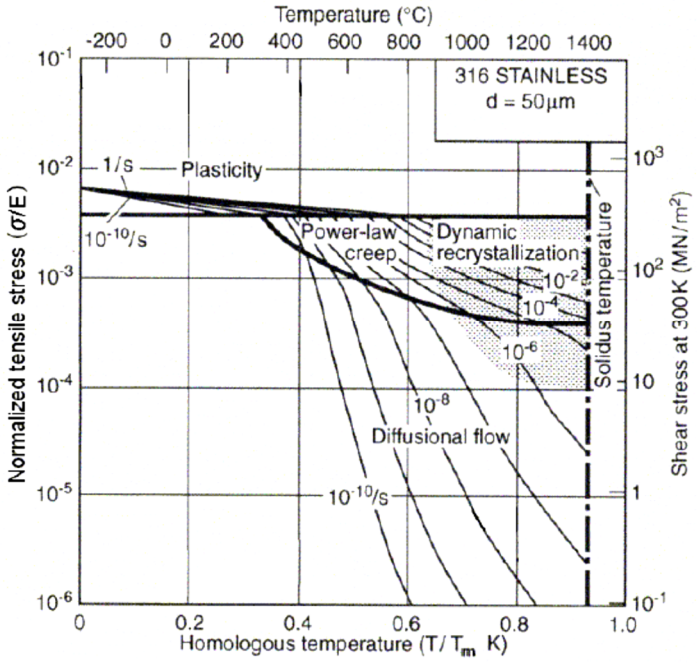

Figure 2.1 Example of a creep deformation map [4]

2.2 Classification of Creep Deformation

Experimental study of creep is carried out by uniaxial creep tests. In these tests, the specimen is subjected to a constant load (the applied stress could be higher or lower than the yield strength of the material) and the engineering strain is monitored as a function of time. A typical creep curve obtained from a uniaxial creep test is illustrated in Figure 2.2.

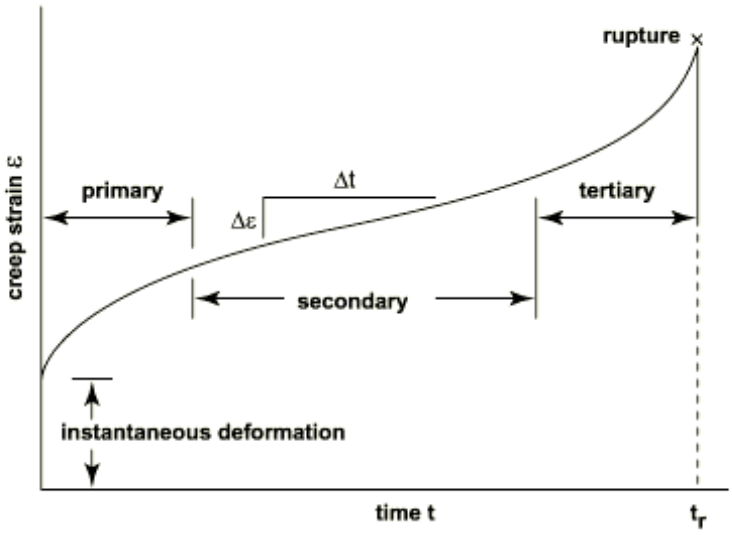

Figure 2.2 Typical creep strain vs time curve

Generally, a typical creep curve exhibits three distinct ranges. The application of the load, beginning at time $t = 0$, naturally leads to an instantaneous stain, ε_0. This strain, ε_0, maybe partly elastic and partly plastic depending on the initial load and temperature. This is followed by a primary creep regime in which the strain rate $\dot{\varepsilon}_{cr}$ (the slope of the creep curve) decreases with time as the material settles down towards a steady-state regime or the minimum strain rate. During the next interval of time, the secondary stage, the minimum strain rate $\dot{\varepsilon}_{cr}$ is maintained due to a balance between dynamic recovery and strain hardening [5]. In the tertiary creep regime, the strain rate continues to increase under the sustained stress and temperature until at time, $t = t_R$, the specimen ruptures (where t_R is the rupture time). The increase in the strain rate $\dot{\varepsilon}_{cr}$ is partly due to necking of the specimen which increases the true stress. However, tertiary creep can occur before the onset of necking, due to accumulation of creep damage (e.g. voids). The extent of each of the stages in the creep curve varies with the temperature, the stress and the material, Figure 2.3(a). Creep data can also be represented in terms of the variation of strain rate $\dot{\varepsilon}_{cr}^{\cdot}$ as a function of time, in order to identify the minimum creep strain rate, as in Figure 2.3(b). The secondary stage or steady-state creep is centred on the minimum in the plot of creep strain rate $\dot{\varepsilon}_{cr}$ against time. The minimum creep rate has great significance in the analysis of the creep life of a material as components spend most of their service time in the secondary creep regime.

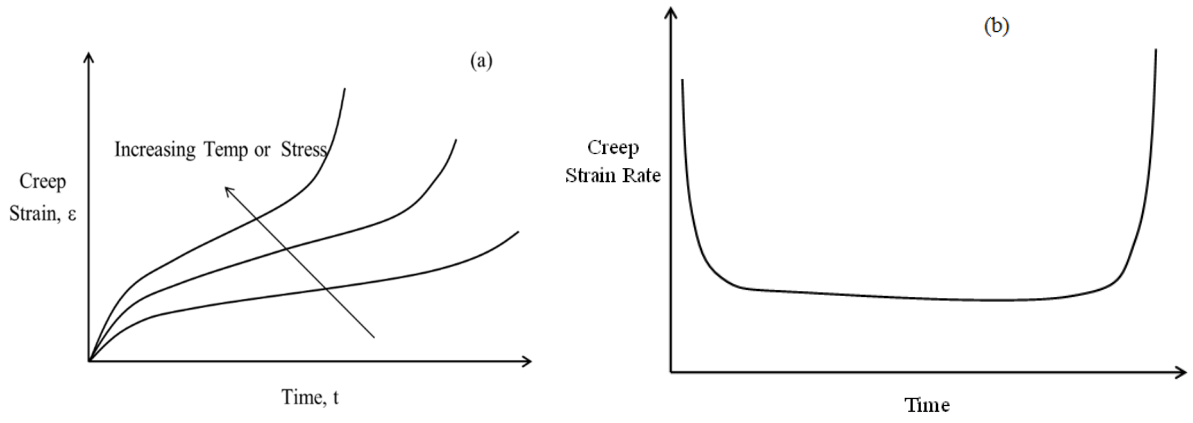

Figure 2.3 (a) Effect of temperature and stress on creep strain (b) Typical creep strain rate vs time curve [6].

2.3 Creep Modelling

A wide range of creep models are used in characterising the creep behaviour of high temperature materials. The basis for most empirical models is that the total creep strain

accumulated by a component subjected to external loads at high temperature is composed of the primary, secondary and tertiary creep strain, expressed as,

$$\varepsilon_{tot} = \varepsilon_p + \varepsilon_s + \varepsilon_t \qquad (2.1)$$

where ε_p, ε_s and ε_t are the primary, secondary and tertiary creep strain, respectively. Most models seeking to describe the entire curve, apart from continuum damage models which are mostly focused on predicting the creep ductility of the material using coupled models [7-9], are based on this simple summation of creep strains at any given point.

2.3.1 Creep Models for Austenitic Stainless Steel

The European Creep Collaborative Committee (ECCC) report on creep strength and rupture outlines some of the most widely used creep models and the materials to which these models can be applied [10]. For austenitic stainless steels, the Norton-Bailey, the RCC-MR, Garofalo and the modified Garofalo model are among the most widely used models. The five models considered and applied in this work are outlined in the following Sections.

2.3.1.1 Norton-Bailey model

In the Norton-Bailey model, the primary creep strain at any given stress is expressed in power law form as,

$$\varepsilon_p = B\sigma^{n_1}t^m \qquad (2.2)$$

where B, n_1 and m are temperature dependent material constants. During steady state secondary creep, a power law expression also known as Norton's law is used to describe the creep strain rate,

$$\dot{\varepsilon}_s = A\sigma^n \qquad (2.3)$$

where $\dot{\varepsilon}_s$ is the steady-state creep strain rate, A and n are temperature dependent material properties. For a creep curve composed of primary and secondary creep strain, the total creep strain at any given point can be expressed as,

$$\varepsilon = B\sigma^{n_1}t^m + A\sigma^n t \qquad (2.4)$$

2.3.1.2 The RCC-MR model

The RCC-MR model is an empirical creep law derived from many experimental creep tests carried out at various temperature and stress ranges. The model provides a good approximation of measured constant load creep data from tests on stainless steels. The model is similar to the Norton-Bailey model in that the total creep strain is described by a primary expression up to a time, t_{fp}, at the end of primary creep, and thereafter by a secondary expression which is the sum of the primary and secondary creep strains [11].

The primary creep is defined by the expression,

$$\varepsilon_p = C_1 t^{C_2} \sigma^{n_1} \qquad \text{For } 450℃ \leq \theta \leq 700℃ \text{ and } t \leq t_{fp} \qquad (2.5)$$

where ε_p is primary creep strain (conventionally in %), t is the time (conventionally in hours), σ is the stress (in MPa), and C_1, C_2 and n_1 are material constants. The secondary creep expression is based on the power law equation (Equation 2.3) expressed as,

$$\dot{\varepsilon}_{min} = C\sigma^n \qquad (2.6)$$

where $\dot{\varepsilon}_{min}$ is the minimum creep rate in units of $\%h^{-1}$, C and n are material constants. Therefore, the total creep strain for both primary and secondary creep is given in % as,

$$\varepsilon_c = C_1 {t_{fp}}^{C_2} \sigma^{n_1} + 100C\sigma^n \left(t - t_{fp}\right) \qquad (2.7)$$

The time at the end of primary creep is determined from,

$$t_{fp} = C_3 \sigma^{n_3} \qquad (2.8)$$

where $C_3 = \left(\frac{100C}{C_1 C_2}\right)^{\frac{1}{(C_2-1)}}$ and $n_3 = \frac{n-n_1}{C_2-1}$ [11]

2.3.1.3 Garofalo model

In Garofalo's model [12], the total creep strain at any given time and stress can be expressed as,

$$\varepsilon = \varepsilon_{tp}(1 - e^{-rt}) + \dot{\varepsilon}_s t \qquad (2.9)$$

where ε_{tp} is the maximum primary creep, r is a constant related to the rate of exhaustion of the primary creep strain or the hardening characteristic of the material during primary creep. $\dot{\varepsilon}_s$ is the steady-state or minimum creep rate. The stress dependence of the steady-state or minimum creep rate at any given temperature is described the hyperbolic sine function expressed as,

$$\dot{\varepsilon}_s = A_1 \sinh(\alpha\sigma)^n \qquad (2.10)$$

where A_1, α and n are material constants. This expression is suitable for all stress ranges including higher stresses where the power law stress dependence of the steady-state creep rate does not apply. At low stress, Equation 2.10 reduces to the power law stress dependence of the steady-state creep rate, Equation 2.3. A modified Garofalo model is also widely used and is expressed as,

$$\varepsilon = \varepsilon_t\left(1 - e^{-rt^u}\right) + \dot{\varepsilon}_s t \qquad (2.11)$$

were u is a material constant. Although the Garofalo creep model and its modified version are widely used, due to their simplicity, they have been found to overestimate the creep strain in austenitic stainless steels [11].

2.3.1.4 Theta projection

The theta projection model is based on the physical processes characterising creep such as the hardening behaviour in the primary creep regime and the damage process in the tertiary creep regime and is devised to accurately describe the entire shape of the creep curve [13, 14]. The theta projection model is expressed as,

$$\varepsilon = \theta_1\left(1 - e^{-\theta_2 t}\right) + \theta_3\left(e^{\theta_4 t} - 1\right) \qquad (2.12)$$

where θ_1 is the maximum primary creep strain, θ_2 defines the hardening characteristic of the material in the primary creep regime, θ_3 is the creep ductility of the material and θ_4 characterises the damage process of the material. The parameters θ_1, θ_2, θ_3 and θ_4 are stress and temperature dependent and their dependence is given by,

$$\ln\theta_i = a_i + b_i\sigma + c_i T + d_i\sigma T \qquad (2.13)$$

where a_i, b_i, c_i and d_i are material constants and can be determined by multilinear least squares regression analysis of the stress/$\ln\theta_i$ plots at different creep temperatures. The

conventional theta projection model assumes that the creep behaviour of the material is characterised by strain hardening in the primary creep regime and the damage process in the tertiary creep, and thus does not take into consideration the secondary creep regime. The modified theta projection model is designed to take into consideration the secondary creep regime is expressed as,

$$\varepsilon = \theta_1\left(1 - e^{-\theta_2 t}\right) + \theta_m t + \theta_3\left(e^{\theta_4 t} - 1\right) \qquad (2.14)$$

where $\theta_m = A\sigma^n \exp\left(Q/RT\right)$, A and n are stress and temperature dependent material constant, Q is the activation energy, R is the universal gas constant and T is the temperature.

2.3.1.5 Graham and Walles model

The Graham-Walles model is an empirical representation of the creep data in the form of a series with each part of the series representing the primary, secondary and tertiary creep regime [15]. The model is given as,

$$\varepsilon_c = \sum_{i=1}^{n} C_i\, \sigma^{\alpha_i}\, t^{\beta_i} \qquad (2.15)$$

with primary, secondary and tertiary creep expressed as,

$$\varepsilon_c = C_1\sigma^{\alpha_1}t^{1/3} + C_2\sigma^{\alpha_2}t + \left(C_3\sigma^{\alpha_3} + C_4\sigma^{\alpha_4}\right)t^3 \qquad (2.16)$$

where C_i, α_i and β_i represent the stress coefficients, the stress exponents and the time exponents, respectively.

2.4 Creep of Weldments

Deformation of weldments subjected to external loading is very complex. When an external load is applied, there are interactions among the constituent parts of the weld (weld zone, base material and the different parts of the HAZ), such that the stress-strain distribution exhibited is totally different from that of homogeneous specimens. Reflecting differences in the mechanical properties of the different parts, weldments' deformation is influenced by mismatches in their materials' strength (elastic, plastic or creep), the geometry of the weld and the loading mode.

Generally, the strength mismatch (*M*) of a weld is characterised by the mismatch factor which is defined as [16];

$$M = \frac{Strength\ of\ the\ weld}{Strength\ of\ the\ base\ metal} \qquad 2.17$$

where the term 'strength' may refer to elastic, plastic or creep strength. For tensile testing, the strength mismatch is based on either the elastic (*E*) or the plastic mismatch (the latter in terms of either the yield strength or the ultimate tensile strength), whereas for creep, it is defined in terms of either the creep exponent (*n*) or the creep power law coefficient (*A*). $M < 1$ is referred to as under-matching and $M > 1$ as over-matching with $M \cong 1$ for even-matched welds.

For high temperature deformation, the mismatch between the creep properties of the weld, the different regions of the HAZ and the base material has a major impact on the creep life of weldments [17]. The creep strain rates in the base and the weld metals have generally been reported to differ by a factor of 5 (or even higher in certain instances). For most steel weldments, the HAZ is composed of coarse-grained (CGHAZ) and fine-grained (FGHAZ) regions and these exhibit different creep and rupture properties when the weld is subjected to external loads, Figure 2.4.

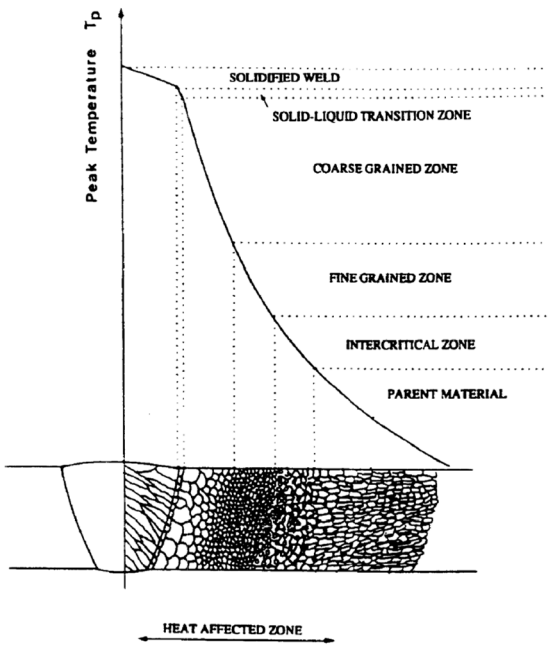

Figure 2.4 Schematic diagram of the various regions across the weld [18].

Extensive research on the creep of steel weldments shows that the fine-grained HAZ (FGHAZ) has inferior creep properties compared to the other regions of the weldment such that when an external load is applied, stress and strain concentrations occur in this region.

The FGHAZ is also referred to as the Type IV region since Type IV cracks initiate in this region because of its poor creep properties [19, 20]. Under a constant applied load, the creep soft region (FGHAZ) of the weldment creeps easily while the adjacent creep hard material remains within its elastic loading range (experiencing elastic strain), therefore, the narrow soft zone is effectively restrained from straining and fracturing by the much stronger material (base metal and weld metal) adjoining it. Any small deformation gives rise to a triaxial stress state which retards further deformation. This results in an enhanced creep life of the narrow soft HAZ due to constraint [21]. On the other hand, it has been reported that, apart from developing high triaxial stresses, the FGHAZ also experiences high creep strains and both have a great influence on the nucleation and growth of voids. Using a four-region model consisting of the weld metal, CGHAZ, FGHAZ and the base metal, Li *et al* [22] simulated the creep behaviour and deterioration of P122 steel. Their results, comparing the development of voids across the weldment to the distributions of maximum principal stress, high hydrostatic stress, equivalent creep strain and equivalent stress, are shown in Figure 2.5. Figure 2.5 shows that the maximum principal stress, hydrostatic stresses and equivalent strain are much higher in the FGHAZ than in other regions of the weldment and that high numbers of voids were determined experimentally in this region. Therefore, it was concluded that the equivalent strain or high creep strain, the maximum principal stress and triaxial stresses play an important role in the formation and coalescence of voids. On the other hand, due to constraint, the equivalent stress is lower in the FGHAZ than in the base and weld metals. Similar results have been reported by Watanabe *et al* [23] and Li *et al* [24] who showed that the presence of high creep strains and high triaxial stresses in the FGHAZ accelerates the nucleation and growth of voids in this region, thus reducing the creep life of the weldment. Therefore, it can be stated that constraint has dual effects on the creep life of weldments. High constraint developing in the soft narrow region of the weldment (FGHAZ) result in a low equivalent stress, delaying failure in this region; however, the resulting high triaxial stresses and high creep strains in the FGHAZ encourage the growth and coalescing of voids in this region. The level of constraint imposed on the FGHAZ is highly influenced by not only the mismatch in creep properties but also depends on the specimen dimensions. Both experiments and simulations have shown that progressively increasing the specimen diameter or thickness whilst maintaining the weld and HAZ width constant, results in increased creep strength of the creep soft material due to the increased constraint [19, 21, 25].

Both experimental and simulation results show that at low stresses failure occurs in the narrow creep soft region (FGHAZ), whereas at high stresses failure has been reported to occur in the base material. This is due to high constraint in the FGHAZ. Other factors affecting the development of constraint in the narrow creep soft HAZ have also been investigated. At low or moderate loads, increasing the angle of orientation of the creep soft narrow HAZ in relation to the applied load increases the creep life [19, 26]. However, at high loads the creep life reduces slightly with increasing weld or HAZ angle.

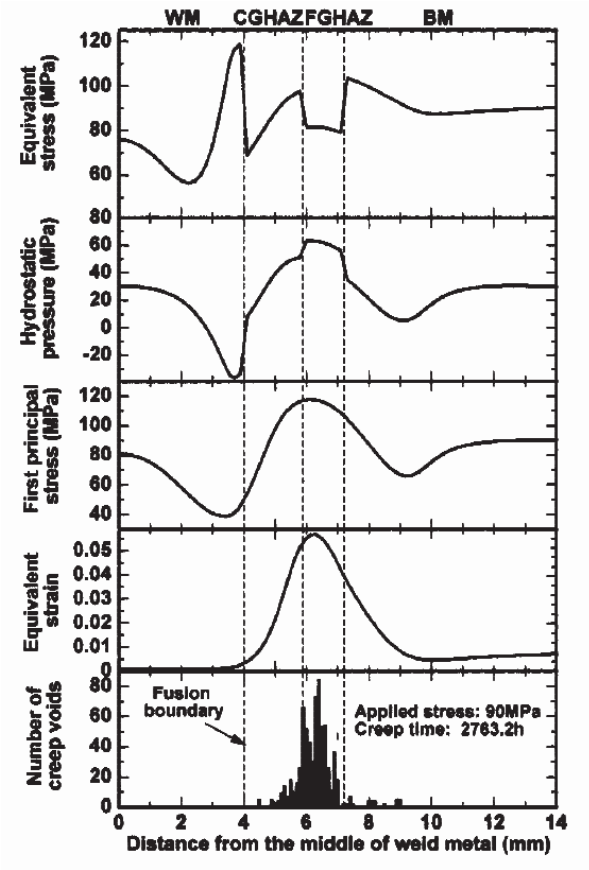

Figure 2.5 Comparison of the distribution of Equivalent stress, Hydrostatic pressure, maximum principal stress and creep voids along the specimen centreline [22].

2.5 Factors Affecting the Deformation of Weldments

2.5.1 The Effect of Geometry

In uniaxial tensile testing [27], since the specimen is considered to have a uniform cross-sectional area and homogeneous material properties, both the stress and strain are reasonably assumed to be homogeneous throughout the gauge section (both along the gauge length and

across the cross-section), Figure 2.6(a). The stress value is determined from the applied load. Therefore, in uniaxal tensile testing, measuring the strain components at any given point in the gauge section provides the link between the stress and the strain, and making it easy to determine the mechanical response of the material. In this case the constitutive mechanical properties (such as the modulus of elasticity, Poisson's ratio, the yield stress or proof stress, and the ultimate tensile strength) governing the response of the specimen to external loads can easily be determined and once the uniaxial applied stress reaches the value of the yield strength of the specimen, the specimen begins to deform plastically.

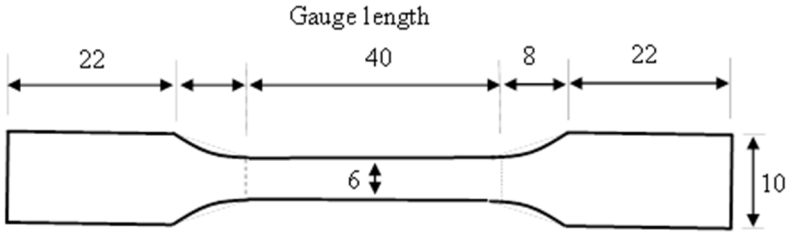

(a)

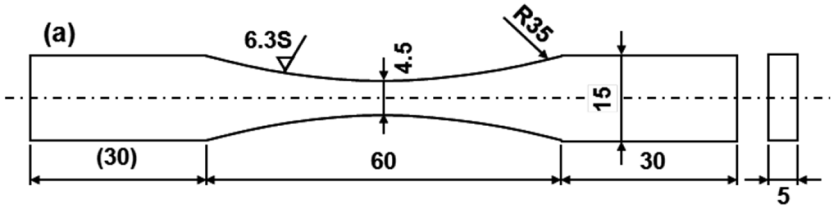

(b)

Figure 2.6 Homogeneous mechanical (tensile and fatigue) testing specimens with (a) uniform cross-section (b) non-uniform cross-section [28, 29].

For multiaxial loading, yielding of the specimen is described using yield criteria such as the von Mises criterion. Under multiaxial loading, a material is predicted to yield when the equivalent stress determined by the von Mises criterion equals the yield strength from a uniaxial tensile test. For yielding in uniaxial loading, the applied uniaxial stress is equal to the equivalent stress or flow stress given by the von Mises criterion. Beyond the yield strength, the specimen is assumed to undergo uniform plastic flow which is accompanied by strain hardening up to the point of necking.

The assumption of uniform deformation is questionable in specimens with non-uniform cross-section area. When a specimen of non-uniform cross-sectional area, such as that shown

in Figure 2.6(b), is subjected to uniaxial loads, the resulting deformation and stress distribution will be non-uniform: the region of minimum cross-sectional area experiencing higher stresses than other sections with larger cross-sectional areas. This will result in localised deformation and, due to high local stresses, the section with minimum cross-sectional area will undergo more plastic deformation than the other regions experiencing lower stresses. In this case, determination of the constitutive mechanical properties will require knowledge of not only the global but also the local mechanical responses of the specimen to external applied loads.

For a more complex geometry such as a notched specimen, Figure 2.7(a), subjected to uniaxial loads, complex non-uniform deformation will result. When an external load is applied, there is stress concentration in the notch region resulting in localised deformation [30, 31]. Whereas the region further from the notched section would experience less stress and deformation compared to the notch region. The level of stress concentration is dependent on the notch radius.

When subjected to uniaxial loads, the notched region of the specimen will yield first and start deforming plastically due to the high local stresses associated with the notch [30, 32]. Due to volume constancy in plastic deformation, the material at the notch root should undergo lateral contraction in response to plastic deformation in the loading direction. However, the surrounding material away from the notch has experienced lower stress (still undergoing elastic deformation), this will constrain or restrict the lateral contraction of the material in the notch region giving rise to triaxial stress state. Therefore, development of a triaxial stress state is associated to plastic or creep constraint in the notch region, such that higher axial stresses will be required to further deform the notch region plastically [32-34].

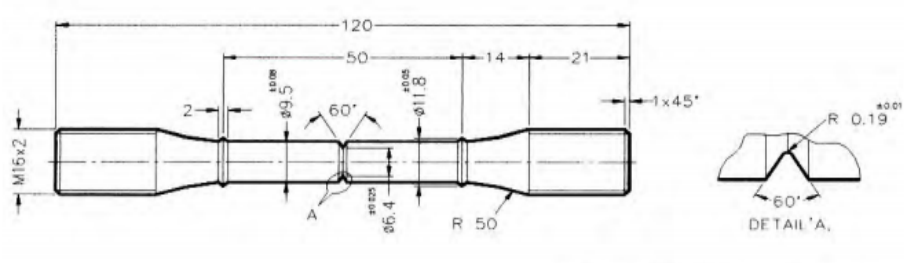

Figure 2.7 Homogeneous specimens with a notch

This is referred to as a constraint effect. Due to the constraint effect, the stress required to cause yielding in notched specimen will be greater than the one observed in a uniaxial tension test and higher axial stresses will be required to further deform the notch region plastically. The level of constraint depends on the notch radius, the net cross-sectional area and the applied load. Similarly, to the case considered above, determination of a material's mechanical properties from a uniaxially loaded notched specimen will require knowledge of both the global and the local mechanical responses of the specimen. As the notch radius reduces, constraint effects increase and the limiting case for the notch is a crack.

2.5.2 The Effect of Inhomogeneity of the Specimen's Material Properties

Apart from geometrical effects, any inhomogeneity of the specimen's material properties has a great influence on its mechanical response and hence its deformation when subjected to uniaxial loads. Although the assumption of homogeneity of material properties is reasonably true for test specimens extracted from as-supplied material, it cannot be applied to heterogeneous materials such as composites or specimens containing weld material or graded properties. The presence of discontinuities such as a weld, alters the stress-strain distribution when the specimen is subjected to external loading. For example, if a specimen has a gradient of a material property, it varying with position along one particular direction, as shown in Figure 2.8, is subjected to uniaxial tension, deformation will vary from point to point and will depend on the local mechanical properties such as the elastic modulus, the yield strength and the flow characteristic. The section with lower elastic modulus would experience higher strains whereas other sections with higher modulus would experience lower strains; the section with lower yield strength would undergo plastic flow once the applied load reaches that yield strength even though other sections remained unyielded, resulting in the localization of plastic deformation.

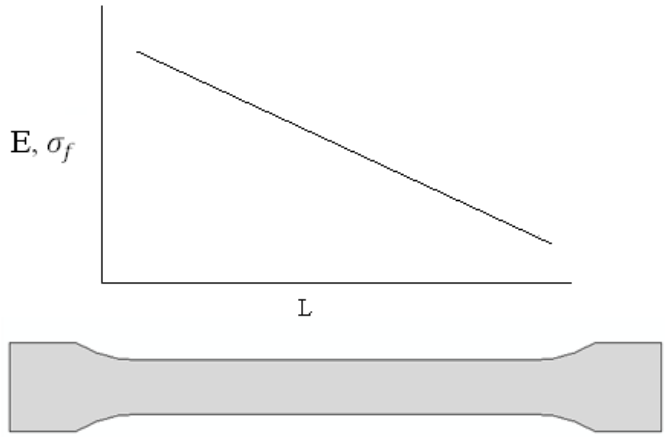

Figure 2.8 Homogeneous specimen with a material property gradient, E varying linearly with position.

To adequately characterize the mechanical properties of such specimens, the local stress-strain behaviour governing the specimen's overall response to an external applied load should be determined.

For an idealised dissimilar metal weld specimen, Figure 2.9(a), with two distinct materials (having different mechanical properties) joined together by a perfect bond or weld, without any gradient in the material properties on either side of the joint, and subjected to external loading in tension, a complex deformation pattern would result around the interface. As the applied load increases, the material of lower yield strength will undergo localized plastic deformation. The high strains in the loading direction, induced in the material with a lower yield strength, should result in lateral contractions in the other perpendicular directions (the x and z directions, if the load is applied in the y-direction). However, lateral contractions of the two materials will be inhibited because of the harder material at the interface, resulting in constrained deformation around the interface (For this type of test specimen, a similar constraint will also be seen in purely elastic loading). This constrained deformation gives rise to errors when the stress-strain properties are determined from the global response of the specimen using conventional test methods.

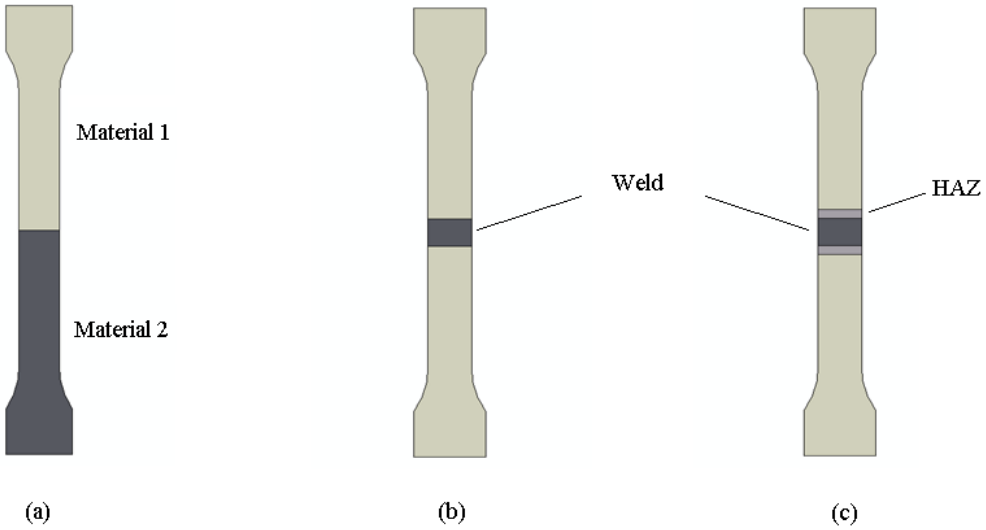

Figure 2.9 Specimens with inhomogeneous properties (a) Idealized dissimilar weld (b) Idealized weld (c) weld with HAZ.

Although the above case reflects the uniaxial mechanical behaviour of an idealized dissimilar weld under simple tensile loading, most welds, in practice, involve fusion, resulting in a weld section with mechanical properties distinct from those of the base material. Fig 2.9(b) shows an example of a specimen containing an ideal weld with mechanical properties lower than those of the base material. When loaded in uniaxial tension, plastic deformation will be confined to the weld. At the onset of the weld's plastic deformation, the presence of the harder base material will result in highly constrained deformation as high triaxial stresses develop in the weld. The triaxial stresses developed completely modify the overall load-displacement response of the welded joint by introducing a significant apparent hardening. This was first experimentally observed by Satoh *et al* [35, 36]; they performed tensile tests on welded plates with an under-matched weld and noted that the weld's apparent increase in strength depended on the weld and specimen geometries. Their results showed that, provided the specimen's width and thickness remain unchanged, as the width of the weld decreases, the overall strength of the joint approaches that of the base material. Any increase in the specimen thickness also resulted in an increase in the overall weld strength. However, any increase in the specimen width resulted in only a limited increase of the weld strength. The apparent increase in the overall strength of the under-matched weld is caused by high triaxiality stresses induced in the specimen due to constraint effects [16]. Ranatowski *et al* [37], analysed the stress state at the interface of mismatched weld; the results showed that the stress state in the vicinity of the weld interface is non-uniform and that the distribution of

stresses near the interface is influenced by the level of mismatch between the mechanical properties the weld and of the base material. A similar conclusion was drawn by Kim *et al* [38], who used FE limit analysis to show that the level of constraint imposed on under-matched welds depends on not only the degree of mismatch but also on the geometry of the weld, particularly on the ratio between the widths of the weld and the specimen. As the width of the weld decreases relative to the specimen width, stress triaxiality in the softer weld material increases significantly.

The case discussed above represents an ideal welded joint, however, in most fusion welds there is a heat affected zone (HAZ) which has properties distinct from those of the weld and base materials, as shown in Figure 2.9(c). Therefore, the stress state developed when a weld with a heat affected zone is subjected to external loading will be more complex than in the case considered above. In the presence of a HAZ, varying levels of triaxiality will develop in the weld and the HAZ depending on the differences in their mechanical properties and their geometries. Generally, the HAZ region is narrow compared to the weld, therefore higher triaxial stresses develop in the HAZ than in the weld. Rodrigues *et al* [39], simulated the deformation of welds with HAZs using various HAZ widths. Their results showed that for very narrow HAZs (HAZ width < 1/3 of the specimen thickness) the strength of the HAZ material could reach a strength equal to that of the base material. Although high constraint effects may seem to be beneficial in increasing the apparent strength of the weaker material, they are detrimental to the failure strength of the component as they decrease the material's failure strength (and ductility) thus encouraging brittle failure and plays a major role in plastic damage evolution [40]. For instance, in the study conducted by Kato *et al* [41], they found that the ductility and plastic strain at fracture position decreased with increase in stress triaxiality. In both room temperature and high temperature creep tests, development of triaxial stresses in welds and notched specimens have been found to greatly affect the development and growth of voids [34, 42, 43].

The interfaces between the regions of the weldment, especially between the HAZ and the base material, are not clearly marked boundaries as idealized above. However, they are characterized by a continuous change in the material properties from one region to another; for instance, the HAZ usually consists of different sections with varying material properties depending on the thermal cycles each region has been exposed to (see Figure 2.4). In this case, when the specimen is subjected to external loading, different levels of stress triaxiality will develop once plastic or creep deformation initiates in the HAZ or in the weld. Therefore,

characterization of the mechanical response of the specimen to external loading will require knowledge of the local mechanical properties and prediction of the constraint effects induced as the specimen undergoes deformation. Using 2D FE analysis, Acar *et al* [44], simulated various weld-HAZ-base material interfaces to study the influence of constraint on the deformation of cross-welds. They concluded that biaxial stresses developing in the softer HAZ are influenced by the presence of the stronger base material and that a multi-material continuous model is more suitable for simulating cross-weld deformation under tensile loads compared to a 3–material model (a model simulating cross-welds as constituting of base, weld and HAZ material only).

Constraint effects due to weld geometry and material mismatch have been studied for high temperature deformation of cross-welds. In the FE analyses carried out by Storesund *et al* [25], it was shown that reducing the HAZ width results in an increase in the creep life of up to 6% in 1Cr-0.5Mo steels. However, results obtained by Li *et al* [45] showed that the development of high triaxial stresses and a concentration of creep strain in the fine-grain HAZ accelerates the formation and growth of voids, thus reducing the creep life. On the other hand, when the weld is overmatched (i.e. the mechanical properties of the weld and HAZ are superior to those of the base material), deformation is concentrated in the base material and high triaxial stresses will develop in the base material near the HAZ-base metal interface [46].

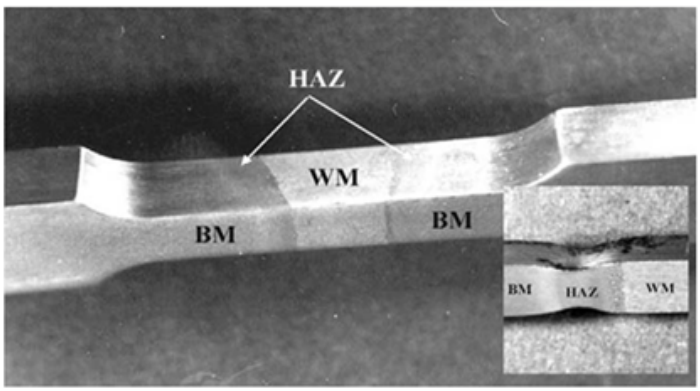

Figure 2.10 Specimen with weld oriented at an angle to the loading direction [16].

For cross-welds with HAZ oriented at an angle to the specimen loading axis (Figure 2.10), it has been observed that increasing the orientation angle increases the creep life of the specimen at low stresses as it increases the triaxial stresses and hence the apparent weld strength [47]. However, FE analysis carried out by Chellapandi *et al* [48] showed that the

induced triaxial stresses are influenced by the orientation angle of the weld to the loading direction and that at high applied stress reduces the creep life of the weldment.

2.6 Optical methods for measurement of deformation

Surface strain and displacement measurements are conventionally carried out using strain gauges, extensometers, LVDTs and other mechanical and electrical displacement measurement instruments. These techniques are highly sensitive and as such can produce accurate surface strain measurements. Therefore, over the years these conventional techniques have been used to assess the stress-strain relationships in regions of structural components where the strain variation is known to be uniform.

Although conventional strain measurement techniques are highly sensitive and capable of producing accurate surface strain measurements, their major limitation is that they only provide averaged information over a limited region. This renders them unsuitable for surface strain measurement for complex structures such as welds. Due to high strain gradients in welds, to characterise its mechanical response to external loading using conventional strain measurement techniques, entails that many separate measurements are carried out, making it tedious and time consuming. For measurement of surface strains in structural components operating at high temperature and in thermo-mechanical experiments, convention strain measurement techniques are unsuitable due to their limitations at high temperature. In the case of contact mechanics problem, the contact length can be very small, especially under small loading, and measuring strain for such contact region using conventional techniques might be very difficult, inaccurate and time consuming.

Despite being inexpensive and effective in some applications, conventional strain-displacement measurement techniques provide only localised measurements averaged over a small region with uniform deformation rendering them unsuitable for complex structures such as welds. To obtain the strain-displacement measurements using conventional techniques, the measurement instrument must be in contact with the surface of the object which makes then unsuitable for high temperature and contact mechanics applications. Due to the above stated limitations of conventional strain measurement techniques, alternative methods which are optical based techniques have been developed. The advantages of optical techniques are that they are non-contact and provide the whole-field strain measurements compared to conventional techniques.

Optical based strain-displacement measurement techniques can be macroscopically classified into two major groups, (i) interferometric and (ii) correlation based approaches [49]. In interferometric strain-displacement measurement techniques, the measurement surface, usually characterised by uniform white texture, is illuminated using structured light such as lasers or fringe projectors. The measurement is performed by processing the phase difference of the scattered light wave from the surface of the specimen before and after loading by means of fringe processing and phase analysis [50].

In correlation based strain-displacement measurement techniques, images of the specimen before (reference image) and after loading are acquired, stored in a digital format and apply image analysis to extract the whole-field shape, displacement or deformation measurements [51]. The technique of using computer based image acquisition and deformation measurements of materials was first proposed by Peters and Ranson in 1982, [52]. Over the years, this technique has been known with different names, such as digital speckle correlation, texture correlation, computer-aided speckle interferometry, electronic speckle photography and today, it is widely referred to as digital image correlation (DIC) [49, 53-57]. In contrast to interferometric techniques, digital image correlation relies on the specimen surface texture, which can be either inherent or artificially applied, for accurate surface deformation measurements and therefore do not require the use of structured light sources such as lasers. Apart from using ordinary incoherent light, optical components such as beam splitters, spatial filters, piezoelectric transducers and vibration isolation table are not required for DIC strain-displacement measurement.

For typical application of DIC strain-displacement measurements, only a specimen surface with random surface features capable of providing unique distributed light intensity, an image acquisition device (a single camera for 2D and two cameras for 3D), and the digital image analysis algorithm for extracting the load induce deformation are required. Note that, in DIC, image acquisition is not only limited to cameras, various acquisition techniques has been applied such scanning electron microscopy (SEM), atomic force microscopy (AFM), scanning tunnelling microscopy (STM) and x-ray imaging [58-62].

2.6.1 Principles of Digital Image Correlation (DIC)

Digital image correlation is a non-contact, full-field measurement technique which provides sub-pixel displacement and strain accuracy by comparing the gray intensity changes of the digital images of the specimen surface acquired before and after deformation [49, 51]. A

series of images captured during the loading period (test duration) are digitized by converting to gray-scale and loaded on to the correlation software. The basic principle operation of DIC software is that the light intensity of the surface features of the specimen subjected to external loading does not change with induced deformation. Therefore, the primary requirement to carry out a DIC test is to ensure that the light intensity remains considerably uniform during imaging and that the specimen possesses surface features that can be tracked by the DIC software. Also important is that the specimen should remain in-plane with the imaging system for the entire test duration, this is especially important for 2D DIC measurements as will be discussed later. The following sections outline detailed description of digital image correlation (DIC) applied for two-dimensional (2D) whole-field strain measurements.

2.6.2 Two-dimensional (2D) Digital Image Correlation

2.6.2.1 Basic Experimental Set-up

As stated above, the basic requirements for carrying out 2D DIC strain-displacement measurements are; a well-prepared specimen surface, a digital image acquisition device such as a camera, specimen surface illumination and an image processing algorithm for displacement/strain computation. Figure 2.11 shows a basic experimental set of 2D DIC strain/displacement measurements.

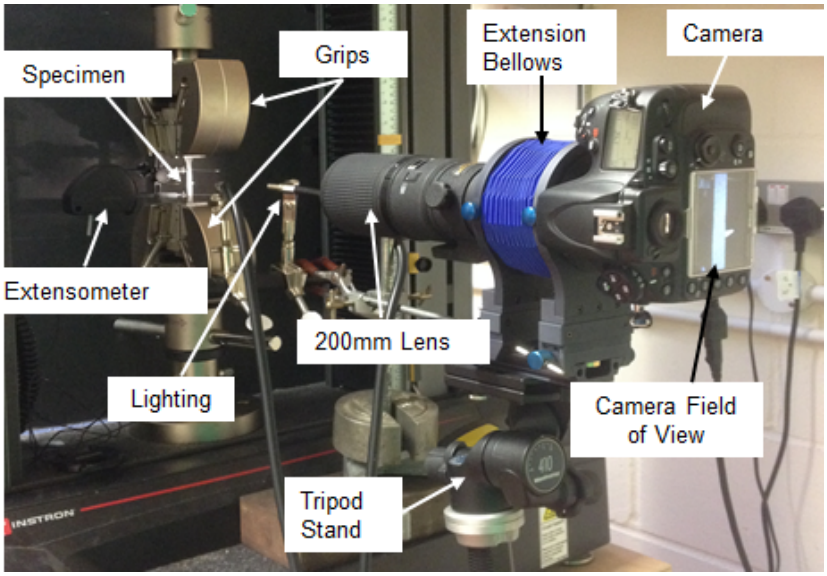

Figure 2.11 2D DIC experimental setup for room temperature tensile testing

For 2D DIC strain measurements, a single camera is used and therefore for accurate strain measurements, the specimen surface is required to be flat and perpendicular to the optical axis of the camera. This eliminates errors due to pseudo-strains which arise when there is literal movement of the specimen surface towards or away from the focal plane of the camera (in the z-direction) [51, 63]. Prior to the experimental test, a reference digital image of the specimen in its undeformed state is taken and during the test, a series of digital images are acquired at specified time intervals or load steps. After the test, each of the images acquired during the test are analysed independently with respect to the reference image to quantify the whole-field strain at specific load steps. For successful image correlation between the undeformed and the deformed image, the specimen surface is required to have unique surface features which should be tracked during deformation of the specimen. This is discussed in the next section.

2.6.2.2 Subsets and Speckle Patterns

As stated above, digital image correlation relies on surface textures of the measurement specimen for the correlation algorithm to computing the whole field displacement/strain map by comparing the light intensity (gray level) changes of the specimen surface between the deformed and the undeformed image. The correlation algorithm computes the whole-field displacement/strain map by searching local matched points between the reference image and the one captured after the specimen is deformed. Since the gray level associated to a single pixel in the reference image can be found in thousands of other pixels in the image captured when the specimen is in the deformed state; correlation between two images using a single pixel is impossible as a unique solution cannot be obtained. Therefore, the image is virtually subdivided into zones of interests known as subsets or sub-regions with unique light intensity (gray-level) thus forming a virtual mesh or surface grid for easy tracking of surface features. Figure 2.12 shows an example of a DIC software generated surface grid and a subset tracking mechanism used.

In the case were the specimen surface does not possess a random texture, correlation of subsets between two images would not be found. This is referred to as the ‘aperture problem’ [51]. Therefore, the fundamental requirement for digital image correlation is that the specimen surface should have a random texture capable of producing unique light intensity from point to point such that the correlation process should find only one valid matching

position within the search region of the subset. For this reason, regular textures such as grids or repeated patterns should not be used.

For a subset to possess a unique light intensity, a speckle pattern covering the surface of the specimen is required. The speckle pattern with unique shape and gray level can be natural or artificially applied by using paint. Figure 2.13 shows an artificially speckle pattern on the surface of the specimen applied by fine spraying of black paint on a white background. The speckle size is very important in image correlation because it has a direct bearing on the accuracy of the measurements and is dependent on the size of the subset used. For instance, if the applied speckle pattern is too large, the subset size used in the correlation process should be large. This will improve the accuracy of the correlation process; however, the spatial resolution would be decreased. Alternatively, a lower magnification can be used to decrease the speckle size. For accurate displacement/strain measurement using DIC, it has been found that at least 3 speckle features in a subset are required [51, 64]. The effect of subset size on the accuracy of the displacement/strain measurements are discussed later.

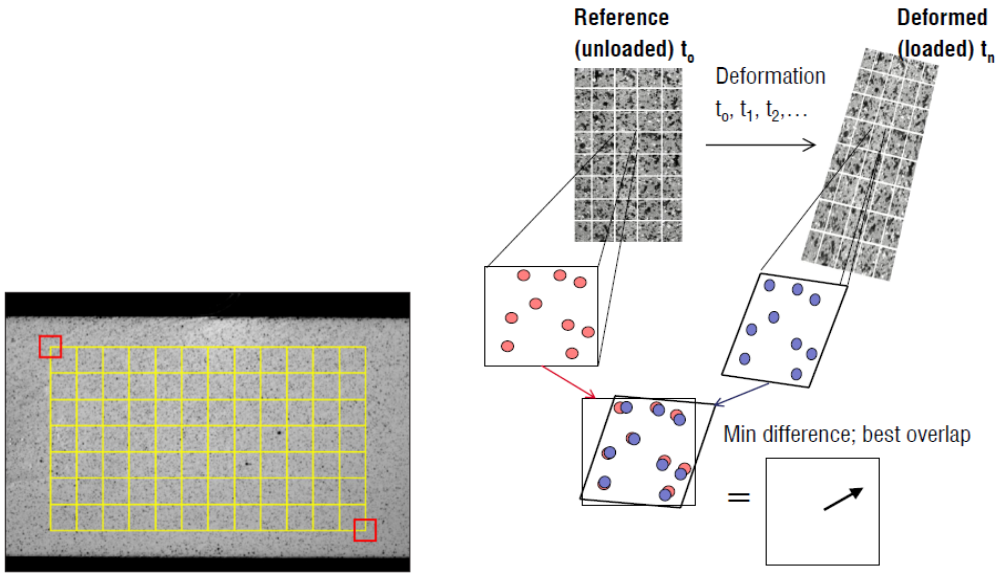

(a) (b)

Figure 2.12 (a) subdivision of the region of interest into subsets (b) subset tracking [49, 65]

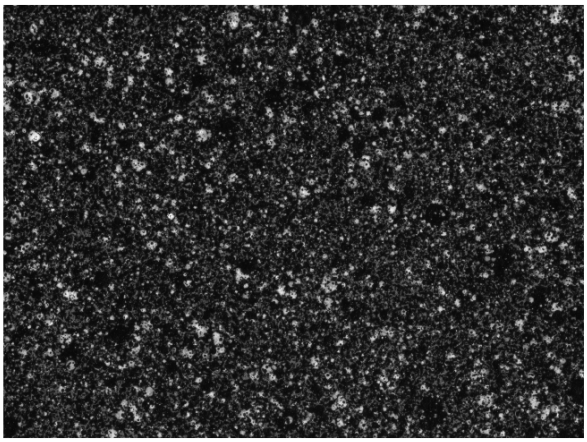

Figure 2.13 Example of a speckle pattern

2.6.2.3 Correlation algorithm

The concept for matching subsets from the reference image to the ones taken when the specimen is in its deformed state is based on the facts that each subset has a unique light intensity that can be tracked throughout the experimental test duration. Therefore, to compute the displacement, the subset on the reference image should be found in the image taken after deformation by searching the area of same light intensity distribution. Once the location of the reference subset in the image taken after deformation, is found, the horizontal (u) and vertical (v) displacements of the centre point of the subset is computed. For a unique displacement solution to be obtained, the subset must be unique (that is; should have a unique light intensity), hence the need for a random speckle pattern on the surface of the specimen as explained in the previous section.

2.6.2.4 Correlation Functions

To locate the reference subset in the image taken after deformation, a quantitative evaluation of the similarity between the reference subset and any selected area of the image taken after deformation should be carried out. This is achieved by using correlation functions. Although the subset matching process is based on the fact that each subset has a unique light intensity that can be tracked throughout the test duration, local density and hence the local light absorption and scatter changes with deformation of the specimen. Therefore, the gray-level conservation concept is not exactly satisfied, for this reason gray-level corrections methods are applied [61, 66]. Various correlation functions have been developed [49, 51]. One of the

commonly used correlation functions is the least squares correlation function which is, for simplicity, defined such that $f(x, y)$ and $g(x', y')$ are the gray value distributions of the reference image and the one from the image taken after deformation, respectively. For a square subset of size $(2M + 1) \times (2M + 1)$ pixels, the correlation coefficient C is defined as,

$$C = \sum_{i=-M}^{M} \sum_{j=-M}^{M} [f(x_i, y_i) - g(x_i', y_i')]^2 \qquad 2.18$$

where (x_i, y_i) and (x_i', y_i') represents coordinates of a point on the subset before and after deformation, respectively. The parameters of the correlation function above have been shown to be sensitive to changes in light intensity on the surface of the specimen, which can easily arise during a standard test [51]. Therefore, the normalised version of the least squares correlation criterion (zero-normalised sum of squared differences – ZNSSD) capable of accommodating change in light intensity is preferred, and is defined as,

$$C = \sum_{i=-M}^{M} \sum_{j=-M}^{M} \left[\frac{f(x_i, y_i) - f_m}{\Delta f_m} - \frac{g(x_i', y_i') - g_m}{\Delta g_m} \right]^2 \qquad 2.19$$

When the correlation coefficient $C = 1$; the subset in the reference image is fully correlated to the one taken after deformation and when $C = 0$, the two subsets are not correlative. Therefore, the best match between two images is achieved by minimization of the correlation coefficient C and this is achieved by using iterative methods for non-linear optimisation process.

2.6.2.5 Gray level interpolation

Digital images are composed of thousands of pixels with varying gray-scale values. Usually, these values change abruptly from one pixel to another. The coordinates of a point (x_i', y_i') in the image taken after deformation may locate at non-integer pixel position referred to as subpixel location. If a correlation criterion accurate to within one pixel is applied, the results obtained would have errors much larger than the quantity to be measured (sub-pixel displacement). Therefore, for accurate computation of sub-pixel displacements, interpolation between the pixels to obtain a continuously varying intensity pattern is required [67]. Several interpolation algorithms have been developed and implemented. Figure 2.14 illustrates how the gray level interpolation scheme is implemented using a simple bilinear interpolation for four-pixel points. In digital images, the gray value of a pixel is assumed to be the value at the centre of the pixel, denoted as; $G(i, j)$, $G(i + 1, j)$, $G(i, j + 1)$ and $G(i + 1, j + 1)$ for the four pixels in Figure 2.14. (i, j), $(i + 1, j)$, $(i, j + 1)$ and $(i + 1, j + 1)$ are the integer pixel

positions. The gray value, $G(x^*, y^*)$, at a sub-pixel point (x^*, y^*) can be obtained using a bilinear interpolation function expressed as,

$$G(x^*, y^*) = a_{00} + a_{10}x' + a_{01}y' + a_{11}x'y' \qquad 2.20$$

where x' and y' are the distance along the x and y direction from (i, j) to (x^*, y^*), which is $x' = x^* - i$ and $y' = y^* - j$. $a_{00}, a_{10}, a_{01} and\ a_{11}$ are the coefficients of the bilinear interpolation function and are dependent on the gray values at the integer pixel points of the four pixels.

Although lower order gray value interpolation schemes have been used, high order ones such as bicubic or biquintic spline interpolation have been found to give more accurate results compared and are generally preferred [68, 69].

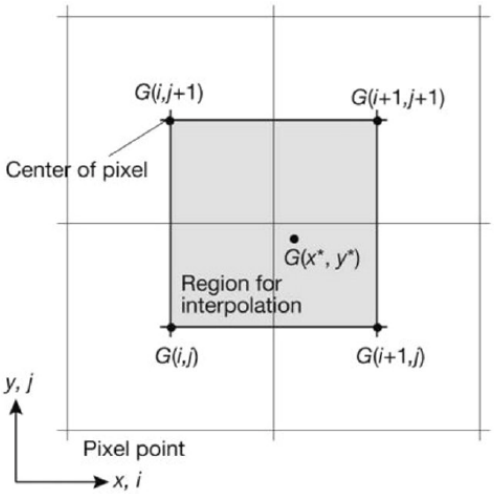

Fig. 2.14 Pixel points and the interpolation region for bilinear interpolation

2.6.2.6 Subset shape function

Figure 2.15 schematically illustrates the deformation process of a square pixel array of 20×20 pixels in both x and y directions. A 6×6 pixels subset is shown within this square array, the dashed line represents the reference subset and the solid line symbolizes the corresponding subset in the image taken after deformation. The point $P(x_0, y_0)$ is the centre of the subset and point $Q(x, y)$ is one of the neighbouring points within the reference subset. If the specimen undergoes rigid body translation only, correlation between the reference

subset and the subset in the image taken after translation can be carried out by rigidly moving the original subset. This is referred to as a zero-order shape function. However, for most complex displacement measurements, the specimen undergoes elongation, compression and shear. Therefore, the use of in-plane translated subsets, or zero-order shape function would result in serious decorrelation between the reference subset and the target subset. For this reason, additional reason, first order or higher order shape functions which gives the subset additional degrees of freedom are used [52, 53]. Considering point P and its neighbouring point Q in Figure 2.15, if deformation is sufficiently small, the location of the neighbouring point after deformation Q' can be estimated using a first order shape function or affine transformation,

$$x' = x + u + \frac{\partial u}{\partial x}\Delta x + \frac{\partial u}{\partial y}\Delta y \qquad 2.21(a)$$

$$y' = y + v + \frac{\partial v}{\partial x}\Delta x + \frac{\partial v}{\partial y}\Delta y \qquad 2.21(b)$$

where Δx and Δy are the *x* and *y* directional components of the distance from the centre of the subset to the point *(x,y)* respectively. u and v are the subset displacements in the x and y directions; $\frac{\partial u}{\partial x}$, $\frac{\partial u}{\partial y}$, $\frac{\partial v}{\partial x}$ and $\frac{\partial v}{\partial y}$ are displacement gradients. For more complex deformation, second order shape functions have been used to improve the accuracy of displacement/strain measurements [70]. However, higher order shape functions are more computation demanding due to increased number of variables involved.

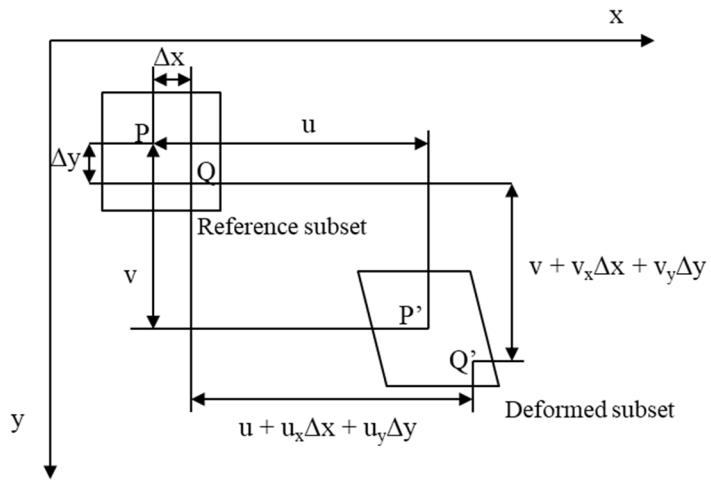

Figure 2.15 Schematic representation of 2D deformation of a square pixel array

2.6.2.7 Correlation Process

As stated above, the displacements are determined with subpixel accuracy by searching for the displacements (u, v) and displacement gradients $\left(\frac{\partial u_x}{\partial x}, \frac{\partial u_x}{\partial y}, \frac{\partial u_y}{\partial y}, \frac{\partial v}{\partial y}\right)$ which minimize/maximize the correlation coefficient, C. To achieve subpixel accuracy, the correlation process is carried out in two consecutive steps. In the first step (initial guess), the approximate displacement of a subset is estimated to be within the accuracy of a pixel using a zero-order shape function. In the second step, the initial estimate of the displacements and displacement gradients are refined by applying gray level interpolation scheme and a first order or higher order subset shape function in order to achieve subpixel accuracy. Therefore, for subpixel accuracy, an initial displacement estimate close to the true value of the actual displacement is required. For instance, for iterative spatial cross-correlation algorithms such as the Newton-Raphson method, proper convergence would only occur if the initial displacement estimate is within ±7 pixels off the actual displacement [69]. A number of subpixel correlation algorithms have been developed over the years and detailed reviews of these algorithms are given in reference [49] and [71]. In the current study, all the DIC displacement computations were carried out using an iterative least squares algorithm of a commercial DaVis Software developed by LaVision [65]. The following section gives a summary of how whole-field displacements are computed using the iterative least squares algorithm.

2.6.2.8 DIC using Iterative Least Squares Algorithm

The whole-field displacement computation using DIC is time consuming due to the number of subsets and the number of iterations required for the algorithm to converge. The iterative least squares algorithm is one of the algorithms which has been developed to improve the efficiency of the displacement vector computation without compromising on the accuracy of the obtained results [72]. As stated above, the principle of DIC is fundamentally based on the assumption that the gray level intensity of a point in the reference image remains the same compared to the image taken after specimen surface has been deformed. Therefore, in optical flow methods, the basic expression for matching a point (x_i, y_i) in two successive images is given as [51],

$$f(x_i, y_i) = g(x_i', y_i') \qquad i = 1,2, \dots, n \qquad 2.22$$

where $f(x_i, y_i)$ and $g(x_i', y_i')$ are gray intensity value in the reference image and the one taken after deformation, respectively. n represents the number of pixels contained in the reference subset. The x and y displacement of the neighbouring point is given by $u(x_i, y_i)$ and $v(x_i, y_i)$, respectively. In reality, the conservation of gray intensity value is difficult to attain. Therefore, a model capable of reducing displacement measurement errors due to change in gray intensity value such as a linear intensity change model can be used;

$$a \times f(x_i, y_i) + b = g(x_i', y_i') \qquad i = 1,2,\ldots,n \qquad 2.23$$

where a and b are the scale factor and offset of the intensity change, respectively. For subpixel displacement measurements, it is assumed that the deformation between the reference and the target image is quite small. Therefore, the first order shape function, given in Equation 2.21, together with interpolated subpixel gray intensity values are applied. Substituting, Equation 2.21 into the linear intensity change model, Equation 2.23, gives [72];

$$g\left(x_i + u + \frac{\partial u}{\partial x}\Delta x_i + \frac{\partial u}{\partial y}\Delta y_i, y_i + v + \frac{\partial v}{\partial x}\Delta x_i + \frac{\partial v}{\partial y}\Delta y_i\right) - a \times f(x_i, y_i) + b = 0 \qquad 2.24$$

For a neighbouring point in a subset of the image taken after deformation, $g(x_i + u, y_i + v)$, Equation 2.24 yields the following function,

$$\boldsymbol{F_i(p)} = g_i + g_{x_i}u + g_{x_i}\frac{\partial u}{\partial x}\Delta x_i + g_{x_i}\frac{\partial u}{\partial y}\Delta y_i + g_{y_i}v + g_{y_i}\frac{\partial v}{\partial x}\Delta x_i + g_{y_i}\frac{\partial v}{\partial y}\Delta y_i - af_i + b \cong 0 \qquad 2.25$$

where $\boldsymbol{p} = \left\{u \;\; v \;\; \frac{\partial u}{\partial x} \;\; \frac{\partial u}{\partial y} \;\; \frac{\partial v}{\partial x} \;\; \frac{\partial v}{\partial y} \;\; a \;\; b\right\}^T$ is the unknown parameter vector containing subpixel displacements, displacement gradients and gray intensity value correction parameters. The x and y directional spatial gradients of the image taken after deformation at position (x_i', y_i') are given by g_{x_i} and g_{y_i}, respectively.

To obtain accurate displacement measurement, the non-linear function $\boldsymbol{F(p)}$ (Equation 2.25) is solved using iterative least squares algorithm. This is implemented through optimization using the Newton-Raphson method expressed as,

$$\boldsymbol{F}_i(\boldsymbol{p}^{k+1}) = \boldsymbol{F}_i(\boldsymbol{p}^k) + \nabla \boldsymbol{F}_i(\boldsymbol{p}^k)(\boldsymbol{p}^{k+1} - \boldsymbol{p}^k) = 0 \qquad 2.26$$

where $\boldsymbol{p}^{k+1}$, $\boldsymbol{p}^k$ are solutions of $(k+1)$th and kth round iteration, respectively. The detailed derivation and implementation of iterative least squares algorithm is described in [72].

Prior to subpixel displacement measurements, the initial estimate of the parameter vector $\boldsymbol{p}$ is obtained using a direct spatial domain searching scheme which gives integral-pixel displacements of a given point. The calculation path is based on the reliability guided technique, such that the displacement calculation initiates by searching for a point in the image taken after deformation corresponding to the seed point in the reference image [73].

Thereafter, four or eight neighbouring points are analysed, and the image correlation scheme is applied by selecting a neighbouring point which minimizes/maximizes the correlation function. By applying this technique, a reliable image matching path with computed displacements independent of the path is obtained.

2.7 Uncertainties in Digital Image correlation

2.7.1 Displacement Accuracy and Precision

Despite major improvements in digital image correlation, displacement accuracy and precision remain important aspects of the technique. In the early stages of DIC development, the displacement accuracy was limited to the pixel size, however with the development of algorithms for grey-level interpolation within a subset, subpixel displacement accuracy is now achieved [74].

The accuracy and precision of the measured displacements in DIC are influenced by uncertainties in the measurements made. The uncertainties in DIC measurements can be divided into two categories: those arising from systematic errors which affect the accuracy, and random errors which have a bearing on the precision of the measured displacement/strain. Displacement accuracies of 0.01pixel have been reported [65, 75, 76] with DIC. However, accuracy can be improved by using a high-resolution imaging system and optimising the experimental set-up to minimise both systematic and random errors. It should be noted that the accuracies reported in the literature do not give a benchmark of the absolute displacement accuracy that can be attained when using DIC as there are many different factors that affect DIC measurements. As a result, the attainable accuracy and precision in DIC measurements vary depending on the experimental set-up, the imaging system and the correlation software used. It is important to understand the sources of uncertainties in DIC measurements and the following sections discuss uncertainties due to both systematic and random errors.

2.7.2 Systematic Errors

These are errors associated with the measurement system and the experimental set-up and have been widely investigated. In DIC, the systematic errors can be classified into errors due to the image accusation system, to the experimental set-up and to the correlation algorithm.

2.7.2.1 Image Acquisition system

2.7.2.1.1 Non-parallel camera sensor and image distortion

Among the major requirements of 2D DIC is that the specimen surface should be parallel to the camera sensor target. Although it is commonly assumed that this requirement is fulfilled, even where the camera sensor is considerably non-parallel to the specimen surface, this may give rise to errors in the measured displacements. The errors introduced on the measured in-plane displacement depend on the level of tilt of the camera sensor and are similar to the ones obtained by any out-of-plane rotation as shown in section *2.7.2.1.3*.

Image distortion can occur as a result of an imperfect lens. Calibration methods have been developed which remove the effects of image distortion from the measured results [51].

2.7.2.1.2 Speckle Pattern

Displacement measurement using DIC is fundamentally based on tracking speckle patterns on the surface of a specimen as it undergoes deformation and the accuracy and precision of DIC measurements depend on the shape, size and intensity of the speckle pattern used. Pan *et al* [77] developed a mathematical model, which indicates that the speckle pattern induces random errors in the measured displacement, as the standard deviation of the measured displacement is closely related to the speckle pattern. Using virtually translated digital images, Haddadi *et al* [63] noted the dependence of the speckle pattern on the subset size used in DIC, concluding that poor speckle patterns result in more uncorrelated regions in the displacement field thus affecting the accuracy of the results. Lecompte *et al* [78] used numerically deformed images to study the effects of the speckle pattern on the accuracy of DIC measurements. They concluded that, to reduce errors in the measured displacement, an optimal ratio between the speckle pattern and the subset size should be obtained for a given experimental set-up. Crammond *et al* [64] investigated the effects of speckle size, morphology, distribution and density on uncertainties in the measured displacement and concluded that to reduce uncertainties, the speckles should be evenly distributed and of even sizes. Generally, although the speckle pattern has a great influence on the measured displacement, its effect depends on the subset used and this is discussed in section 2.7.2.1.8.

2.7.2.1.3 Out-of-plane translation and rotation

Out-of-plane motion in the z-direction is one of the major sources of displacement measurement errors in 2D DIC. Any movement of the object/specimen in the z-direction changes the magnification of the image resulting in a uniform extension or contraction which is measured by the DIC software as displacement in the x-y plane. For 2D DIC, the pseudo strains due to out-of-plane movement can be obtained from,

$$\varepsilon_{xx} = \varepsilon_{yy} = -\frac{\Delta Z}{Z} \qquad 2.27$$

where z is the working the distance and Δz is the change in working distance [79].

Besides, rigid body motion in the z-direction could result in the specimen moving out of the depth of focus thus making correlation between the deformed and the undeformed image difficult. These errors are easily dealt with by using telecentric lens [63] [79].

Apart from out-of-plane translation, out-of-plane rotation is also one of the major sources of error in 2D DIC. Sutton *et al* [79] derived an expression describing the effects of out-of-plane rotation on in-plane displacement based on a pin-hole camera system as;

$$\varepsilon_{xx} \approx -\frac{Y \sin\theta}{Z} \qquad 2.28(a)$$

$$\varepsilon_{yy} \approx \cos\theta - 1 - \frac{Y \sin 2\theta}{Z} \qquad 2.28(b)$$

where Y is the in-plane y-dimension of the object and Z is the object distance.

Apart from out-of-plane rotation, in-plane rotation also gives rise to errors in the measured in-plane displacement and these were found to be in the range of 0.4 to 1.5×10^{-3} mm [63].

The effects of out-of-plane motion and rotation can be dealt with by using telecentric lens or increasing the distance between the specimen and the image plane in the camera. It should be noted that these techniques can only be applied to reduce the effects of in or out-of-plane motion and rotation. On the other hand, in the case were in-plane displacement results in non-uniform deformation of the specimen surface (such as curved surfaces around a crack), errors from this type of out of place deformation can only be dealt with by using 3D DIC which involves using two cameras so as to capture the out-of-plane deformation [51] [79].

2.7.2.1.4 Correlation Algorithm

Uncertainties in 2D DIC displacement measurements can arise due to systematic errors from the correlation algorithm as the accuracy of the measured displacement is influenced by correlation algorithm parameters such as the correlation function, the sub-pixel interpolation scheme, the subset shape function and the subset size used for displacement computation. The following sections outline the effects of these parameters on the measured displacement.

2.7.2.1.5 Correlation Functions

As Discussed in section 2.6.2.4, several different correlation functions can be applied in displacement measurement and these have been found to have varying effects on the uncertainties in the measured displacement. For instance, the zero-normalised sum of squared difference (ZNSSD) and zero-normalised cross-correlation (ZNCC) functions have been found effective in correlating images with variable lighting as these correlation functions are insensitive to change in the illumination on the specimen surface [51, 80].

2.7.2.1.6 Subpixel interpolation

To attain subpixel accuracy in the measured displacement field, various subpixel interpolation schemes have been applied. Generally, higher order subpixel interpolation schemes such as bicubic interpolation, B-spline interpolation and biquintic-spline are found to be robust and accurate in reconstructing the intensity and the intensity gradients, although at the expense of computation time [69]. Using both theoretical and experimental techniques, Wang *et al* [81] [82] carried out quantitative error assessment in pattern matching, in the presence of uncorrelated Gaussian intensity noise for each pixel location, as a function of the subpixel interpolation scheme, pattern noise intensity, subset size, strain and image contrast. From their theoretical results, they concluded that the expectations of measured motions are biased and that the bias is a function of the interpolation difference between the translated and the reference images, the magnitude of the white noise, decimal part of the motion and the pattern intensity gradient. They also noted that increasing the pattern noise intensity results in increased systematic errors. Since bias in the measured displacement due to the interpolation scheme directly translates to a bias in the strain measurements, it is recommended that higher order interpolation methods are employed to improve accuracy in DIC measurements [51] [83].

2.7.2.1.7 Subset shape function

The subset shape function transforms pixel coordinates in the reference subset into coordinates in the image after deformation. During deformation, the specimen may experience elongation, compression, and/or shear or in-plane rotation. In the presence of such complex displacement fields, application of a 0-order shape function (square subset translation) could lead to errors, due to decorrelation between the reference image and the one taken after deformation. For this reason, first-order (Affine) and second-order correlation functions are used. Schreier *et al* [84] analysed systematic errors due to under-matched subset shape functions and found that second order shape functions produce smaller systematic errors in the measured displacement than linear shape functions, at approximately the same levels of random error. Theoretical analysis carried out by Lu *et al* [70] confirms that using second-order shape functions improves the displacement accuracy.

2.7.2.1.8 Subset size

The spatial resolution of DIC is governed by the subset size, making it one of the critical parameters of the technique [85]. A subset is required to have unique features (speckle pattern) that distinguish it from its neighbouring subsets. This sets a limit on the minimum subset size that can be applied for DIC measurement and it has been suggested that a subset should be big enough to contain at least 3 speckle patterns [51, 78]. To avoid aliasing, each speckle must contain at least 3pixels. Therefore, the choice of subset used is governed by the size of the speckle patterns applied to the surface of the specimen. For instance, for accurate correlation, large speckles necessitate the use of large subset sizes which results in reduced spatial resolution. However, increasing the subset size does not necessary guarantee an increase in accuracy, Reu *et al* [86] noted that increasing the subset size beyond the optimum size for a given speckle pattern increase uncertainties in the measured displacement. Besides, using large subset sizes results in increased errors due to variation in the displacement gradients within the subset and is not ideal in characterising specimens with high strain gradients such as cracks and weld interfaces. Large step sizes and displacement filter lengths also reduce the ability to resolve strain gradients [87]. Therefore, small subset sizes are recommended for accurate measurement of displacement gradients and these, in turn, require small speckles [88]. Considering the two conflicting demands on subset size selection, there is always a trade-off when making a choice of subset size. To select an appropriate subset

size with a minimum influence on noise, Pan *et al* [77] developed a parameter based on the sum of the squared differences in intensity gradients (SSSIG), as a quantification of subset entropy, which is used for selecting the ideal subset size.

2.7.3 Random Errors

2.7.3.1 Noise

The measured displacement in DIC is sensitive to image acquisition noise such as digitisation noise, read-out noise and photon noise, and these have been assessed to establish the extent to which they affect measurement results. For example, Besnard *et al* [89], analysed the effects of image acquisition noise by corrupting a reference image with varying levels of zero mean Gaussian noise without superimposing any displacement field on the image. From their analysis, they concluded that the standard deviation of the displacement error is proportional to the standard deviation of the image noise and inversely proportional to the average squared grey-level gradients and the subset size. Similar conclusions have been made by Amiot *et al* [76] who used synthetic software generated images with speckle patterns similar to the ones used in real DIC specimens. They studied discrepancies between the DIC-evaluated displacements and prescribed ones statistically in terms of random errors and concluded that the standard deviation of random error increases with noise level and decreases with subset size.

2.7.4 Summary

Displacement measurements in 2D DIC are influenced by a few factors as discussed above. Generally, uncertainties in DIC measurements can be classified into systematic ones which have a bearing on the accuracy of the measurements and random ones which affect the precision of the DIC measurements. Although the effects of the above discussed factors, are studied separately; experimentally, it is challenging to isolate one error source and ascribe a value to its contribution to uncertainties compared to other factors. Therefore, for high accuracy in DIC measurements, optimisation of the experimental set-up and image acquisition system is recommended. Further review of literature is given in Chapters four and five.

2.8 REFERENCES

1. Evans, W.R. and B. Wilshire, *Introduction to Creep*. 1993, Institute of Materials: London.
2. Kassner, M.E., *Fundamentals of Creep in Metals and Alloys (2nd Edition)*. 2009, Elsevier.
3. Evans, R.W. and B. Wilshire, *Introduction to creep*. The Institute of Materials. 1993, London.
4. Frost, H.J. and M.F. Ashby, *Deformation mechanism maps: the plasticity and creep of metals and ceramics*. 1982: Pergamon press.
5. Dieter, G.E. and D.J. Bacon, *Mechanical metallurgy*. Vol. 3. 1986: McGraw-hill New York.
6. Evans, R. and B. Wilshire, *Creep of Metals and Alloys, The Inst.* Metals, London, 1985. **6**.
7. Hayhurst, D.R., *Computational Continuum Damaged Mechanics: Its use in the Prediction of Creep in Structures — Past, Present and Future*, in *IUTAM Symposium on Creep in Structures: Proceedings of the IUTAM Symposium held in Nagoya, Japan, 3–7 April 2000*, S. Murakami and N. Ohno, Editors. 2001, Springer Netherlands: Dordrecht. p. 175-188.
8. Kowalewski, Z., D. Hayhurst, and B. Dyson, *Mechanisms-based creep constitutive equations for an aluminium alloy.* The Journal of Strain Analysis for Engineering Design, 1994. **29**(4): p. 309-316.
9. Murakami, S., *Continuum damage mechanics: a continuum mechanics approach to the analysis of damage and fracture*. Vol. 185. 2012: Springer Science & Business Media.
10. Holdsworth, S., *Developments in the assessment of creep strain and ductility data.* Materials at high temperatures, 2004. **21**(1): p. 25-31.
11. British Energy, G., *AGR Materials Data Handbook R66*. July 2004.
12. Garofalo, F., *Fundamentals of creep and creep-rupture in metals*. 1965: Macmillan.
13. Evans, R.W., B. Wilshire, and I.o. Metals, *Creep of Metals and Alloys*. 1985: Institute of Metals.
14. Harrison, W., Z. Abdallah, and M. Whittaker, *A model for creep and creep damage in the γ-titanium Aluminide Ti-45Al-2Mn-2Nb*. Materials, 2014. **7**(3): p. 2194-2209.

15. Penny, R.K. and D.L. Marriott, *Design for creep*. 2012: Springer Science & Business Media.
16. Dexter, R.J., *Significance of strength undermatching of welds in structural behaviour.* in: K.H. Schwalbe, M. Koçak (Eds.), Mismatching of Interfaces and Welds, GKSS Research Center Publications, 1997: p. 55–73.
17. Chellapandi, P. and S. Chetal, *Influence of mis-match of weld and base material creep properties on elevated temperature design of pressure vessels and piping.* Nuclear Engineering and Design, 2000. **195**(2): p. 189-196.
18. Viswanathan, R., *Damage mechanisms and life assessment of high temperature components*. 1989: ASM International.
19. Kimmins, S. and D. Smith, *On the relaxation of interface stresses during creep of ferritic steel weldments.* The Journal of Strain Analysis for Engineering Design, 1998. **33**(3): p. 195-206.
20. Smith, D.J., N.S. Walker, and S.T. Kimmins, *Type IV creep cavity accumulation and failure in steel welds.* International Journal of Pressure Vessels and Piping, 2003. **80**(9): p. 617-627.
21. Iwadate, T., Prager, M., and Humphries, M. J., *Reliability of New and Old Chrome-Moly Steels for Hydrogen Processing Vessels: Part II: Enhanced Perfomance.* In New Alloys for Pressure Vessels and Piping, ASME, New York, 1990: p. 38 - 47.
22. Li, D., Shinozak, K., and Kuroki, H., *Stress-strain deterioration in heat affected weld zone in high Cr ferritic heat resistant steel.* Materials Science and Technology, 2003. **19**: p. 1253 - 1260.
23. Watanabe, T., et al., *Creep damage evaluation of 9Cr–1Mo–V–Nb steel welded joints showing Type IV fracture.* International Journal of Pressure Vessels and Piping, 2006. **83**(1): p. 63-71.
24. Li, Y., et al., *Evaluation of creep damage in heat affected zone of thick welded joint for Mod. 9Cr–1Mo steel.* International Journal of Pressure Vessels and Piping, 2009. **86**(9): p. 585-592.
25. Storesund, J. and S.T. Tu, *Geometrical effect on creep in cross weld specimens.* International Journal of Pressure Vessels and Piping, 1995. **62**(2): p. 179-193.
26. Hyde, T., et al., *Effect of weld angle and axial load on the creep failure behaviour of an internally pressurised thick walled CrMoV pipe weld.* International Journal of Pressure Vessels and Piping, 2001. **78**(5): p. 365-372.

27. ASTM-E8/E8M, *13a Standard Test Methods for Tension Testing of Metallic Materials*. 2013.
28. Standard, A., *E8/E8M-13a*. Standard test methods for tension testing of metallic materials. ASTM International, West Conshohocken, PA, 2013.
29. E606/E606M-12, A., *Standard test method for strain-controlled fatigue testing*. 2012, ASTM International West Conshohocken, PA.
30. Hertzberg, R.W., *Deformation and fracture mechanics of engineering materials.* Journal of Materials Education, 1997. **19**: p. 227-232.
31. Qu, R., P. Zhang, and Z. Zhang, *Notch effect of materials: strengthening or weakening?* Journal of Materials Science & Technology, 2014. **30**(6): p. 599-608.
32. Xu, X., et al., *Effects of creep ductility and notch constraint on creep fracture behavior in notched bar specimens.* Materials at High Temperatures, 2016. **33**(2): p. 198-207.
33. Luo, Y., et al., *Creep failure prediction of brazing joints with double notches.* Materials & Design, 2016. **100**: p. 271-279.
34. Wen, J.-F., et al., *Effects of Stress Level and Stress State on Creep Ductility: Evaluation of Different Models.* Journal of Materials Science & Technology, 2016. **32**(8): p. 695-704.
35. Satoh, K. and M. Toyoda, *Static strength of welded plates including soft interlayer under tension across a weld line.* Transactions of the Japan Welding Society, 1970. **1**(2): p. 10-17.
36. Satoh, K. and M. Toyada, *Joint Strength of Heavy Plates With Lower Strength Weld Metals.* Welding journal, 1975. **54**(9): p. 311.
37. Ranatowski, E., *Some remarks on stress state at interface of the mismatched weld joints*. 1997, Mis-Matching of Interfaces and Welds. Editors: K.-H. Schwalbe, M. Koçak, GKSS Research Center Publication, Geesthacht, FRG, ISBN. p. 185-196.
38. Kim, Y.-J. and C.-S. Oh, *Finite element limit analyses of under-matched tensile specimens.* Engineering Fracture Mechanics, 2006. **73**(10): p. 1362-1378.
39. Rodrigues, D., et al., *Numerical study of the plastic behaviour in tension of welds in high strength steels.* International Journal of Plasticity, 2004. **20**(1): p. 1-18.
40. Rodrigues, D., L. Menezes, and A. Loureiro, *The influence of the HAZ softening on the mechanical behaviour of welded joints containing cracks in the weld metal.* Engineering Fracture Mechanics, 2004. **71**(13): p. 2053-2064.

41. Kato, T., et al., *Evaluation of impacts of stress triaxiality on plastic deformability of RAFM steel using various types of tensile specimen.* Fusion Engineering and Design, 2016. **109-111**: p. 1631-1636.
42. Ma, Y.-S., et al., *Influences of initial porosity, stress triaxiality and Lode parameter on plastic deformation and ductile fracture.* Acta Mechanica Solida Sinica, 2017. **30**(5): p. 493-506.
43. Peng, et al., *Effect of Stress Triaxiality on Plastic Damage Evolution and Failure Mode for 316L Notched Specimen.* Metals, 2019. **9**: p. 1067.
44. Acar, M.O., et al., *Numerical study of strength mismatch in cross-weld tensile testing,* in *International Congress on Advances in Welding Science and Technology for Construction, Energy and Transportation Systems (AWST 2011)*. 2011: Antalya, Turkey.
45. Li, Y., et al., *Evaluation of creep damage in heat affected zone of thick welded joint for Mod.9Cr–1Mo steel.* International Journal of Pressure Vessels and Piping, 2009. **86**(9): p. 585-592.
46. Sakanashi, Y., S. Gungor, and P.J. Bouchard, *Measurement of Creep Deformation in Stainless Steel Welded Joints,* in *Optical Measurements, Modeling, and Metrology, Volume 5*, T. Proulx, Editor. 2011, Springer New York. p. 371-378.
47. Hyde, T.H., et al., *Effect of weld angle and axial load on the creep failure behaviour of an internally pressurised thick walled CrMoV pipe weld.* International Journal of Pressure Vessels and Piping, 2001. **78**(5): p. 365-372.
48. Chellapandi, P. and S.C. Chetal, *Influence of mis-match of weld and base material creep properties on elevated temperature design of pressure vessels and piping.* Nuclear Engineering and Design, 2000. **195**(2): p. 189-196.
49. Pan, B., et al., *Two-dimensional digital image correlation for in-plane displacement and strain measurement: a review.* Measurement science and technology, 2009. **20**(6): p. 062001.
50. Dally, J.W. and W.F. Riley, *Experimental stress analysis.* 2005.
51. Sutton, M.A., J.-J. Orteu, and H.W. Schreier, *Image correlation for shape, motion and deformation measurements: basic concepts, theory and applications.* 2009: Springer.
52. Peters, W. and W. Ranson, *Digital imaging techniques in experimental stress analysis.* Optical engineering, 1982. **21**(3): p. 213427-213427-.

53. Zhou, P. and K.E. Goodson, *Subpixel displacement and deformation gradient measurement using digital image/speckle correlation (DISC).* Optical Engineering, 2001. **40**(8): p. 1613-1620.
54. Bay, B.K., *Texture correlation: a method for the measurement of detailed strain distributions within trabecular bone.* Journal of Orthopaedic Research, 1995. **13**(2): p. 258-267.
55. Chen, D., et al., *Digital speckle-displacement measurement using a complex spectrum method.* Applied optics, 1993. **32**(11): p. 1839-1849.
56. Sjödahl, M. and L. Benckert, *Electronic speckle photography: analysis of an algorithm giving the displacement with subpixel accuracy.* Applied Optics, 1993. **32**(13): p. 2278-2284.
57. Sjödahl, M. and L. Benckert, *Systematic and random errors in electronic speckle photography.* Applied Optics, 1994. **33**(31): p. 7461-7471.
58. Kammers, A.D. and S. Daly, *Digital image correlation under scanning electron microscopy: methodology and validation.* Experimental Mechanics, 2013. **53**(9): p. 1743-1761.
59. Di Gioacchino, F. and J. Quinta da Fonseca, *An experimental study of the polycrystalline plasticity of austenitic stainless steel.* International Journal of Plasticity, 2015. **74**(Supplement C): p. 92-109.
60. Chasiotis, I. and W.G. Knauss, *A new microtensile tester for the study of MEMS materials with the aid of atomic force microscopy.* Experimental Mechanics, 2002. **42**(1): p. 51-57.
61. Vendroux, G. and W. Knauss, *Submicron deformation field measurements: Part 2. Improved digital image correlation.* Experimental Mechanics, 1998. **38**(2): p. 86-92.
62. Bay, B.K., et al., *Digital volume correlation: three-dimensional strain mapping using X-ray tomography.* Experimental mechanics, 1999. **39**(3): p. 217-226.
63. Haddadi, H. and S. Belhabib, *Use of rigid-body motion for the investigation and estimation of the measurement errors related to digital image correlation technique.* Optics and Lasers in Engineering, 2008. **46**(2): p. 185-196.
64. Crammond, G., S. Boyd, and J. Dulieu-Barton, *Speckle pattern quality assessment for digital image correlation.* Optics and Lasers in Engineering, 2013. **51**(12): p. 1368-1378.
65. LaVision, *StrainMaster DaVis 8.1 Digital Image Correlation Software.* 2013.

66. Rastogi, P.K. and E. Hack, *Optical Methods for Solid Mechanics: A Full-Field Approach*. 2013: Wiley.
67. Chu, T., W. Ranson, and M.A. Sutton, *Applications of digital-image-correlation techniques to experimental mechanics.* Experimental mechanics, 1985. **25**(3): p. 232-244.
68. Knauss, W.G., I. Chasiotis, and Y. Huang, *Mechanical measurements at the micron and nanometer scales.* Mechanics of materials, 2003. **35**(3): p. 217-231.
69. Schreier, H.W., J.R. Braasch, and M.A. Sutton, *Systematic errors in digital image correlation caused by intensity interpolation.* Optical engineering, 2000. **39**(11): p. 2915-2921.
70. Lu, H. and P. Cary, *Deformation measurements by digital image correlation: implementation of a second-order displacement gradient.* Experimental mechanics, 2000. **40**(4): p. 393-400.
71. Khoo, S.-W., S. Karuppanan, and C.-S. Tan, *A Review of Surface Deformation and Strain Measurement Using Two-Dimensional Digital Image Correlation.* Metrology and Measurement Systems, 2016. **23**(3): p. 461-480.
72. Pan, B., et al., *Digital image correlation using iterative least squares and pointwise least squares for displacement field and strain field measurements.* Optics and Lasers in Engineering, 2009. **47**(7): p. 865-874.
73. Pan, B., *Reliability-guided digital image correlation for image deformation measurement.* Applied optics, 2009. **48**(8): p. 1535-1542.
74. Bing, P., et al., *Performance of sub-pixel registration algorithms in digital image correlation.* Measurement Science and Technology, 2006. **17**(6): p. 1615.
75. Zhang, J., et al., *Application of an improved subpixel registration algorithm on digital speckle correlation measurement.* Optics & Laser Technology, 2003. **35**(7): p. 533-542.
76. Amiot, F., et al., *Assessment of digital image correlation measurement accuracy in the ultimate error regime: main results of a collaborative benchmark.* Strain, 2013. **49**(6): p. 483-496.
77. Pan, B., et al., *Study on subset size selection in digital image correlation for speckle patterns.* Optics express, 2008. **16**(10): p. 7037-7048.
78. Lecompte, D., et al., *Quality assessment of speckle patterns for digital image correlation.* Optics and lasers in Engineering, 2006. **44**(11): p. 1132-1145.

79. Sutton, M., et al., *The effect of out-of-plane motion on 2D and 3D digital image correlation measurements.* Optics and Lasers in Engineering, 2008. **46**(10): p. 746-757.
80. Tong, W., *An evaluation of digital image correlation criteria for strain mapping applications.* Strain, 2005. **41**(4): p. 167-175.
81. Wang, Y., et al. *Image matching error assessment in digital image correlation.* in *Proceedings of the SEM Annual Conference.* 2009.
82. Wang, Y., et al., *Quantitative error assessment in pattern matching: effects of intensity pattern noise, interpolation, strain and image contrast on motion measurements.* Strain, 2009. **45**(2): p. 160-178.
83. Luu, L., et al., *Accuracy enhancement of digital image correlation with B-spline interpolation.* Optics letters, 2011. **36**(16): p. 3070-3072.
84. Schreier, H.W. and M.A. Sutton, *Systematic errors in digital image correlation due to undermatched subset shape functions.* Experimental Mechanics, 2002. **42**(3): p. 303-310.
85. Bornert, M., et al., *Assessment of digital image correlation measurement errors: methodology and results.* Experimental mechanics, 2009. **49**(3): p. 353-370.
86. Reu, P.L., et al. *Uncertainty quantification for digital image correlation.* in *Proceedings of SEM Conference*. 2009.
87. Rajan, V., M. Rossol, and F. Zok, *Optimization of digital image correlation for high-resolution strain mapping of ceramic composites.* Experimental mechanics, 2012. **52**(9): p. 1407-1421.
88. Reu, P., *All about speckles: speckle size measurement.* Experimental Techniques, 2014. **38**(6): p. 1-2.
89. Besnard, G., F. Hild, and S. Roux, *"Finite-element" displacement fields analysis from digital images: application to Portevin–Le Châtelier bands.* Experimental Mechanics, 2006. **46**(6): p. 789-803.

CHAPTER THREE

3 EXPERIMENTAL TECHNIQUES AND MATERIALS

3.1 Introduction

This Chapter describes the experimental techniques applied and the materials used in the research described in this thesis. The methods used for micro- and nano-hardness testing, uniaxial tensile testing, creep testing and elastic modulus measurement are described in section 3.2. The working principle of solid-state diffusion bonding of dissimilar materials is discussed in section 3.3 together with the parameter control required to produce sound joints. Section 3.4 describes the microstructural assessment techniques used in the current work, including optical microscopy, scanning electron microscopy and energy dispersive X-ray spectroscopy, for characterising the as received materials and diffusion bonded samples. In section 3.5, the procedures used for DIC data analysis are outlined. Finally, in section 3.6 the materials used and their mechanical properties are presented.

3.2 Mechanical Testing

3.2.1 Hardness Measurement

A material's hardness is a measure of its resistance to penetration or indentation and hardness testing is widely applied in materials characterisation due to its relation to the resistance of the material against plastic deformation. In the current work, hardness measurements were used to determine the size (width) of the bond interface or bond line and to characterise the as received ex-service header material containing a weld to ascertain positions where the test specimens could be extracted.

3.2.1.1 Macro-hardness

For macro-hardness measurements, a Struers Duramin-A300 Vickers hardness testing machine with a square-base diamond pyramid indenter with an angle of 136^{o} between opposite faces was used. For all the measurements, a maximum force of 5kgf applied for 10s and an indenter spacing of 0.5mm were used in accordance with BS EN ISO 6507-1:2005 [1]. The specimens used for hardness measurements were prepared by fine polishing down to 1 micron to minimise surface hardening due to mechanical surface preparation. The two diagonal dimensions of the indentation made on the polished surface of the material after removal of the load were automatically measured using a microscope and image processing

software, and their computed average was used for calculating the hardness of the material. The results from these measurements are expressed in terms of the Vickers hardness number which is computed from the expression [1],

$$\boldsymbol{HV = \frac{2F\ \sin\left(136^o/_2\right)}{d^2} = 1.854\ \frac{F}{d^2}} \qquad 3.1$$

where F is the applied load in kgf, and d is the arithmetic mean of the two indentation diagonals in mm. All the indents were spaced in accordance with BS EN ISO 6507-1:2005 which requires the spacing between indents to be three times larger than the average length of the indentation diagonals to avoid overlapping of indentation strain fields [1].

3.2.1.2 Nano-Hardness measurements

Nano-hardness measurements were carried out using a MTS Nano Indenter XP machine fitted with a diamond indenter and controlled by TestWorks-4 software [2]. To limit uncertainties and errors in the nano-hardness measurements arising from changes in test environment, the nano indenter machine is isolated from external vibrations and the laboratory temperature was maintained within ±1°C. All the nano-hardness measurements were carried using a maximum force of 49mN at a rate of 3.3mN/s and the indent spacing was 15µm [3]. The specimen surface for nano indentation was prepared by fine polishing to 1µm surface finish as for electron microscopy to minimise preparation induced surface hardness. To assess the size (width) of the bond interface in diffusion bonded specimens, line measurements with the above-mentioned indent spacing stated were carried out. The measured nano-hardness is calculated from the expression [3],

$$\boldsymbol{H_n = \frac{F_{max}}{A_p}} \qquad 3.2$$

where F_{max} is the maxmimum applied force in N and A_p is the projected area of contact between the indenter and the sample in mm^2.

3.2.2 Elastic Modulus Measurements

The elastic modulus is one of the intrinsic properties of any engineering material and gives a measure of the resistance of the material against mechanical deformation when subjected to any external load lower than that needed to induce plastic deformation. It is important not only in design but also in modelling and simulation of the mechanical responses of engineering components and structures. In the current work, the measured elastic modulus

was used in finite element simulations of the tensile deformation of diffusion bonded specimens. Although there are a number of methods that are used for measuring elastic modulus [4-6], in the current work it was measured using the impulse excitation technique, which is non-destructive, cheap and accurate (with accuracy values around 1% [5, 7]).

The basic principle of the impulse excitation technique is that the material's elastic modulus is directly proportional to the resonance frequency of flexural vibration, determined by the velocity of wave propagation within a bar of the material, which depends on the density of the material as [8],

$$\boldsymbol{E = \rho v^2} \qquad 3.3$$

where E is the elastic modulus, ρ is the density of the material and v is the velocity of wave propagation. For any prismatic specimen, the material's dynamic elastic modulus can be determined provided its geometrical dimensions and the mass are known. Based on this principle, a number of expressions for computing the dynamic elastic modulus from specimens of different geometric shapes has been derived [8]. For a rectangular shaped beam, the dynamic elastic modulus is computed from the expression [8],

$$\boldsymbol{E = 0.945m\left(\frac{f}{t}\right)^2\left(\frac{l^4}{b}\right)T_i} \qquad 3.4$$

where m is the mass, f is the resonance frequency and l, b and t are the specimen length, width and thickness, respectively. T_i is the correction factor given by

$$\boldsymbol{T_i = 0.585(1 + lt)} \qquad 3.5$$

Although, the impulse excitation measurement technique is quite simple and gives accurate measurements, it depends on precise measurements of the geometrical dimensions and the mass of the specimen as these determine the accuracy of the measured elastic modulus [5].

3.2.2.1 Specimen preparation

Specimen preparation and elastic modulus measurements were carried out in accordance with ASTM E1876-15 standard [5]. Rectangular specimens were machined using an electro-discharge machine (EDM) to a very fine surface finish of 0.01mm and with regular corners from diffusion bonded samples of 316H austenitic stainless steel and Esshete1250. Prior to measurement of its dimensions, the specimens' surfaces were prepared by submerging the specimens in 60% nitric acid for 5 seconds and ultrasonically washing them in acetone to

ensure that the surfaces were clean. The specimens' length, width and thickness were measured using a micrometer screw gauge. A minimum of 10 measurements were carried out for each dimension and the average value was used for elastic modulus measurements. The mass of the specimens was measured using a calibrated analytical balance with the balance doors shut to ensure accuracy in the measured mass. The measured dimensions and the mass of the specimens are given in Table 3-1

3.2.2.2 Elastic modulus measurement

The equipment used for impulse excitation elastic modulus measurements is composed of a test frame fitted with strings for supporting the specimen, a mechanism for inducing vibration or impulse, a receiver for recording the signal and the software for processing and analysing the signal, see Figure 3.1. The specimen was supported on nylon strings at the flexural nodal points of the beam computed by the software based on the specimen length (Figure 3.1). The vibrational impulse was produced by striking the beam with a small hammer. The signal was recorded using a microphone and Resonant Frequency and Damper Analyser (RFDA) software used to process the data and compute the flexure resonance frequency from which the elastic modulus is calculated.

3.2.3 Uniaxial Tensile Testing

3.2.3.1 Room Temperature

Uniaxial tensile tests at room temperature (24^{o}C) were carried out using an electro-mechanical Instron tensile testing machine with a maximum load capacity of 50kN. The tests were carried out in displacement control with a displacement rate of 0.1mm/min or 1.667×10^{-3} mm/s for all the tests. The displacement of the specimen was controlled by a screw-driven crosshead and the specimens were held in position using wedge grips coupled to the head with universal joints to improve the alignment. The alignment of the specimen and the grips has a great bearing on the accuracy of the results obtained. Therefore, to ensure that the specimen was well aligned, it was positioned in the wedge grips using angle bars and the top and bottom grips aligned using a bracket to hold them in position while tightening the specimen in the grips.

3.2.3.2 High Temperature

Uniaxial high temperature tensile tests were carried out at 525^{o}C to characterise the tensile properties of the Type 316H stainless steel material extracted from an ex-service header. The

tests were conducted on an Instron 8862 machine with a load capacity of 100kN, fitted with a single screw electro-mechanical actuator and capable of very slow strain rates. Like the Instron room temperature tensile testing machine, the machine for high temperature tensile testing was controlled with in-built Instron Bluehill software. High temperature tests were performed at a constant displacement rate of 0.1mm/minute.

For tensile tests at elevated temperature, the Instron machine was fitted with a furnace of split shell construction with three heating zones. The furnace had a large access window which was used to attach a high temperature extensometer to the specimen surface during the test. The temperatures of the 3 independent heating zones of the furnace were controlled by a Eurotherm 3216 controller. The specimen temperature was monitored by means of type-N thermocouples attached to the specimen surface at the top and lower ends of the specimen's gauge length. The furnace temperatures were controlled manually to give a uniform temperature along the specimen gauge length.

3.2.4 Strain measurement techniques

3.2.4.1 Extensometers

Strain measurement was carried out using an extensometer with knife-edges attached to the specimen and DIC deformation monitoring. For small parent material specimens, with a parallel section 20mm long, a 12.5mm gauge extensometer with a maximum travel of 6mm was used. Whereas for standard flat tensile specimens with a parallel section 40mm long, a 25mm gauge extensometer was used. To measure the specimen displacement, the extensometer has a calibrated strain gauge fitted on a pivoting beam which provides information on the extension by converting the mechanical displacement between the arms into an electrical signal. Care was taken when attaching the extensometer to the specimen gauge section to ensure that the extensometer knife edges did not slip during the test. The knife-edges of the extensometer were attached to one side of the specimen using extensometer clippers for the 25mm gauge extensometer and small springs for the 12.5mm gauge extensometer. The extensometers where calibrated using an Instron extensometer calibration gauge each time they were used to ensure accuracy and repeatability of the tests.

At high temperature, strains were measured using a high temperature extensometer attached to the surface of the specimen using heat resistant, chisel-ended alumina rods through the furnace window, because the electronics of the extensometer are not heat resistant. The gauge

length of the extensometer used was 12.5mm with a maximum travel of 2.5mm. To improve the accuracy of the measured strain, the extensometer was calibrated every time it was used. Upon setting up the test, the specimen was heated to the strain measurement temperature and held for an hour to allow temperature homogenisation. During the test, the resultant temperature gradient across the specimen gauge length was maintained to $<1^{o}C$ and the variation from the test temperature was kept within $\pm 1^{o}C$.

3.2.4.2 Room temperature DIC strain measurement

The surface of a specimen must have a random speckle pattern which can be used to track the displacements across the surface during mechanical loading, from which strain can be determined. For low magnification DIC measurements the random surface speckle pattern produced by wire EDM machining was enhanced by submerging the specimens in 60% nitric acid for up to 60 seconds, then washing with water followed by acetone for quick drying. For high magnification DIC measurements the specimen surface was prepared by applying a black speckle on a white painted background using a high temperature resistant, silica ceramic based, paint (VHT FlameProof^{TM})

A high-resolution Nikon D800E camera, with 7360x4912 pixels resolution fitted with a 200mm focal length macro lens (Nikkor 200mm microf4 IF-ED) and Novoflex Ballpro macro bellows was used to acquire the images. The camera was mounted on a tripod stand and a 5kg load attached to curtail any vibration arising from the shutter movement. For all the tests, a low ISO of 100 and an aperture of F8 were used to minimise image noise and increase the depth of field of the image, respectively. The shutter speed was set to 1/250s. Figure 3.2 shows a pictorial diagram of the DIC-tensile test set-up at room temperature. The specimen surface was uniformly illuminated using optical fibre glass cables connected to a light source. To minimise the errors in the DIC measured strain, the specimen is required to remain in-plane with the optic system of the camera during the tensile test. To achieve this, the specimen was aligned with the camera using a level ruler.

For all the tensile DIC strain measurements, the rate of image acquisition in the early stages of the test was set to one image in every 5 seconds. The image acquisition rate was changed to one image in every 30 seconds once the strain recorded by the extensometer reached 2%. The processing of the acquired images to determine the displacement vector and the subsequent strain computation are discussed later in section 3.5.

3.2.5 Creep Testing

High temperature creep tests were carried out using conventional creep testing machines composed of a test frame with a lever arm supported on a knife-edge, as illustrated in Figure 3.3. The specimen was positioned in the mid-section of the furnace to help maintain a uniform temperature distribution along on the specimen gauge length. A creep frame with lever arm ratio of 10:1 was used to test all the diffusion bonded specimens, whereas all the hour-glass shaped specimens and validation tests using conventional creep specimens were tested using creep test frames with a lever arm ratio of 25:1. For accurate specimen loading, the lever arm was kept horizontal, maintaining the ascribed lever arm ratio, by a motor connected to the load train. To ensure accurate strain measurement, the applied load was calibrated by inserting an up-to-date calibrated load cell into the load-train and then adding weights until the required applied load for the actual creep test specimen was recorded on the load cell.

The creep frames were equipped with 3-zone furnaces supplied by Severn Thermal Solutions. The furnaces were conductively heated and ceramic wool was used for insulation of the furnace. The specimen temperature was monitored by means of type-N thermocouples attached to the specimen surface at the top and lower ends of the specimen's gauge length. The furnace temperatures were controlled manually to give a homogenous temperature distribution across the specimen surface. Prior to attaching the thermocouples to the specimen, they were calibrated using a portable thermocouple calibration furnace equipped with a type-R thermocouple which was used as a reference temperature indicator.

3.2.6 Creep strain measurement techniques

3.2.6.1 Linear variable differential transformers (LVDT)

The extension of the specimen due to the applied load at high temperature was measured using a pair of LVDTs within a frame attached to the shoulders of specially designed flat samples via adapted inserts, as shown in Figure 3.4. During creep testing, as the specimen elongates, the outer arms of the LVDT frame moves upwards and this upward movement is registered as the extension of the specimen by the LVDT. The sampling rate of LVDTs is often varied in accordance with the creep rates expected, for example higher sampling rates in the primary and tertiary stages of the creep test. The sampling rate in the current study was

kept constant at every minute. Prior to attaching the LVDT frame to the specimen, it was calibrated using an Instron extensometer calibration gauge.

3.2.6.2 DIC creep strain measurement

For DIC creep strain measurements, the furnaces used had a window allowing optical access for specimen imaging during the creep test. The furnace window was sealed and insulated to minimise heat loss. A detailed description of the DIC creep testing system used is given in [9]. Figure 3.5, shows the schematic set-up of the DIC creep strain measurement system. A high-resolution Nikon D800E camera, with 7360x4912 pixels resolution fitted with a 200mm focal length macro lens (Nikkor 200mm microf4 IF-ED) and Novoflex Ballpro macro bellows was used to acquire the images. The camera was mounted on a vibration-isolated laboratory table.

For creep tests, specimens were prepared by dipping in 60% nitric acid for 60 seconds and then washing with water to get rid of any particles remaining on the surface due to EDM machining. The specimen dimensions were then measured at 10 approximately equidistant positions along the gauge length and average values of the width and thickness calculated. The speckle pattern for the creep test specimens was applied by spray painting the specimen surface with black and white high temperature resistant, silica ceramic based, paint (VHT FlameProof^{TM}). Fine speckle patterns were applied by spraying the black paint on a white painted background from approximately 1m or more. The paint was then cured in a furnace at 150^{o}C, 204^{o}C and 315^{o}C successively for 30 minutes at each given temperature and cooling in air for 30 minutes immediately after each curing temperature.

The specimen was carefully aligned with the camera to ensure that the specimen deformed in-plane during the entire creep test. At the beginning of the test, a reference image was taken prior to the initial loading of the specimen. After application of the full load to the specimen, the image capturing rate was set to every 20 minutes in the first 24 hours. Thereafter the image capturing rate was changed to once every hour. During the creep tests, the tests data (temperature, displacement readings and the images captured for the DIC strain measurements) were logged onto the computer using the National Instruments (NI) data logging system.

3.3 Diffusion Bonding

Diffusion bonding is a solid-state joining process accomplished by local plastic deformation of asperities on the surfaces of the two materials being joined, at relatively high temperature, thus facilitating inter-diffusion at the joint interface. Unlike most welding processes, diffusion bonding is carried out in an inert atmosphere, to prevent oxidation, and requires the application of controlled loads at high temperatures. During diffusion bonding, the applied load causes plastic collapse of contacting asperities leading to the formation of a planar array of interfacial voids. Because the bonding load is applied for an extended period (up to an hour in the current study), creep and diffusion processes takes place, resulting in the transportation of atoms across the bonding region, thus reducing the interfacial voids.
Solid state diffusion bonding creates a very thin bond interface zone between the two materials being joined. Moreover, it can produce very high-quality joints, with bonding efficiencies approaching 100%, and bond strengths approaching that of parent material. Because of its versatility, diffusion bonding is widely applied in joining dissimilar metals and materials that cannot be easily joined using conventional welding methods and has found success in joining aluminium to other materials.

This joining technique was chosen for the present research because it can be used to create a near step-change in material properties across the bond. It was used to join Type 316H austenitic stainless steel to Esshete 1250 (an austenitic stainless steel with high Mn content). In the literature, much of the work that has been carried out on diffusion bonding of stainless steels has focused on the bonding of austenitic steel to wide range of materials. For instance, diffusion bonding of stainless steel to nickel based superalloys, aluminium, and copper has been reported [10-13]. Kurt *et al* [14, 15] successfully bonded stainless steel to a carbon steel at 900^{o}C, using an applied load of 8MPa for 30 minutes. With these bonding parameters, a bond with shear strength of 475 MPa was achieved. Although diffusion bonding has the capability of producing high quality joints, its major disadvantage is the potential development of discontinuities due to lack of bonding and the formation of intermetallic compounds across the entire area of contact between two materials. Therefore, to ensure uniform contact between two materials, the contact surfaces of the samples were carefully prepared including careful consideration of the machining of the two surfaces to be in contact.

3.3.1 Sample preparation and the diffusion bonding process

20mm diameter billets, 50mm long were wire EDM machined from Type 316H stainless steel and Esshete 1250 steel. The contact surfaces were then prepared by grinding with a 4000 grit silicon carbide paper. Further, gallium was applied to the contact surfaces by light polishing the billets on gallium coated polishing cloths. Pairs of samples were then placed in the bonding chamber with the Esshete 1250 billet placed on top of the 316H stainless steel one. A thermocouple was attached to the surface of the top billet (Esshete1250) for bonding temperature control. Figure 3.6 shows a picture of the diffusion bonding chamber with the samples and the heating coil connected. The samples were heated using a water-cooled copper induction heating coil. At the beginning of the test, a controlled load was applied mechanically to the top of the billet pair via a shaft. For optimum bonding, the bonding temperature was kept constant and the machine was operated in displacement control such that the applied stress could relax. Figure 3.7 shows a plot of the temperature and the applied load recorded during the diffusion bonding process.

Several trial tests with varying temperature and stress were carried out to establish the optimum bonding parameters for diffusion bonding Type 316 stainless steel to Esshete 1250. Table 3-2 shows the test parameters for the trial diffusion bonding tests. For each trial test, longitudinal specimens showing the bonding interface were cut and prepared for bond-line analysis using an optical microscope and SEM [see section 3.4.1.1]. Figure 3.8 shows SEM micrographs of the diffusion bonded interfaces produced at two different bonding temperature and stresses. The bond interface became narrow with fewer pores and least un-bonded region when the bonding temperature was increased 880^{o}C to 1100^{o}C and the applied load doubled. However, it should be noted that increasing the bonding temperature and applied load resulted in increased grain size, as shown in Figure 3.8.

From the trial diffusion bonding tests, it was found that a good bonding interface between 316H stainless steel and Esshete1250 was produced when the bonding temperature was set at 1100^{o}C with an initial applied load of 400kg which was equivalent to 12.5MPa compressive stress. Further, from the samples bonded at this temperature and stress, uniaxial tensile test specimens were machined and tested as described in section 3.2.3. The test specimens failed in the parent material away from the bond-interface. Therefore, all the diffusion bonded specimens used in the current work were bonded at 1100^{o}C and an applied compressive stress of 12.5 MPa.

3.4 Metallographic Analysis Methods

3.4.1 Optical microscopy

In the current study, optical microscopy was used to examine the microstructure of as-received materials and to assess the quality of the bond interface in the diffusion bonded samples. A Leica DMI 5000M inverted reflected light microscope fitted with a Leica DFC280 digital camera was used to capture the optical images. The microscope was operated in Bright field (BF) mode in which the polished surface of the specimen appears bright and surface irregularities such as grain boundaries, precipitates, inclusions, slip bands and pits appear dark, as their reflected light are not reflected back into the objective lens of the microscope.

3.4.1.1 Sample preparation

The specimen surfaces to be analysed were prepared following the standard metallographic sample preparation procedures [16, 17]. The samples were mounted in a conductive thermosetting resin and the surface prepared by grinding the samples down to a 4000 grit finish using silicon carbide paper (Table 3-3). The final surface finish was achieved by fine polishing the samples in three steps using metal-backed soft nap cloths (MD-Nap) coated with 6µm down to 1µm diamond suspension to ensure that the surfaces were free of grinding scratches (Table 3-4).

The microstructure of the as-received 316H stainless steel was revealed by electro-etching, using an electrolyte consisting of 60% nitric acid and a 2V, potential applied for 5 seconds, whereas the diffusion bonded samples were electro-etched using a 10% oxalic acid electrolyte with a 6 - 8V potential applied for 5 seconds. It should be noted that application of the 60% nitric acid electrolyte to etch diffusion bonded samples resulted in preferential attack on some grains of the 316H stainless steel.

3.4.1.2 Grain size measurement

Grain size measurements were carried out by measuring line intercepts using a Leica optical microscope. The grain size measurements were carried out in accordance with ASTM E112-13 standard [18]. The lines were positioned in such a way that grains of various sizes were intercepted, ensuring that all sizes of grains were considered in the measurement.

3.4.2 Scanning electron microscopy and energy dispersive X-ray spectroscopy (EDS)

A scanning electron microscope (SEM) was used to analyse the soundness of the bond interface by considering the microstructure and the distribution of precipitates in the regions near the bond interface. A FEGSEM (Zeiss Supra 55VP) operated at 5keV with a 30µm objective aperture was used in the secondary electron imaging mode to acquire micrographs in the regions near the interface. The sample preparation procedures described in section *3.4.1.1* Sample preparation, were used to prepare the samples for SEM imaging.

Energy dispersive x-ray spectroscopy, which is widely applied for near surface chemical characterisation of materials, was applied in this study to characterise the width of the bond interface based on the change in chemical composition in the regions near the bond line. The working principle of EDS is that atoms of any element produce characteristic X-ray photons on interacting with a high energy electron beam. Therefore, analysing the energies of the emitted X-rays gives the chemical composition of the material. The FEGSEM used in this study is fitted with an X-Max 50mm^2 EDS detector. Characterisation of the width of the bond interface was carried out using line scans perpendicularly across the bond interface using an acceleration voltage of 20keV and a 30µm objective aperture at a working distance of 8.5mm. The chemical composition spectra were acquired and analysed using Aztec software [19].

3.5 DIC Data Analysis

3.5.1 Image processing

For all the experimental tests carried out, the captured raw colour images were transferred to a superfast computer equipped with the DIC analysis software for displacement computation. The DIC displacement computation is based on tracking the patterns of intensity (in terms of grey-level scale) in the images and therefore the acquired images were converted into 16 bit grey-scale tiff images. The conversion was carried out using an in-house developed Matlab code which applies colour pixel conversion such that the resulting 16-bit images obtained have no aliasing or image distortion during conversion. When compared to popular image conversion algorithms, the conversion algorithm used has been found to give better accuracy in the computed displacements [20]. The 16 bit tiff images were uploaded onto the DaVis 8.2 DIC software developed by Lavision for displacement vector computation [21].

3.5.2 Calibration and rigid body motion

The system was calibrated to improve the accuracy of the displacements measured using DIC. The calibration process involved placing a rectangular calibration plate, with regular black spots on a white background, in the plane of the specimen perpendicular to the camera prior to the test. The spots on the calibration plate used were of 0.125mm diameter and spaced 0.25mm apart. Images of the calibration plate were taken before the start of each test and these images were used in the calibration procedure of the DaVis 8.2 DIC software[21]. DIC calibration helps in eliminating errors arising from camera lens distortion and non-perpendicular positioning of the specimen in relation to the camera. The calibration process also computes the magnification of the image of the specimen or the image scale factor. The scale factor for all the room temperature DIC tensile tests was approximately 3µm /pixel, whereas for the DIC creep tests, it varied from test to test. It should be noted that calibration does not deal with errors due to any out-of-plane movement or rigid body motion of the specimen which may occur as the specimen settles in the grips during the test.

As explained in *Chapter 2*, out-of-plane movement changes the magnification of the images acquired, resulting in pseudo strains which may either increase or lower the measured strains in the loading direction. To limit the effects of out-of-plane movements, specimens where loaded up to 70MPa prior to the start of each test.

Rigid body motion and in-plane rotations were eliminated by carrying out the shift correction step provided in the DIC software. Shift correction was carried out by selecting a point on the reference image onto which all the subsequent images are aligned. In the current study, a region of 128x128 pixels at the mid-point of the reference image was used for shift correction. Since all the deformed images are aligned with respect to the reference image, rigid body motion and in-plane rotations are eliminated. The overall image light intensity was also corrected with respect to the reference image thus eliminating possible errors that may arise due to any change in the light intensity of the images during the test.

3.5.3 Displacement computation parameters

3.5.3.1 Region of interest and subset size

Displacement computation was carried out by first extracting the region of interest excluding the edges of the specimen. For all the uniaxial loading tests, the whole specimen parallel

section was extracted for the displacement calculation, cropping off the edges as they tend to give erratic measurements.

The DaVis 8.2 DIC software used in the current study is based on subset tracking. The choice of subset size used affects the accuracy of the results obtained, as explained in *Chapter 2*. Generally, for homogeneous materials with uniform deformation, a large subset size is preferred as it gives accurate results. However, in the case of steep displacement gradients such as around cracks or in heterogeneous materials, using a large subset size would result in errors as there may be a local change in the displacement gradient within a subset, resulting in erratic displacement measurements [22]. On the other hand, the use of small subset sizes may give rise to errors, especially when the speckle size on the surface of the specimen is large. Therefore, an optimal subset size, taking into consideration the speckle pattern size, is required to obtain accurate DIC results from heterogeneous materials[22]. In the current study, the best subset size was found to be 31x31 pixels with a step size of 8 pixels. Reducing the step size increases the spatial resolution of the measured displacements and the computation time, however it does not improve the accuracy of the measurements. In this case, for the DIC uniaxial tensile tests with the region of interest defined as approximately 6mm x 40mm, a subset size of 31x31 pixels, a step size of 8pixels and a scale factor of 3µm/pixel, a total of approximately 416,000 subsets were tracked on each deformed image. It should be noted that subsets at the edge of the region of interest were excluded from the analysis and that the number of subsets tracked (and hence the number of vectors determined) depends only on the area of the region of interest and the step size.

3.5.3.2 Image Correlation Process

Selecting the subset size in the DIC software applies a virtual mesh to the reference image, which is used for tracking the subsets in the deformed images. To correlate the deformed and the undeformed subsets, the unique grey-level intensity within the subset is tracked on the deformed image assuming that the grey-level intensity within the subset remains constant throughout the test. A detailed description of the principles of image correlation is given in *Chapter 2*. In the DIC software, the process of correlating subsets of two successive images, referred to as cross-correlation, can be carried out in two ways. In the first method (1), the deformed images are correlated relative to the first image such that the final computed displacement of a subset in the n_{th} image is determined relative to the reference image (1*2,

1*3, 1*4, …, 1*n). This method gives more accurate displacement measurements however it can result in decorrelation for large displacements.

In the second method (2), the deformed images are correlated relative to the $(n-1)_{th}$ image such that the final computed displacement in the n_{th} image is a sum of differential vectors computed by correlation of every two successive images until the n_{th} image (1*2, (1*2+2*3), (1*2+2*3+3*4), …, (1*2+2*3+….+(n-1)*n)). Although the second method is suitable for larger displacements, any errors in the measurements are amplified, since the final computed displacement is a sum of the differential vectors. In the current study, the first method was used because it does not amplify the errors in the computed displacements. Although using this method for larger displacements, such as around the necked region of a tensile specimen, would result in decorrelation of the images, in the current study the displacements prior to specimen necking were not of prime concern and so the first method was chosen for displacement vector computation.

3.5.3.3 Strain computation

Although strain can be computed by numerical differentiation of the calculated displacement field, this technique amplifies the noise in the displacement field. Therefore, to obtain reliable computed strain fields by numerical differentiation, the determined displacement fields are smoothed. In the current study, the strain fields were computed by a two-step surface fitting, based on least squares optimisation, implemented in Matlab [23]. In this technique, the first step of surface fitting removes any spurious vectors, so the technique does not require thorough smoothing of the displacement field prior to strain computation.

To compute strain at any given point on the surface of the specimen, the displacement fields obtained from DaVis 8.2 were sampled in the form of rectangular regions or strain windows along the length of the specimen. To improve the spatial resolution of the computed strain, the sampled regions were overlapped by 75%. 10% of the specimen width close to each edge was excluded from the strain computation process to avoid errors arising from erratic displacement vectors which are obtained in the regions near the edge.

Figure 3.9 gives a summary of the strain computation procedure used in the current study. For each strain computation region or window, the displacement vectors within the region are first decomposed into x-direction vectors (across the width of the region) and y-direction vectors (along the length of the gauge). Then a first order two-dimensional polynomial was

fitted separately to the x-direction and y-direction displacement vectors. The difference between the computed displacements and the measured ones was used to identify and remove any vectors that significantly deviated from the mean value.

Thereafter the fitting procedure was carried out the second time and the gradients of the two fitted polynomials (x and y data) were then taken as the differential of the displacements for the whole strain computation window and subsequently for the whole image at the given load step in the uniaxial tensile tests or time step for the creep tests. The displacement gradients were then converted to Lagrange strain for the whole image. The strain across the width of the specimen at any given point was assumed to be uniform and therefore the strain within the strain computation window was taken to be uniform. This allowed the construction of spatially resolved local stress-strain curves for the uniaxial tensile tests and spatially resolved local creep curves from the creep tests.

3.6 Materials

Austenitic stainless steels used in the construction of steam headers in nuclear power plants were used in this thesis. Due to their mechanical properties such as retention of strength and corrosion resistance at high temperatures and pressure, austenitic stainless steels are extensively used in nuclear power plants. Although, they are many grades and varieties of austenitic stainless steels available, the AISI Type 316H and Esshete 1250 austenitic stainless steels were used in the current research work.

3.6.1 Type 316H austenitic stainless steel

Type 316H austenitic stainless steel used was obtained from two different casts of ex-service steam headers. The following sections give a brief history of the two types of ex-service austenitic stainless steels used in the current study.

3.6.1.1 Ex-service Type 316H - Cast 55882

Type 316H stainless steel supplied by EDF was extracted from the dome section of an ex-service super-heater header identified as Heysham I -1D2/2 (Cast number 55882). The header was removed from service after an estimated 87,790 hours at a mean effective creep temperature of 515^{o}C. The internal diameter and thickness of the header was 304.8mm and 63.5mm, respectively. Figure 3.10(a) shows the dome section of the steam header and the cut section from which the material used in the current study was extracted. All the creep testing specimens used in Chapter 4 were extracted from block AHK, Figure 3.10(b). To ensure that

the creep specimens were extracted from regions away from the weld section to avoid variation in mechanical properties due to welding, a series of hardness tests were carried out to map out the weld and the heat affected zones. Macro hardness testing was carried as described in section *3.2.1.1* and Figure 3.11 shows the weld hardness map outlining the weld and the heat affected zones. Using Figure 3.11, all the creep specimens were extracted from the regions away from the weld and the heat affected zones with certainty.

3.6.1.2 Ex-service Type 316H - Cast 69431

This ex-service Type 316H stainless steel was part of the plant steam header identified as HRA 2B2/1 removed from service after 90,930 hours at about 516^{o}C and under an internal steam pressure of about 16MPa. The internal diameter and thickness of the header were 304.8mm and 63.5mm respectively. All the Type 316H stainless steel billets for diffusion bonding in Chapter 5 were extracted from this ex-service header material. Figure 3.12 shows the image of the section of the steam header from which diffusion bonding billets were extracted. All the billets were extracted from a region remote from the nozzle section of the header.

3.6.2 Esshete 1250 stainless steel

Esshete 1250 stainless steel was supplied in its as-manufacture state by EDF. In the current study, Esshete 1250 was used for manufacturing of dissimilar metal welds mechanical testing specimens by diffusion bonding it to Type 316H stainless steel extracted from cast 69431 steam header. Figure 3.13 summarises the steps involved in the diffusion bonding of Esshete 1250 stainless steel virgin material to Type 316H austenitic stainless steel. Detailed description of the diffusion bonding process is given in section 3.3.1.

3.6.3 Materials Characterisation

3.6.3.1 Hardness and Elastic Modulus Measurements

Characterisation of the hardness and Elastic modulus of the materials used in the current study were carried in their as received state and after diffusion bonding. The measurements were carried out as outlined in sections 3.2.1 and 3.2.2, respectively. Table 3.5 gives the summary of the hardness and Elastic Modulus measurements for the three materials used. Table 3.5 shows that the measured hardness values for Type 316H stainless steel are slightly higher than that of Esshete 1250 in their as received state. The hardness values for the two

distinct 316H stainless steel casts are similar despite the difference in their service life. The Elastic modulus values are similar for all three materials in their as received state.

3.6.3.2 Tensile Properties

To characterise the tensile properties of the materials, uniaxial tensile test specimens extracted from both the as received materials and the diffusion bonded ones were tested. Standard size tensile test specimens with parallel gauge section of 40mm and gauge length of 25mm as shown in Figure 3.14(a) were extracted from Type 316H-cast 55882 as received material. Whereas smaller sub-size specimens with parallel section of 20mm and gauge length of 12.5mm were extracted from Type 316H-cast 69431 and Esshete 1250 used in the production of diffusion bonded specimens, Figure 3.14(b). The displacement measurements for all the tensile tests of monolithic specimens extracted from both the as received materials and the diffusion bonded ones were carried out using an extensometer attached to the specimen gauge section. Figure 3.15 shows the stress-strain curves of monolithic specimens extracted from the as received materials and the ones subjected to the diffusion bonding process. From Figure 3.15, the as received materials have relatively higher yield strength and strength hardening characteristics compared to the ones subjected to the diffusion bonding process. This expected as the diffusion bonding process was carried out at 1100^{o}C which is slightly higher than the solution heat treatment temperature for austenitic stainless steels.

Table 3.6 shows the yield strength of both the as received and the monolithic specimens subjected to the diffusion bonding process. From Figure 3.15 and Table 3.6, the diffusion bonding process has significant effects on the mechanical properties of austenitic stainless steels used in the current study. Both Type 316H and Esshete 1250 material subjected to the diffusion bonding process shows significant reduction in their tensile properties, however the reduction in strength and hardening characteristics are more pronounced in Type 316H – cast 69431. This could be because it has been exposed to service temperatures and stresses which may have a bearing on its current performance under diffusion bonding.

3.7 Summary

This chapter has introduced the materials used in the test programme supporting this thesis and described the range of experimental techniques used including mechanical tensile testing, creep testing, diffusion bonding, metallography and application of DIC deformation monitoring at both room and high temperatures. The latter is particularly important for the

present work which examines the spatial variation of strain in tensile and creep test specimens having geometric and material property inhomogeneity.

FIGURES AND TABLES

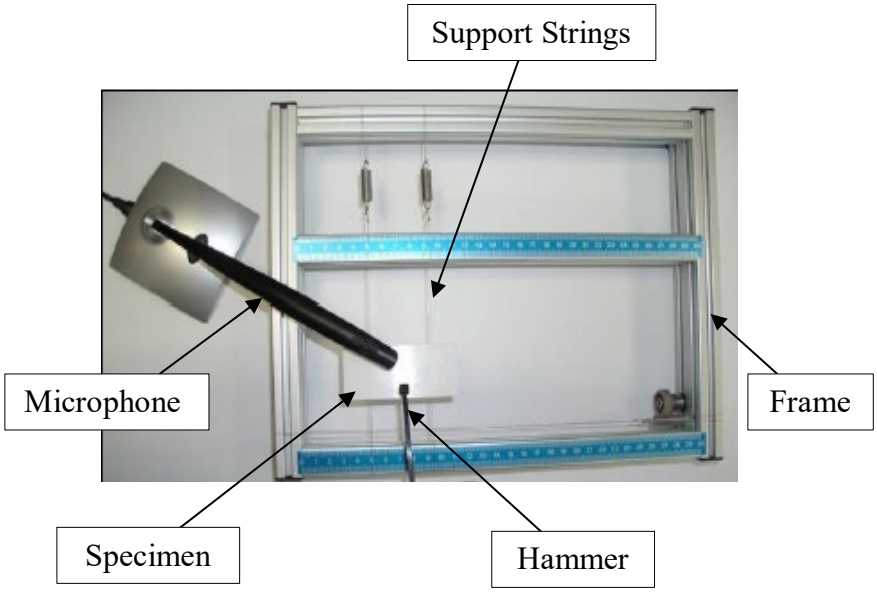

Figure 3.1 The dynamic elastic modulus testing equipment used in the current study

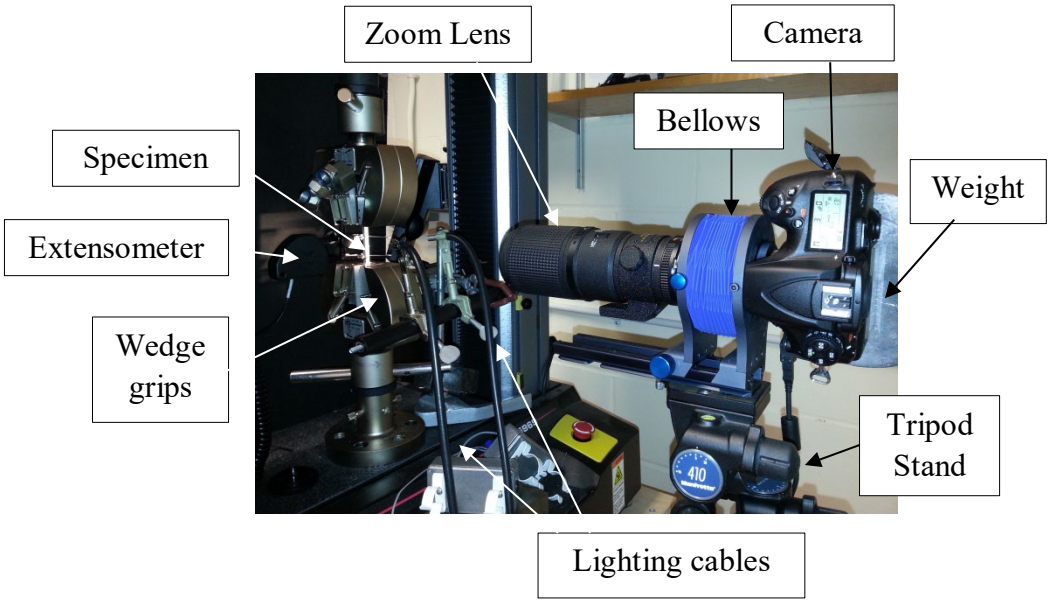

Figure 3.2 DIC-uniaxial tensile testing set-up at room temperature

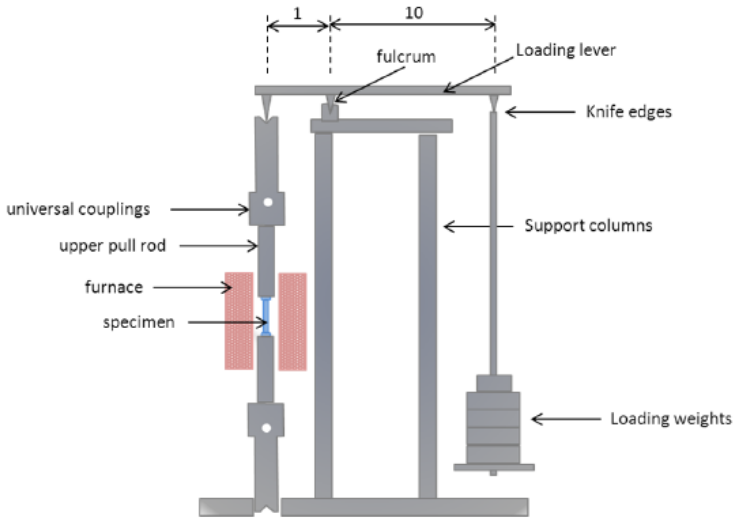

Figure 3.3 Schematic drawing of a conventional constant load creep testing rig used in the current work [24].

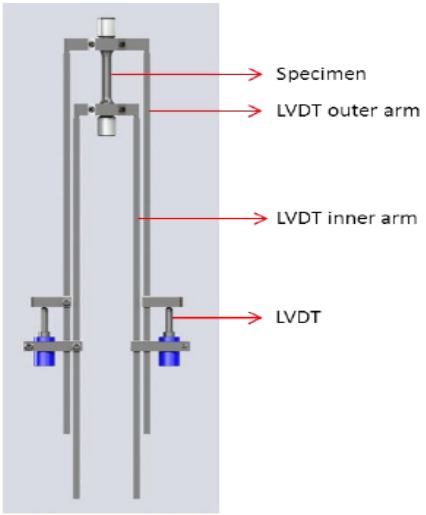

Figure 3.4 Attachment of the LVDT frame to a creep specimen [24].

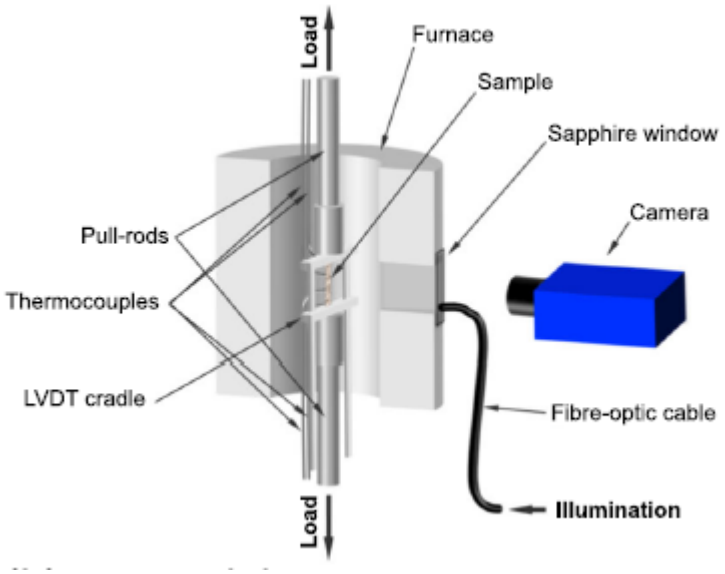

Figure 3.5 Schematic drawing of the DIC creep strain measurement system [23].

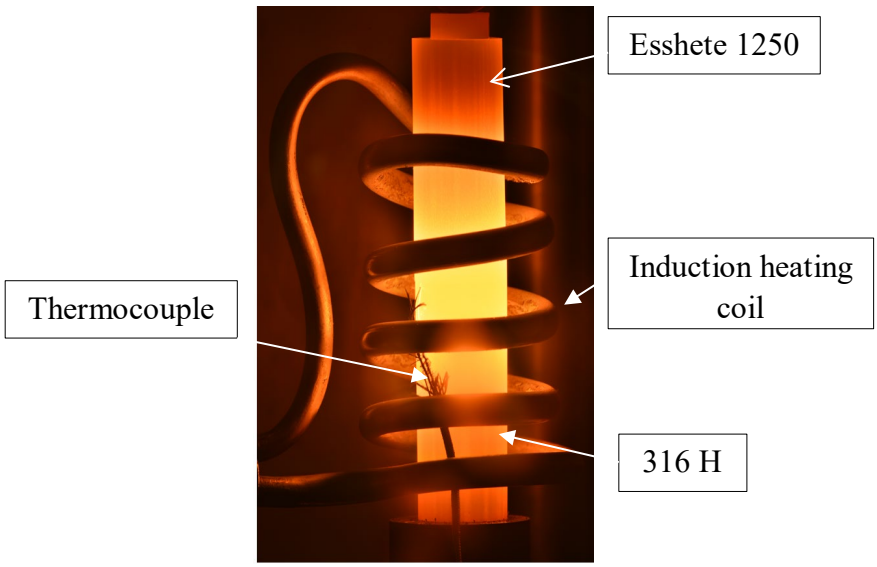

Figure 3.6 Diffusion bonding process showing the samples and the induction heating copper coil.

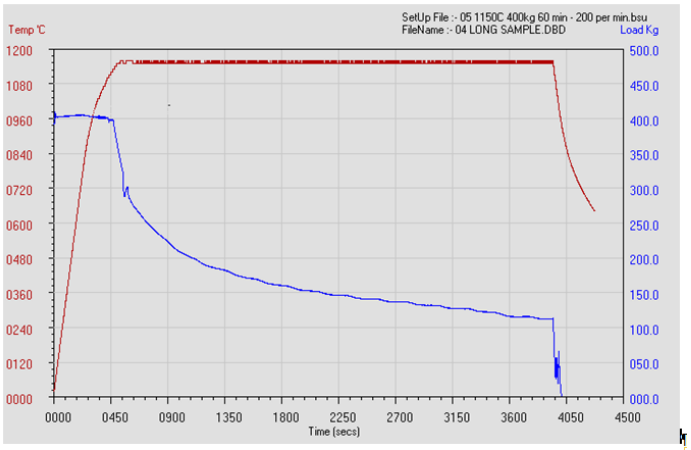

Figure 3.7 Plot of the temperature and the applied load recorded during the diffusion bonding process.

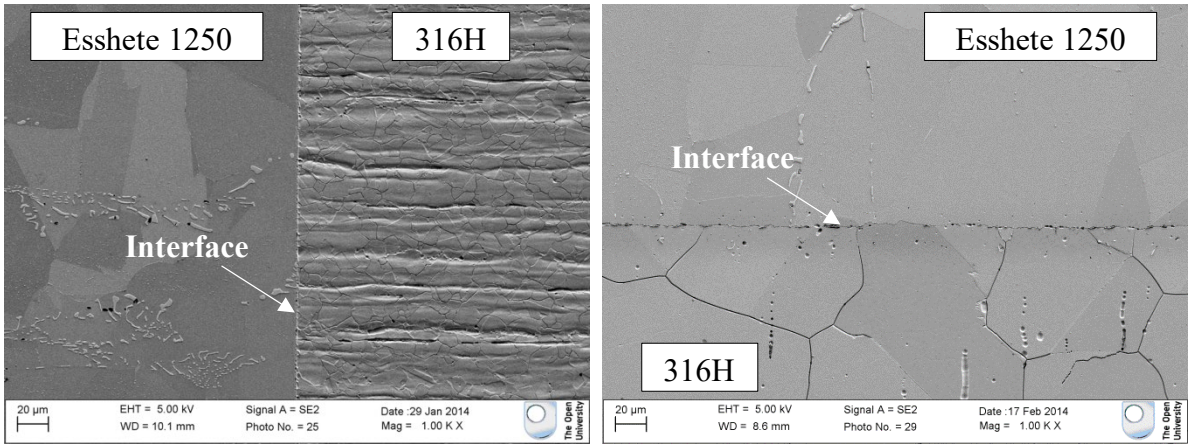

(a) 6.25MPa at 950°C (b) 12.5MPa at 1100°C

Figure 3.8 SEM micrographs of the diffusion bonded interfaces produced at different bonding temperature and stresses.

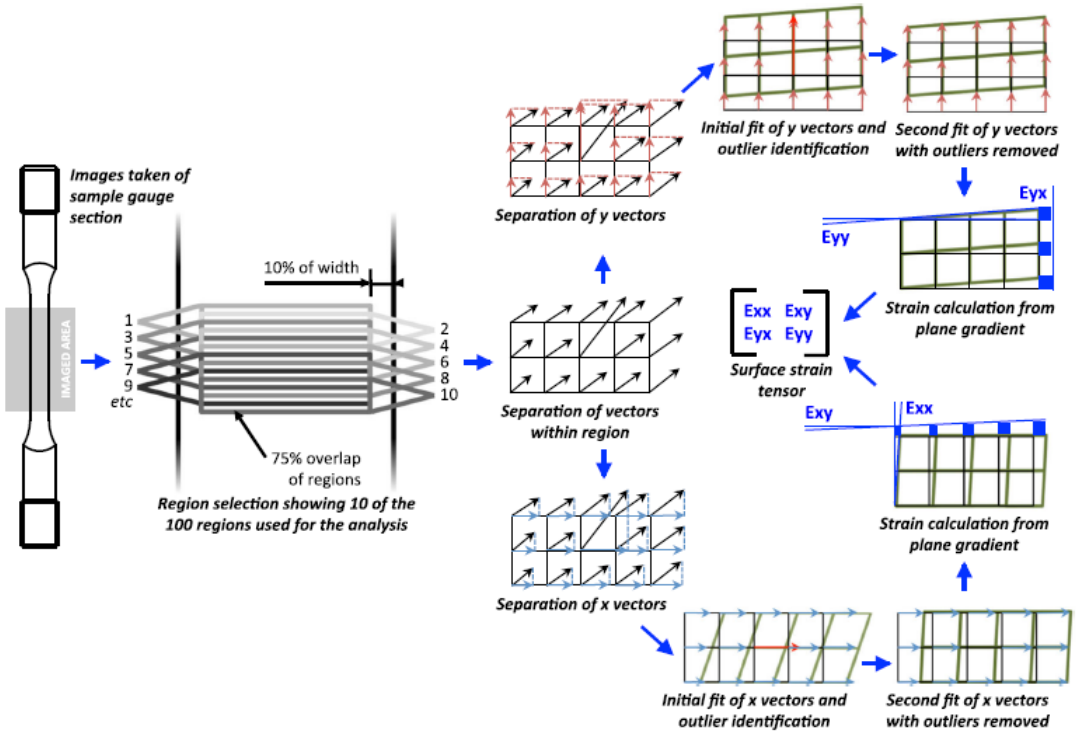

Figure 3.9 Schematic diagram summarising the spatial strain computation procedure used in the current study, adapted after [23].

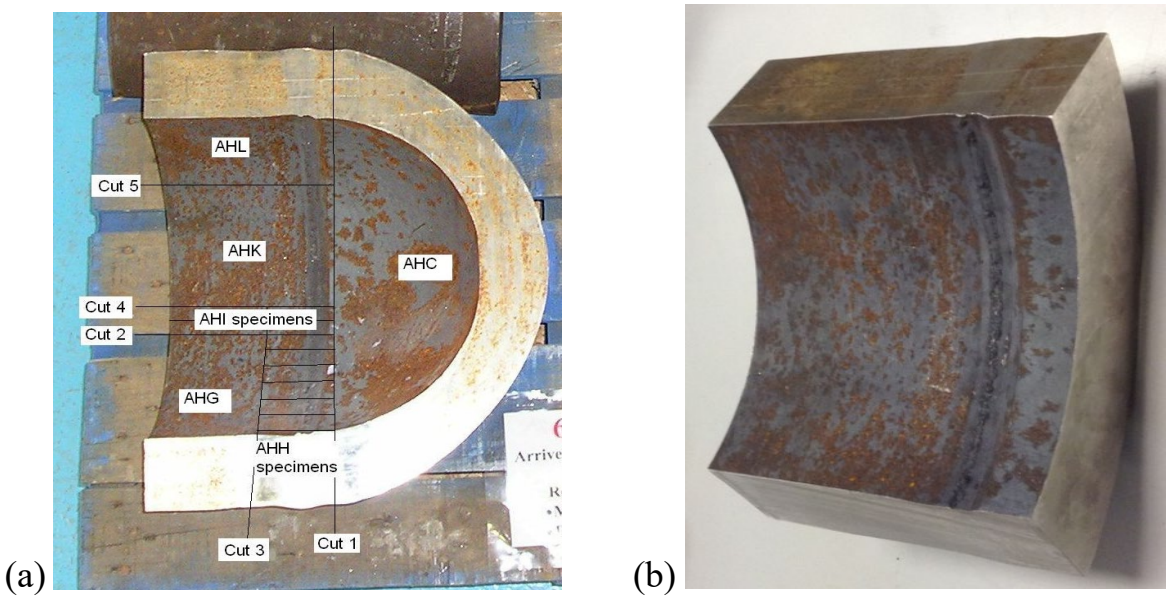

Figure 3.10 Images of Type 316H austenitic stainless steel steam header material (a) dome section showing the cut-section of AHK region (b) AHK region from which creep test specimens in Chapter 4 were extracted.

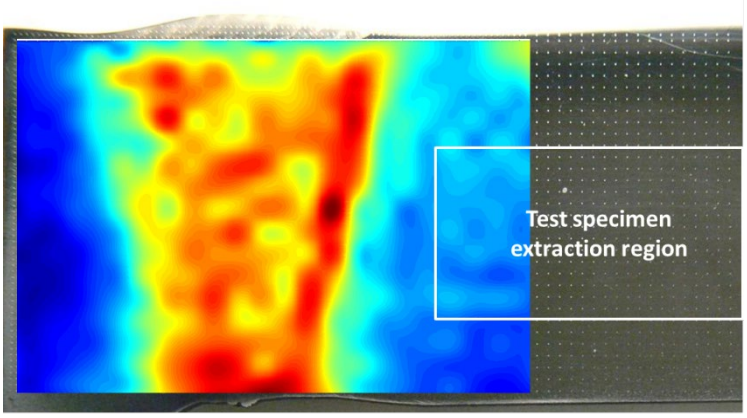

Figure 3.11 Weld hardness map superimposed on the AHK-weld region. The white rectangular section shows the region from which all creep test specimens were extracted.

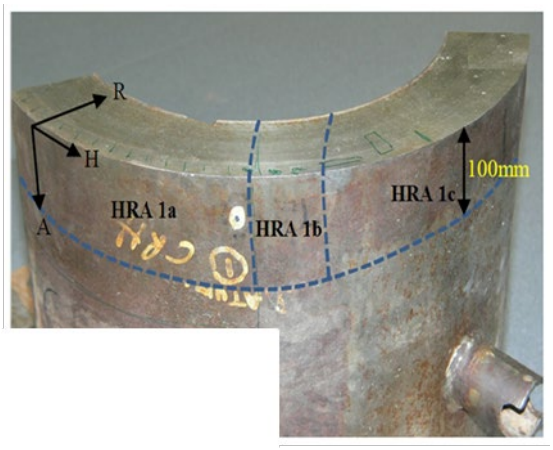

Figure 3.12 Type 316H (cast 69431) ex-service steam header section, diffusion bonding billets where extracted from region HRA 1c [25].

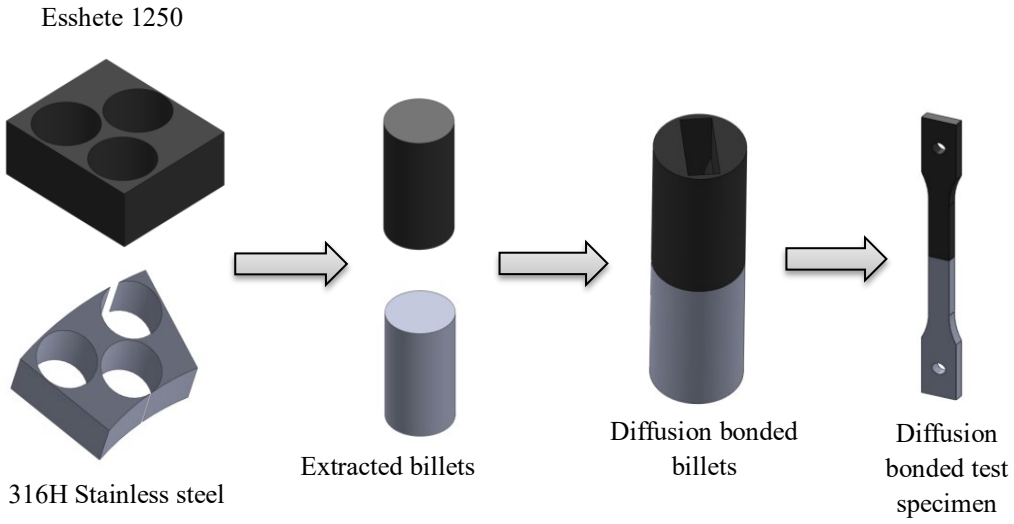

Figure 3.13 Summary of the diffusion bonding process

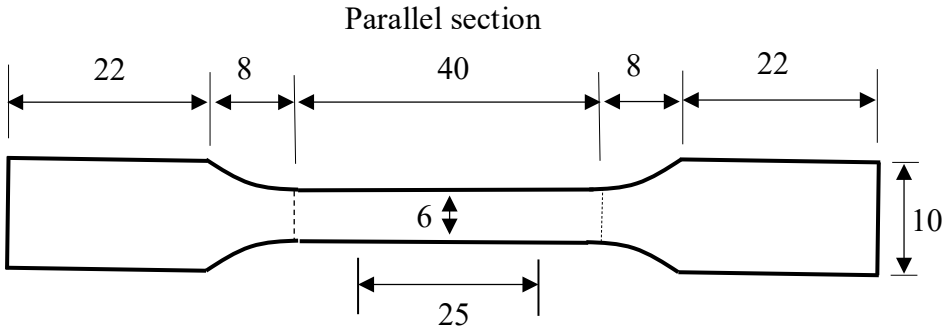

(a)

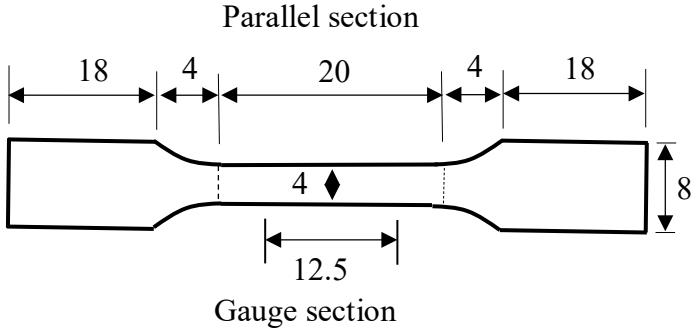

(b)

Figure 3.14 Schematic drawing of specimen dimensions (a) standard size test specimen dimensions extracted from Type 316H-cast 55882 stainless steel. (b) sub-size test specimen dimensions extracted from Type 316H-cast 69431 and Esshete 1250 stainless steels.

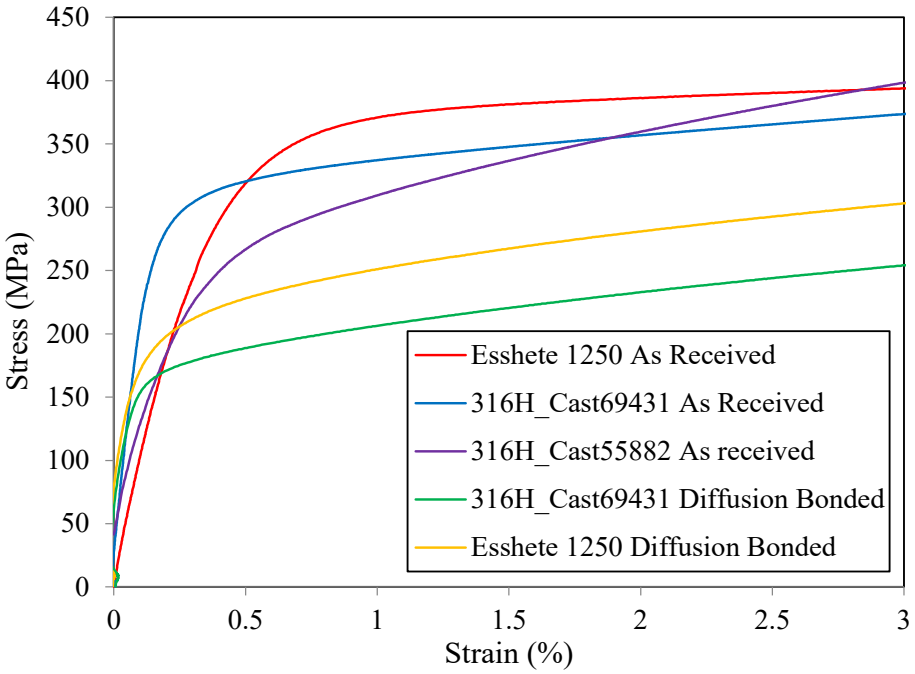

Figure 4.15 stress-strain curves of monolithic specimens extracted from the as received materials and the ones subjected to the diffusion bonding process.

TABLES

Table 3-1 Average dimensions and mass of the elastic modulus specimens

Material	Length (mm)	Width (mm)	Thickness (mm)	Mass (g)
316H	40.03	4.0	3.0	3.80
Esshete1250	39.94	4.0	3.0	3.78

Table 3-2 Trial test parameters for the diffusion bonding process

Test no.	Temp °C		Vacuum Pressure (pa)	Applied Load (kg)	Time (min)
	Set	Actual			
1	1100	950	3×10^{-4}	200	30
2	1000	880	3×10^{-4}	400	30
3	950	950	3×10^{-4}	400	60
4	1100	1100	3×10^{-4}	400	60

Table 3-3 Grinding parameters used in the current study

Grit Number	**Grit size (µm)**	**Applied Load (N)**	**Time (minutes)**
P240	58.5	10	5
P500	30.2	10	5
P800	21.8	10	5
P1200	15.3	10	10
P4000	5.0	10	10

Table 3-4 Polishing parameters applied in the current study

Particle Size (µm)	**Applied Load (N)**	**Time (minutes)**
6	10	10
3	10	10
1	10	20

Table 3-5 Hardness (Hv) and elastic modulus measurement results

No:	Material	Elastic Modulus (GPa)	Hardness (Hv)	
			As Received	Diffusion Bonded
1	316H - Cast 55882	196.2	169.4 ± 7	-
2	316H - Cast 69431	196.7	170.6 ± 3	158.5 ± 4
3	Esshete1250	195.1	165.3 ± 5	144.6 ± 5

Table 3-6 Yield stress (MPa) of Type 316H and Esshete 1250 stainless steels

No:	Material	0.2% - Yield Stress (MPa) -	
		As Received	Diffusion Bonded
1	316H - Cast 55882	197.3	-
2	316H - Cast 69431	241.5	168.8
3	Esshete 1250	253.7	190.6

3.7 REFERENCES

1. *BS EN ISO 6507-1:2005. Metallic materials - Vickers hardness test - Part 1: Test method*.
2. *MTS Systems Corporation - TestWorks® 4 Software for Nanoindentation, Eden Prairie, MN, USA.*
3. *ASTM E2546-15 Standard Practice for Instrumented Indentation Testing*. 2015, ASTM International.
4. *ASTM E111-04(2010) Standard Test Method for Young's Modulus, Tangent Modulus, and Chord Modulus*. 2010, ASTM International.
5. *ASTM E1876-15 Standard Test Method for Dynamic Young's Modulus, Shear Modulus, and Poisson's Ratio by Impulse Excitation of Vibration*. 2015, ASTM International.
6. Oliver, W.C. and G.M. Pharr, *Measurement of hardness and elastic modulus by instrumented indentation: Advances in understanding and refinements to methodology.* Journal of materials research, 2004. **19**(01): p. 3-20.
7. Wolfenden, A. and W. Schwanz, *An Evaluation of Three Methods to Measure the Dynamic Elastic Modulus of Steel.* 1995.
8. Spinner, S., T. Reichard, and W. Tefft, *A comparison of experimental and theoretical relations between Young's modulus and the flexural and longitudinal resonance frequencies of uniform bars.* Journal of Research of the National Bureau of Standards—A. Physics and Chemistry, 1960. **64**(2).
9. Sakanashi, Y., *Measurement of Creep Deformation in Weldments.* PhD Thesis, The Open University, 2013.

10. Bhanumurthy, K., et al., *Diffusion bonding of nuclear materials.* BARC, 2013. **2**: p. 19.
11. Kundu, S., et al., *Diffusion bonding of commercially pure titanium to 304 stainless steel using copper interlayer.* Materials Science and Engineering: A, 2005. **407**(1): p. 154-160.
12. Sabetghadam, H., A.Z. Hanzaki, and A. Araee, *Diffusion bonding of 410 stainless steel to copper using a nickel interlayer.* Materials Characterization, 2010. **61**(6): p. 626-634.
13. Ghosh, M., et al., *Diffusion bonding of titanium to 304 stainless steel.* Journal of Nuclear Materials, 2003. **322**(2): p. 235-241.
14. Kurt, B., *The interface morphology of diffusion bonded dissimilar stainless steel and medium carbon steel couples.* Journal of Materials Processing Technology, 2007. **190**(1): p. 138-141.
15. Kurt, B. and A. Çalik, *Interface structure of diffusion bonded duplex stainless steel and medium carbon steel couple.* Materials Characterization, 2009. **60**(9): p. 1035-1040.
16. VanderVoort, G.F., *Metallography Principles and Practice.* 1984, New York: Mc Graw-Hill.
17. *ASM Mechanical grinding and polishing. In VanderVoort, Editor. ASM Handbook: Metallography and Microstructures*

    Vol. 9. 2004, Materials Park.
18. *ASTM E112-13 Standard Test Methods for Determining Average Grain Size*. 2013, ASTM International.
19. *Aztec 2.1 Software, Oxford Instruments NanoAnalysis, 2010-2013.*
20. Forsey, A. and S. Gungor, *Demosaicing images from colour cameras for digital image correlation.* Optics and lasers in engineering, 2016. **86**: p. 20-28.
21. LaVision, *StrainMaster DaVis 8.1 Digital Image Correlation Software*. 2013.
22. Lecompte, D., et al., *Quality assessment of speckle patterns for digital image correlation.* Optics and lasers in Engineering, 2006. **44**(11): p. 1132-1145.
23. Sakanashi, Y., et al., *Measurement of Creep Deformation across Welds in 316H Stainless Steel Using Digital Image Correlation.* Experimental Mechanics, 2017. **57**(2): p. 231-244.

24. Evans, R.W. and B. Wilshire, *Introduction to creep*. The Institute of Materials. 1993, London.
25. Githinji, D.N., *Characterisation of Plastic and Creep Strains From Lattice Orientation Measurements*. 2014, The Open University.

CHAPTER FOUR

4. Measurement of creep properties using an hour-glass shaped test specimen

4.1 Introduction

Transient and steady-state creep properties are required for design and remaining life assessments of safety critical components in power plants, operating under load at high temperature. Multiple uniaxial creep tests, using standard specimens, are generally used to characterize the transient and steady-state creep properties as a function of stress and temperature. For component life assessment, availability of test material is often a problem, if archive material is unavailable or material ageing is of concern. Very small samples of material must be extracted from power plant components which are still in service as minimal repair work must be done to make good the components for future use. This has led to use of conventional design sub-size (miniature) specimens and the development of non-conventional creep testing techniques such as impression creep, small punch creep specimens and indentation creep testing[1-3]. Results from these test specimens have been applied for component life assessment through characterisation of creep properties of the weld and the heat affected zone. Compared to conventional creep testing, the use of miniature, impression and small punch creep specimens offers the advantage that test pieces with small dimensions can be used allowing extraction of specimens from thin-walled plant components such as super-heater tubes. However, in all the test methods mentioned above, to characterize the creep properties of a material, multiple tests at various levels of stress and temperatures are carried out. Considering the test duration of creep tests, this is costly and taxing in terms of time.

This chapter presents a novel method for extracting creep deformation curves at multiple levels of stress from a single test specimen using digital image correlation (DIC), and thereby characterizing the creep properties of materials at high temperature. Using a single specimen reduces the aggregated testing time several fold and therefore is very cost-effective. Moreover, extracting multiple creep curves from adjacent locations in the same specimen has advantage of minimising microstructural variations, which may be an issue when multiple specimens are removed from different regions of large cast and forged components. It also eliminates the random errors associated with multi-specimen testing.

A method for extracting multiple creep curves from a single specimen was first demonstrated by Levy *et al* [4]. They used a tapered specimen with a strain replica approach. The experimental tests were carried out as interrupted tests, which involved heating, holding, loading, cooling and unloading of the specimen in order to carry out strain replica measurements at particular time intervals. Such practices involving cyclic conditions are likely to alter the mechanical behaviour of the material. Moreover, the limited data collected were insufficient to describe the entire creep curve. The strain measurement technique was a limiting factor in this method. Following developments in photo elasticity, Cloud *et al* [5] demonstrated the capability of the method for extraction of multiple creep deformation curves from a single tapered specimen. Although photo elasticity is a non-contact strain measurement technique, making it ideal for extracting multiple creep deformation curves from a single specimen, the complexity of image phase extraction and the effects of thermo-currents on the measured strain limits its application. Therefore, the data obtained were only for a short period of time and not ideal for characterization of creep properties of engineering materials.

Further, Rist *et al* [6] used a circular specimen with a waist (concave shaped) coupled with inverse modelling to determine the tertiary creep properties of a single crystal nickel super-alloy. The data obtained correlated very well with predicted results even though the creep strain measurements as function of time were based on the displacement of the specimen grips and as such the entire gauge length was used to measure the creep deformation. This method is likely to introduce errors in the measured creep strain as the specimen would undergo non-uniform deformation with higher creep rates at the centre compared to other regions of the gauge length. The spatial strain distribution was determined by precise measurement of the specimen geometry before and after the creep test. The limitation of this technique is that spatially distributed strain along the gauge length cannot be obtained as a function of time. The strain measurement technique applied by Rist *al et* [6], can be applied to characterise tertiary creep properties but is not suitable for characterisation of the entire creep behaviour of engineering materials.

Recently, Sinha *et al* [7] extracted transient creep properties from a single specimen using strain relaxation and recovery tests. In this method, various elastic stresses are applied to a single specimen for a given period and when the specified time is reached, the stress is removed completely, and the recovery strain is monitored. Inelastic strain curves are extracted and from these curves, transient creep properties of the material can be determined.

This technique is only limited to measurement of transient creep properties and thus cannot be used for extraction of steady-state creep properties which are useful for component design and remaining life assessment.

In the present work, DIC was used for extracting load-controlled creep deformation curves at multiple stress levels from a single specimen. The advantage of using DIC is that spatially resolved creep strain as function of time can be determined and relatively long creep tests can be carried out [8]. One of the limiting factors of using DIC for creep tests is the endurance of the high temperature paint which has to be used to generate a random speckle pattern on the surface of the specimen and to inhibit oxidation, however test durations over 2000 hours of austenitic stainless steels using a silicon ceramic based high temperature paint (VHT FlameProof^{TM}) has been reported [9]. Apart from the strain measurement technique, a suitable specimen design with the capability of generating a non-uniform stress along the gauge length is required to extract multiple creep deformation curves from a single specimen. The following section describes the specimen design developed in the present work.

4.2 Specimen Design

To ensure that the specimen type used can give a stress range suitable for extracting multiple creep deformation curves from a single specimen, it was essential that a specimen with optimum design fit for this purpose is developed. This Section describes how the specimens used in this study were designed. Since a single camera is used for strain measurements in this study (2D DIC), a flat specimen design was adopted.

The starting point for specimen design was consideration of a conventional tensile creep testing specimen given by the Standards [10-12]. For conventional creep test, a flat test specimen is designed with a gauge section within the region with reduced uniform cross-section area relative to the rest of the specimen so that deformation and failure would be localised in this region. To reduce the effects of stress concentration at the two ends of the parallel section, a gradual transition radius between the parallel section and the specimen tabs is used. The ASTM Standard encourages the use of flat specimens with proportional design dimensions (that is, the length of the gauge length is given by $= 5.65\sqrt{(cross\ section\ area)}$) which requires that the gauge length is about 4 to 5 times the width of the specimen. Figure 4.1 shows the drawings of an ASTM standard flat 25mm gauge length, 6mm wide and 3mm thick with a parallel section of up to 40mm long within the reduced section of the creep specimen.

A simplified plane stress finite element (FE) analysis was carried out to illustrate the stress and strain distribution in a standard flat tensile creep testing specimen using ABAQUS software. Elastic properties of austenitic stainless steel at room temperature were used as input data to the FE model (elastic modulus = 196GPa and Poisson's ratio 0.3). Quadrilateral 8-node plane stress elements with reduced integration (CPS8R) were used for the model, Figure 4.1(b).

Figure 4.2 (a) and (b) shows the FE elastic stress and strain distribution extracted from the centre of the parallel section of the specimen. From Figure 4.2, the stress and strain are uniformly distributed across the parallel section. Towards the ends of the parallel section, both the stress and strain reduce gradually. For this type of specimen, the gauge length would be 25mm, as such; the stress and strain within the gauge length will be uniformly distributed. Note that even when the specimen undergoes yielding and deforms plastically, the stress and strain distribution would remain uniform up to the point of necking.

To extract multiple creep deformation curves from a single specimen, a standard flat conventional creep testing specimen should be modified resulting in a non-uniform gauge section suitable for giving a varying stress range within the gauge length. A tapered specimen has been previously used in demonstrating that multiple creep strain curves can be extracted from a single specimen at varying stress levels and therefore was the initial choice in this study.

4.2.1 Tapered Specimen Design

To design a tapered specimen, a standard 120mm long, 6mm wide, 3mm thick creep tensile test specimen with gauge length of 25mm, given in the standard, was modified by introducing a tapered region in the gauge section as shown in Figure 4.3(a). The tapered section was designed such that there is a gradual change in geometry from the region with a larger cross-section to the one with a smaller one. The gauge length is as defined in Figure 4.3(a). Simplified elastic finite element (FE) analyses were carried out to assess the merits of the tapered specimen design using ABAQUS software [13]. Elastic material model input data and element type used for the assessment of the standard specimen in Section 4.2 were used, Figure 4.3(b).

Figure 4.4 shows the elastic stress and strain distribution along the gauge section of the tapered specimen. In Figure 4.4(a), the elastic stress distribution along the gauge length does

not change significantly as the applied load increases. At a lower maximum stress of 100MPa, the difference between the maximum stress in the region with minimum cross-section and the minimum stress in the region with a larger cross-section about 25MPa. On the other hand, at higher maximum stress (such as 300MPa) the difference between the maximum and minimum stress increases to about 80MPa. Although there is an increase in the difference between the maximum and minimum stress, a gradual transition in the stress distribution from the region with minimum stress to the one with the maximum stress is maintained. A similar trend can also be seen in elastic strain distribution, Figure 4.4(b) and no significant localised deformation can be seen in the region with minimum cross-section. From the FE results in Figure 4.4, it can be concluded that with an initial elastic applied load, the tapered specimen is ideal for extracting multiple creep curves from a single specimen. However, it is known that at lower applied load, the creep process is slow resulting in longer test durations. Considering the creep testing duration, initial applied loads exceeding the yield strength of the material are commonly used. When the initial applied load induces plastic deformation, it is difficult to conclusively establish how the tapered specimen would respond based on the results from elastic FE analysis shown in Figure 4.4. Therefore, elastic-plastic FE analyses were carried out to assess the behaviour of the tapered specimen under plastic deformation.

4.2.1.1 Elastic-plastic FE analysis of tapered specimen design

Elastic-plastic properties of ex-service Type 316H austenitic stainless steel at room temperature were used as input data to the FE model (elastic modulus = 196GPa, Poisson's ratio 0.3, yield stress = 170MPa and plastic deformation characteristics given in Chapter 3 were used). Quadrilateral 8-node plane stress elements with reduced integration (CPS8R) were used for the FE model. Figure 4.5 shows the stress distribution and development of plastic strain as the tapered specimen undergoes yield and plastic deformation beyond the yield point. From Figure 4.5(a), the stress distribution does not change significantly as deformation progress beyond the yield strength. However, local yielding initiates in the region between the area with reduced cross-section and the transition radius. This is as a result of local deformation in this region due to sharp transition in dimensions between the specimen shoulder and the region with minimum cross-section. Further increase in applied load resulted in increased localised deformation, and gradually plastic deformation was spread to other regions in the area with reduced section when the applied load is higher than the theoretical load required to cause yield of the material, Figure 4.5(b). Although there is

gradual spread of plastic deformation as the applied load increased further beyond the yield strength of the material, significant localised deformation could be seen in the region with minimum cross-sectional area.

Further modifications of the tapered specimen geometry did not reduce the effects of local yielding of the material in the region with reduced cross-section area. Therefore, it was concluded that, the tapered specimen is only ideal for extracting multiple creep curves from a single specimen when the initial applied load does not induce plastic deformation. Due to time constraint, high initial applied loads will be used for all the creep tests and for this reason, it was concluded that the tapered specimen was not ideal for the present work. A specimen of non-uniform cross-section area along the gauge section with the smallest width dimension at the centre of the gauge length (referred to as a hour-glass specimen design) was considered.

4.2.2 Hour-glass Specimen Design

Like the tapered specimen, the initial design of the hour-glass specimen was based on a 120mm long standard flat creep tensile test specimen with 6mm wide and 3mm thick. The width of the specimen at the centre of the gauge length was 6mm and at the ends of the gauge length, the specimen width was 8mm. A gradual transition curvature from the centre of the gauge length to the ends of the gauge length was introduced to have a varying stress distribution from the centre to the ends of the gauge length. Figure 4.6(a) shows schematic drawing of the hour-glass specimen. For elastic-plastic FE assessment of the merits of the hour-glass specimen design, material model input data and element type used for the assessment of the tapered specimen in Section 4.2.1.1 were used, Figure 4.6(b).

Figure 4.7 shows the elastic-plastic stress and strain distribution along the gauge length of the hour-glass specimen design. There is a gradual increase in the stress from the ends to the centre of the specimen gauge length which is required for extracting multiple creep deformation curves from a single specimen. Figure 4.7(b) shows development of plastic strain in the hour-glass specimen as it undergoes yielding. Although initial yielding starts on the edges at the centre of the specimen, plastic deformation is quickly spread onto the entire section of the centre of the specimen gauge length. The area undergoing plastic deformation on initial yielding is larger in the hour-glass specimen design thus reducing the effects of localised deformation. As the applied load increase, the peak plastic strain and the size of the region undergoing plastic deformation at the centre of the gauge length increases. There is a

gradual decrease in the true plastic strain from the centre of gauge length to the regions where the material is yet to undergo yielding.

It was noted that the size of the region experiencing plastic deformation in the hour-glass shaped specimen is larger compared to the tapered specimen at the same applied load. This indicates that in a hour-glass shaped specimen the effects of localised deformation due to specimen geometry are reduced as the region undergoing plastic deformation increases with increase in load compared to the tapered specimen where initial yielding is highly localised.

For the hour-glass specimen, it was noted that slight increase in the gauge length resulted in change of the gauge width curvature thus introducing a smooth geometrical transition from the region of low stress (at the ends of the gauge length) to the region with high stress (gauge centre). For these reasons, an hour-glass shaped specimen design was chosen.

4.2.2.1 Final hour-glass shaped specimen design

The hour-glass specimen design was refined by iteratively varying the length and curvature of the gauge section in order to create a well distributed stress and strain field (avoiding noticeable localised deformation due to specimen geometry). A final specimen geometry of 3mm thickness, 50mm gauge length, 6mm wide at the gauge centre and 8mm wide at the two ends of the gauge length, with a transition curvature radius of 310mm was selected, Figure 4.8(a). The total length of the specimen was modified to 130mm. Thereafter, a 3mm thick 3D elastic-plastic FE model was developed with dimensions given in Figure 4.8(a). Material properties used in Section 4.2.1 where used as input data to the 3D FE model. Quadrilateral 20-node plane strain elements with reduced integration (C3D20R) were used for the model, Figure 4.8(b).

Figure 4.9 shows the distribution of stress and strain along the gauge length for the chosen hour-glass specimen design. With these dimensions, there is a gradual transition of stress from the region with low stress (at the ends of the gauge length) to the one with high stress (gauge centre). The FE results shows that a nominal stress range, at initial loading, of about 70MPa under elastic-plastic deformation condition can be achieved, giving a cross-section stress variation factor of about 1.3 along the gauge length, Figure 4.9. The test specimens will be gripped using wedge grips with a position pin at the centre of the specimen tab. To avoid development of stress concentration at the ends of the gauge length, a large transition radius

between the specimen tab and the gauge length was chosen. From Figure 4.9, there is no stress concentration at the two ends of the gauge length.

4.3 Experimental set-up

Specimens were prepared using wire electro-discharge machining (EDM) from ex-service Type 316H stainless steel material to the drawing shown in Figure 4.10. The final machined profile of the specimen was measured using a coordinate measurement machine (CMM) with a touch probe (radius of 2.0mm) and an average measurement point spacing of 0.2mm. The specimen thickness was measured using a micro-meter screw gauge at 10 points along the gauge section giving an average thickness of 3.01mm. From the CMM profile and the specimen thickness, the cross-section area of the specimen at any given point was determined. The load applied for the test was selected to achieve a maximum nominal stress of 320MPa at the centre of the hour-glass shaped creep specimen. The load-train for the creep machine was calibrated using a load-cell. A detailed description of how the nominal stress distribution along the specimen gauge length was determined is given in Section 4.4.

The creep tests were carried out using the testing system with DIC monitoring as described in Ref [9]. The furnace used has a window which allows the acquisition of digital images at high temperature. To carry out digital image correlation, the specimen is required to have a natural or artificial speckle pattern which acts as a carrier of specimen surface deformation that can be tracked by imaging. In this case, a commercial high temperature black and white paint (VHT FlameProof^{TM}) was applied on the specimen surface to give it a random speckle pattern. To produce a fine speckle pattern on the specimen surface, the specimen was hand-sprayed from a distance of at least 1m away from the specimen. A Nikon D800E camera with an image resolution of 7360x4912 pixels (36 mega-pixels), mounted on a stable laboratory table, was used for image acquisition. The area of interest was set such that only one half of the gauge section of the hour-glass specimen was imaged assuming that the creep strain distribution will be the same on the other half of the specimen. This is due to the limitation in the size of the furnace window, which has a maximum height of 40mm, and therefore was unable to monitor the whole gauge length of the specimen. The specimen was illuminated using an in-built camera flash to obtain uniformly distributed light across the specimen surface. Figure 4.11 shows the experimental set-up of the integrated DIC-creep testing system.

The creep test was carried out at a nominal target temperature of 525^{o}C. Two Type-N thermocouples, calibrated at 525^{o}C using a portable furnace and a standard Type-R thermocouple, were attached to the top and bottom tabs of the specimen (as indicated in Figure 4.10 and were used for temperature control. The specimen temperature was maintained within +/- 1^{o}C of the set temperature within the limits given in the creep testing standard [10, 11]. Once the temperature had stabilized, the specimen was then loaded in steps. For each load added, an image was taken allowing the loading strains to be determined. The total loading time for the hour-glass specimen was 11minutes. At the end of the loading process, a reference image was taken, and the image acquisition rate was set to one image in every 20 minutes. After 24 hours, the image acquisition rate was set to one image per hour. The test was stopped after 1900 hours and the acquired raw colour images were converted into 16bit grayscale images using an in-house developed Matlab code [15, 16] and then imported into DIC software (DaVis 8.2 developed by La Vision [17]) for displacement analysis.

4.3.1 Validation tests

To validate the results obtained by extracting multiple creep deformation curves at various stress levels from a single specimen, creep tests were carried out using monolithic conventional creep specimens at 525^{o}C with applied nominal stresses of 320MPa and 300MPa. The test specimens for validation were extracted from the same material and location as the hour-glass specimen along the x-x plane as shown in Figure 4.12. The dimensions of the specimens used for validation purposes were machined according to the creep testing standards [10, 12], with 6mm width, 3mm thickness and a gauge length of 40mm, Figure 4.13.

The validation with 320MPa applied initial nominal stress was carried using both DIC and high temperature creep gauge extensometers. High temeprature extensometers were attached to the ridges just beyond the gauge length of the specimen and a speckle pattern was applied to the entire gauge length to facilitate DIC strain measurements. The gauge length was defined as shown in Figure 4.13. Since, DIC was also used for strain measurement for the validation tests, the loading procedure descibed in Section 4.3 was used, where an image was taken for every load added to the load-train during the initial loading stage of the specimen and the total loading time for the validation tests was 11minutes which is the same as the loading time obtained for the hour-glass shaped specimen. The temperature for both tests was

controlled to within 525 +/-2^{o}C. The results from these tests were then compared with those obtained using DIC from the hour-glass specimen.

4.4 Determination of nominal stress distribution

The measured width of the hour-glass specimen as a function of position from the centre of the gauge length is shown in Figure 4.14 (a). A quadratic function was fitted to the data as shown in Figure 4.14(a) allowing the width of the specimen at any given point along the gauge length to be determined. Knowing the applied load and the initial specimen geometry, the distribution of nominal stress along the gauge length was determined. Figure 4.14(b) shows a plot of the distribution of nominal stress as a function of gauge length. However, since the resulting stress upon loading is higher than the yield strength of Type 316H stainless steel at 525^{o}C, the specimen experienced initial plastic deformation prior to inelastic creep the significance of this is discussed in later. Figure 4.15 shows a comparison between the measured nominal stress profile calculated from the measured dimensions of the hour-glass specimen and the one predicted by elastic-plastic FE analysis of the specimen geometry (see Figure 4.8). The stress distribution from the machined hour-glass specimen compares well with the FE predicted results and that there is no significant stress concentration in the machined specimen. Towards the end of the gauge length, there is a slight difference in the stress distribution. This difference can be attributed to the fact that for the FE results the specimen is deformed and as result, the stress developing in the transition region between the specimen tabs and the gauge length has an influence on how the stress is distributed at the end of the gauge length compared to the nominal stresses calculated from the non-deformed machined test specimen.

4.5 Digital image correlation analysis

For DIC analysis, the area of interest was selected by masking off the edges of the specimens and regions outside the gauge length. Various combinations of the subset and step sizes were tried, and better displacement correlations were found when a subset size of 51 x 51pixels and a step size of 9 were used. The displacement computations were carried by correlating all the images to the first image; this reduces the errors in the computed displacements. Upon calculating the displacement fields from the images, the data was exported and further processed for spatial and time resolved strain computation using an in-house developed MATLAB script [18].

4.5.1 Strain Computation

A schematic illustration of the procedure for DIC data analysis is given in Figure 4.16. To process the computed displacement fields, 5% of the edges of the displacement maps were masked off. The strain calculation area was then divided into equal spaced regions of 0.45mm [18]. To plot the creep strain-time curves at any given position along the gauge length, it was assumed that the strain across the width of the specimen at any given point is uniform. With this assumption, a plane was fitted separately to the displacement vectors resolved into the x and y-direction. Note that the plane is fitted for the whole defined width of the specimen excluding 5% of the region edges on both sides of the specimen. Differentiating the fitted surfaces gives the strain gradient in both the x and y directions, ε_{xx} and ε_{yy}, respectively. Therefore, knowing stress distribution as described in Section 4.4, multiple creep deformation curves at varying stress levels were extracted from a single specimen.

4.6 Results

Figure 4.17 and 4.18 show plots of longitudinal and transverse creep deformation at multiple stress levels extracted from a single hour-glass specimen as a function of time. The nominal stress distribution ranges from 250MPa to 320MPa as described above. From Figure 4.17 and 4.18, the material at the centre of the gauge length experiences higher creep rates compared to the material at the far end of the gauge length. The difference in creep strain rates in the secondary creep regime between the low stress region and the high stress one is in the order of 5. In Figure 4.17, there is a slight kink in the creep curves at about 115 hours. This was caused by a slight movement in the camera which occurred when an aluminium shield was put between the camera lens and the furnace window to minimise the effects of thermal currents due to changes in temperature in the laboratory. From the creep curves in Figure 4.17, it can be concluded that the slight movement in the camera did not have an adverse effect on the creep test as the creep curves did not show a sharp change in creep strain rate. Figure 4.19 shows a plot of the evolution of longitudinal and transverse creep strain at various positions across the gauge length as a function of time. As the time increases, the rate of increase in creep rates of material at the centre of the gauge length is higher than for the material towards the end of the gauge length. From Figure 4.19, it can be seen that there is a gradual increase in accumulated tensile creep strain in the longitudinal direction and compressive strain in the transverse direction from the end of the gauge length towards the gauge centre for all the curves; as expected considering the nominal stress distribution given

in Figure 4.14(b). Figure 4.20 shows a plot of the measured temperature of the specimen as function of time during the creep test. Measurements from the two thermocouples positioned at the top and bottom part of the specimen show that the specimen temperature was well controlled at 525±1^{o}C and therefore did not significantly affect the creep test results.

Figure 4.21 gives a 3D pictorial view of how the creep strain increases along the specimen gauge length with time, and with this data, by interpolation, a creep curve can be extracted at any given position along the specimen gauge length as a function of time and stress. The multiple-stress creep curves as shown in Figures 4.17, 4.18 and 4.21 characterise both the primary and secondary creep behaviour of the material. This behaviour can be idealised by fitting a creep model to the data and then extracting the model coefficients as described later in Section 4.7. Because the applied stress at any given point along the gauge length on initial loading of the specimen is considerably higher than the yield strength of the material at 525^{o}C, significant plastic deformation occurs which is enough to change the true stress at the beginning of the creep test. The following Section describes how the distribution of true stress along the gauge length on initial loading was determined.

4.6.1 Determination of true stress distribution at initial specimen loading

Section 4.4 described how the nominal stress distribution was determined from the measured geometry of the specimen. However, since the resulting stress along the entire gauge length on initial loading was higher than the yield strength of Type 316H stainless at 525^{o}C, the specimen experienced initial elastic and plastic deformation prior to accumulating inelastic creep strain. That is the cross-sectional dimensions changed on initial loading giving slightly higher local true stress distribution than the nominal stress based on the original geometry. The creep deformation behaviour will be dependent on both the true stress and accumulated plastic strain. To determine the distribution of true stress, the accumulated strain upon initial loading and throughout the test must be known. The loading strain was measured by capturing images during the specimen's initial loading until the full load was applied. Prior to loading, a reference image was taken and thereafter an image was taken each time a load was added to the load-train. A total of 6 images were captured and then analysed to calculate the spatially resolved strain induced upon initial loading. Figure 4.22 shows the evolution of inelastic strain in both the loading and transverse directions. As expected, from Figure 4.22, the middle section of the gauge length experienced higher strains than the section towards the end of the gauge length and that the strain increased as the applied load was increased. The

computed transverse strain (ε_{xx}), Figure 4.22(b), was used to determine the reduction in the cross-sectional area of the specimen. The original specimen width at any given point corresponding to the DIC measurement points was determined using the quadratic function from Figure 4.14(a). The reduction in specimen width upon initial loading was calculated using the following expression, $l_f = l_0\,(1 + \varepsilon_{xx})$, where l_f is the final width upon loading, l_0 initial width and ε_{xx} is the transverse strain measured by DIC. During loading, for any reduction in width, there is a corresponding reduction in specimen thickness and therefore, to determine the true stress distribution, strain induced in the transverse direction was assumed to be equal to the strain induced in the through thickness direction. The final dimensions of the specimen, upon applying the full load, were calculated from the strain induced in the transverse and through thickness directions. Since the applied load and the final cross-sectional area at each point along the specimen gauge length were known, the resulting true stress distribution as a function of position along the specimen gauge length could be calculated. Figure 4.23 (a) shows the distribution of the true stress at the beginning of the test compared to the nominal stress and Figure 4.23 (b) shows the plot of the true stress distribution compared to the distribution of strain (ε_{yy}) accumulated during the initial loading of the specimen. The determined true stresses are significantly higher than the nominal stresses because of the elastic and plastic deformation the material experiences during initial loading.

Figures 4.24 and 4.25 show plots of creep strain as a function of time (Figure 4.17 and 4.18) corrected for true stress at the beginning of the test.

4.6.2 Evolution of true stress throughout the creep test

This section considers the evolution of true stress as a function of time during creep deformation for the purpose of establishing how the true stress changes with time during the creep test. The method of determining true stress outlined in Section 4.6.1 was used to analyse the evolution of true stress with time. Figure 4.26 shows a plot of the evolution of the true stress distribution along the specimen gauge length with time. The change in true stress with time along most of the specimen gauge length is relatively small but increases by about 10MPa at the centre.

4.6.3 Evolution of Poisson's ratio

From the longitudinal and transverse creep strains obtained, the evolution of Poisson's ratio throughout the creep test can be analysed. Poisson's ratio at any given time was calculated from the transverse and longitudinal creep strains. Figure 4.27 shows the distribution of Poisson's ratio as a function of time extracted from the top end of gauge length (20mm from the specimen centre), mid gauge section (12.5mm from the specimen centre) and bottom section which the specimen centre). From Figure 4.27, there is a large scatter in the calculated values of Poisson's ratios extracted from a region 20mm away from the specimen centre. This can be attributed to a low signal-to-noise ratio as this section of the specimen underwent minimal deformation compared to other regions of the gauge section. The mean value of the Poisson's ratio from 500 hours to the end of the test along the gauge length (from 0 to 20mm) is close to 0.5, as shown in Figure 4.28. However, towards the end of the gauge length there was increased variability in the measured Poisson's ratio and as such results from this region (From 20mm to 25mm from the specimen centre) were not included in the Figure 4.28.

4.6.4 Validation test results

Figure 4.29 shows comparisons between creep strains obtained from the hour-glass specimen and those from the validation tests using conventional specimens at applied initial stresses of 320MPa. From Figure 4.29(a), it can be seen that the creep curve constructed from the creep strain measured using the extensometer on the conventional specimen and the one constructed from the DIC creep strain extracted at the same stress level (320MPa) from the hour-glass specimen are very similar up to about 1100 hours. Beyond 1100 hours, the creep curve extracted from the hour-glass specimen curves upward signifying the beginning of tertiary creep whereas the one extracted from the conventional specimen continues in the secondary creep regime. Figure 4.30 shows the temperature distribution for validation test, the temperature was well controlled and compares well with the temperature distribution shown in Figure 4.20 for the hour-glass specimen. Both Figure 4.20 and 4.30 indicates that the change in the creep strain curve for the hour-glass specimen was not due to temperature effects as the temperatures were controlled within the recommended limits of $\pm 2^{o}C$ of the set temperature [10, 11]. The difference in the two creep curves could be due to the fact that in the hour-glass specimen, local creep strain is measured at a point where the specimen geometry has a minimum cross-section which experienced higher localised damage during the initial loading compared to the surrounding region, resulting in increased creep strain rate

with time. Whereas for the conventional validation test specimen, the induced damage on initial loading would be uniform across the gauge length hence the difference in the time at which the tertiary creep regime begins for this specimen type. Although the validation test continued in secondary creep regime beyond 1100 hours, it failed at about 1900 hours without exhibiting significant tertiary creep. The failure point of the validation test was within the gauge length, although it was close to the shoulders onto which the high temperature extensometer was attached to the specimen. Therefore, the failure of the validation test specimen could be attributed to either the presence of a defect or possible bending stress due to the attached extensometer.

Apart from the creep strain measured using an extensometer on the validation test specimen, DIC strain measurements were also carried out and the DIC measured strains were averaged across the entire gauge length of the specimen. The average DIC measured strain correlates well with both creep strain measured on the validation test specimen using an extensometer and the DIC creep strain extracted from the hour-glass specimen at 320MPa nominal stress, Figure 4.29(a). From Figure 4.29(a), the DIC measured strain from validation test was only measured up to 800 hours, this was due to a malfunction in the camera as it stopped capturing images during the test. Despite the limited data from the DIC measurements on validation test specimen, the three data sets correlated very well signifying the validity of extracting multiple creep curves from a single specimen.

4.7 Creep Data Analysis and Model Fitting

4.7.1 Determination of creep rates and minimum creep rate

A least squares method for calculating creep rates from experimental data described by Evans *et al* [24] is widely used. This method was applied to the hour-glass specimen creep data by calculating the creep rates at every 9, 21, and 41 data points. It was found that when fewer data points were used, the creep rate vs time curves were noisy whereas when more data points were used, the creep rate curves were overly smoothed. A Polynomial fitting method to partitioned experimental creep strain vs time curves was tried. The best fit was obtained when a fifth order polynomial was fitted to DIC measured creep deformation curves. Note that the best fits of the fifth order polynomials were obtained when strains in the early stages of the test (from 0 to 150 hours) were excluded from the analysis. The fitted fifth order polynomials were differentiated with respect to time to obtain the creep rates for all the creep

deformation curves. Figure 4.31 shows a plot of the creep rate as a function of time calculated using the best least squares method compared to the creep rates calculated by differentiating a fifth order polynomial fitted to the same creep deformation data (for strains at times greater than 150 hours). From Figure 4.31, there is less scatter in the creep strain rates obtained by differentiating a fifth order polynomial compared to the ones calculated using the least squares method.

Improved creep data fitting can sometimes be obtained by piece-wise fitting third order splines to the creep strain deformation curves. To calculate the creep rates, the coefficients of the splines are differentiated. This method was applied in the current study and varying lengths of splines were examined. However, the results obtained were similar to those from the least squares method. It was concluded the fifth order polynomial approach produced the best results and was used to determine the minimum creep rates at any given stress. The minimum creep rates were determined from the second derivative of the fifth order polynomial fitted to the experimental data at any given stress level.

4.7.2 RCC-MR model fitting

4.7.2.1 Determination of primary creep model parameters

The Norton-Bailey model given in Equation 2.4 is similar to the RCC-MR model given by Equation 2.7. Due to the similarities of these two models, only one of them was used. The RCC-MR model was chosen as it is widely used in modelling ex-service austenitic stainless steel material[14]. The standard model coefficients for the RCC-MR code at 525^{o}C are given in Table 4.1. Various fitting methods can be used for determining the coefficients of the RCC-MR model. Moffat *et al* [26] used a multiple linear regression method in which the end of primary creep and time are determined from experimental data and an average value of C_2 determined from the relationship,

$$C_2 = \frac{\dot{\varepsilon}_{min}\, t_{fp}}{\varepsilon_{fp}} \qquad (4.1)$$

was used, where ε_{fp} is the end of primary creep strain at time, t_{fp}. To use the multiple linear regression method described by Moffat et al [26], the end of primary creep strain and time must be determined accurately from experimental data. The drawback of using experimentally determined creep strain and time at the end of primary is that any inaccuracies in the determined values affect the average value of C_2 (Equation 4.1) and hence the

subsequent values of the other model coefficients which are determined from multiple linear regression. On the other hand, Wang *et al* [27] noted that the primary creep strain with respect to time at the same temperature, given in Equation (2.5), is highly dependent on stress. Therefore to improve the model fitting, it was assumed that the parameters C_1 and C_2 are linearly dependent on stress and as such linear equations expressing the dependence of C_1 and C_2 on stress were introduced and the value of n_1 given in the conventional RCC-MR code for stainless steel at the test temperature was used. With this fitting method, Wang *et al* [27], obtained RCC-MR model parameters that gave a good fit to the creep data at relatively low stresses, however at higher stresses the predicted data did not correlate with the measured data. Due to the poor correlation between the predicted and experimental data at higher stresses, the method applied by Wang *et al* [27] was not used here for the hour-glass specimen data.

In this work, the coefficients of the primary creep regime of the RCC-MR model were determined using the least squares curve fitting algorithm implemented in Matlab which iteratively finds the model coefficients of any nonlinear system [16]. Using the method described in section 4.7.1 for determining the minimum creep rates, it was noted that for creep strain curves constructed with nominal stresses of 280MPa and below, the minimum creep rate was not found. This implied that all the creep curves extracted with nominal stresses of 280MPa and below were still in the primary creep regime at the time the creep test was terminated. Therefore, creep curves with nominal stresses of 280MPa and below were used for determining the primary creep model parameters. These creep curves were chosen so that the entire creep curves were used for model fitting in order to determine the primary creep model parameters.

In the least square curve fitting algorithm used, the nonlinear least-squares solver finds the coefficients *x* that solve the problem [16],

$$\min_x \|F(x, xdata) - ydata\|_2^2 = \min_x \sum_i (F(x, xdata_i) - ydata_i)^2 \qquad (4.2)$$

where *xdata* and *ydata* are the measured input and output data expressed in matrix or vector form, and the $F(x, xdata)$ is a matrix-valued or vector-valued function of the same magnitude as *ydata*. Therefore, x in Equation (4.2) comprises the RCC-MR model coefficients that define the primary creep behaviour of the material. *xdata* is a matrix

containing the measured input variables time and the stress, whereas *ydata* is a matrix containing the multiple-stress creep strain data extracted from a single hour-glass specimen.

To run the least-squares curve fitting, a matrix containing initial values of C_1, C_2 and $n_1$is used to aid the convergence of the least squares fitting. In this work, initial values of C_1, C_2 and n_1 close to the ones given by the conventional RCC-MR model parameters at 525°C were used, since the experiment was carried out at 525°C. The initial values used were as follows,

$$x0 = [\,1 \times\ 10^{-12}\ \ 0.4\ \ \ 4] \qquad (4.3)$$

The values of the RCC-MR primary creep model parameters C_1, C_2 and n_1 determined from the least-square curve fitting method of multiple creep curves extracted from a hour-glass specimen with nominal stresses of 280MPa and below are given in Table 4.2.

4.7.2.2 Determination of end primary creep strain and time

To determine the end of primary creep, a widely used technique is to fit a straight line to the steady-state creep regime of the creep strain against time curve and then extrapolate this fitted line down to the point where it intercepts the creep strain axis (y-axis). Either the coordinates of a point at which the creep curve intercepts the extrapolated fitted line or a point at which the extrapolated fitted line intercepts the creep strain axis are taken as the end of primary creep strain and time. To improve the accuracy of the determined values, the creep strain and the creep strain rate are plotted as a function of time on to the same graph, see Figure 4.31. The challenge with this method is that the determined end of primary creep strain and time are dependent on how accurate the straight line is fitted to the steady-state creep strain thus the end of primary creep strain and time obtained are dependent on the experimentalist's judgement. For some experimental results, a plot of the creep rate as a function of time gives a good indication of the end of primary creep however this approach is not always feasible.

Rieth *et al* [28] determined the end primary creep by finding the average steady-state creep rate as a percentage of the minimum creep rate. In their work, they found that average creep rate varied within $\pm 20\%$ of the minimum creep rate and using a threshold line at $\pm 20\%$ of the minimum creep rate, the coordinates of a point where the threshold line intercepts the creep rate vs time curve was taken as the end of primary creep. This method relies on

deterministic evaluation of the average steady-state creep rate and thus limits dependence on experimentalist's judgement. Therefore, this method was adopted, and average steady-state creep rates set at 5%, 10%, 15%, 20% and 25% of the minimum creep rate were evaluated.

For each creep curve, the average steady-state creep rate was assumed to be 5%, 10%, 15%, 20% and 25% of the minimum creep rate and at these percentages the end of primary creep strain and time were determined. Figure 4.32(a) gives an illustration of the creep strain rate plotted as function of time and a threshold line indicating the average steady state creep rate at $\pm 10\%$ of the minimum creep rate. Using these determined values of the end of primary creep strains and times as transition points between primary and secondary creep regimes, predicted creep strain vs time curves were constructed. The determined RCC-MR model coefficients given Table 4.2) were used in constructing the predicted creep deformation curves. The RCC-MR predicted creep curves were compared to the experimentally measured ones. The residuals of the fitted data were computed by calculating the sum of squared differences (SSD) between the experimental and predicted data for the creep strain curves at any given stress. To compute the total residuals, all the SSD for each curve were then summed up in accordance to the percent average of the minimum creep rate used to compute the end primary creep strain and time such as 5%, 10%, 15%, 20% and 25%. The total residuals were then plotted as a function of percent average steady-state creep rate to assess the best fit. Figure 4.32(b) shows a plot of the total residuals as a function of percent average steady-state creep rate. The values of the total residuals plotted in Figure 4.32(b) are normalised by dividing by 25 which is the maximum percent average steady-state creep rate used. The best fitted data would give a lowest value of residues and from Figure 4.32(b) the lowest value of residues is obtained when the average steady-state creep rate is 15% of the minimum creep rate. Therefore, all the end of primary creep strains and times were determined by taking the coordinates of a point at which the threshold line, indicating the average steady-state creep rate at 15% of the minimum creep rate, intercepts the creep strain rate vs time curve.

4.7.2.3 RCC-MR Model fitting using the nominal stress

In this Section, the RCC-MR primary creep model was fitted to the multiple creep curves plotted as function of time at varying nominal stress levels as described above in section 4.7.2.1. The values of the RCC-MR primary creep model parameters C_1, C_2 and n_1 determined from the least-square curve fitting method described above are given in Table 4.2.

The secondary creep model parameters C and n were obtained by linear regression. Figure 4.33(a) shows a plot of the minimum creep rate as a function of nominal stress. From Figure 4.33(a), the minimum creep rates data cannot be fitted to a single straight line. The points from 284.5MPa up to 316.5 can be easily fitted to a single straight line and beyond 316.5MPa the minimum creep rates increase sharply. The reason for this change in minimum creep rate could be that the initial higher plastic deformation induced at the centre of the specimen has significantly changed the stress applied during the creep deformation tests especially in the regions near the centre of the specimen. For this reason, to determine the RCC-MR secondary creep model coefficients, a power law was fitted to the minimum creep rates plotted as a function of nominal stress ranging from 284.5 to 316.5MPa, Figure 4.33(b). The values of C and n obtained are given in Table 4.2.

The experimentally determined creep deformation curves at various nominal stress levels are compared to the ones predicted using the determined RCC-MR model fitted parameters in Figure 4.34. There is a relatively good agreement between the RCC-MR predicted creep curves and the experimental data at low and intermediate stresses. But at stress levels beyond 300MPa the difference between the predicted and the experimentally determined creep curves increases. All the fitted parameters are within the range of the model coefficients given in the conventional RCC-MR code (see Table 4.1). The major difference is in the value of C_2 for the primary creep regime which is slightly higher than in RCC-MR code.

The poor correlation, especially at higher stresses, maybe associated with the fact that the material has undergone substantial plastic deformation during specimen initial loading which has significantly changed the stress applied during the creep deformation test. This hypothesis is examined in the following Section.

4.7.2.4 RCC-MR Model fitting using the true stress at initial specimen loading

The minimum creep rates of the multiple creep deformation curves extracted from a single specimen at varying true stress at initial loading were determined by fitting a fifth order polynomial to the data and taking the second derivative as described in section 4.7.2.1. Using this method, the minimum creep rates were determined from creep curves with the true stress ranging from 290MPa up to 338MPa. For the creep curve extracted from true stresses below 290MPa, it was found that the curves in this true stress range did not reach secondary creep regime as the minimum creep strain rates could not be determined. The creep curves with true stresses of 290MPa and below were used for determining the RCC-MR primary creep model parameters as described in section 4.7.2.2. The values of the RCC-MR primary creep model

parameters C_1, C_2 and n_1 determined from the least-square curve fitting method as described above are given in Table 4.3.

The end of primary creep strains was determined using the method described in section 4.7.2.3 and similarly analysis of the residuals between the experimental and predicted creep strain showed that the best fit was obtained when the average steady-state creep rate was $\pm$15% of the minimum creep rate. The determined minimum creep rates were plotted as a function of the true stress on initial loading as shown in Figure 4.35(a). Like the data in Figure 4.33, there is a sharp increase in the minimum creep rates at higher stresses in the region near the centre of the specimen. In section 4.7.2.3, this increase in the minimum creep rates was associated with substantial initial plastic deformation which may have slightly changed the stress applied during the creep deformation test. If this hypothesis is correct, then extracting multiple creep deformation curves at varying true stress at initial loading should not reflect an increase in minimum creep rates in the regions near the centre of the specimen when plotted as a function true stress at initial loading. The fact that the results in Figure 4.35(a) do not fit to a single straight line require further investigation in order to explain the cause of this increase and this is discussed later.

In Figure 4.35(b), the power law is fitted to the minimum creep rate plotted as a function of true stress ranging from 290MPa up to 333.5MPa. The RCC-MR model coefficients determined are given in Table 4.3. Figure 4.36(a) shows the comparison between the experimental data and the predicted creep deformation curves using the RCC-MR fitted model parameters given in Table 4.3 for three true stress levels. From Figure 4.36(a), it can be seen that there is a relatively better agreement between the RCC-MR model predicted creep curves and the experimental data over the entire stress range in which the power law is fitted (see Figure 4.35(b)) compared to the results shown in Figure 4.34. It is worth noting that at higher stress levels such as 330MPa, the predicted creep curves are slightly lower than the experimental data however the discrepancy between the two data sets are better than the ones obtained at higher nominal stresses in Figure 4.34. It can also be noted that in the low stress region, there is a very good correlation between the experimental and the predicted data sets compared to the results in Figure 4.34. The RCC-MR model parameters determined in Table 4.3 compares well with the conventional RCC-MR model parameters (in Table 4.1) for both the primary and secondary creep regimes.

Figure 4.36(b) includes the comparison between the experimental data from the hour-glass specimen and the predicted creep deformation curve based on RCC-MR fitted model parameters at 338MPa applied stress. At 338MPa, the RCC-MR fitted model parameters predicted strains that are far lower compared to the experimental data at this stress level. It should be noted that 338MPa is beyond the stress range through which the power law was fitted, Figure 4.35(b), therefore it is expected that the fitting would be poor in this region.

4.7.5 RCC-MR model fitting to 3D data

Multiple creep deformation curves extracted from the hour-glass specimen were plotted as function of time and stress in a three-dimensional surface plot as shown in Figure 4.21. The RCC-MR primary creep model can be fitted to this surface to extract the model parameters characterising the creep behaviour of the material. The advantage of using a surface fit to the data is that the entire creep strain data extracted from the hour-glass specimen can be used to characterise the creep behaviour of the material. Also, for surface fitting, the strain data is not separated into primary and secondary creep but rather it is fitted as a single surface assuming that the primary and secondary creep is defined by the RCC-MR primary creep model expressed as a logarithmic function,

$$\log \varepsilon = \log C_1 + C_2 \log t + n_1 \log \sigma \qquad (4.4)$$

where ε is strain data and includes both primary and secondary creep strain.

Therefore, for surface fitting there is no need to define the time and strain at the end of primary creep regime. The RCC-MR creep model defined by Equation 4.4 was fitted to the surface plot in Figure 4.21 using Matlab to determine the model coefficients C_1, C_2 and n_1 [16]. To implement this, the strain (ε), time (t) and the stress (σ) matrices were converted into logarithmic matrices and used as input variables. From Figures 4.17 and 4.21, it can be seen that the multiple-stress creep curves extracted at the centre of the specimen and the surrounding regions, exhibit not only primary and secondary creep but tertiary creep to some extent. Therefore, for 3D model fitting, the data was only fitted up to 1200 hours to ensure that all the creep curves are in either primary or primary and secondary creep regime. In Figure 4.37, the fitted data are compared to the experimental data, and from this Figure, it can be seen that there is a good correlation between the fitted surface and the experimental data at higher creep strains as the experimental data points (black dots) lies in the same plane as the fitted surface whereas at lower creep strains (close to the start of the test), there is a

considerable scatter in the experimental data (experimental data points are below the fitted surface plane indicating poor correlation). Much of the scatter is between the time zero (beginning of the creep test) up to about 100 hours. Beyond 100 hours, the fitted data compares very well to the experimental data.

The extracted RCC-MR model coefficients are shown in Table 4.4. The surface fitting was also carried out on 3D creep data plotted as a function of time and true stress at the beginning of the test. The results from these 3D surface fitting is also shown in Table 4.4. From Table 4.4, the RCC-MR model coefficients obtained when the creep data is plotted as a function of time and true stress at the beginning of the creep test are closer to the conventional RCC-MR model coefficients than the ones obtained from 3D fit based on nominal stress. From this, it can be concluded that analysis of multiple creep deformation curves as a function of the true stress at the beginning of the creep test yields better model fit results for material undergoing substantial plastic deformation at initial loading than analysis of creep deformation data based on nominal stress.

4.7.6 Garofalo model fitting

From Equations 4.9 and 2.14, both the Garofalo model and the modified Theta model have a similar formulation for the primary creep regime. The Garofalo model was chosen as an example for this type of formulation and model fitting was carried out using the true stress at the beginning of the test. The end of primary creep was defined as described in section 4.7.2.3. The fitting of the Garofalo primary creep model was carried out by using MATLAB curve fitting toolbox. For steady-state creep regime, the stress dependence of the Garofalo secondary creep model is the same as Norton's law (power law creep model) at low stress, therefore the secondary creep model parameters obtained in section 4.7.4 were used.

Figure 4.38 shows the comparison between the primary creep model prediction and experimental data. The predicted creep deformation curves correlated with the data well at intermediate times but deviate at the beginning and towards the end of the creep test. Similar results were obtained when the modified Garofalo primary creep model was used. From these results it was concluded that the Garofalo creep model and similarly the Theta model, were not ideal for modelling the creep deformation behaviour using the creep data extracted from a single hour-glass specimen.

4.7.7 Graham and Walles model fitting

The Graham and Walles creep model is similar to the Norton-Bailey and the RCC-MR creep model for both the primary and secondary creep regime. The only difference is in the formulation of the time exponent for the primary creep regime which is given as $^1/_3$ in the Graham and Walles model, Equation 4.15. As previously described (section 4.6.1 and 4.7.2.2), the true stress at the beginning of the test and the definitions of the end of primary creep were adopted. Primary creep model fitting was carried using the least squares nonlinear model fitting method described in section 4.7.2.2. Initial values were obtained by fitting individual creep curves at varying true stress levels with the Graham and Walles primary creep model and averaging the values of the model coefficient C_1 and the stress exponent α_1, the initial values used were,

$$[1.5188 \times 10^{-8} \quad 2.6178] \quad (4.5)$$

Figure 4.39 shows a comparison between the model prediction and experimental data. From Figure 4.39, the model fit is poor. Therefore, it can be concluded that although the Graham and Walles model is similar to both the Norton-Bailey and RCC-MR model, it is not suitable for modelling the creep behaviour of the hour-glass specimen.

4.8 DISCUSSIONS

4.8.1 Multiple creep deformation curves from a single hour-glass specimen

Multiple creep deformation curves at varying stress levels can be extracted from a single specimen by using DIC and an hour-glass design of gauge length at any given temperature. This wealth of information can be used to characterise the creep deformation behaviour of the material. The advantage of using DIC is that both the longitudinal and transverse creep strain can be measured during the creep test, Figure 4.17 – 4.19. With DIC, the entire gauge section of the specimen is used for creep strain measurements and thereby providing creep deformation data in three-dimensions (space, stress and time), Figure 4.21.

Since the creep strain along the gauge length is measured in both the longitudinal and transverse direction, the DIC data are invaluable when the applied load during specimen initial loading is higher than the yield stress of the material, which was the case in the current study. The transverse loading strain was used to compute the true stress at the beginning of the creep test and to monitor the change in true stress during the entire creep test. Figure

4.23(a) shows that the true stress at the beginning of the creep test is higher than the nominal stress and the major difference between the two stress types is at the centre of the specimen gauge length where the true stress is about 20MPa higher than the nominal stress. Away from the specimen gauge centre, the difference between the true stress and nominal stress reduces with increase in distance from the gauge centre. It is worth noting that due to high applied initial load, the entire specimen gauge length extended by approximately 3 mm. This explains why the creep strain curves in Figure 4.19 and the true stress curves in Figure 4.23 plotted as a function of gauge length extends beyond 25mm. Another advantage of DIC measurements is that the true stress distribution can be approximated with a relatively high degree of accuracy. However, the effects of any initial plastic deformation and hence the complication in determining the true stress distribution can be avoided by using applied stresses that are lower than the material's yield strength at the test temperature.

The measured longitudinal and transverse creep strains have also been used to assess the evolution of Poisson's ratio during the creep test (see Figures 4.27 and 4.28). The measured value of Poisson's ratio during creep was close to the theoretical value of 0.5 for isotropic materials undergoing plastic deformation. A higher degree of scatter in Poisson's ratio was found at low strains (due to low signal to noise ratio), such that the expected transition from elastic behaviour (0.3) to plastic behaviour (0.5) could not be observed [29, 30].

4.8.2 Validation Test at 320MPa initial loading stress

Both the extensometer and DIC measured creep strains from the validation test correlated very well with the DIC creep strains extracted from a hour-glass specimen at the same stress level as the validation test up to 1100 hours, Figure 4.29(a). This correlation signifies the validity of extracting multiple creep curves from a single specimen. Beyond 1100 hours, the creep strain curve from the hour-glass specimen curved upwards as it goes into tertiary creep whereas the creep strains from a conventional specimen (validation test) continued in secondary creep regime. The difference in the trajectories of the creep curves beyond 1100 hours is expected since the DIC creep strains from an hour-glass specimen were extracted at the centre of the specimen which inevitably underwent significant localised damage compared to a conventional specimen. It is known that initial induced damage during specimen loading, plays a significant role in the subsequent creep deformation of the specimen and thus affects the time to initiation of tertiary creep [31].

4.8.3 Creep modelling

To characterise the creep behaviour of the material, creep models widely used in modelling austenitic stainless steels were fitted to the multiple creep deformation curves extracted from the hour-glass specimen. The models used in this study include the RCC-MR, the Garofalo and the Graham-Walles models.

For the RCC-MR creep model, two different model fitting techniques were used. To obtain the primary creep model parameters, the RCC-MR primary creep model was fitted using a least squares optimisation technique implemented in MATLAB to creep curves with nominal stresses of 280MPa and below or true stress of 290MPa and below. Whereas, using the end of primary creep strains obtained in Section 4.7.2.3, the secondary creep model parameters of the RCC-MR were obtained using a linear regression method. The RCC-MR model was fitted to the multiple creep deformation curves plotted as a function of time at varying nominal stress and varying true stress at the beginning of the creep test. The values of calculated RCC-MR model parameters are given in Tables 4.2 and 4.3. The comparison between the RCC-MR model predicted creep deformation and the experimental data given in Figures 4.34 and 4.36 shows that a better fit is obtained when the multiple creep deformation curves are plotted as a function of time at varying true stress at the beginning of the test.

Although best fit between the predicted and the experimental data were obtained when multiple creep deformation curves were plotted as a function of true stress at the beginning of the test, this did not eliminate the curvature in the power law fit to the log of the minimum creep rate plotted as a function of the log true stress at the beginning of the creep test, Figure 4.35. To improve the fit in the secondary creep regime, it has been suggested that if the power law does not fit all the data points on the plot of the log of the minimum creep rate as a function of the log of true stress, an exponential function can be used in correlating the minimum creep rate to the stress [38]. The exponential function is expressed as,

$$\dot{\varepsilon}_{min} = Be^{m\sigma} \qquad (4.6)$$

where $\dot{\varepsilon}_{min}$ is the minimum creep rate, σ is the true stress at the beginning of the test, B and m are material costants and are obtained by linear fitting of the plot of the log of minimum creep strain rate as a function of stress. Equation 4.6 has been ideally applied in the analyses of the creep deformation of Type 316 stainless steel, P91 and the welds of Esshete 1250 steel [39, 40]. Figure 4.40(a) shows a plot of the log minimum creep rate as a function of true

stress at the beginning of the test. Comparing Figure 4.40(a) to Figure 4.35(a), there is no difference in the two plots, showing that the exponential function given by Equation 4.6 does not improve the data fit in the regions with higher applied true stress.

Further, to deal with the non-linearity of the plot of minimum creep rate as a function of stress, a hyperbolic function (Equation 2.10) suggested by Garofalo has been found ideal for presenting the minimum creep rate as a function of stress for all the stress range, in a situation where both the power law and the exponential model does not ideally fit the data [23, 38]. Figure 4.40(b) shows a plot of the log of minimum creep rate as a function of log of $\sinh \alpha\sigma$. Comparing Figure 4.40(b) to Figure 4.35(a), there is no improvement as the data did not fit to a single straight line.

Considering that none of the methods (the power law, the exponential model and the hyperbolic function) used could ideally fit all the data to a single straight line, this shows that there are errors in the true stresses obtained at the centre of the gauge length and the surrounding region since the data from this region does not correlate with any of the models used. It is possible that the true stresses at initial loading at the centre of the gauge length and the surrounding regions are slightly higher than the values obtained. This can be explained by the fact that the initial high loading strains in the hour-glass specimen are accompanied by high and concentrated damage at the centre and in the regions surrounding the centre of the hour-glass specimen. The true stress at initial loading is calculated based on the assumption that the measured transverse strain on the surface of the specimen is equal to the strain in the thickness direction ($\varepsilon_{xx} = \varepsilon_{zz}$). Considering that DIC only measures surface strains, the induced initial damage may be higher across the centre and the surrounding region, making the actual true stress to be slightly higher than the calculated value based on the measured transverse strain. This explains why the three proven models (the power law, exponential model and the hyperbolic function) could not fit all the data points.

Due to initial damage, subsequent creep deformation is accompanied by the creep damage process hence the creep deformation curve extracted from the hour-glass specimen at 320MPa initial applied nominal stress exhibited earlier signs of tertiary creep deformation compared to the creep deformation curves extracted from the conventional specimen (validation test) at the same stress level, Figure 4.29(a).

The Garofalo creep model was also fitted to the multiple creep deformation curves extracted from the hour-glass specimen at varying stresses. As shown in section 4.7.6, the primary

model parameters were fitted using the curve fitting tool in MATLAB and the values of the end of primary creep obtained in section 4.7.2.3 were used. Relatively good fit between the model predicted and experimental data were obtained in the intermediate parts of the creep curves with poor correlations at the beginning and towards the end of the creep test duration.

The fitted Graham-Walles creep model did not give good correlation between the predicted and experimental data. The reason for poor correlation could be in the formulation of the Graham-Walles model as the time function in the primary part of the model is raised to the power 1/3. This factor works well when the creep data is extracted from creep tests with an initial applied stress inducing elastic deformation, resulting in a more pronounced primary creep compared to tests were the initial applied stress induces plastic deformation, which is the case in the current study.

The three models used in this study were compared to establish which model best predicts the multiple creep deformation curves extracted from the hour-glass specimen. The comparison was carried out by computing the sum of the squared differences between the predicted and experimental data at selected stress levels of 290MPa and 250MPa. Table 4.5 shows the sum of the squared differences obtained from the three models. From Table 4.5, the RCC-MR model gives the smallest value of the sum of the squared differences implying that it gives better fit compared to the other two models used. It should be mentioned that although only three creep models were used in this study, the modelling of multiple creep deformation curves extracted from a single specimen at varying stress is not only limited to these models, other models can also be used.

Another advantage of using the technique developed in this study is that the obtained data can be modelled by fitting a surface to the data. The procedure for fitting a surface to the creep data is straight forward and does not require definition of the end of primary creep strain and time. The advantage of surface fitting is that the entire creep deformation data is used to characterise the creep behaviour of the material. As shown in Section 4.7.5, the RCC-MR primary model was used for surface fitting the creep data. The results obtained from the surface fitted data where similar to the ones given by the conventional RCC-MR model parameters. It is worth noting that surface fitting was only applied to the creep data up to 1200 hours because as stated earlier, the creep curves extracted at 320MPa applied nominal stress and the surrounding regions exhibit tertiary creep as the curves bend upwards at about 1100 hours.

4.8.4 Significance of this Experimental Technique

Application of DIC to extract multiple creep curves at varying stress levels from a single specimen yields a vast amount of data that can be used in characterising the creep behaviour of the material. The data can be used to assess the change in Poisson's ratio and evolution of the true stress during the creep test. Moreover, the information can be used in modelling the creep behaviour of the material.

The fact that multiple creep deformation curves can be extracted from a single specimen at varying stress levels, this implies that the number of creep tests and the time required for characterisation of the creep behaviour of any given material can be reduced several folds thus making the process economical. The design criteria for high temperature materials guarantees that neither excessive creep distortion nor creep rupture of a component applied at high temperature under stress would not occur within the planned service life of the component [41, 42]. For this reason, extensive creep strength and rupture data are required for high temperature materials, for instance the ASME design code requires test durations of more than 30,000 hours for a material with design life of 100,000 hours at 50^{o}C intervals within the operating temperature [41]. The entire creep tests programme would include at least 3 casts with a minimum of 2 tests for a given temperature and at least 4 different stress levels at any given temperature. Similarly, the European code of practice for creep strength and rupture assessment requires test durations of up to about one third of the planned life of 250,000 hours from at least 3 casts, at temperature intervals of 25^{o}C and 50^{o}C higher than the application temperature [42]. For any given temperature a minimum of 5 tests at different stress levels are required. The creep testing programmes required by design codes entails the high cost of developing new high temperature materials such that the 'development cycle' for new high performance power plant steels is currently over 10 years [43]. To reduce the astronomical cost of acquiring material data for new high temperature steels, the current focus is on development of creep data extrapolation techniques [44-46]. The ultimate go is to use creep data acquired from short term tests and extrapolate it to forecast the long-term behaviour of the material thus cutting down the cost of data acquisition. However, extrapolation of creep data from short term tests is hampered by the fact that the mechanisms controlling creep and creep fracture evolves as the test conditions changes and during long term creep tests the pre-service microstructure varies with time, a characteristic not exhibited in short term tests.

In relation to reduction of the costs of acquisition of creep data, the use DIC to extract multiple creep deformation curves from a single specimen at varying stress levels would reduce the number of creep tests required thus reducing the cost of data acquisition. For instance, as stated above, a minimum of 4 tests are required at any given temperature at varying stresses according to the European code of practice for creep strength and rupture assessment, however using the technique developed in this study, only one test would be required at any given temperature and the data acquired from a single test would cover a wide range of stress levels. Therefore, the technique developed in this study, does not only reduce the cost of data acquisition but also provides a wealth of information that can be used in modelling the creep behaviour of the materials at any given temperature.

The technique developed in this study would also be useful in acquisition of creep strength data for component life assessment, especially in cases where the design life of the component is based on a limiting strain allowable for a planned life of the component. This technique is not only applicable to steel or metallic materials; it can be applied for characterisation of the creep behaviour of a wide range of materials including cross-welds and in various testing atmosphere.

The technique can also be used to study the effects of elastic and plastic loading on the creep behaviour of high temperature materials (especially newly developed ones) using a single specimen. In such studies, a single specimen can be loaded in such a way that the middle section of the hour-glass specimen undergoes plastic loading whilst the rest of the gauge length undergo elastic deformation on initial loading. Apart from obtaining spatially resolved multiple creep curves from a single specimen, microstructural study of samples extracted from regions of the specimen gauge length relative to the stress experienced, would reveal the microstructural evolution of the material during creep deformation in relation to the initial applied stress such as elastic or plastic. Similarly, the creep damage of the material can be studied using a single specimen.

Considering the advantages of the technique developed in this study, it can be seen that the technique has the capability of transforming the way creep testing is carried as it is cost saving and it produces a vast amount of data that can used in various ways such as modelling. Further development of this technique would lead to developing capabilities of not only extracting multiple creep curves at varying stress levels but also at varying temperature from a single specimen.

4.8.5 Limitations

The limitations of using a single specimen to characterise the creep behaviour of the material are well outlined by Levy *et al* [4]. The major limitation is that this technique cannot be used for assessing the creep rupture behaviour of the material. Whether a hour-glass or tapered specimen is used, when the material at the region with minimum cross-section experiences tertiary creep, it is likely that high triaxial stresses would develop and these are known to accelerate localised creep failure of the material [47-49]. Therefore, the failure of the material in this region would be governed by triaxial stresses which will influence the creep deformation of adjacent material and limit the validity of spatially resolved data extracted in this region.

The other limitation is the durability of the high temperature refractory paint which is used for applying a speckle pattern on the surface of the specimen. For longer creep testing durations, it is known that the painted speckle pattern can degrade with time. Currently, only relatively short creep tests with creep durations of up to 4000 hours has been carried out, further tests are required to assess the durability of high temperature refractory paint used thus improving the capability of this technique. Alternatively, tests could be carried out under vacuum.

4.9 CONCLUSIONS

i. An hour-glass test specimen was designed to create a gently varying stress magnitude along its gauge length minimising any stress concentrations at the minimum cross-section.

ii. The hour-glass specimen design was tested at 525^{o}C with DIC surface deformation monitoring producing multiple creep deformation curves at nominal stress levels varying from 250MPa to 320MPa.

iii. The RCC-MR, Garofalo and Graham-Walles models have been fitted to the creep deformation data from the hour-glass specimen test. Better correlations were found between the predicted and experimental data using the true stress at the beginning of the test. Comparing the three creep models, best fits were obtained using the RCC-MR model.

iv. A three-dimensional surface fit of the RCC-MR primary creep model to the hour-glass specimen creep data showed a good fit up to 1200 hours based on the true stress at the start of the test.

FIGURES AND TABLES

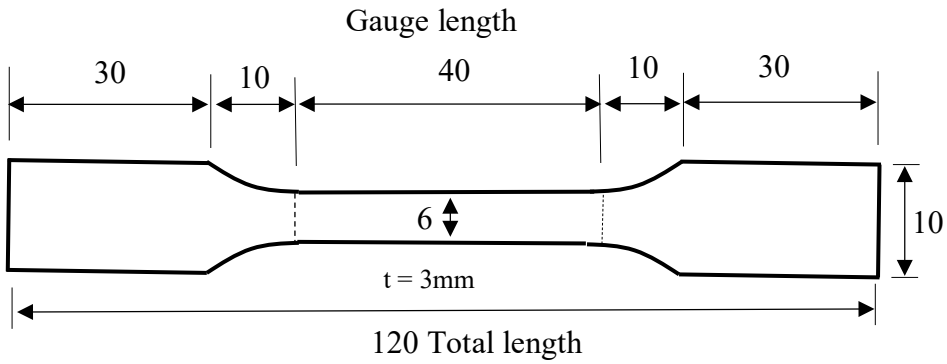

Figure 4.1 Standard tensile test specimen dimensions (all dimensions are mm)

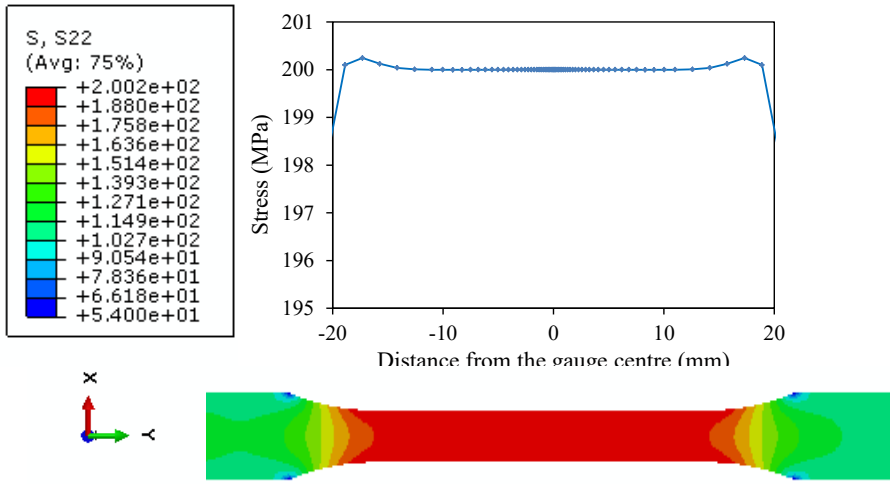

(a)

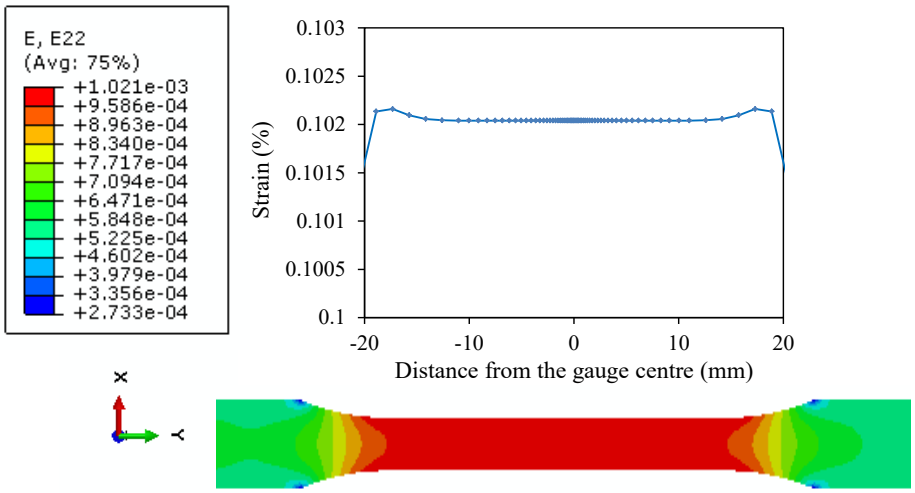

(b)

Figure 4.2 Elastic FE results showing (a) stress and (b) strain distribution extracted from the centre of the parallel section of the standard tensile test specimen model.

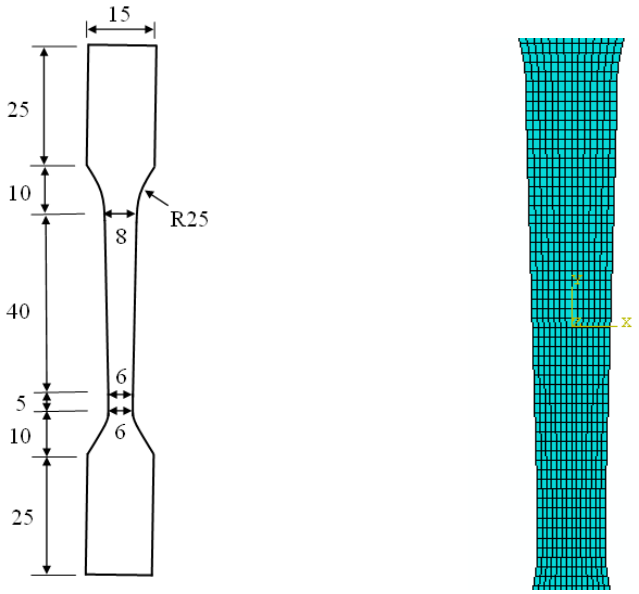

(a) (b)

Fig. 4.3 (a) Schematic drawing of a flat-sided 3mm thick tapered specimen proposed for DIC creep testing, dimensions are in mm (b) Quadrilateral 8-node plane stress elements (CPS8R) used for linear elastic FE analysis.

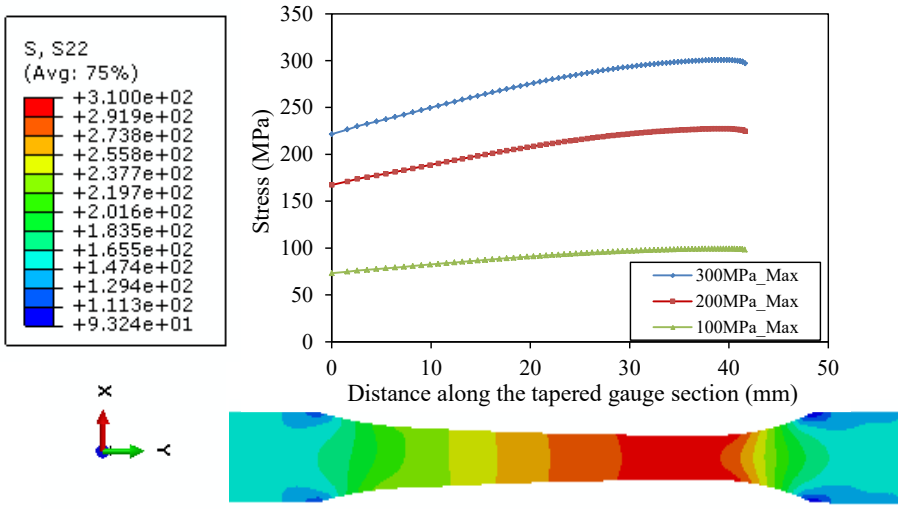

(a)

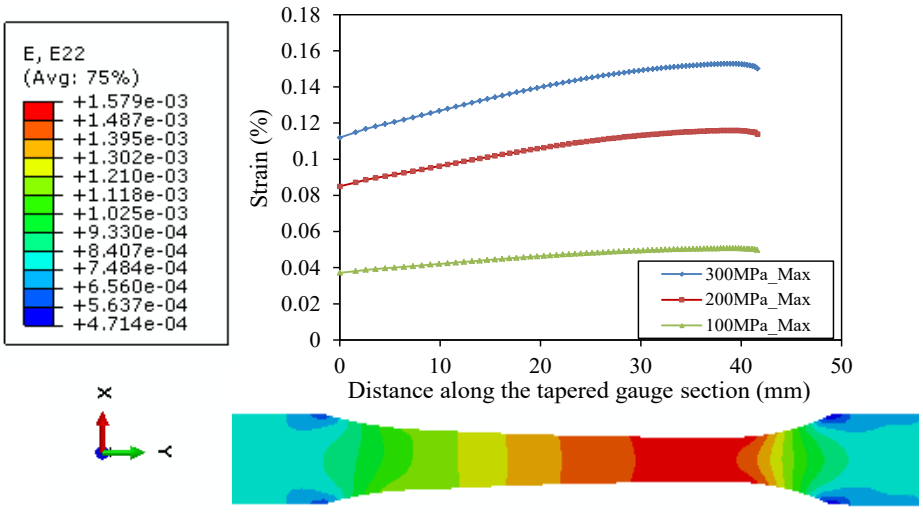

(b)

Figure 4.4 Elastic FE results showing (a) stress and (b) strain distribution along the gauge section of the tapered specimen

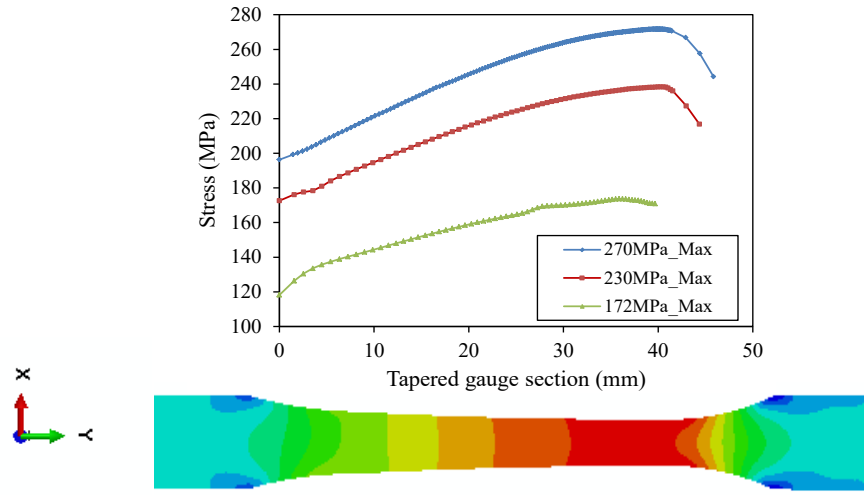

(a)

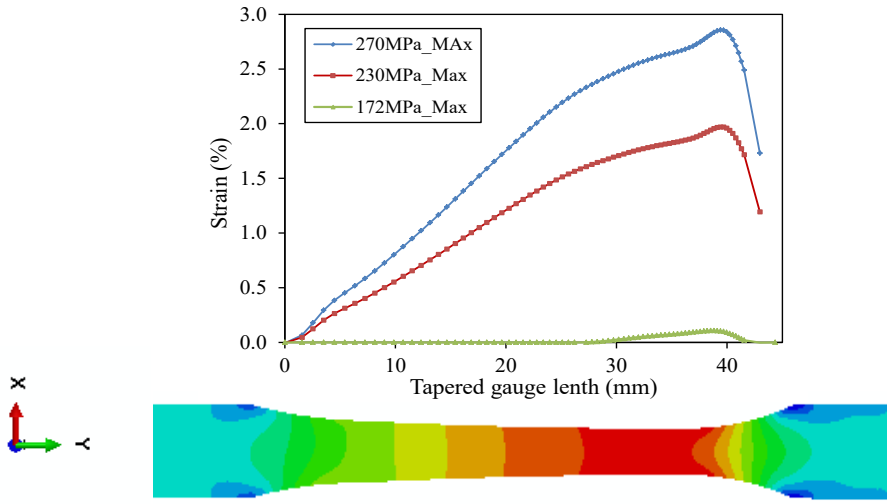

(b)

Fig. 4.5 Elastic-plastic FE results showing (a) the predicted stress distribution along the gauge length in the tapered specimen (b) strain distribution as a funcion of the tapered gauge length.

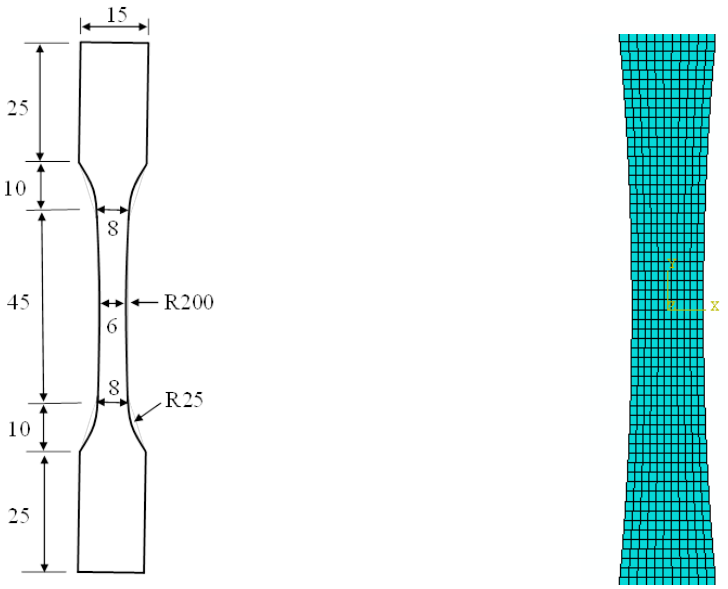

(a) (b)

Fig. 4.6 (a) Schematic drawing of a flat-sided 3mm thick hour-glass specimen proposed for DIC creep testing, dimensions are in mm (b) Quadrilateral 8-node plane stress elements (CPS8R) used for linear elastic FE analysis.

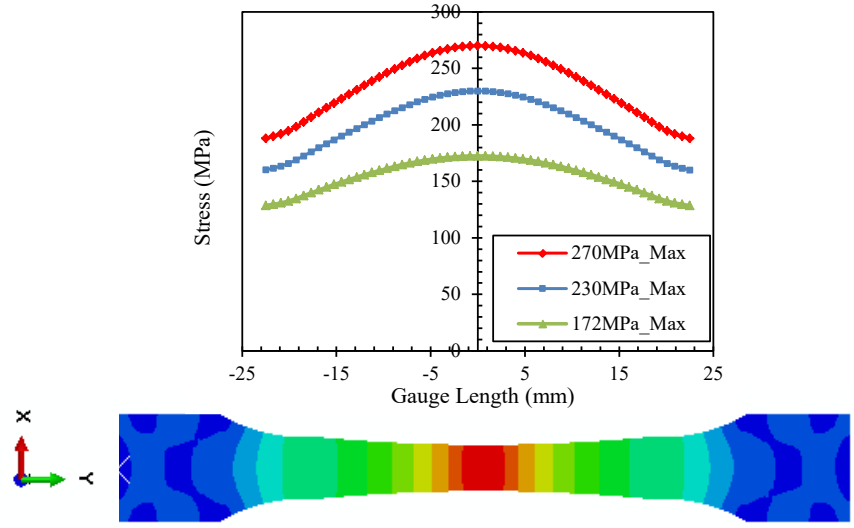

(a)

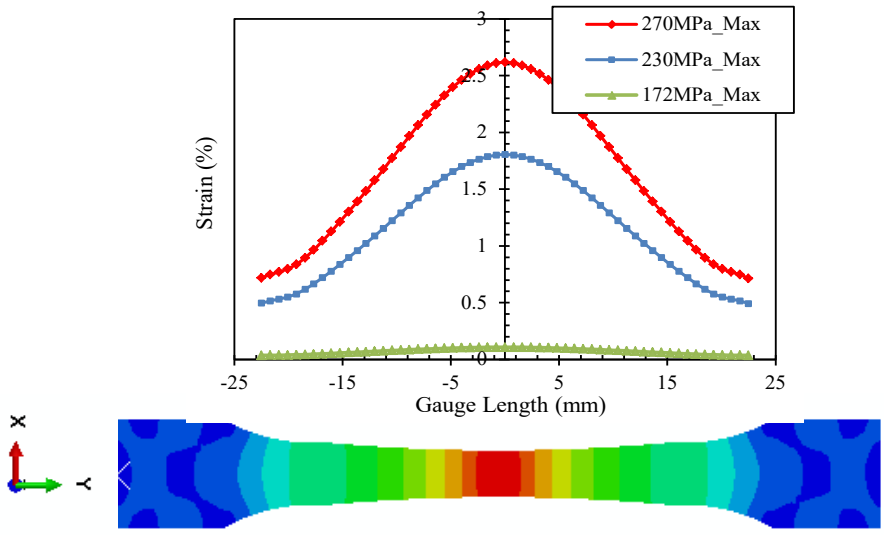

(b)

Fig. 4.7 Elastic-plastic FE results (a) predicted stress distribution along the gauge length of the hour-glass specimen shown in Figure 4.6(a); (b) plot of average strain across the gauge width as a function of gauge length at varying peak (maximum) stress in the region with minimum cross-section.

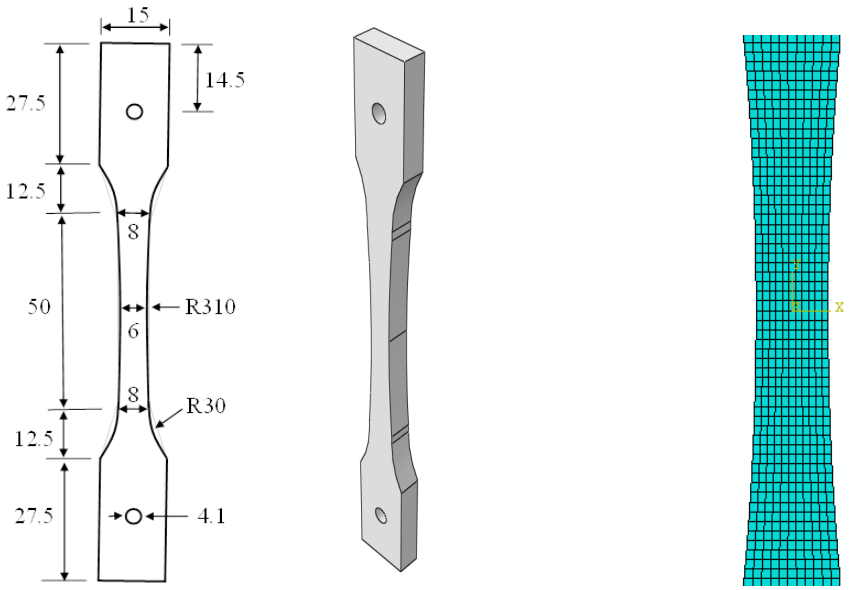

(a) (b)

Fig. 4.8 (a) Schematic drawing of the final design of a flat-sided 3mm thick hour-glass specimen used for measuring creep deformation as a function of stress levels (b) CPE8R plane strain mesh used for FE analysis.

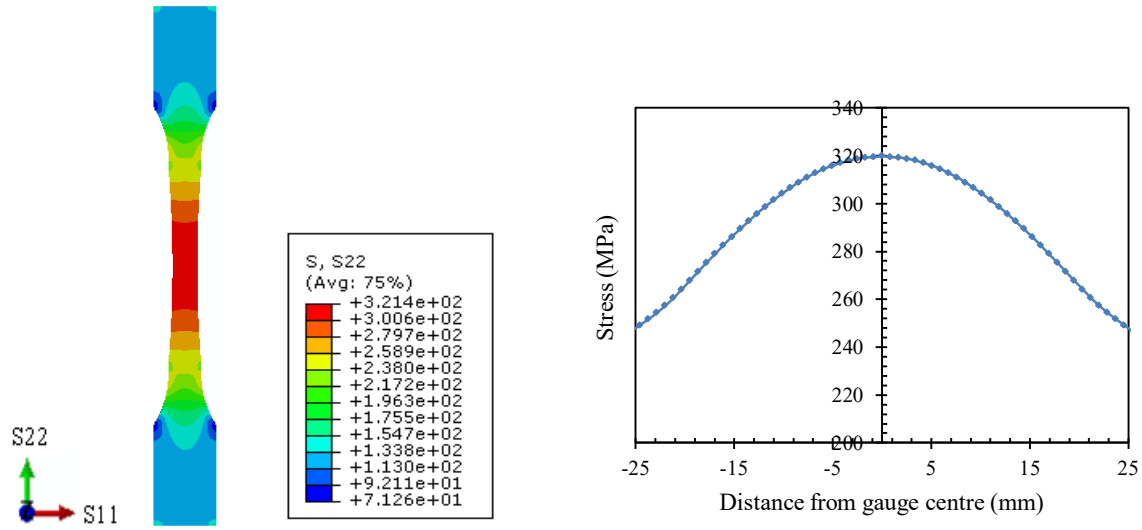

(a) (b)

Fig. 4.9 FE results showing the predicted elastic-plastic stress distribution along the gauge length for the final design of hour-glass specimen (a) FE elastic-plastic stress map at 320MPa maximum stress at the mid-section of the specimen (b) plot of predicted average stress across the width as a function of gauge length of the hour-glass specimen model.

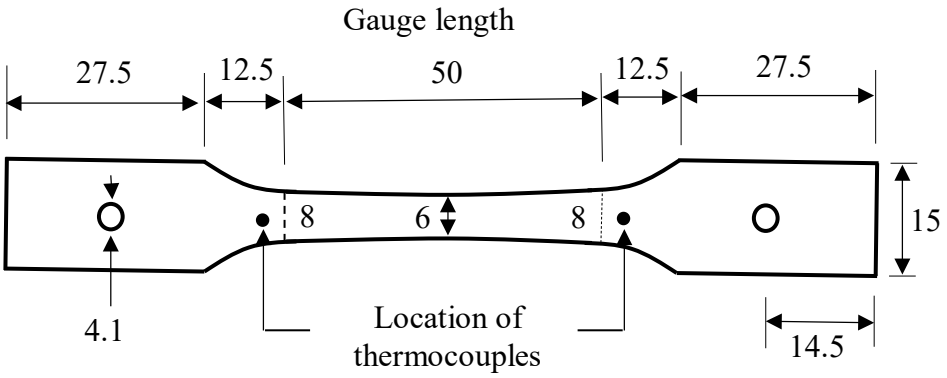

Fig. 4.10 Schematic drawing of the final design of the hour-glass shaped specimen showing positions where thermocouples were attached to the specimen.

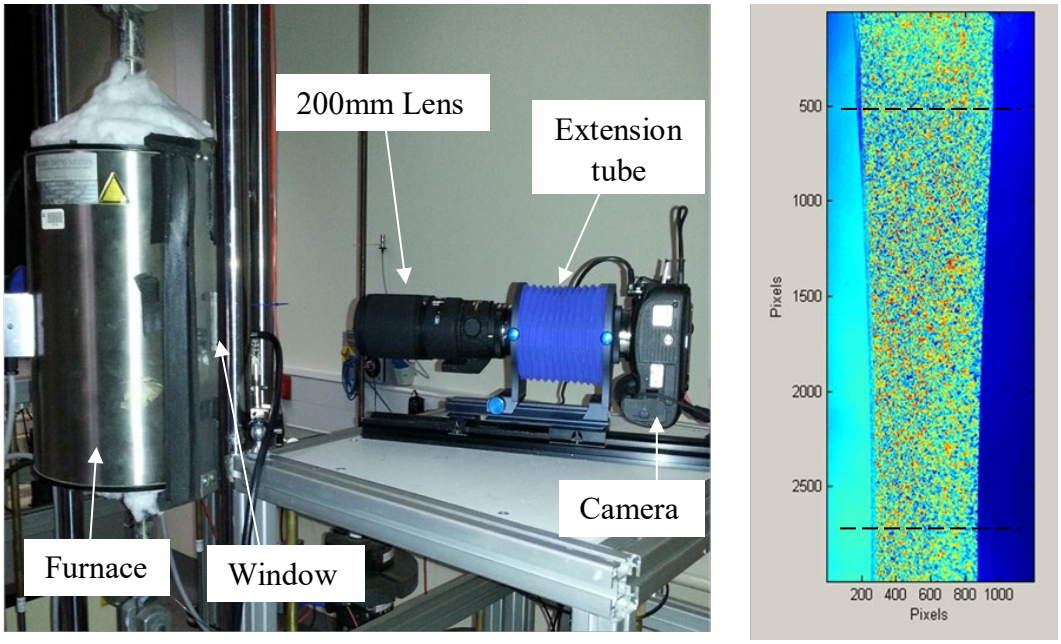

(a) (b)

Fig. 4.11 (a) Experimental set-up for DIC monitored creep test of the hour-glass specimen (b) the specimen as viewed through the furnace window.

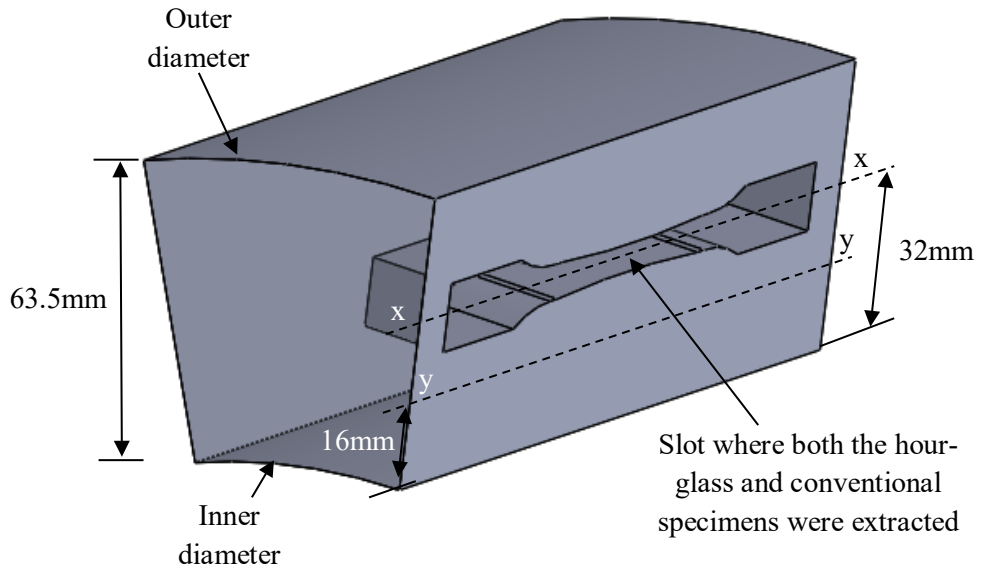

Figure 4.12 3D schematic drawing of ex-service header material (supplied by EDF energy) indicating the slot where both the hour-glass specimen and the conventional validation test1 and test2 specimens were extracted (along line x-x). Validation test3 specimen was extracted in the same orientation as the other specimens with its centre line along line y-y on the diagram.

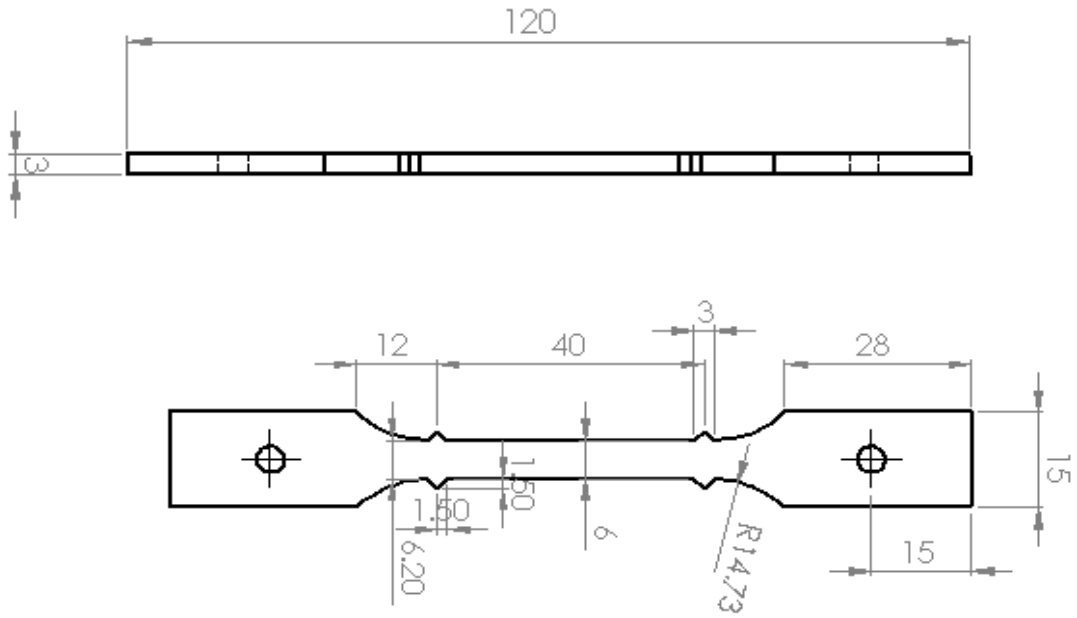

Fig. 4.13 Schematic drawing of the flat-sided creep specimen design used for creep validation tests.

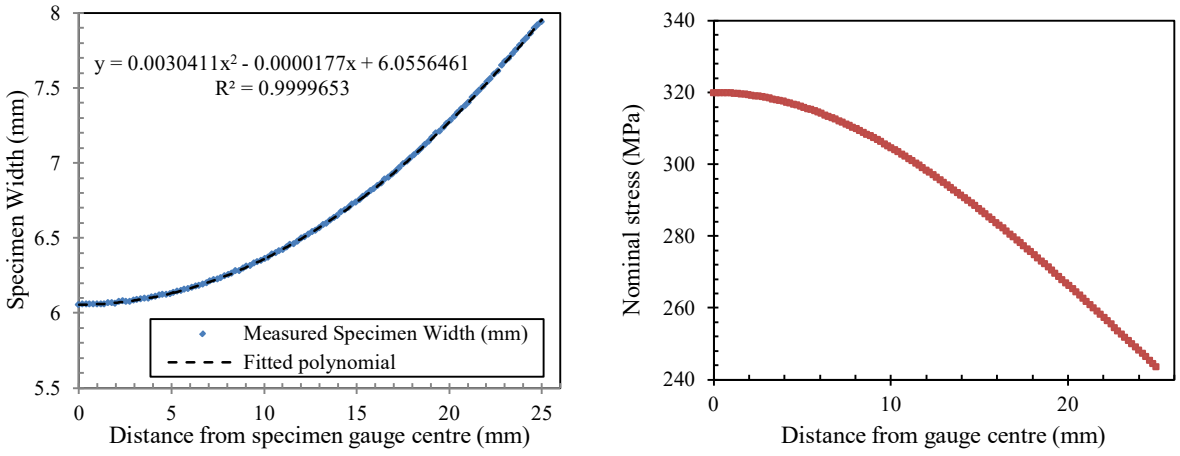

(a) (b)

Fig. 4.14 Measured variation in width along the gauge length of the hour-glass test specimen and fitted polynomial (b) nominal stress distribution plotted as function of distance along the gauge length of the hour-glass specimen.

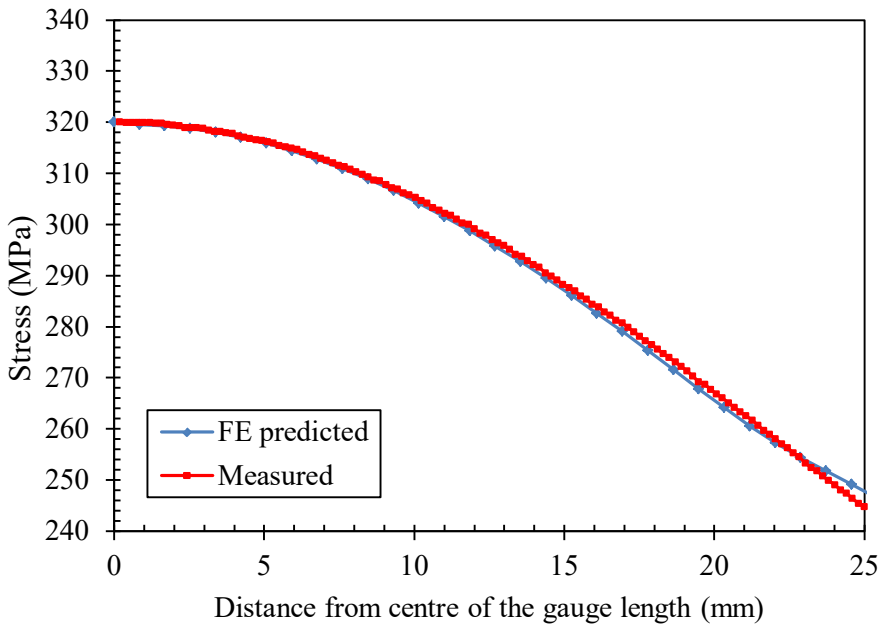

Fig.4.15 Comparison of the distribution of the nominal stress calculated from the measured geometry of the machined hour-glass specimen with FE predicted nominal stress (averaged across width) as a function of the gauge length.

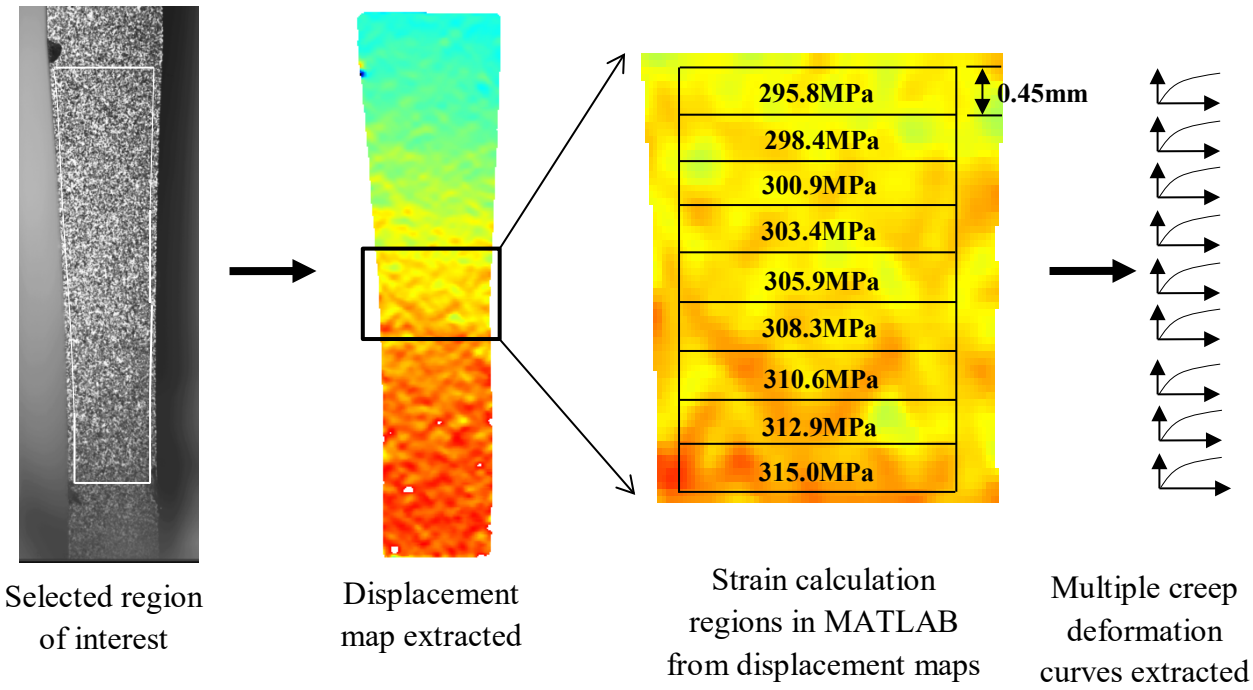

Fig.4.16 Schematic illustration of the DIC data analysis procedure for extracting multiple creep deformation curves at varying stress levels from a single hour-glass specimen.

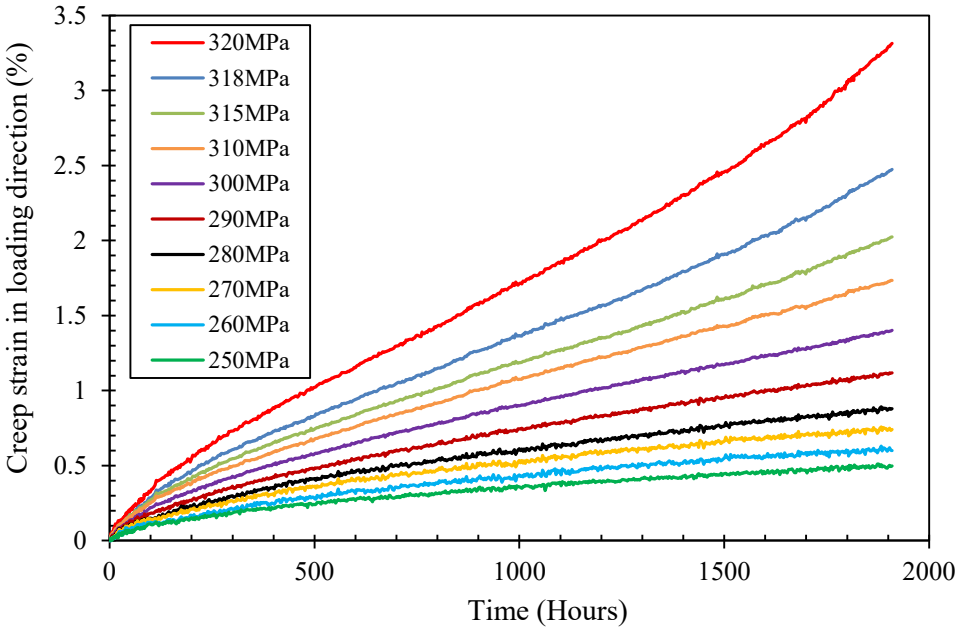

Fig. 4.17 Measured longitudinal creep strain accumulation as a function of time at varying nominal stress at the test temperature of 525°C.

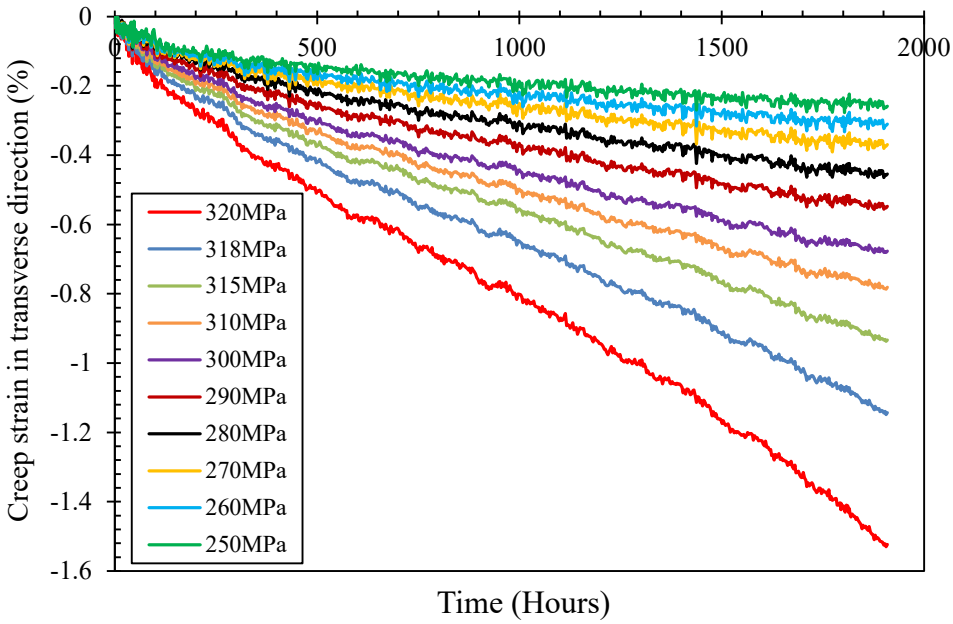

Fig. 4.18 Measured transverse creep strain accumulation as a function of time at varying nominal stress at the test temperature of 525°C.

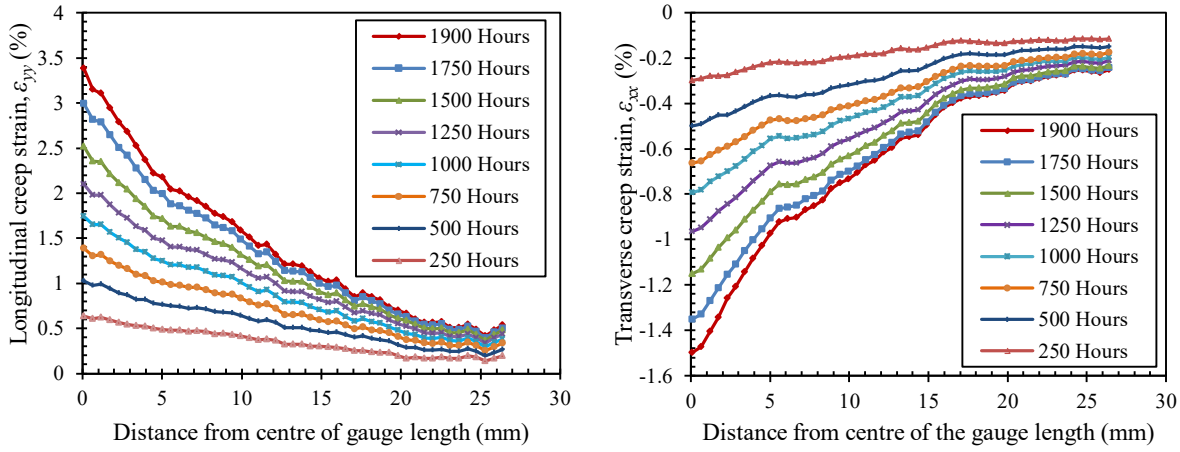

(a) (b)

Fig. 4.19 Evolution of creep strain with time along the specimen gauge length (a) longitudinal creep strain (b) transverse creep strain.

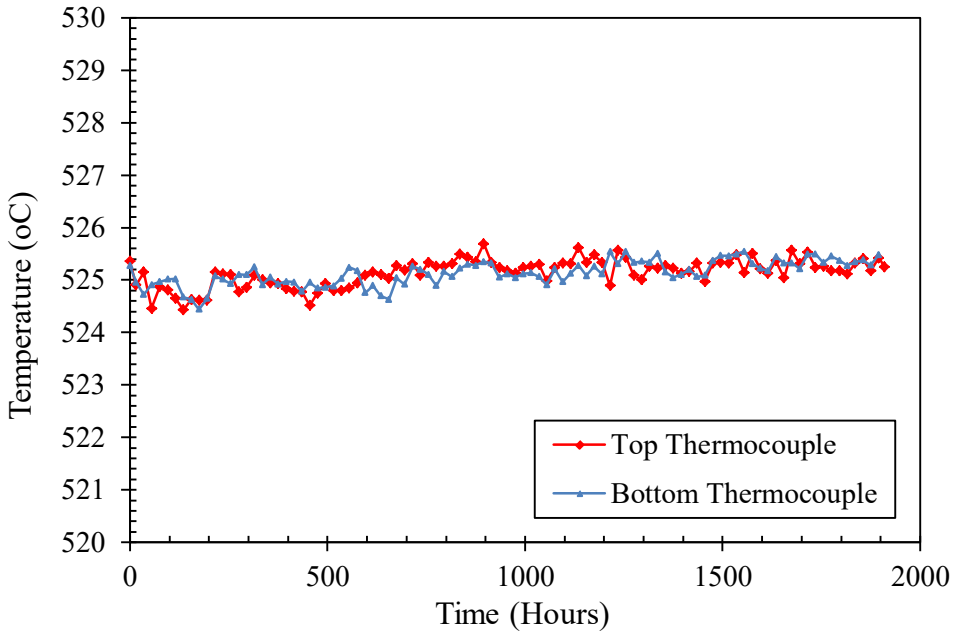

Fig. 4.20 Measured specimen temperature as a function of time during creep testing

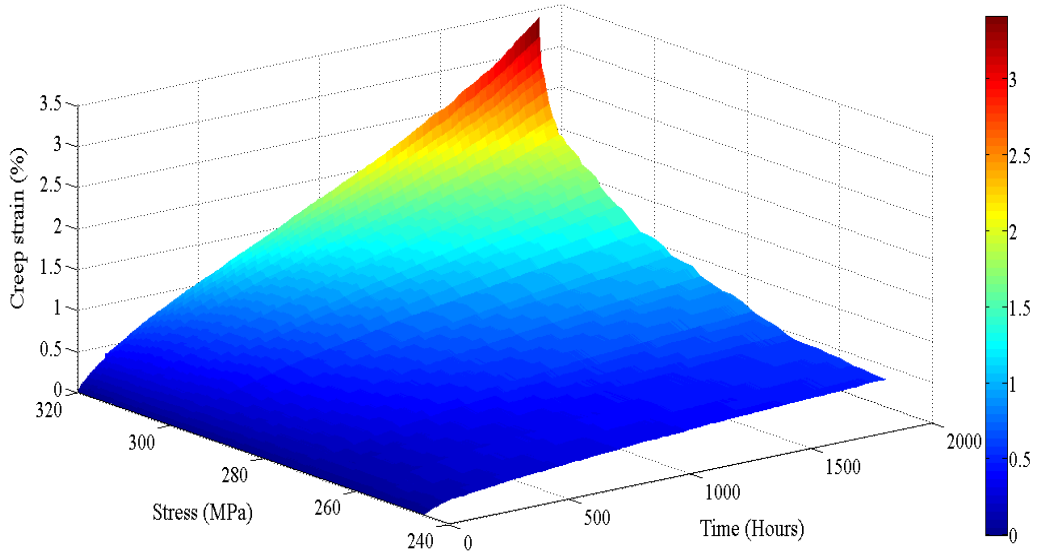

Figure 4.21 Three-dimensional plot of measured creep deformation surface as a function of time and nominal stress

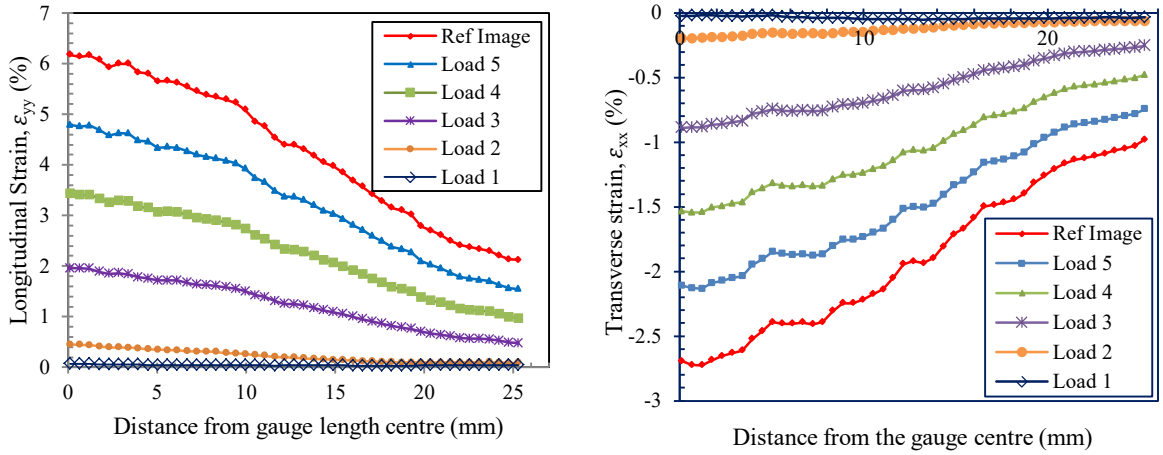

(a) (b)

Figure 4.22 Evolution of inelastic strain during specimen initial 6 increments of loading (a) loading direction (b) transverse direction. The Ref Image represents the final initial loading state from which subsequent creep strains is measured.

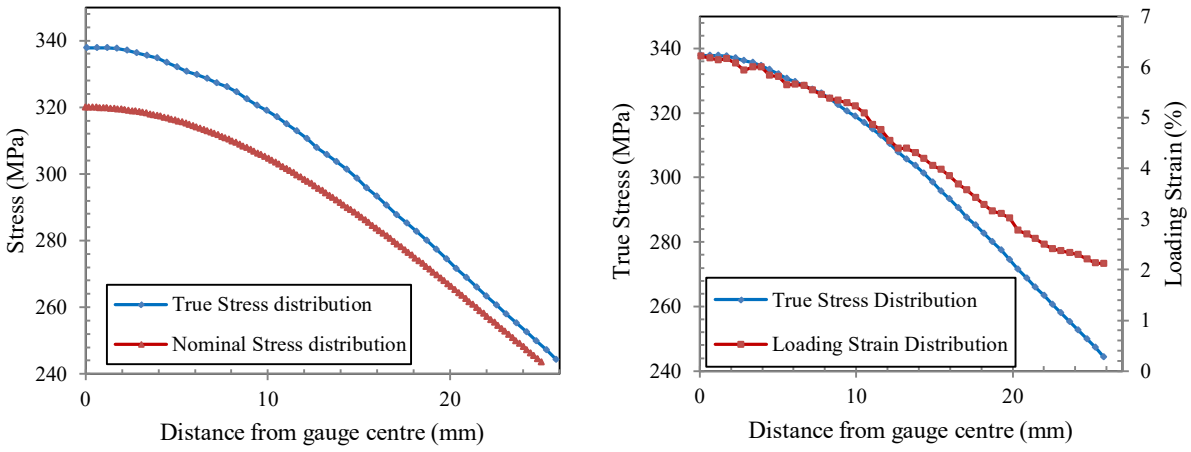

(a) (b)

Figure 4.23 (a) Distribution of the true stress at the beginning of the test compared to the nominal stress (b) true stress distribution compared to the strain (ε_{yy}) accumulated during specimen initial loading.

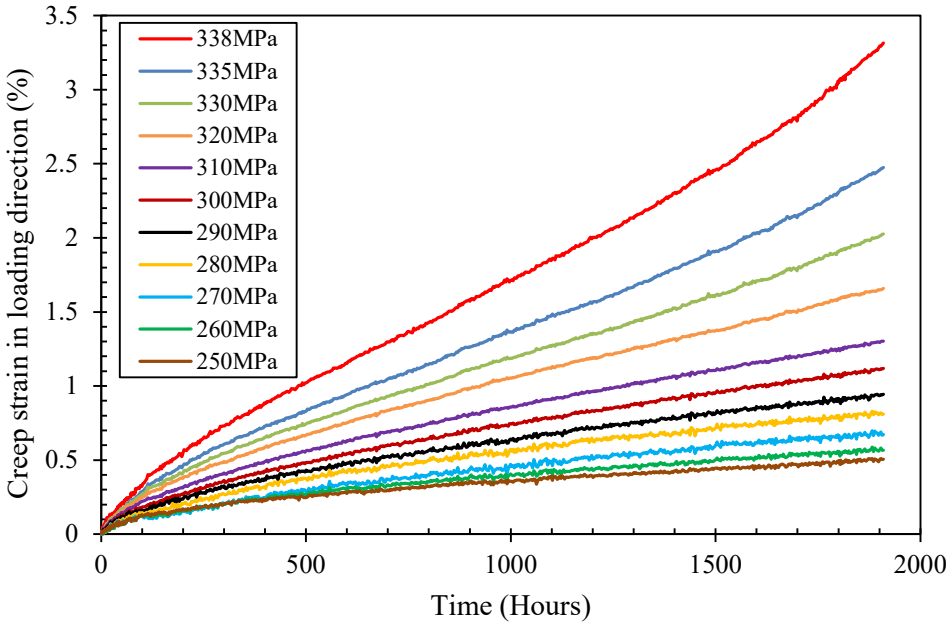

Fig. 4.24 Measured longitudinal creep strain as a function of time and true stress at the beginning of the test at the test temperature of 525°C.

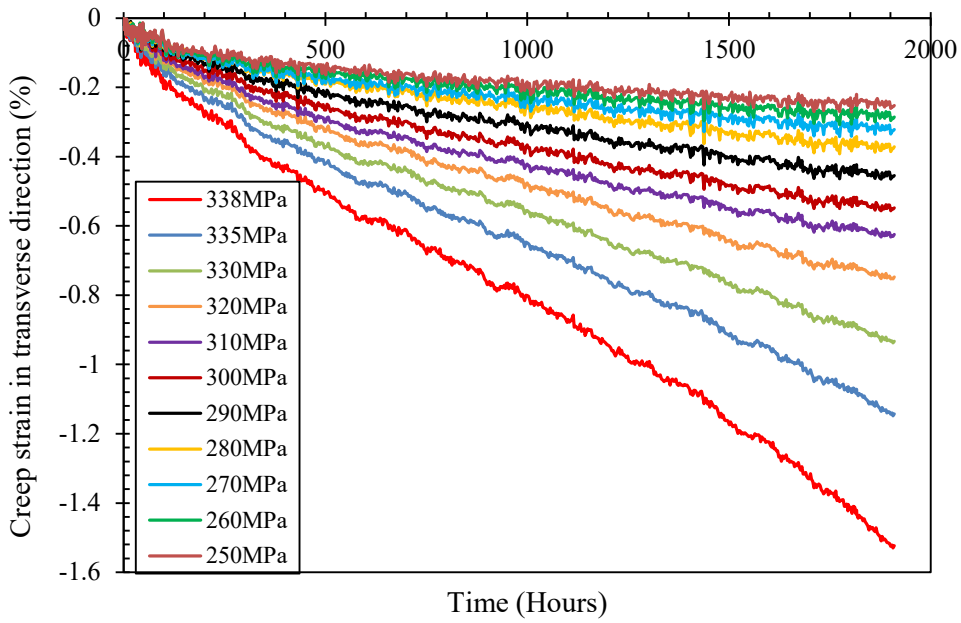

Fig. 4.25 Measured transverse creep strain as a function of time and true stress at the beginning of the test at the test temperature of 525°C.

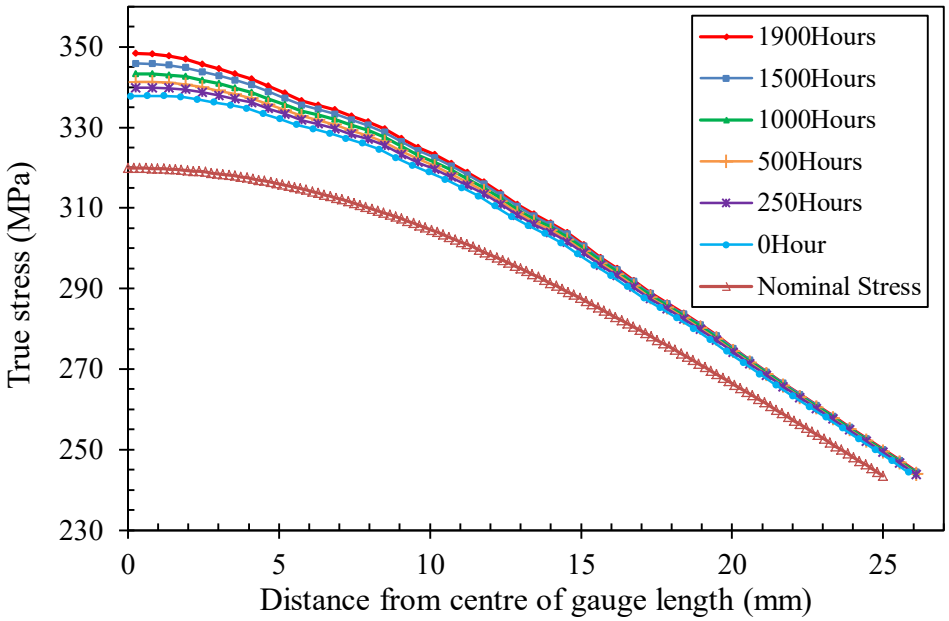

Fig. 4.26 Distribution of true stress along the specimen gauge length as a function of time

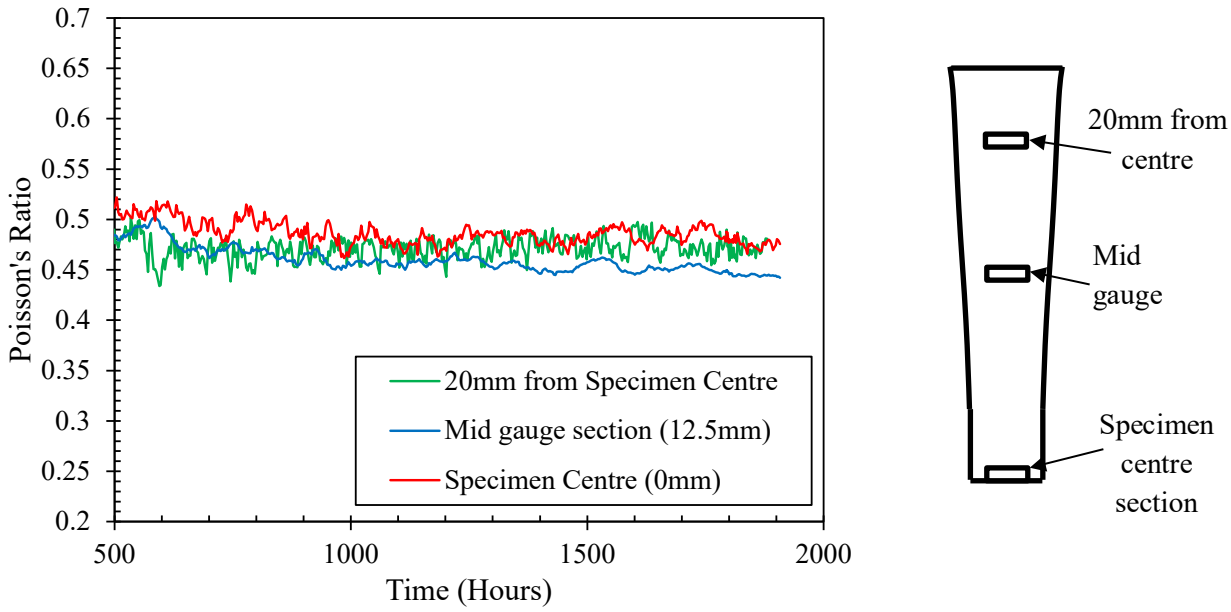

(a) (b)

Figure 4.27 (a) Change of Poisson's ratio as a function of time extracted from the specimen centre (0mm), the mid gauge section (12.5mm) and 20mm from the specimen centre. (b) Illustrates the locations along the specimen gauge section from which the Poisson's ratios where extracted.

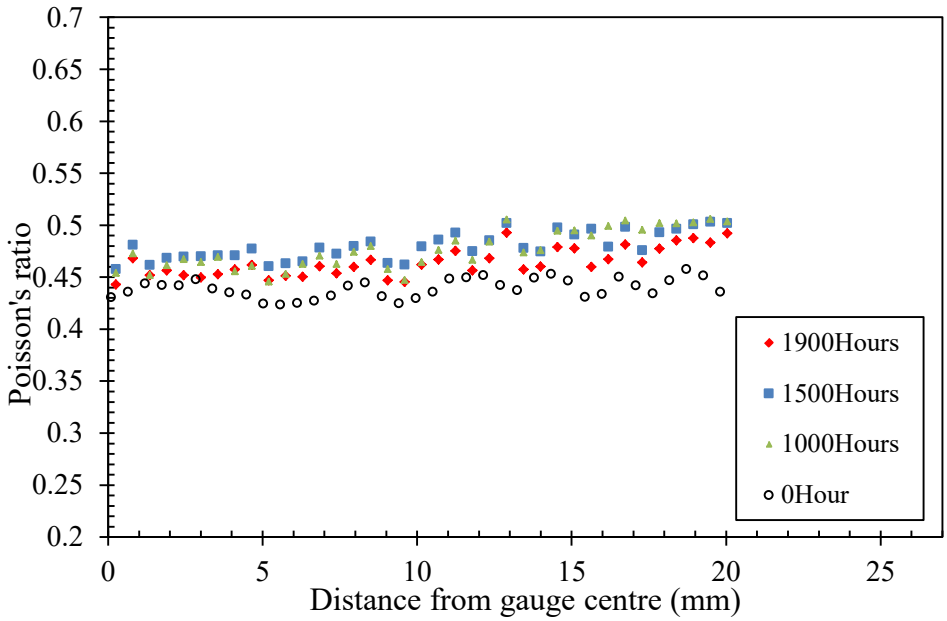

Fig. 4.28 Distribution of Poisson's ratio along the specimen gauge length as a function of time. The Poisson's ratios along the gauge section were extracted from the specimen centre up to 20mm away from the centre, beyond 20mm the signal to ratio was very low resulting in high variability in the calculated Poisson's ratios.

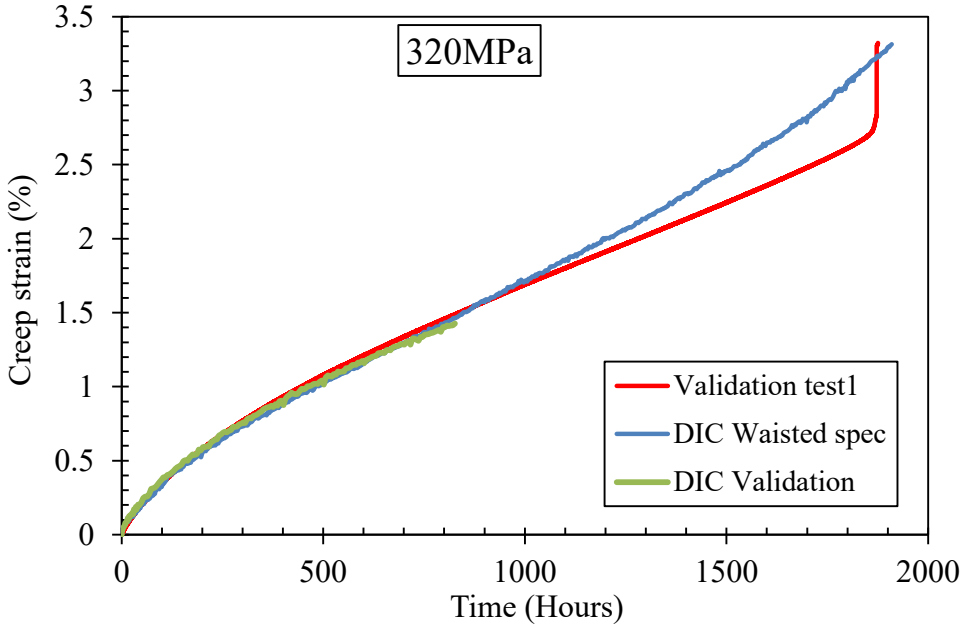

Fig. 4.29 Comparison of creep strain measured from a hour-glass specimen and the ones measured from conventional specimens using extensometers at 320MPa initial nominal stress.

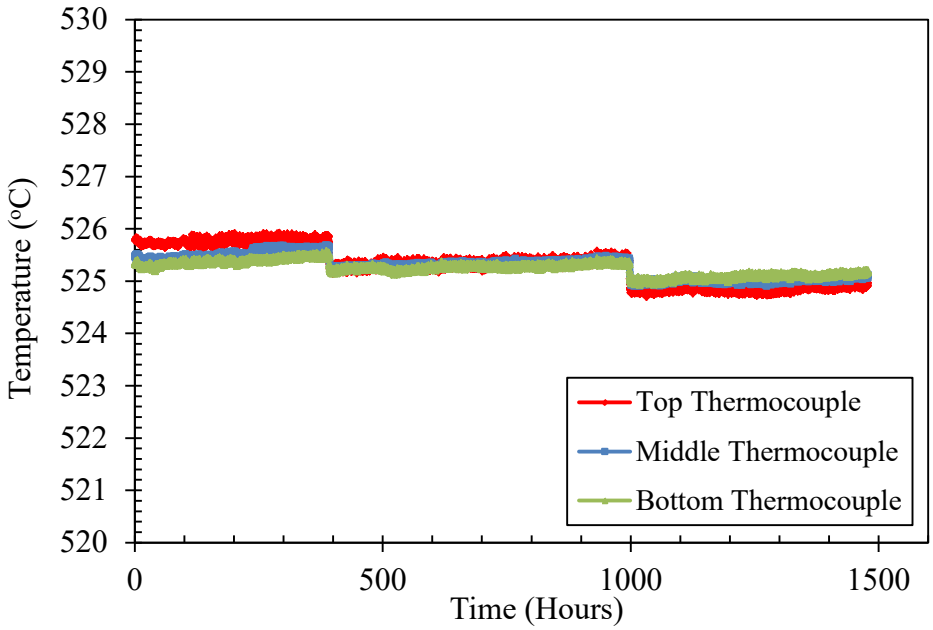

Figure 4.30 Measured specimen temperature plotted as a function of time during creep testing of conventional specimens at 525°C and an applied initial nominal stress of 320MPa

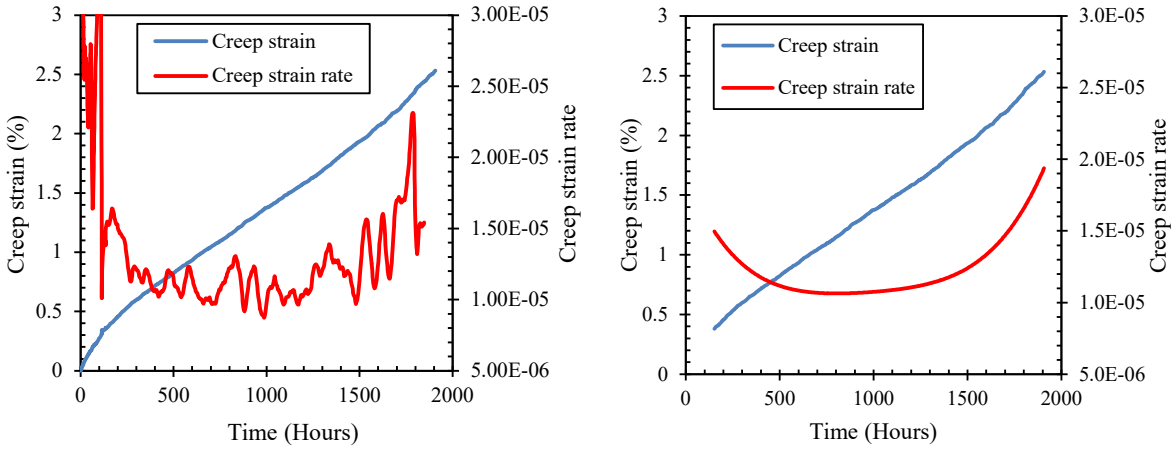

(a) (b)

Figure 4.31 Plot of creep strain and creep strain rate as function of time at 335MPa applied true stress. Creep strain rate calculated by using (a) least squares method (b) differentiation of a fitted fifth order polynomial starting from 150 hours to the end of the creep test.

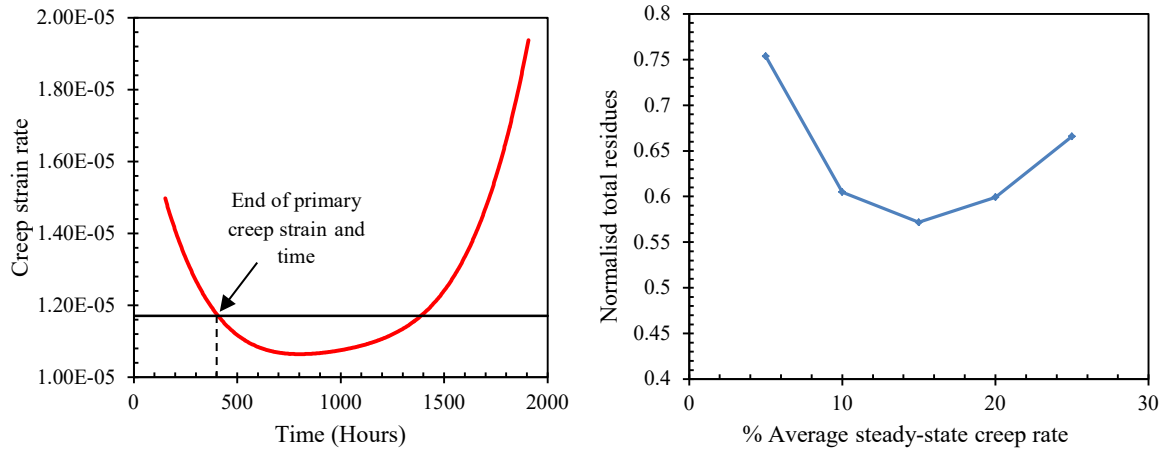

(a) (b)

Fig. 4.32(a) Threshold line indicating the average steady-state creep rate at ±10% of the minimum creep rate, the end of primary creep strain and time were determined from the coordinates of the interception point. (b) A plot of the total residuals as a function of percent average steady-state creep rate.

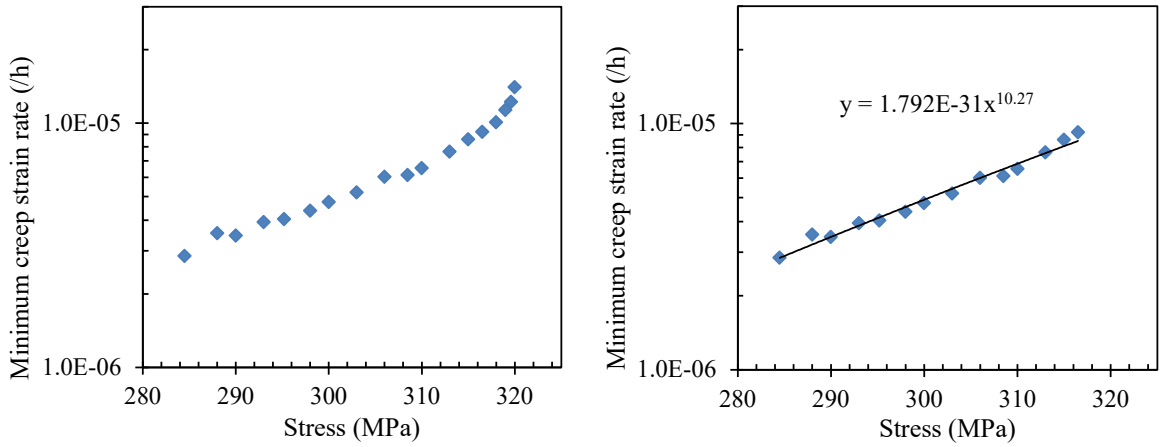

Fig. 4.33 (a) Minimum creep rate plotted as a function of nominal stress (b) Determination of the stress coefficient and the stress exponent by fitting a power law to the minimum creep rate as a function of nominal stress in the stress range 284.5MPa to 316.5MPa.

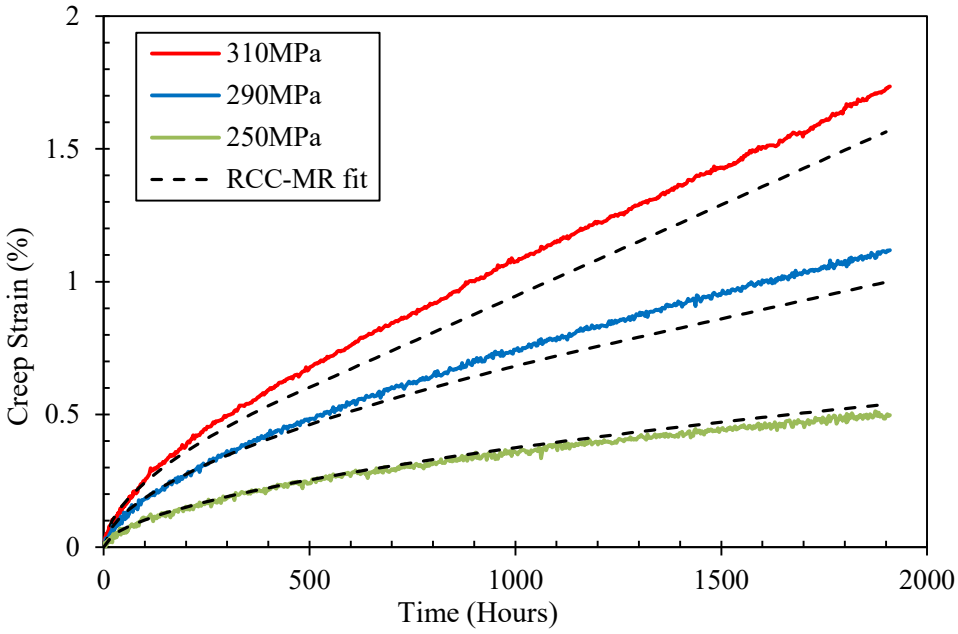

Fig. 4.34 Comparison between hour-glass specimen experimental data and the predicted deformation curves based on RCC-MR fitted model parameters for three nominal stresses.

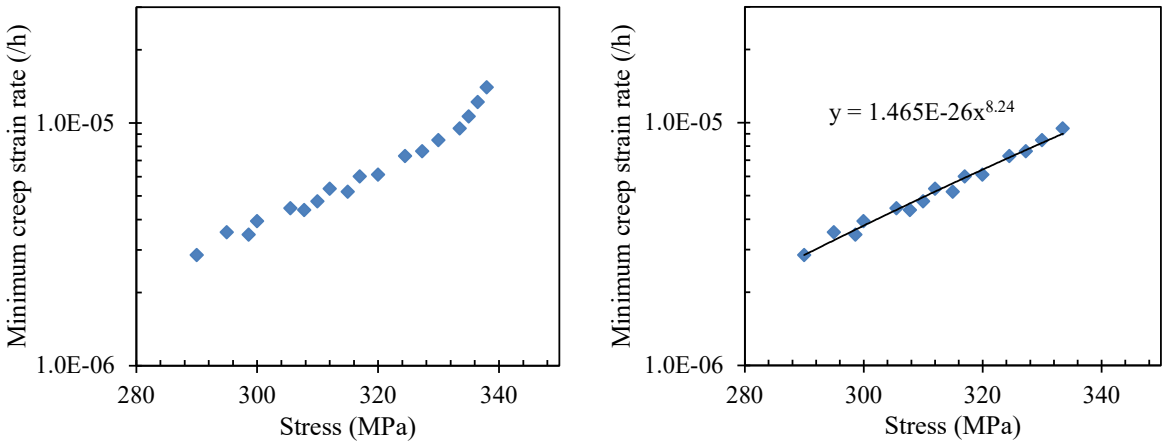

Fig. 4.35 (a) Minimum creep rate plotted as a function true stress at initial loading (b) Determination of the stress coefficient and the stress exponent by fitting a power law to the minimum creep rate plotted as a function of true stress in the stress range 290MPa to 333.5MPa.

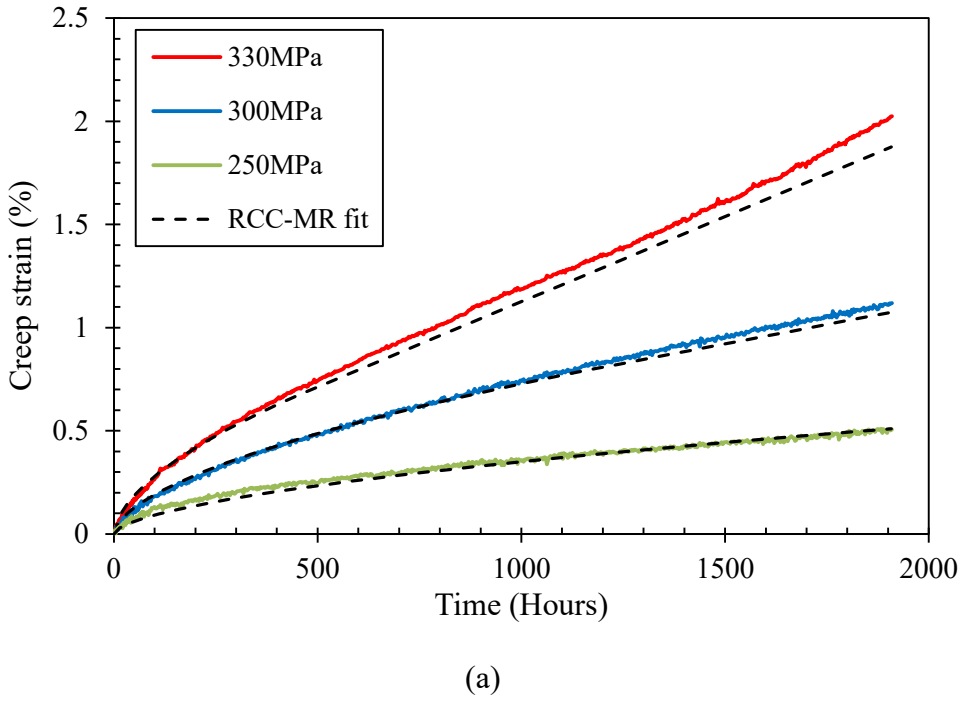

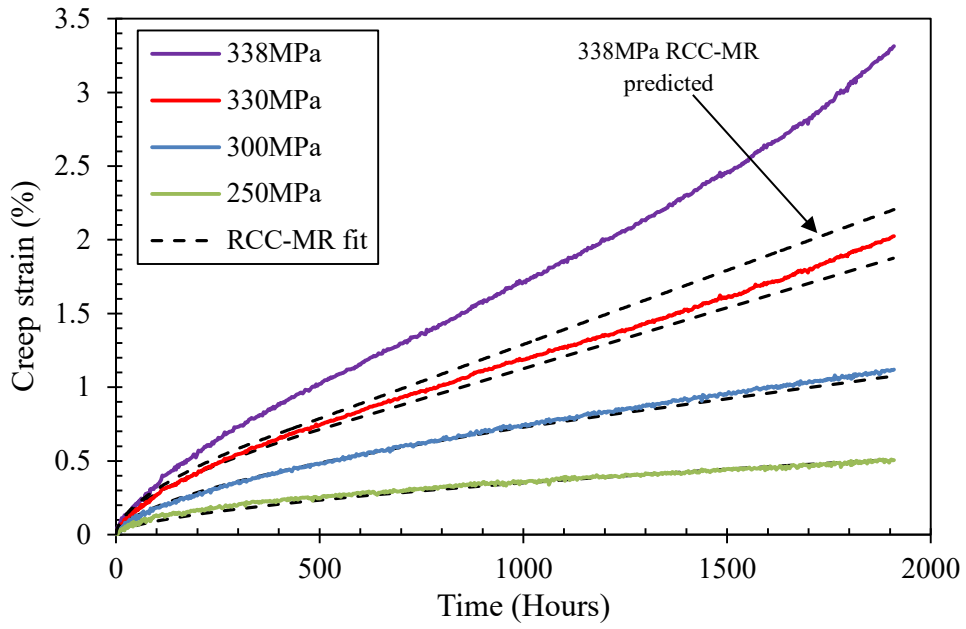

(b)

Fig. 4.36 Comparison between hour-glass specimen experimental data and the predicted deformation curves based on RCC-MR fitted model parameters (a) for three true stress levels within the stress range where the power law was fitted (see Figure 4.35(b)). (b) For four true stress levels including the maximum true stress at the region with minimum gauge section.

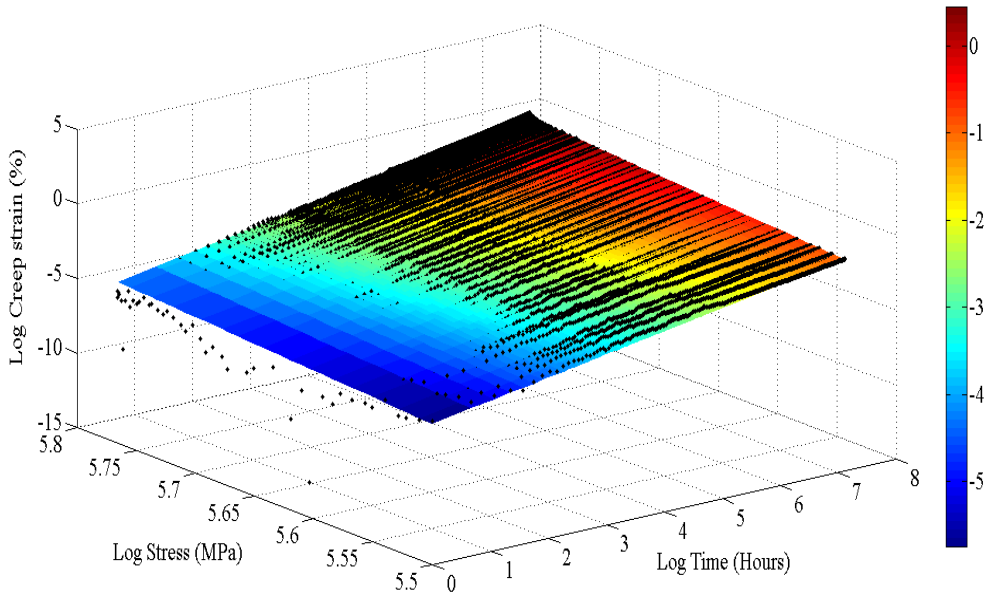

Figure 4.37 Comparison between the surface fit and experimental data (scatter points)

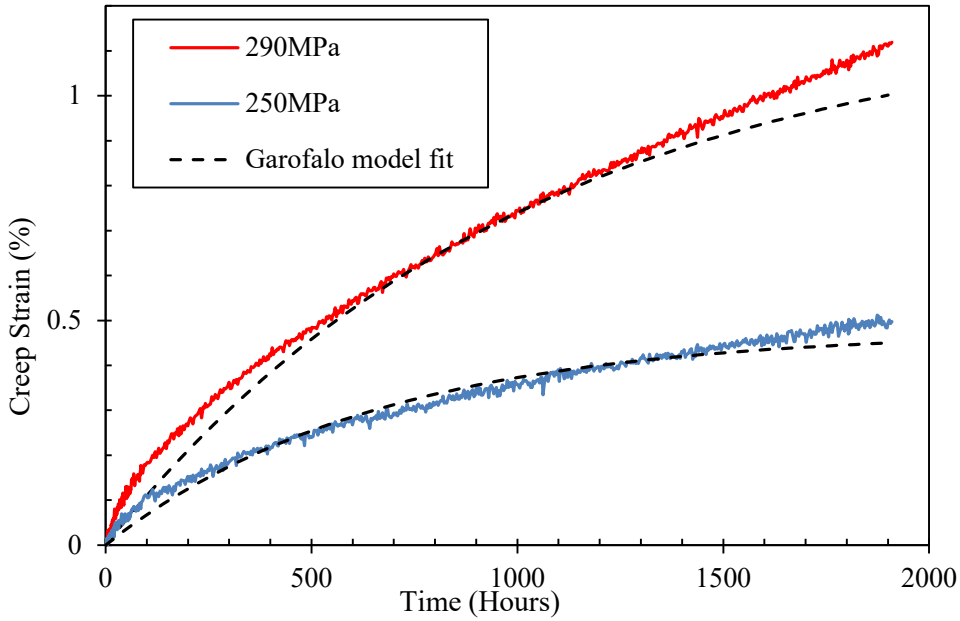

Figure 4.38 shows the comparison between the Garofalo primary creep model prediction and experimental data.

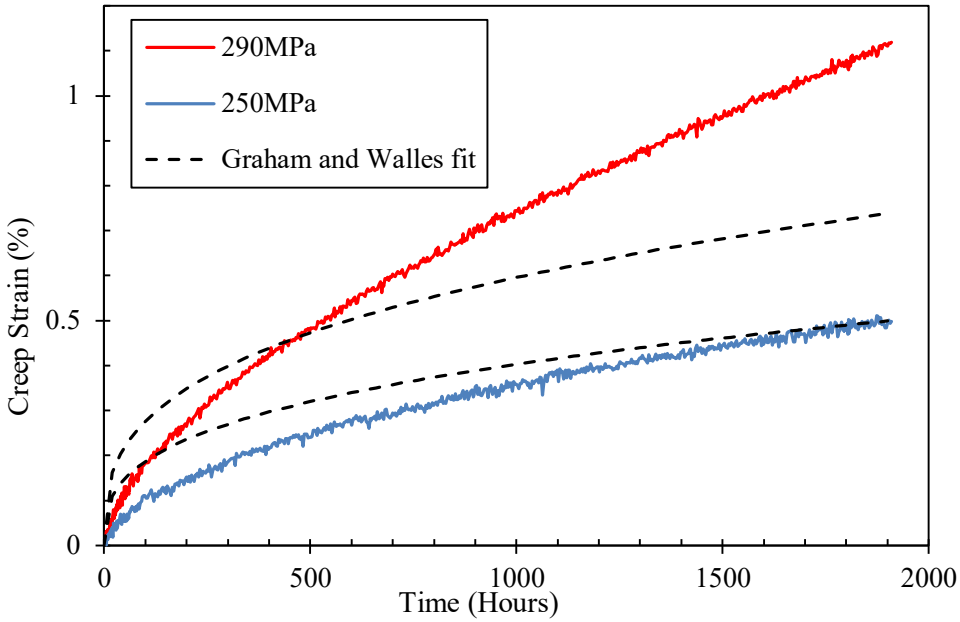

Figure 4.39 shows a comparison between the Graham and Walles primary creep model prediction and experimental data.

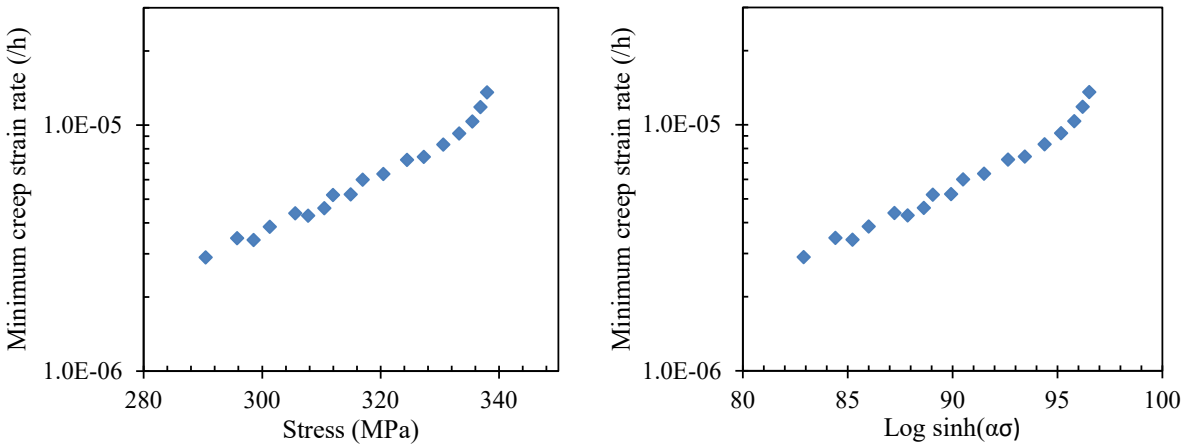

Figure 4.40 Plot of the minimum creep rate as a function of stress as determined by (a) exponential model (b) hyperbolic function.

TABLES

Table 4.1 Standard RCC-MR model parameters at 525°C

C1	C2	n1	C	n
1.88E-12	0.40	4.13	4.152E-29	9.06

Table 4.2 RCC-MR model parameters determined from multiple-stress creep strain curves extracted from a hour-glass specimen at varying nominal stress.

C1	C2	n1	C	n
1.57E-12	0.56	4.04	1.79E-31	10.27

Table 4.3 RCC-MR model parameters determined from multiple-stress creep strain data plotted as a function of time and true stress at the beginning of the creep test.

C1	C2	n1	C	n
1.51E-12	0.58	4.01	1.47E-26	8.24

Table 4.4 Summary of the RCC-MR model coefficients obtained from 3D surface fitting

Stress	C_1	C_2	n_1
Nominal stress	1.31E-15	0.68	5.18
True stress (0 hours)	2.65E-13	0.68	4.22

Table 4.5 Sum of Squared Difference (SSD) between the measured creep strains and the ones determined using the RCC-MR, the Garofalo and the Graham-Walles models at 290MPa and 250MPa

Model	Sum of Squared Differences (SSD)	
	290MPa	250MPa
RCC-MR	0.08	0.06
Garofalo	0.53	0.22
Graham-Walles	3.65	1.08

4.10 REFERENCES

1. Hyde, T. and W. Sun, *A novel, high-sensitivity, small specimen creep test.* The Journal of Strain Analysis for Engineering Design, 2009. **44**(3): p. 171-185.
2. Hyde, T., W. Sun, and J. Williams, *Requirements for and use of miniature test specimens to provide mechanical and creep properties of materials: a review.* International materials reviews, 2007. **52**(4): p. 213-255.
3. Kumar, J.G. and K. Laha, *Small Punch Creep deformation and rupture behavior of 316L (N) stainless steel.* Materials Science and Engineering: A, 2015. **641**: p. 315-322.
4. Levy, J. and I. Bàròdy, *A Set of Creep Curves from a Single Test using a Tapered Specimen.* Journal of Mechanical Engineering Science, 1964. **6**(3): p. 236-239.
5. Cloud, G., *Optical methods of engineering analysis*. 1998: Cambridge University Press.
6. Rist, M. and R. Reed, *Inverse method for parameter optimisation in superalloy tertiary creep equations.* Materials science and technology, 2002. **18**(2): p. 179-186.
7. Sinha, N.K., *Stress exponent and primary creep parameters using single specimen and strain relaxation and recovery test.* Materials Science and Engineering: A, 2009. **510–511**: p. 450-456.

8. Sakanashi, Y., S. Gungor, and P.J. Bouchard, *Measurement of Creep Deformation in Stainless Steel Welded Joints*, in *Optical Measurements, Modeling, and Metrology, Volume 5*, T. Proulx, Editor. 2011, Springer New York. p. 371-378.
9. Sakanashi, Y., *Measurement of Creep Deformation in Weldments.* PhD Thesis, The Open University, 2013.
10. 204:2009, B.E.I., *Metallic materials. Uniaxial creep testing in tension. Method of test*. 2009, BSI.
11. ASTM-E139, *Standard Test Methods for Conducting Creep, Creep-Rupture, and Stress-Rupture Tests of Metallic Materials*. 2011.
12. ASTM-E8/E8M, *13a Standard Test Methods for Tension Testing of Metallic Materials*. 2013.
13. ABAQUS, V., *6.13 User's manual.* Inc. and Dassault systemes, 2013.
14. British Energy, G., *AGR Materials Data Handbook R66*. July 2004.
15. Forsey, A. and S. Gungor, *Demosaicing images from colour cameras for digital image correlation.* Optics and Lasers in Engineering, 2016. **86**: p. 20-28.
16. MATLAB. R2012a, The MathWorks, Inc.: Natick, Massachusetts, United States.
17. LA-Vision, *StrainMaster DaVis 8.1 Digital Image Correlation Software*. 2013.
18. Sakanashi Y, G.S., Forsey A and Bouchard P.J, *Measurement of creep deformation across welds in 316H stainless steel using digital image correlation.* In Press, 2016.
19. Hayhurst, D.R., *Computational Continuum Damaged Mechanics: Its use in the Prediction of Creep in Structures — Past, Present and Future*, in *IUTAM Symposium on Creep in Structures: Proceedings of the IUTAM Symposium held in Nagoya, Japan, 3–7 April 2000*, S. Murakami and N. Ohno, Editors. 2001, Springer Netherlands: Dordrecht. p. 175-188.
20. Kowalewski, Z., D. Hayhurst, and B. Dyson, *Mechanisms-based creep constitutive equations for an aluminium alloy.* The Journal of Strain Analysis for Engineering Design, 1994. **29**(4): p. 309-316.
21. Murakami, S., *Continuum damage mechanics: a continuum mechanics approach to the analysis of damage and fracture*. Vol. 185. 2012: Springer Science & Business Media.
22. Holdsworth, S., *Developments in the assessment of creep strain and ductility data.* Materials at high temperatures, 2004. **21**(1): p. 25-31.
23. Garofalo, F., *Fundamentals of creep and creep-rupture in metals*. 1965: Macmillan.

24. Evans, R.W., B. Wilshire, and I.o. Metals, *Creep of Metals and Alloys*. 1985: Institute of Metals.
25. Penny, R.K. and D.L. Marriott, *Design for creep*. 2012: Springer Science & Business Media.
26. Moffat, A., et al. *Development of the RCC-MR Creep Deformation Model for the Prediction of Creep and Stress Relaxation in Type 321 Stainless Steel*. in *ASME 2014 Pressure Vessels and Piping Conference*. 2014. American Society of Mechanical Engineers.
27. Wang, Y., C.E. Truman, and D.J. Smith, *CREEP DEFORMATION OF TYPE 316H AUSTENITIC STAINLESS STEEL AT 550 C AND THE EFFECTS OF ELASTIC FOLLOW-UP.*
28. Rieth M, F.A., Graf P, Heger S, Jäntsch U, Klimiankou M, Materna-Morris E, Zimmermann H, *Creep of the austenitic steel AISI 316 L(N). Experiments and models.* . Scientific Report, 2004. FZKA-7065.
29. MacKenzie, P., et al., *Measurement of Poisson's ratio through the elastic-plastic transition.* Strain, 1986. **22**(1): p. 13-19.
30. Mazzotti, C. and M. Savoia, *Nonlinear creep, Poisson's ratio, and creep-damage interaction of concrete in compression.* ACI Materials Journal, 2002. **99**(5): p. 450-457.
31. Abe, F., T.-U. Kern, and R. Viswanathan, *Creep-resistant steels*. 2008: Elsevier.
32. ECCC-Recommendations, *Data acceptability criteria and data generation - Volume 3 Part I [Issue 5]*. 2005.
33. Kubushiro, K., et al. *Effect of pre-strain on creep properties of alloy 740*. in *Advances in Materials Technology for Fossil Power Plants, Proceedings from the Sixth International Conference*. 2011.
34. Willis, M., A. McDonaugh-Smith, and R. Hales, *Prestrain effects on creep ductility of a 316 stainless steel light forging.* International journal of pressure vessels and piping, 1999. **76**(6): p. 355-359.
35. Auzoux, Q., et al., *Intergranular damage in AISI 316L (N) austenitic stainless steel at 600° C: Pre-strain and multiaxial effects.* Nuclear engineering and design, 2005. **235**(21): p. 2227-2245.
36. Davies, C., et al. *Compressive pre-strain effects on the creep and crack growth behaviour of 316H stainless steel*. in *ASME 2010 Pressure Vessels and Piping Division/K-PVP Conference*. 2010. American Society of Mechanical Engineers.

37. Mehmanparast, A., et al., *The influence of pre-compression on the creep deformation and failure behaviour of Type 316H stainless steel.* Engineering Fracture Mechanics, 2013. **110**: p. 52-67.
38. Conway, J.B., *Numerical methods for creep and rupture analyses.* GORDON AND BREACH SCIENCE PUBLISHERS, INC., NEW YORK. 1967, 204 P, 1967.
39. RCC-MR, *Design and construction rules for Mechanical Components of FBR Nuclear Islands, AFCEN, France*. 2007.
40. Spindler, M. and S. Spindler, *Creep deformation, rupture and ductility of Esshete 1250 weld metal.* Materials Science and Technology, 2014.
41. ASME, *Boiler and Pressure Vessel Code - Section II, Part D - Material Properties*. 2010.
42. ECCC-Recommendations, *High temperature component analysis overview of assessment and design procedures - Volume 9, Part II [Issue 1]*. 2005.
43. Garwood, D.A.S., *Energy material - strategic research agenda.* . 2007, Materials UK Energy Review.
44. Wilshire, B. and M. Bache. *Cost effective prediction of creep design data for power plant steels*. in *ECCC Creep Conference*. 2009.
45. Wilshire, B. and H. Burt, *Creep strain analysis for steel.* Creep resistant steels. Cambridge: Woodhead Publ, 2008: p. 421-45.
46. Wilshire, B. and P. Scharning, *Rationalization and extrapolation of creep and creep fracture data for Grade 91 steel.* Materials at High Temperatures, 2014.
47. Li, D., Shinozak, K., and Kuroki, H., *Stress-strain deterioration in heat affected weld zone in high Cr ferritic heat resistant steel.* Materials Science and Technology, 2003. **19**: p. 1253 - 1260.
48. Watanabe, T., et al., *Creep damage evaluation of 9Cr–1Mo–V–Nb steel welded joints showing Type IV fracture.* International Journal of Pressure Vessels and Piping, 2006. **83**(1): p. 63-71.
49. Li, Y., et al., *Evaluation of creep damage in heat affected zone of thick welded joint for Mod.9Cr–1Mo steel.* International Journal of Pressure Vessels and Piping, 2009. **86**(9): p. 585-592.

CHAPTER FIVE

5. Measurement of deformation properties in heterogeneous materials

5.1 Introduction

The previous Chapter considered the application of DIC in extracting multiple creep strain curves from a single specimen with varying stress fields. The objective of this Chapter is to investigate the application of DIC to characterise mechanical properties of a specimen with varying material properties along the gauge length which results in varying stress fields when the specimen is subjected to external loads. The extreme case of test specimens having a sharp interface (i.e. step change in elastic-plastic stress-strain properties) at mid-length of the gauge section is modelled using FE analysis and measured in test specimens where two different materials have been joined by diffusion bonding. The effect of specimen geometry (thickness to width ratio) is also examined to assess the influence of material property mismatch constraint. The FE modelled and measured results are compared and used to inform on the validity of applying DIC to characterise the local mechanical properties of cross-weld test specimens.

In a standard tensile test, it is required that the specimen is subjected to a uniaxial load and that the resulting stress state is uniformly distributed along the gauge section [1]. This requirement is easily met when a specimen with homogeneous material properties is used. This is not the case when a cross-weld specimen is subjected to uniaxial load because of the inhomogeneity of material properties from base metal to HAZ to weld metal. This makes it impossible to characterise the local material properties of weldments when displacement is measured spanning the variable property zone using a standard extensometer, and difficult to achieve with small strain gauges. A further critical issue is that the measured local strain is affected by the local stress state which is function of the variation in material properties and the specimen cross-sectional geometry (aspect ratio) [2-4]. The importance of these effects is uncertain when local strains in cross-weld specimens are measured by small strain gauges or full field techniques like 2D-DIC (where rectangular cross-section specimen geometry is used). This raises questions regarding the validity of using local measured strains to infer local stress-strain properties from full field DIC deformation measurements on cross-weld specimens.

Alternatively, the local mechanical properties of cross-welds, such as the proof stress and hardening characteristic, can be measured by extracting thin specimens from the various sections of the weldment and testing them individually. This is not only time consuming but costly as many thin sectioned specimens are required to get enough data points across the weld [5]. The results from thin sectioned specimens are based on the assumption that the material is homogenous in any given specimen extracted however this cannot always be guaranteed as steep gradient in material properties may exist within the weld. Besides, thin sectioned specimens are mostly extracted from the weld in specific orientations which may not necessarily be the loading direction of the cross-weld thus results from such specimens may not be accurate due to anisotropic behaviour of welds and the surrounding regions. The local mechanical behaviour of thin sectioned specimens would also be different from that of the material deforming in a cross-weld adjacent to a stiffer material, due to differences in the levels of constraint. Therefore, the development and availability of full-field displacement measurement techniques such as DIC provides a unique opportunity of characterising the local mechanical properties of cross-welds [6].

The capability of DIC to characterise mechanical properties of cross-welds was first demonstrated by Reynolds *et al* [7]. Further, Lockwood *et al* [8-10] applied DIC to measure the spatially resolved local deformation of friction stir welds. In these measurements, characterisation of local mechanical properties was based on the iso-stress assumption, which implies that the various regions of the weld are arranged in series and that the cross section area at any given location in the specimen is homogenous. Therefore, the local mechanical properties were extracted by mapping the measured local strain against the global stress. To check the validity of this method of characterising local mechanical properties by mapping the local strains to the global stress, the measured local deformation were compared to plane stress, plane strain and three dimension (3D) finite element predictions. It was found that the measured local deformation correlated well with plane stress FE predictions and a relatively good agreement between the experimental and the FE measured properties was observed [9]. Further, detailed weld characterization results using DIC, where the parameters have been optimised for room temperature tensile testing, have been published [11-13].

However, there remains a need to understand the fundamental effects of geometric and material property variation constraints on the local deformation of cross-weld tensile specimens subjected to uniaxial loads. The influence of these factors raises questions concerning the interpretation of local strain measurements using DIC and other full field

techniques. Specifically, there is uncertainty as to whether the measured variation in local strain versus average cross-sectional stress (average global stress) represents the local mechanical properties of the material with negligible error. The severity of potential constraint errors will be influenced by the specimen geometry (particularly the tensile specimen thickness to width ratio for 2D DIC strain measurements) and the gradient of material property inhomogeneity along the specimen gauge length [4, 14]. Therefore two questions need to be addressed, what level of inhomogeneity gradient introduces significant error and how is this error distributed within the test specimen (along the gauge length, across the width and through the thickness) and secondly how is the local deformation affected by the test specimen geometry. From a DIC application point of view, guidance is required on what specimen thickness (or aspect ratio) is best to use for determining the actual local mechanical properties of cross-weld specimens.

This Chapter seeks to address the questions raised above. Due to the potential complexity of deformation patterns that might develop in cross-weld specimens subjected to an external load, an idealised test specimen containing a step-change in tensile material properties at mid-length is studied here; that is a sharp interface joint between dissimilar materials. Finite element analysis is used to examine the influence of material mismatch and specimen geometry (thickness to width ratio of the rectangular cross-section) in a parametric sense. This is supplemented by experimental DIC strain measurements of dissimilar material joints with sharp interfaces, manufactured by diffusion bonding. To study the effects of change in aspect ratio (thickness to width ratio) on local deformation of heterogeneous materials, the FE model width and experimental test specimen width were kept constant (6mm wide for all the cases), whereas the thickness was varied resulting in change in aspect ratio. Therefore, in the current study the effect of change in aspect ratio is at times represented by a change in model or specimen thickness. The first sections 5.2 to 5.4 present the FE parametric analysis results and these are compared with the experimental data in section 5.5.

5.2 Finite Element Analysis

The geometry of the models used were based on the standard flat tensile test specimens with a total length of 100mm, 40mm parallel sided section, a width of 6mm and varying the model thickness to give aspect ratios (t/w) of 0.167, 0.5 and 1, Figure 5.1. The dimensions of the models used were chosen based on the tensile test specimens extracted from dissimilar metal diffusion bonded billets which were used for DIC experimental tests. The mechanical

behaviour of the 3D models under uniaxial loading was analysed using commercial software, ABAQUS 6.14 [15]. Two types of stress analysis were performed: linear elastic and elastic-plastic hardening material responses. Due to the symmetry of the loading condition and the specimen geometry, one-quarter FE models with mid-planes constrained in the x and z-directions were used. A step change in the material properties (elastic modulus and non-linear stress-strain behaviour) was introduced in the model at the interface between the two materials. In practice, joints made by solid state diffusion bonding have a high quality thin material transition region in the order of 100μm or less [16, 17]. But the nature and properties of this transition region were not investigated in the present work. Instead it was recognised that the sudden transition in properties would have to be studied and dealt with to avoid predicting unrealistic strains close to the joint interface (owing to the step change singularity in the properties modelled).

Boundary conditions similar to a uniaxial tensile test were applied to the model such that the bottom end of the specimen was fixed (in the loading direction) whereas a uniform displacement was applied to the top end of the specimen. 3D brick 20-noded (C3D20R) quadratic elements with reduced integration were used. The mesh was designed with a single bias towards the specimen interface with finer elements in the region near the interface. Figure 5.2 shows the mesh around the interface.

5.2.1 Mesh Sensitivity

For a 1mm thick (t/w = 0.167) elastic model subjected to a 300MPa stress, a typical local strain distribution in the regions near the interface are shown in Figure 5.3. Figure 5.3(a) shows a strain map in the regions near the interface and (b) shows the predicted longitudinal elastic strain distribution extracted from the centre-line shown in (a) across the idealised interface joining the dissimilar materials having an elastic stiffness mismatch ratio of 0.5, that is the elastic modulus for Material1 and Material2 was 100GPa and 200GPa, respectively. Away from the interface, the uniaxial engineering strain is equivalent to $e = {}^{\sigma}/_{E}$ (where σ – far field applied stress and E – elastic modulus of the material) on both sides of the interface. However, near the interface, deformation of the weak material is constrained by the stronger one resulting in stress/strain perturbation due to the development of a triaxial stress state in this region.

The elastic strains in the two materials approaching the interface vary from a distance of about 1.5 mm from the interface, as can be seen in Figure 5.3(b). There is an intermediate

effect on both sides of the adjacent materials, (Material 1 and 2), and a short range perturbation adjacent to the interface line. Both of these effects can be influenced by mesh size used on the FE analysis. Therefore, mesh sensitivity study was carried out by varying the mesh density around the interface and the strain distributions at points (1) and (2) near the interface in Figure 5.2(b) were monitored. A 1mm thick model was used for the mesh sensitivity study and a summary of the element sizes used for the mesh sensitivity study in the vicinity of the interface is given in Table 5.1.

Figure 5.4 shows a plot of longitudinal surface strain against the mesh density around region (1) and (2). Figure 5.4(a) focuses on the strain distribution in the vicinity of the interface within the weaker material at region (1), whereas Figure 5.4(b) focuses on region (2) which is in the stronger material. From Figure 5.4(a), it can be seen that the short-range strain reduction near the interface due to constraint on the weak material reduces with increase in mesh density. The position of the minimum local strain in the weak material moves slightly towards the interface as the mesh density increases. In Figure 5.4(b), the maximum local strain increases with increase in the mesh density, and similar to Figure 5.4(a), the position of the local maximum strain changes with increase in mesh density. Figure 5.5 shows the plot of local minimum and maximum elastic strain in the vicinity of the interface as a function of mesh density. It can be seen that the model has not converged even with the very fine mesh size, where the model for a 1mm thick sample has reached an impractical size (approaching 200,000 elements). Models for thicker samples (3mm and 6mm) would be proportionately larger. This modelling issue was treated as follows.

Since, the FE model results will be used to inform and interpret the deformation and strain fields measured by DIC across the diffusion bonded specimens, the length scale over which the measured strain can be resolved by DIC is important. The DIC spatial resolution depends on the subset size, the step size and the speckle pattern size used for extracting displacement fields. In the current study, a subset size of 31x31 pixels and a step size of 7 pixels were used. The DIC strain measurement system was calibrated and the pixel size was determined to be 3.8μm. Since the minimum length scale within which strain can be resolved is taken as the sum of the subset and step size, for this study, the minimum resolution length scale was calculated to be 0.144mm. The element size used approaching the interface was chosen to be 0.1mm, which is of the order of the DIC spatial resolution.

Figure 5.6 compares the chosen mesh design (having a smallest element size adjacent to the bond line equal to 0.1mm) to the mesh sensitivity results given in Figure 5.4. It can be seen that this pragmatic modelling compromise captures the minimum strain whilst filtering the short range profile perturbation immediately next to the bond. Also the strains more than 0.3mm away from the interface are unaffected by the mesh design. Comparison between the surface transverse strains obtained from the chosen mesh size of 0.1mm and the one obtained from finer mesh (Figure 5.7), shows that there is no significant difference in elastic strain distribution in the transverse direction. This justifies the use of the chosen mesh size and as such, it will be used for all the models in this study.

5.3 Finite Element Analysis Results

5.3.1 Elastic FE Results

Two sets of linear elastic FE analyses were carried out. The first set focused on studying the effects of differing degrees of elastic modulus mismatch including both realistic and extreme cases using a 3mm thick model (t/w = 0.5). As described above the bond interface was modelled as a sharp interface with a step-change in material properties. The elastic modulus of the stiffer material (E_2) was taken to be 200GPa, whereas the elastic modulus of the weaker material was varied giving a modulus ratio in the range $E_1/E_2 = 0.1$ to $E_1/E_2 = 1$. The Poisson's ratio for both materials was taken to be 0.3.

5.3.1.1 Effects of elastic mismatch

Figure 5.8 shows a plot of the longitudinal surface strain as a function of distance from the specimen interface. From Figure 5.8, it can be seen that, as the E_1/E_2 ratio reduces, the elastic strain in the weaker material increases. In both materials, the far field strain is uniformly distributed and material properties can be easily obtained from a simple stress/strain relationship. However, in the regions near the interface, the strain distribution is nonlinear. In the weak material, deformation of the region near the interface is constrained due to the adjacent stiffer material. The level of constraint is characterised by low strain in the region adjacent to the interface in the weaker material. Away from the interface, the strains increase to a peak point, beyond which they reduce to be uniformly distributed.

Figure 5.9 shows the normalised surface strains plotted as a function of the distance from the interface. The normalised elastic strains are calculated by dividing the local surface strains by the far-field surface strain. In Figure 5.9, a strain concentration point labelled as (1) and a

region with minimum local strain labelled (2) are noted. Considering point (1), the peak strain increases by only 2% compared to the far field strain, as the elastic modulus ratio E_1/E_2 is reduced from 0.875 to 0.1. The 2% increase in the strain concentration factor is insignificant considering that the elastic strains are quite small. In the case of point (2), the local minimum point adjacent to the interface, it can be seen that the local minimum strain reduces and the position of the minimum moves away from the interface as the elastic modulus ratio is reduced. However, the steep strain gradients in this region (up to ≈0.25 mm from the interface) cannot be reliably resolved using the conventional DIC experimental set-up implemented in the present work.

The cross-over distance (the point at which the normalised strain curves intercept the horizontal line passing through the value 1 in the normalised strain axes) can be characterised by the distance L marked in Figure 5.9. As the strain concentration at point (1) is negligible, the cross-over point is a convenient measure of the zone of influence of the interface, within which the strain is perturbed due to the constraining effects of the adjacent stiffer material. Figure 5.10, shows the plot of the cross-over points as a function of the elastic mismatch ratio. The distance of the cross-over point from the interface increases with a reduction in the elastic mismatch ratio. This is expected since the level of constraint increases with a reduction in strength of the weaker material [14, 18]. It should be noted that the increase in strain perturbation distance is quite minimal compared to the change in the elastic mismatch of the materials under consideration.

In DIC, the local surface strain of the specimen is measured and only the global stress of the specimen is known. Therefore, to characterise the spatially resolved mechanical properties of specimens/components with varying mechanical properties along the gauge section, the local measured strain is mapped against the global stress assuming the condition of iso-stress applies [8, 9]. The resulting spatial resolved properties are widely referred to as 'local' mechanical properties of the material even though the local stresses are not taken into account. This inevitably may result in errors on the measured local mechanical properties. Therefore, there is a need to assess the errors in the DIC measured local mechanical properties of specimens/components with inhomogeneous material distribution across the gauge length. To assess the errors in the elastic local mechanical properties due to elastic mismatch, the model input elastic modulus of the weaker material was compared to the ones obtained from mapping the local strains against the global axial stress. Surface and model mid-section local strains (averaged within 80% of the model width) were extracted at varying

distance from the interface whereas the global stress was obtained from the far-field region of the weaker material, 15mm away from the interface. The 'local elastic modulus' was obtained by a linear fit to the plot of the global stress as a function of local strain. The elastic modulus error was calculated as follows,

$$Error\ (\%) = \left(\frac{'Local\ modulus' - model\ input\ modulus}{model\ input\ modulus}\right) \times 100 \quad (5.1)$$

Figure 5.11, shows a comparison between the errors obtained when the local elastic modulus is determined from the linear fit to the plot of the global-stress against the local-strain, and when its determined from the linear fit to the plot of the local-stress against the local-strain, for a case of elastic mismatch ratio of E1/E2 = 0.95 and 3mm thick model. It can be seen that, for both cases, the obtained errors are higher in the regions near the interface and reduces with distance from the interface. Slightly higher errors are obtained when the elastic modulus is determined from a linear fit to the plot of the global-stress as a function of local-strain compared to when the elastic modulus is determined from the linear fit of the plot of the local-stress against the local-strain. However, it should be noted that, for the elastic modulus ratio of 0.95, the maximum error obtained when the 'local elastic modulus' was determined from a plot of the global-stress as a function of local-strain is very small, approximately 0.7%.

Figure 5.12 shows the effect of change in elastic mismatch on the errors in the determined 'local elastic moduli' from linear fit to the plot of the global-stress as a function of local-strain for a 3mm thick model. The percent error in the regions near the interface increases with reduction in the elastic mismatch ratio, signifying the effects of elastic mismatch ratio on the percent error in the determined elastic modulus. Assuming that errors less than 1% are insignificant, for E1/E2 = 0.5, significant errors are obtained in the region 1.8mm from the interface and the maximum occurs at about 0.5mm from the interface. As for E1/E2 = 0.75, significant errors are obtained in the regions within 1.4mm from the interface, whereas for E1/E2 = 0.95, the obtained errors are within 1%. This implies that significant errors in the determined 'local elastic modulus' are only obtained when the adjacent materials in a weld joint are highly mismatched. Considering that the maximum error in the determined elastic

modulus for elastic mismatch ratio of 0.95 is less than 1%, it can be concluded that for elastic mismatch ratios in the range of 0.95, local elastic mechanical properties can be determined by linear fit to the plot of the global-stress as a function of the local-strain. For the elastic mismatch ratio of 0.75, the maximum error of the determined local elastic modulus in the region near the interface is about 3.5%, and therefore, for mismatch ratios in this range, an error of 3.5% should be taken into consideration when the determined local elastic modulus is determined by linear fit of the plot of the global-stress as a function of local-strain, as is the case for DIC local mechanical properties characterisation.

Comparing the cross-over distance (L) in Figure 5.10 and the length scales from the interface within which significant elastic modulus error occurred (Figure 5.12); it can be concluded that the cross-over distance (L) of the normalised strain from the interface gives an estimate of the region from the interface within which significant errors in the measured local mechanical properties would occur when extracted from a plot of global-stress as a function of local-strain.

5.3.1.2 Effects of specimen geometry on local deformation

To understand the effects of a change in the specimen geometry on the local deformation owing to a step-change in elastic properties, three model thicknesses (1mm, 3mm and 6mm) representing aspect ratios t/w = 0.167, 0.5 and 1.0 were analysed. Figure 5.13 shows a plot of the surface strain distributions as a function of distance from the interface for the three cases, at an applied stress of 170MPa and an elastic modulus mismatch ratio of 0.95. The condition of plane stress presents a limiting case for low constraint whereas plane strain is an extreme case of high constraint in mismatched materials and therefore they have been included in Figure 5.13, 5.14(a) and (b) for comparison. The strain distributions are similar to the ones in Figure 5.8, with more strain perturbation near the interface compared to the far field strain. Figure 5.13 and 5.14(a) shows that the plane stress condition gives a small strain concentration at about 2 mm from the interface and provides a profile bounding the finite thickness cases. However, the thicker the specimen the greater the extent of the transition zone before intercepting the plane stress bounding profile. Interestingly, length of the transition zone is approximately equal to that of the model thickness, for instance, the strain distribution curve for the 1 mm specimen intercepts that of the plane stress condition at approximately 1mm from the interface. Figure 5.14(b) shows a plot of the mid-section elastic strain distributions as function of distance from the interface for the three model thicknesses.

The strain distributions from the mid-section are compared to both the plane stress and plane strain cases. All three model thicknesses compare well with a plane stress condition. This would be expected as the largest model size (6mm thick and 6mm wide) considered in this study is not big enough to warrant plane strain condition.

The effect of specimen geometry on the local deformation of elastically mismatched materials can be seen in the normalised strains plotted as a function of distance from the interface in Figure 5.15. For E1/E2 = 0.95, the local strain concentration factors for 1mm and 3mm thick models are about 0.1%, which is negligible. However, the distance of the strain cross-over point from the interface, defined by the distance L in Figure 5.15 increases as the model thickness increases leading to notable differences in the strain gradient approaching the interface.

Figure 5.16 compares the effects of elastic mismatch (E1/E2 = 0.95 and E1/E2 = 0.5) on the local deformation for two model thicknesses extracted at the same stress level. It is interesting to note that the cross-over distance does not change significantly with change in the material mismatch for a given specimen thickness (See Figure 5.10). However the strain gradient shows significant change as the elastic mismatch changes. Figure 5.17 compares the effects of change in constraint due to the material mismatch and the specimen geometry on the cross-over distance (L) in the region near the interface. As noted above, a change in the constraint due to elastic mismatch does not result in a significant change in the cross-over distance (L).

As stated above, characterisation of local mechanical properties by mapping the global stress to the local strain gives rise to errors. Figure 5.18, shows the effect of geometry on the errors in the measured 'local elastic modulus' obtained by linear fit to the plot of the global stress as function of local strain for case of elastic mismatch. In Figure 5.18(a) and (b), the error distributions are similar to the ones shown in Figure 5.11. The errors in the measured local elastic modulus are higher in the regions near the interface and reduce away from the interface. For both elastic mismatch ratios, it can be seen that the errors in a 1mm thick specimen extends only up to about 1mm from the interface whereas for a 6mm thick, the errors extends as far as 4mm from the interface. This signifies that the region from the interface within which the errors occurred in the measured local elastic modulus increase with increases in the specimen thickness or aspect ratio. In should be noted that the magnitude of the errors is dependent on the elastic mismatch between the adjacent materials.

Although the errors in the regions near the interface are similar for all the model thicknesses, the 1mm thick model has a smaller region within which the errors would occur when the local elastic modulus is calculated by linear fit to the plot of the global stress as function of the local strain. This implies that a 1mm thick model is more ideal for measurement of local elastic modulus compared to the 3mm and 6mm thick model (for a model width of 6mm).

5.4 Elastic-Plastic FE models

In DIC strain measurements, construction of local stress-strain curves is based on an iso-stress assumption such that the global axial stress determined from the measured applied load is plotted against the local axial strain measured by DIC [8, 9]. In section 5.2.1, errors in the measured local elastic properties due to material mismatch and model aspect ratio were considered. It was established that the magnitude of the errors in the measured local elastic modulus, obtained by linear fit to the plot of the global stress as a function local strain, were dependent on the material mismatch. Whereas the size of the region within which these errors occur is dependent on the model thickness or aspect ratio. In this section, errors in measured local mechanical properties of a weaker material adjacent to a stronger one undergoing elastic-plastic deformation are considered.

Since the results in this section were compared to experimental data in the later sections, the material properties of the two adjacent materials in these models were not varied. However, three model thicknesses, 1mm, 3mm and 6mm were studied. For all the elastic-plastic FE models, the material properties of 316H stainless steel and Esshete1250 obtained from parent materials which has been subjected to conditions of diffusion bonding process were used as input data (detailed description of the diffusion bonding process is give in Chapter 3). From the DIC tensile test results of dissimilar material diffusion bonded specimens, history dependent axial displacement values at locations at the end of the parallel section of the specimen, approximately 20mm away from the specimen gauge centre, were extracted and used in the FE simulations as boundary conditions. The models were formulated as described in section 5.2.

5.4.1 Errors in local mechanical properties obtained from Elastic-Plastic FE model results

To assess the effects of the iso-stress assumption on the local measured mechanical properties of a weaker material adjacent to a stronger one in cross-welds, the global axial stress plotted

against the local axial strain are compared to the local von Mises stress plotted against local axial strain, Figure 5.19. Figure 5.20 shows the typical surface strain distribution map of deformed 1mm thick model and the white lines indicate elements which were used for computing the local axial strains used for plotting the stress-strain curves. For both the 1mm and 6mm modelled thickness, the local von Mises stress plotted against the local axial strain in the regions near the interface, are similar to the stress-strain curve for 316H parent constructed by plotting the global axial stress against the local axial strain in the region about 14mm from the interface (Figure 5.19). It should be noted that the stress-strain curve for 316H parent is equivalent to the FE model input stress-strain curve. This is expected as the local axial strain is extracted from the region further away from the interface and in such regions the model is uniaxially loaded compared to the regions near the interface where deformation is influenced by the adjacent stronger material resulting in multiaxial loading.

Regardless of the location from the interface and the thickness of the model, the plot of the local Mises-stress against the local axial strain gives stress-strain curves similar to the stress-strain curve representing the 316H parent material, Figure 5.19. In DIC tensile tests, the Mises stress cannot be measured and only the global stress is measured. Therefore, the stress-strain curves constructed by plotting the global axial stress against the local axial strain were compared to the stress-strain curve for 316H, representing the FE model input curve, to assess the effects of iso-stress assumption on local mechanical properties extracted from DIC measurements, Figure 5.21. For all the model thicknesses, it can be seen that the curves as extracted from DIC (global axial stress vs local axial strain) deviates from the stress-strain curve for the 316H which defines the underlying material properties (Figure 5.19 and 5.21). The deviation from the FE model input curve signifies that the measured local mechanical properties obtained from DIC have marginal errors compared to the actual material properties. For the 1mm thick model, In Figure 5.21(a), deviations of the global-stress/local-strain curves from the 316H FE input curve extends only up to about 1mm and at about 1.5mm from the interface, the two stress-strain curves are similar. For the 3mm and 6mm thick models, the global-stress/local-strain curves deviation from the 316H FE input curve extends up to about 2mm and 3mm, respectively. This signifies that the 1mm thick model would give a smaller region within which errors would occur in the measured local mechanical properties using DIC.

To quantify the errors in the measured local mechanical properties when the local stress-strain curves are constructed by plotting the global axial stress against the local axial strain,

mechanical properties obtained in the regions near the interface were compared to the 316H FE input material properties. The plastic properties compared in this section are the 0.1% yield stress, the strain hardening exponent, n, and the strength coefficient K. The strain hardening exponents and the strength coefficients were computed by fitting a modified power law to the plastic region of the stress-strain curves [19],

$$\sigma = \sigma_0 + K(\varepsilon_p)^n \qquad (5.2)$$

where σ_0 is the yield stress, K is the strength coefficient, ε_p is the plastic strain, and n is the strain hardening exponent. Figure 5.22 shows a comparison between the experimentally determined stress-strain curve for 316H and the one predicted by the power law given in Equation 5.2. The two stress-strain curves correlates very well. Therefore, the strain hardening exponent, n, and the strength coefficient, K, computed from the plot of the global stress against the local strain at varying distance from the interface were compared to that of the 316H to compute the errors.

The errors in the measured local mechanical properties for the 3 modelled thicknesses are shown in Figure 5.23. For all the 3 modelled thicknesses, the measured errors are higher in the regions near the interface and reduce in the regions away from the interface. For yield strength, the 1mm thick model has slightly higher percent errors in the region near the interface (approximately 5.3% maximum error); however the region within which the errors occur extends does not extend further away from the interface compared to the 3mm and 6mm thick models, Figure 5.23(a). Assuming a threshold of 1% error in the measured yield strength, the region within which errors occur in the measured yield strength extends only up about 1.3mm from the interface for the 1mm thick model. For the 3mm and 6mm thick models, the errors extend to about 1.9mm and 2.8mm from the interface, respectively. Although, the 6mm thick model has generally lower errors in the measured local yield strength, it has a larger region within which these errors occur.

The strain hardening exponent and the strength coefficient shows a similar trend in the error distribution for the 3 modelled thickness as the errors in the yield strength Figure 5.23(b) and (c). The only difference is that the percent errors for the measured strain hardening exponents and stress coefficient are much higher in the regions near the interface, approximately 14% and 18%, respectively. The region from the interface within which errors in the measured strain hardening exponent would occur extend to approximately 1.4mm for the 1mm thick

model, 2mm for the 3mm thick model and 3.5mm for the 6mm thick model, assuming an error threshold of 2%, Figure 5.23(b). Considering the strength coefficient, the trends are similar to the ones for the strain hardening exponent.

Generally, the 1mm thick model has a smaller region within which errors in the measured local mechanical properties occur compared to the other model thicknesses. This implies that when it comes to practical measurement of local mechanical properties of cross-welds using DIC, a specimen with smaller aspect ratio, for example 1mm thick specimen, would give a small region near the interface where marginal errors in the measured local mechanical properties would occur. The maximum error in the measured 0.1% yield strength is approximately 5% for a 1mm thick, however it should be noted that this measured error is dependent on the material mismatch between the adjacent materials and also the nature of the joint such as sudden or gradual change in material properties at the interface.

5.4.3 Implication of the Elastic-Plastic FE results

The region from the interface within which errors in the measured local mechanical properties occur increases with increase in the model thickness. Whereas the magnitude of the measured errors in the regions near the interface is almost the same for all the models thicknesses, this indicates that change in model geometry has minimal effect of the magnitude of the errors obtained. Similar conclusion was made for determination of local elastic mechanical properties from linear fit to the plot of global stress as a function of local strain. The results shows that the use of thinner specimen to extract local mechanical properties from a plot of global stress as a function of local strain would give better results compared to thick specimens.

5.5 Experimental tests of diffusion bonded specimens

Apart from FE modelling of mechanical response of diffusion bonded specimens, room temperature tensile and creep testing of diffusion boned specimens were carried out. Both tensile and creep testes were carried out on specimens of varying thickness (1mm, 3mm and 5mm thick). The width of the all the specimens was 6mm and strain measurement for all the tests were carried using DIC. The following sections outline the tensile and creep test results obtained.

5.5.1 Room Temperature DIC tensile tests

The room temperature DIC tensile testing was carried using an Instron testing machine with a constant crosshead displacement rate of 0.1mm/min. As outlined in Chapter three, the principle loading axis was perpendicular to the bond interface at the mid-section of the specimen gauge length. The tests were carried out in accordance to test standard ASTM-E8/E8M [20]. All the specimens were EDM machined to 6mm wide, whereas the thickness was varied (1mm, 3mm and 5mm). The strain evolution during each test was captured using a single camera (2D DIC) with image acquisition rate of one image in every 5 seconds for the first part of the tests and one image in every 30 seconds for the later stage of the test. Two sets of tensile test experiments were carried out. In the first set, the EDM surface of the machined specimens was used as the speckle pattern, providing a very fine (small) speckle size. Therefore, these specimens are referred to as specimens with small speckle size. For the second set of experiments, a speckle pattern was applied to the surface of the machined specimen by spray painting black speckles on a white background. Specimens used in the second set of experiments are referred as specimens with large speckle size. On completion of each experimental test, the digital images captured were exported and processed for displacement/strain measurements using the Davis 8.2 DIC software [6]. Details of the experimental set up, specimen preparation and DIC strain computation are given in section 3.2.3.

5.5.2 DIC tensile test results

Figure 5.24 shows the room temperature DIC tensile test results from both the 1mm and 3mm thick specimens with a small speckle size. In all the DIC tensile tests, the distance between the optical centre of the camera and the specimen plane was set at distance that allowed the whole specimen gauge section to be captured during deformation. For each specimen thickness, the global axial stress obtained from the Instron tensile testing machine was plotted against the local axial strain measured by DIC. The results in Figure 5.24 are similar to the ones presented in Figure 5.21 obtained from elastic-plastic FE results. In both the 1mm and the 3mm thick specimens, the 'local stress-strain curves' obtained from the regions near the interface exhibit different hardening characteristic and hence different mechanical properties compared to the local stress-strain curves obtained from the region further away from the interface which signify the 316H parent material. It should be noted that the yield strength of the local stress-strain curves extracted at varying distance from the interface in 316H are

similar however the major difference is in the hardening characteristic which can be seen in Figure 5.24. This is expected as the material near the interface is constrained by the adjacent stronger material thus inhibiting its plastic deformation. Therefore, extracting local mechanical properties from the plot of the global stress as a function of local strain would result in errors in the measured local mechanical properties as explained in the previous section.

Errors in the measured local mechanical properties were assessed by comparing the measured local properties obtained from plots of global axial stress as function of local axial strain extracted at varying distance from the interface to the one obtained further away from the interface signifying 316H stress-strain curve. The local mechanical properties were obtained by fitting the modified power law model given in Equation 5.2 to the local stress-strain curves obtained at varying distance from the interface. The errors were computed according Equation 5.1. Figure 5.25 shows the errors in the measured strain hardening exponent and the strength coefficient in both the 1mm and 3mm thick specimen. In both Figure 5.25(a) and (b), it can be seen that the maximum errors of about 10% in the hardening coefficient and about 22% for the strength coefficient occurs in the regions near the interface for both the 1mm and 3mm thick specimens. However, in the 1mm thick specimen, significant errors are exhibited in the regions up to about 1.3mm and beyond this distance the errors become negligible. In the 3mm thick specimen, significant errors extend up to about 2mm for the hardening exponent and about 2.5mm for the strength coefficient. The results obtained in Figure 5.25 are similar to the ones obtained in Figure 5.23. The results indicates that when local mechanical properties are obtained from the plot of the global stress as a function of the local strain, a small region within which errors would occur is obtained when a thinner specimen is used, therefore making the 1mm thick specimen ideal for measurement of local mechanical properties using DIC. However, it should be noted that the magnitude of the errors arising in the regions near the interface are highly dependent on the mismatch in material properties between adjacent materials.

5.5.3 Comparison between elastic-plastic FE and DIC experimental test results

Since the input data for the elastic-plastic FE models considered in section 5.4 was obtained from 316H and Esshete1250 parent material which was subjected to the diffusion process condition as the diffusion bonded specimens used in section 5.5, their results were compared.

The comparison of the two data sets would facilitate application of the conclusions obtained from elastic-plastic FE models to the DIC experimental data.

Strain distributions along the specimen gauge length extracted from both the elastic-plastic FE models and the DIC tensile test results from specimens with a small speckle size pattern were compared at the same stress level. Figure 5.26 compares the longitudinal strain distribution at 200MPa as a function of distance along the gauge length between the small speckle size pattern DIC test specimens and elastic-plastic FE model results for the 1mm and 3mm thick specimens. In both Figure 5.26(a) and (b), the FE predicted strains in the Esshete1250 are lower than the experimental results although there is a good correlation between the two data sets in the region near the interface. Whereas the FE predicted strains in the 316H correlates well with the experimental results in the regions near the interface. Away from the interface, the FE predicted strain distribution in the 316H is slightly higher than the ones obtained from experimental tests. It should be noted that the FE predicted strains exhibit a peak point at about 2.5mm from the interface. Although it is difficult to see a peak in the DIC measured strains due to the scatter in the data, the trend in the strain distribution for the 3mm thick specimen at 200MPa in Figure 5. 26 (b) might suggest a peak in strain at a similar distance from the interface (2.5mm – 5mm) compared to the FE predicted strains (3mm).

Figure 5.27 compares the strain distribution between the FE predicted and the DIC measured strain distribution at 250MPa. Trends in the strain distributions similar to the ones exhibited in Figure 5. 26 can be seen and a good agreement can be seen between the two data sets for both the 1mm and 3mm thick specimens. In Figure 5.27 (a), although the strain in Esshete1250 compares well with the FE predicted ones, the strains in 316H in the vicinity of the interface shows significant scatter. Away from the interface, both the FE predicted and the mean value of the DIC measured strains in 316H correlate very well (although there is significant scatter in the latter) for the 1mm thick specimen. For the 3mm thick specimen, there is a very good correlation between the FE predicted and the DIC measured strains, Figure 5.27(b). From these results it can be concluded that although the DIC measured strains from specimens with small speckle size exhibited high scatter, the trends in the strain distributions are similar to the ones predicted by the FE models for both the 1mm and 3mm thick specimens.

5.5.3.1 Comparison between elastic-plastic FE and DIC results from specimens with large speckle size

To reduce the scatter in the DIC measured strain, DIC tensile tests using diffusion bonded specimens with relatively large speckle size (applied by spray painting the specimen surface) were carried out. To capture the local deformation near the bond interface, the distance between the optical axis of the camera and the surface plane of the specimens was reduced. The camera was positioned so as to capture the deformation in 316H and the regions near the interface. Therefore, only part of Esshete1250 was capture in these tests. Figure 5.28 shows a comparison between the FE model results and the DIC measured longitudinal strain distributions along the specimen gauge length for the 1mm and 3mm thick specimens at 200MPa. In Figure 5.28, the FE predicted strains in Esshete1250 correlates very well with the DIC results in both the 1mm and 3mm thick specimens. However, there is poor correlation between the FE predicted and the DIC measured strains in the 316H. For the 1mm thick specimen, the DIC measured strains are much higher than the FE predictions. The peak strain in the FE predicted results for the 1mm thick model occurs at about 2.5mm from the interface whereas for the DIC measured strains the peak strain occurs at about 3.5mm from the interface and there is not much difference between the strains at the peak location and the far field strains, Figure 5.28 (a). For the 3mm thick specimen at 200MPa (In Figure 5.29(b)), although the DIC measured strain distribution in 316H differs considerably from the FE predicted ones in the regions near the interface, there is a good correlation between the measured and the FE predicted strains in the far field regions of the specimen. In the regions near the interface, the DIC measured strains exhibit higher deformation with peak strain occurring in the region from 3mm to about 8.5mm. On the other hand, the peak strain for the FE predicted strains occur at about 3mm from the interface.

Figure 5.29 shows a comparison between the FE predicted and the DIC measured strain distributions in both the 1mm and 3mm thick specimens at 250MPa. Similar trends are observed in the strain distributions for both the 3mm and 1mm thick specimens, as shown in Figure 5.28. From Figure 5.28 and 5.29, it is interesting to note that although both the 1mm and 3mm thick specimens were extracted from the same diffusion bonded billet, they exhibit different local strain distribution along the specimen gauge length. The 1mm thick specimen shows higher deformation than the 3mm thick one at the same stress level. This could be due to the difference in the location from which each specimen was extracted from the diffusion

bonded billet. The 1mm thick specimen was extracted from the region near the edge of the billet whereas the 3mm thick specimen was extracted from the region closer to the centre of the billet. The diffusion bonding billets used were 20mm in diameter, therefore it is possible that the material near the outer-section, exposed to induction heating, would experience different heating and cooling rates compared to the material at the mid-section of the billet. However, this does not explain the overall high DIC measured strains in both the 1mm and 3mm thick specimens compared to the elastic-plastic FE predicted ones.

5.5.4 Comparison of DIC measured strains between small and large speckle size specimens

Comparing the DIC measured strains in Figure 5. 26 and Figure 5.28, high scatter in the measured strains from specimens with a small speckle size can be seen compared to the ones measured from specimens with relatively large speckle size. For all the small speckle size test specimens, the EDM machined surface was used for the speckle pattern and this surface was giving shinny regions in some parts of the specimen gauge section, making it unsuitable for image correlation. Therefore, the surfaces of the specimens used for DIC tensile testing in the second set of experiments were painted. Comparing the strain distribution in Esshete1250 for both the 1mm thick and the 3mm thick specimens at 200MPa and 250MPa, it can be seen that there is less scatter in strain data measured in Esshete1250, from specimens with large speckle size. On the other hand, the measured strains in 316H, from specimens with large speckle size, showed considerable scatter in the data, especially for the 1mm thick. However, the scatter in these measurements is less compared to the ones obtained from specimens with small speckle size. Therefore, it can be concluded that less scatter is obtained in DIC strain measurements when a fine spray painted speckle pattern is applied on the specimen surface compared to using the EDM cut surface. However it should be noted that applying a speckle pattern by painting the specimen surface is only advantageous when the applied speckle is fine enough in relation to the size of the subset size used to warrant good image correlation [21]. Although the difference in specimen surface preparation explains the major difference in the scatter of the DIC measured strains obtained from both the small and the large speckle sized specimens, it does not explain the higher strains measured in 316H compared to the elastic-plastic FE predicted ones. This difference can be explained by considering the effects of the diffusion bonding process.

5.6 Effects of the diffusion bonding process

Comparing Figure 5.26 and 5.27 to Figures 5.28 and 5.29, it is clear that the 316H exhibits different deformation characteristics. Significantly higher strains in 316H are measured from specimens with a large speckle size compared to the ones obtained from specimens with a small speckle size. Comparing Figure 5.26(b) to Figure 5.27(b), the peak strain measured in 316H from specimens with a small speckle size is about 1% and the measured data correlates very well with the elastic-plastic FE model results. Whereas for the ones measured from the specimens with a large speckle size, the measured peak strain is about 1.75%. In Figure 5.27(b), it can be seen that the region with higher strains compared to elastic-plastic FE model results extends from about 3mm to about 11mm from the interface. Beyond 11mm, the experimental measured strains correlates well with the FE predicated ones. Similar trend in the measured strain is observed at higher stress (250MPa) for the 3mm thick specimen with a large speckle pattern. Considering the measured strains from the 1mm thick specimen with a large speckle size, it can be seen that the measured strain is higher than elastic-plastic FE model results at both 200MPa and 250MPa, Figure 5.28(a) and Figure 5.29(a). Both results from the 1mm and 3mm thick specimens with a large speckle size indicates that the underlying mechanical properties of the 316H from which these specimens were extracted are different from the material from which specimens with a small speckle size were extracted.

Although all the materials used in the current study were extracted from the same parent 316H ex-service material and Esshete1250, the difference in material properties could be due to the diffusion bonding process. As stated earlier on, all the specimens with a small speckle size were extracted from a single diffusion bonded billet manufactured by solid state bonding of 316H to Esshete1250. However, due to the limited size (20mm diameter) of the billets that can be diffusion bonded by the bonding machine used, another billet was manufactured using the same diffusion bonding process parameters (as explained in chapter 3) from which all the specimens with a large speckle size were extracted. The major control parameters in the diffusion bonding process are temperature, applied load, time and vacuum pressure [17]. Although the diffusion bonding parameters recorded were the same, it was likely that the process had an effect on the final material properties obtained, as indicated by the results in Figure 5.26 to Figure 5.29, [22]. Therefore, the hardness and microstructure of the diffusion bonded billets (from which the DIC tensile test specimens with small and large speckle size were extracted) were examined and the following sections present the results.

5.6.1 Macro-Hardness test results

Line measurements of macro-hardness distribution in the regions near the interface were carried out on diffusion bonded billets from which DIC tensile test specimens with small and large speckle size were extracted. Figure 5.30 compares the hardness distribution in the diffusion bonded billets used for extracting DIC tensile test specimens. The results shows that the hardness measurements from the two diffusion bonded billets are not significantly different. Besides, the average difference in hardness values between 316H and Esshete1250 is quite small, approximately 12 HV/5. However, the major difference exist in the measured hardness of 316H in the region near the interface for the diffusion bonded billet from which specimens with a large speckle size were extracted. For this billet, the average measured hardness in the region near the interface was about 163 HV/5 which is about 15 HV/5 higher than the average hardness of 316H measured from regions further away from the interface. It can also be seen that there is considerable scatter in the measured hardness in the regions near the interface for the diffusion bonded billet from which specimens with large speckle size were extracted. The region within which higher hardness values were obtained extends to approximately 10mm from the interface. Although the measured hardness values in the regions near the interface are not significantly high compared to the average measured hardness of 316H, the hardness distribution is compared to the distribution of strain as function of distance from the interface given in Figure 5.28(b) for DIC tensile test results from specimens with a large speckle size, Figure 5.31. A good correlation between the hardness and DIC measured strain distribution can be seen, especially in the size of the region within which higher hardness and strain values were obtained. For both the hardness and DIC strain measurements, this region extends to approximately 10mm from the interface signifying the effects of the diffusion bonding process. Since the hardness values measured in the regions near the interface are not significantly high to explain the effects of the diffusion bonding process, microstructure analysis was carried.

5.6.2 Microstructural analysis

For microstructure analysis, a series of micrographs in the regions near the interface and further away from the interface were captured using a Leica optical microscope and grain size measurements were carried out using linear intercept method as described in Chapter 3. Figure 5.32 shows that microstructure of 316H and Esshete1250 obtained from the regions further away from the interface of the diffusion bonded billet from which specimens with a

large speckle size were extracted. Both 316H and Esshete1250 have regular grain size distribution. The average measured grain sizes are 53±12µm and 79±15µm for 316H and Esshete1250, respectively. Figure 5.33 shows the 316H microstructure near the interface of the diffusion bonded billet from which specimens with a large speckle size were extracted. It can be seen that the grain size of 316H in the region near the interface were much larger compared to the ones obtained further from the interface. The average measured grain size of 316H in the regions near the interface is about 300±35µm which is about 6 times larger than the ones obtained in the regions further away from the interface. The significant increase in the grain size of 316H in the regions near the interface compared to regions further away from the interface explains why the local deformation near the interface is much higher compared to other regions, Figure 5.31. The presence of large grains in materials is associated with loss of strength and increased ductility hence the high local DIC measured strain in the regions near the interface of the DIC tensile test results from specimens with a large speckle size [23]. Considering Figure 5.31, the scatter in the measured strain and hardness in the regions near the interface could be due to the large size of grains in this region.

Since the diffusion bonding process was carried out at 1100^{o}C for an hour, it is inevitable that recrystallization would take place in austenitic stainless steels. However, the growth of large grains in the regions near the interface could be due to non-uniform slow cooling (high annealing temperature) of the billet which promotes grain growth [23].

Figure 5.34 shows micrographs of 316H from the diffusion bonded billet from which specimens with a small speckle size were extracted. Despite the difference in the region from which the two micrographs were extracted, it can be seen that the grain size distribution is homogeneous. The averaged measured grain size in the region near the interface is 46±10µm whereas for the region further away from the interface is 47±12µm. The homogeneity in the grain size distribution in the diffusion bonded billet (from which DIC tensile test specimens with a small speckle size were extracted) shows that the local mechanical properties of the billet were not significantly influenced by the bonding process. Hence the good correlation between the DIC measured strain and the elastic-plastic FE results, Figure 5.26 and 5.27. Therefore, further discussion and conclusions on the effects of specimen aspect ratio (thickness) on local mechanical properties measured by DIC will only be based on DIC tensile test results from specimens with small speckle pattern and elastic-plastic FE results.

5.7 DIC Creep testing of diffusion bonded specimens

As stated earlier, welds are composed of not only the base metal and the weld material but also the heat affected zone which is composed of a variety of microstructures depending on the welding technique and the materials being joined. When weldments are applied at high temperature and stress, the various constituents of the welds undergo varying levels of deformation resulting in varying stress fields in the regions surrounding the weld. This makes characterisation of creep properties of weldments challenging when convention methods, such as a two point contact extensometer or strain gauges, are applied.

With the emerging of digital image correlation and its successful application at room temperature to characterise the local tensile properties of cross-welds [7-9, 12], has led to its application at high temperature. A system developed by Sakanashi *et al* [24, 25] showed that DIC can be successfully applied to characterise local creep behaviour of cross-welds, making it one of the outstanding strain measurement technique for mechanical characterisation of welds. However, there are some fundamental factors pertaining to the use of 2D DIC to characterise creep behaviour of cross welds still need to be addressed. One of the factors to be addressed is the specimen geometry ideal for characterisation of local creep properties of cross-welds. For instance, it is know that the size (gauge length and aspect ratio) of the specimens applied in characterising the creep behaviour of monolithic specimens has a bearing on the creep properties measured. The effects of specimen geometry on local creep properties determined are even more profound when cross-weld specimens are used, as evidenced by the review carried by Parker *et al* [26].

In the case of 2D DIC, the specimen is required to have a rectangular cross-section, making it challenging to characterise local creep properties for cross-welds as the measured local strains across the weldment would depend on not only the interaction between the various mismatched weld constituents but also the specimen thickness. Therefore, the level of mismatch between adjacent materials as well as the specimen thickness would influence the constraint effects in the weaker material. Constrained deformation (multiaxial stress state) in the weaker material in the regions near the interface entails that the measured local creep properties in these regions are not the underlying creep properties of the material. Therefore, there is need to understand how the measured local creep properties in cross-welds using DIC are influenced by the specimen geometry and the magnitude of errors in the measured properties in regions near the interface between two adjacent materials.

In this section, diffusion bonded specimen which provides a simplified interface between two adjacent materials compared to cross-welds were used to study the effects of specimen geometry and magnitude of errors in the measured local mechanical properties. As stated in the introduction of this chapter, the use of diffusion bonded specimens eliminates the complex constraint effects which develop in cross-welds when subjected to uniaxial loading.

5.7.1 Experimental Setup

The specimens used were produced by diffusion bonding of 316H stainless steel to Eshete1250 stainless steel as describe in Chapter 3. All the creep tests in this section were carried out at an applied nominal stress of 180MPa and temperature of 575^{o}C. Tests specimens with varying thickness (that is 1mm, 3mm and 5mm thick) were used. The specimens used for DIC-creep testing were similar to the ones used in DIC-tensile tests. However for DIC-creep testing the specimens had threaded ends to ensure good alignment of the specimen during creep testing. This meant that only one creep test specimen was extracted from each diffusion bonded billet. Prior to measurement of specimen dimensions, the specimens were dipped in 60% nitric acid and then washed in water to get rid of any fine EDM particles on the surface of the specimens. This procedure also revealed the diffusion bonding interface of the materials. Upon application of the speckle pattern on the surface of the specimen, the bond interface was then marked by a black paint dot. The dot was located at the edge of the width section of the specimen so that it does not interfere with the DIC strain measurements.

As described in Chapter 3, each specimen was placed in the middle of the furnace and aligned to give the required field of view of the gauge section in the camera. In all the tests, the 316H section of the diffusion bonded specimen were attached to the top pull rod whereas the Esshete1250 section were attached to the bottom pull rod. Two Type R thermocouples were attached at the top and bottom sections of the specimen. Temperature variation between the top and bottom thermocouples were kept within 2^{o}C, in accordance with the ASTM-E139 standard which requires that temperature variation across the specimen gauge section be kept within 2^{o}C [27]. All the tests were carried using an initial applied nominal stress of 180MPa. Specimens were preheated up to 12 hours to ensure temperature stability in the furnace prior to load application. For quality DIC images, the furnace properly insulated and the specimen surface was illuminated using a fibre optic cable attached to the flash of the digital camera. In

the first 24 hours of the test, images were acquired at 20 minutes intervals and thereafter the acquisition rate was set to an image per hour until the test was stopped.

5.7.2 DIC creep test results

The acquired images were processed as described in Chapter 3 to extract multiple creep curves along the specimen gauge length. Only results from the 3mm and 1mm thick specimens are presented. The DIC measured creep strains plotted were smoothed by moving average of 5 points to reduce scatted in the measured data.

5.7.2.1 Evolution of local creep strain as a function of gauge length

Figure 5.35, shows the DIC strain map extracted at 1000 hours from the 3mm thick specimen, showing the strain distribution along the gauge length. The strain distribution shows that Esshete1250 is creep hard thus experiencing lower strains compared to 316H. In 316H, the creep strain is uniformly distributed in the regions further from the interface however in the regions near the interface the distribution is non-uniform. This is expected as deformation in the regions near the interface is highly influenced by the adjacent creep hard material. Figure 5.36 shows the evolution of longitudinal and transverse strain with time along the gauge length extracted from the 3mm thick specimen. It can be seen that creep deformation is concentrated in 316H compared to Essshtet1250. For 316H, in the regions near the interface, the longitudinal strains are much lower and increase with distance away from the interface. The peak longitudinal creep strain of about 1% occurs in the region between 2.5mm and 6mm from the interface. Beyond 6mm from the interface, the measured longitudinal creep strains are uniform signifying that the influence of the adjacent creep strong Esshete1250 only extends up to about 6mm. The evolution of transverse creep strain with time as a function of gauge length is similar to the longitude ones, Figure 5.36(b).

Figure 5.37 shows the evolution of longitudinal creep strain as a function of gauge length extracted from the 1mm thick specimen. The distributions of longitudinal creep strain along the gauge length are similar to the ones extracted from 3mm thick specimen. There is considerable scatter in the measured creep strain from the 1mm thick specimen compared to the ones obtained from the 3mm one. Figure 5.38 shows the plots of temperature as function of time for both the 3mm and 1mm thick specimen. The temperature controls for the two tests were within the recommend range $\pm 2^{o}C$ according to the ASTM standard [27]. The high scatter in the measured creep strain in the 1mm thick specimen could be due to improper

sealing of the furnace window which has subtle effects on the image quality as highlighted by Sakanashi *et al* [25]. Figure 5.39 compares the plot of longitudinal creep strain as a function of gauge length between the 3mm and 1mm thick specimen at 250 and 1000 hours. Although the distribution of the longitudinal strains are almost similar at both 250 and 1000 hours, it can be seen that in the 1mm thick specimen, the region within which the peak strain occur extends from 2.5mm to about 9mm. Whereas in the 3mm thick specimen this region only extends up 6.5mm. The reason for the difference in the size of the regions within which peak strains occur could be due to the effects of the diffusion bonding process as shown in section 5.6.2.

5.7.2.2 Local creep deformation

Figure 5.40 (a) and (b) shows a plot of 316H longitudinal and transverse creep strain curves from a 3mm thick specimen extracted at varying distance from the interface. The accumulated local creep strain extracted at a distance of 1mm from the interface is relatively less compared to other regions away from the interface. This indicates that at this distance (1mm from the interface), the local deformation of 316H is highly influenced by the adjacent creep hard Esshete1250. Constrained deformation in the regions near the interface results in local strain concentration at about 4.5mm from the interface as shown in Figure 5.36. Therefore, the creep strain curve extracted at 5mm from the interface in 316H shows higher secondary creep rate compared to the curves extracted at 1mm from the interface. Away from the interface, deformation is not influenced by the adjacent creep hard Esshete1250, therefore the creep strain is uniformly distributed as can be seen in the similarity between the local creep strain curves extracted from 10mm and 15mm from the interface. It is interesting to note that all the creep strain curves, except the one extracted at 1mm from the interface, exhibit similar primary creep rates and the difference only occurs in the secondary creep rates. The traverse creep strain curves exhibit similar trends as the longitudinal creep strains, Figure 5.40(b). However, there is more scatter in the measured transverse creep strain curves due to low signal to noise ratio.

Local longitudinal and transverse creep strain curves extracted from Esshete1250 at varying distance from the interface in the 3mm thick specimen are given in Figure 5.41. In Esshete1250, the local creep strains curves extracted in the regions near the interface has higher creep rates compared to the ones extracted in the regions away from the interface. The

creep strains in Esshete1250 are relatively small compared to the ones obtained from 316H which is expected considering that Esshete1250 is creep hard.

Figure 5.42 shows 316H longitudinal local creep strain curves extracted at varying distance from the interface from a 1mm thick specimen. Due to high scatter in the measured data from this specimen, the creep strain curves given in Figure 5.42 were constructed by fitting the RCC-MR primary creep model to the experimental data extracted at varying distance from the interface. The local creep strain curves in Figure 5.42 have similar trajectory to the ones extracted from the 3mm thick in Figure 5.40. Figure 5.43 compares the local creep strain curves extracted from the 3mm and 1mm thick specimens at similar distance from the interface. It can be clear seen that the creep curves extracted from the 1mm thick specimen exhibit higher creep rates compared to the ones from the 3mm thick specimen. Since the two creep tests were carried out under similar conditions (load and temperature), the significant difference in the creep rates suggests that the underlying material properties of the two test specimens were different.

As discussed in section 5.6.2, the difference in the creep rates can be ascribed to subtle difference in microstructure induced by the diffusion bonding process, resulting in different mechanical behaviour of diffusion bonded billets. Although there is a marginal difference in the local creep strain rates and the size of the region within which peak strains occur, the local creep strain curves from both the 1mm and 3mm thick specimen shows lower deformation in the material near the interface compared to other regions away from the interface. This signifies that measurement of local creep properties in the material adjacent to a creep strong material may give rise to errors in the measured properties as the deformation the weaker material would be constrained by the adjacent stronger material. The following section considers the length scale within which errors would occur in the weaker material adjacent to the creep strong one.

5.7.2.3 Errors in measured local creep properties

Errors in the measured 316H local creep properties were determined by fitting the RCC-MR primary creep model (equivalent to the Norton-Bailey model) to the creep strain curves extracted from a 3mm thick specimen at varying distance from the interface. The RCC-MR primary creep model is given in Equation 2.5. To compute the errors, the RCC-MR model coefficients (C_1, C_2 and n_1) obtained from 10mm, 12.5 and 15mm were averaged and used as 316H material properties. The averaged model coefficients were then compared to the ones

obtained at varying distance from the interface to compute the percent deviation from the 316H material properties. The %error was computed using Equation 5.1.

Figure 5.44 shows the error distribution of the RCC-MR primary creep model parameters as a function of distance from the interface. Only the errors in the stress exponent, n_1 and time exponent C_2 are plotted. Both the time and stress exponent errors are higher in the regions near the interface and reduce to almost 0% at about 2.5mm from the interface. Beyond 2.5mm, there is a gradual increase in the measured errors up to about 5mm from the interface where the peak errors occur. It can be seen that the region within which errors in the measured local creep properties exist extends to about 6mm from the interface for a 3mm thick specimen.

Due to high scatter in the local creep curves extracted from the 1mm thick specimen, errors in the measured local creep properties were not computed for this specimen. However, considering that constraint effects due to the adjacent stronger material reduce with specimen thickness as indicated by room temperature DIC tensile test and FE results, it is expected that the region within which errors in the measured local creep properties exit would be smaller for a 1mm thick specimen compared to the ones obtained from the 3mm thick specimen. Therefore, it can be concluded that a 1mm thick specimen is more suitable for determination of local creep properties of mismatched materials compared to thicker specimens.

5.8 Conclusions

The study of the effects of specimen geometry (aspect ratio) on local deformation and the measured local mechanical properties of dissimilar material joints was carried out using FE modelling and DIC tensile and creep testing. Simplified joints, plane interface for FE models and diffusion bonded interface for DIC tensile and creep testing, were used in this study avoid the complex effects of material interaction between the various constituents of weld which occur when cross-weld specimens are subjected to using uniaxial loading. The findings from the current study highlight the applicability of 2D DIC measurements on local mechanical properties of mismatched materials and the following conclusions have been derived;

1. The strains extracted from the surface of the FE models showed that surface strains are close to plane stress condition even for a 6mm thick model. This implies that the measured surface strain from 2D DIC can be considered to be plane stress.
2. The local strain distribution in the regions near the interface between two mismatched materials is non-uniform and the length of the crossover point gives an estimate of the region within which errors in the measured local mechanical properties at any given thickness would occur.
3. Results from elastic FE modelling shows that the change in specimen geometry only affects the size of the region from the interface within which errors in the measured local mechanical properties would occur when these properties are obtained from the plot of the global stress as function of local strain. Whereas the magnitude of the errors in the measured local mechanical properties (from plot of global stress as a function of local strain) in the regions near the interface are dependent of the mismatch between the adjacent materials.
4. From both the elastic-plastic FE and DIC measured local stress-strain curves and the length scale within which errors in the measured local properties occurs when mechanical properties are obtained from the plot of the global stress as a function of local strain, it can be concluded that a thinner (1mm thick or less) specimen should be used to extract local mechanical properties from specimens with varying material properties such as welds. It should be noted that the advantage of using a 1mm or less thick specimen to obtain DIC measured local mechanical properties from plots of global stress as a function of local strain, reduces the region from the interface within which the errors in the measured local mechanical properties occur. Therefore, intrinsic properties of the material in the regions near the interface would only be obtained when these properties are extracted from a distance not less than 1mm from the interface.

5. Experimental study of the effects of specimen geometry on measured local mechanical properties extracted from a plot of global stress as function of local DIC measured strain using diffusion bonded specimens shows that diffusion bonding process had an effect on the local microstructure an hence the local mechanical properties. However, the correlation between the elastic-plastic FE strains and DIC measured strains from specimens with small speckle size indicates that these test results were not influenced by the diffusion bonding process.

6. The error distribution in the creep properties extracted in the regions near the interface shows the sensitivity of the creep process to change in local stress due to constraining effects of the adjacent creep hard material. Although the errors were measured from a 3mm thick specimen, the use of a 1mm or less thick specimen would reduce the length scale of the region from the interface within which errors in the measured local properties would occur. This would require further investigation, especially in crossweld specimens.

FIGURES

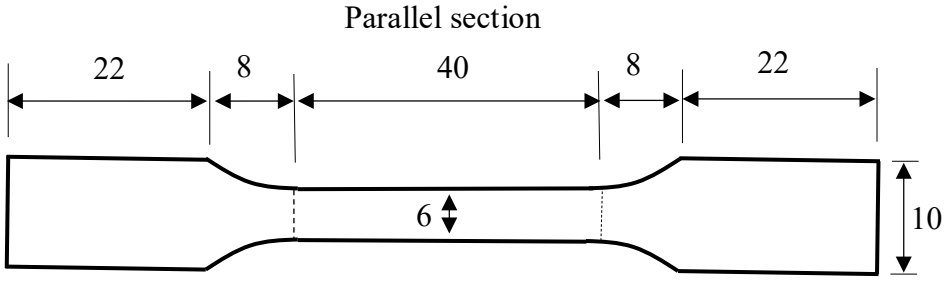

Fig. 5.1 Schematic drawing of the FE model, all dimensions are in mm. The model thicknesses of 1mm, 3mm and 6mm were used. The dimensions are based on the specimen design used for tensile testing of dissimilar metal diffusion bonded samples.

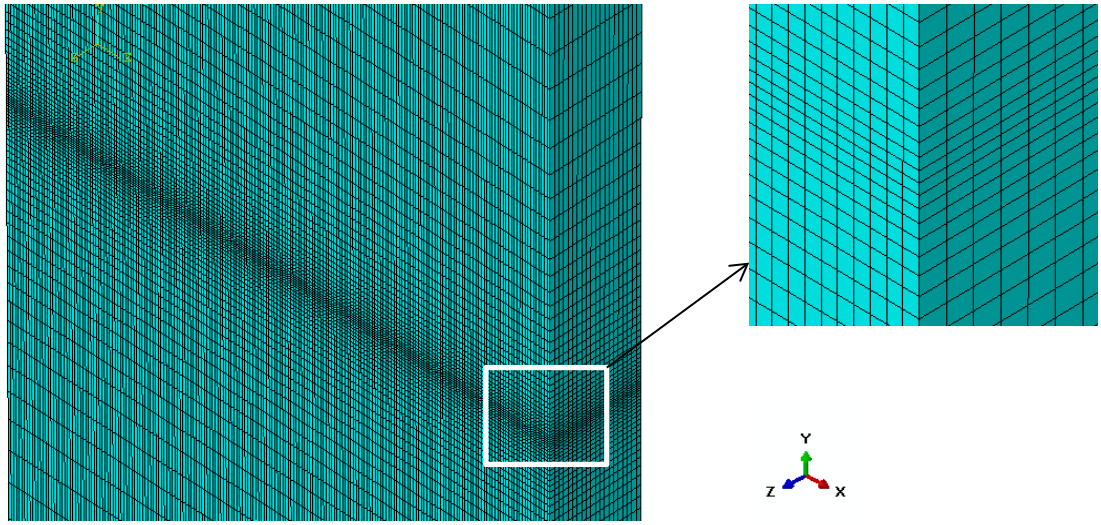

Figure 5.2 Fine mesh of the FE model elements around the interface.

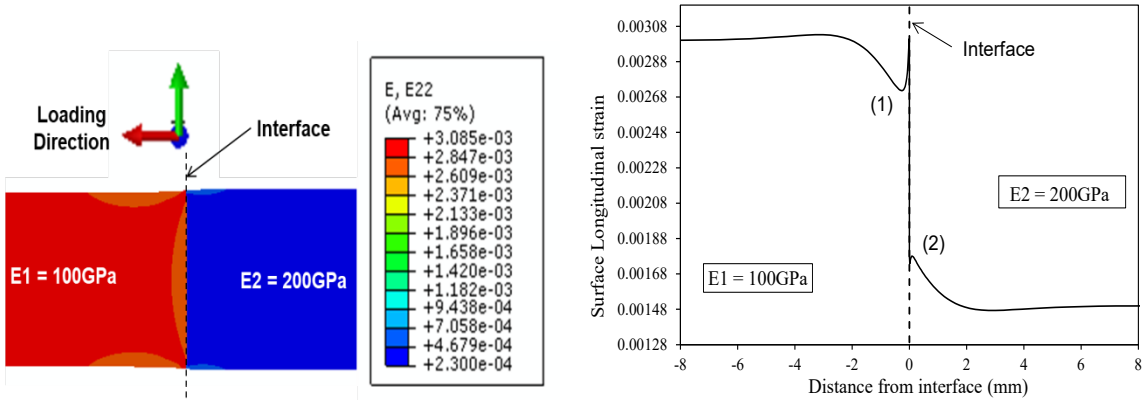

(a) (b)

Figure 5.3 (a) FE surface strain distribution in the vicinity of an idealised sharp dissimilar material interface from a 1mm thick model at 300MPa applied stress (b) Longitudinal elastic strain distribution across the interface extracted from (a) along the centre-line of the model gauge length.

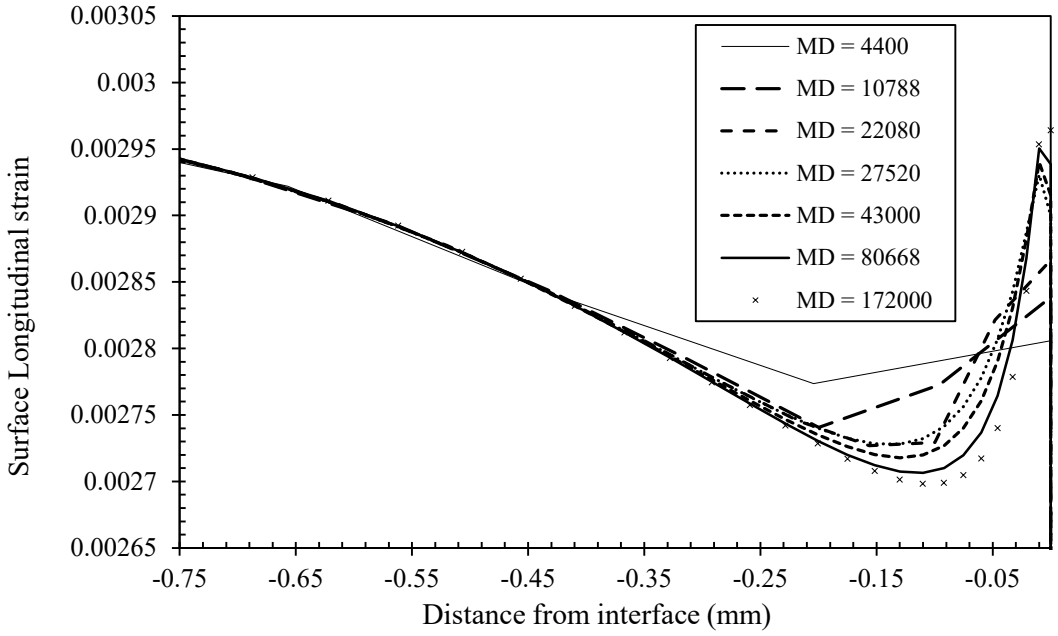

(a)

Figure 5.4(a) Effect of mesh density on longitudinal surface elastic strain in the vicinity of the interface around region (1) in Figure 5.3(b) at 300MPa applied stress.

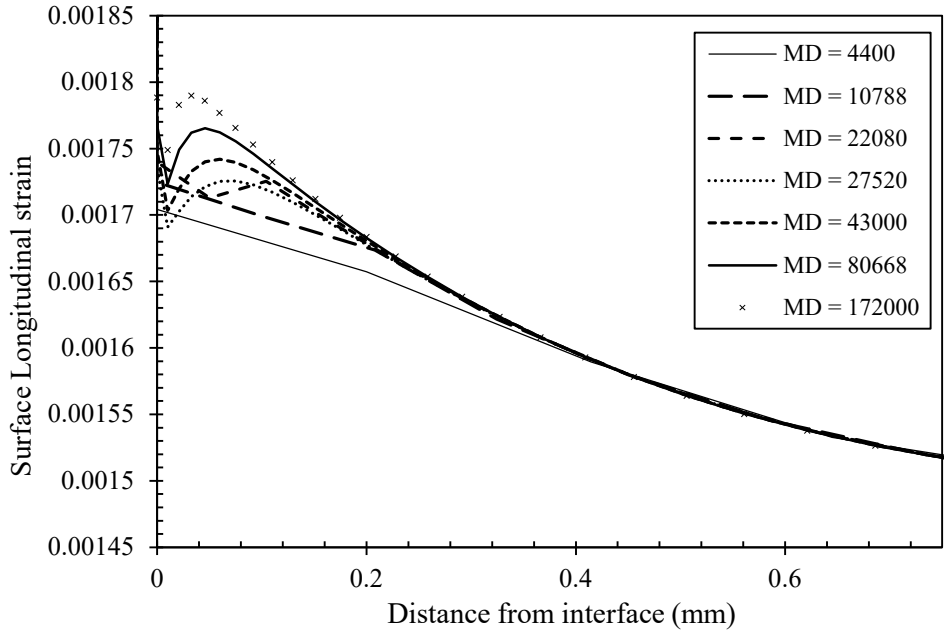

(b)

Figure 5.4(b) Effect of mesh density on the longitudinal surface elastic strain in the vicinity of the interface around region (2) in Figure 5.3(b) at 300MPa applied stress.

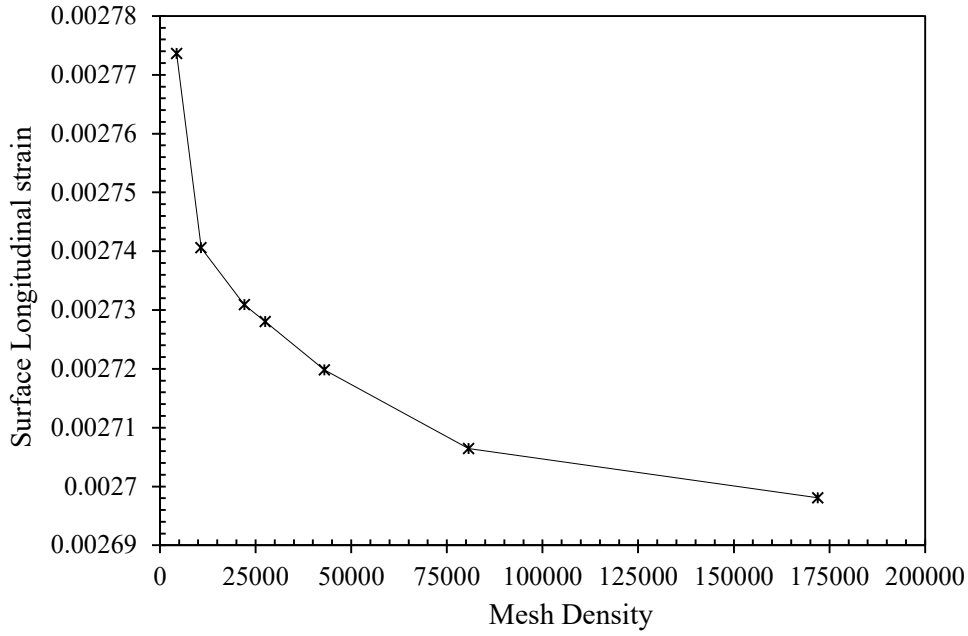

(a)

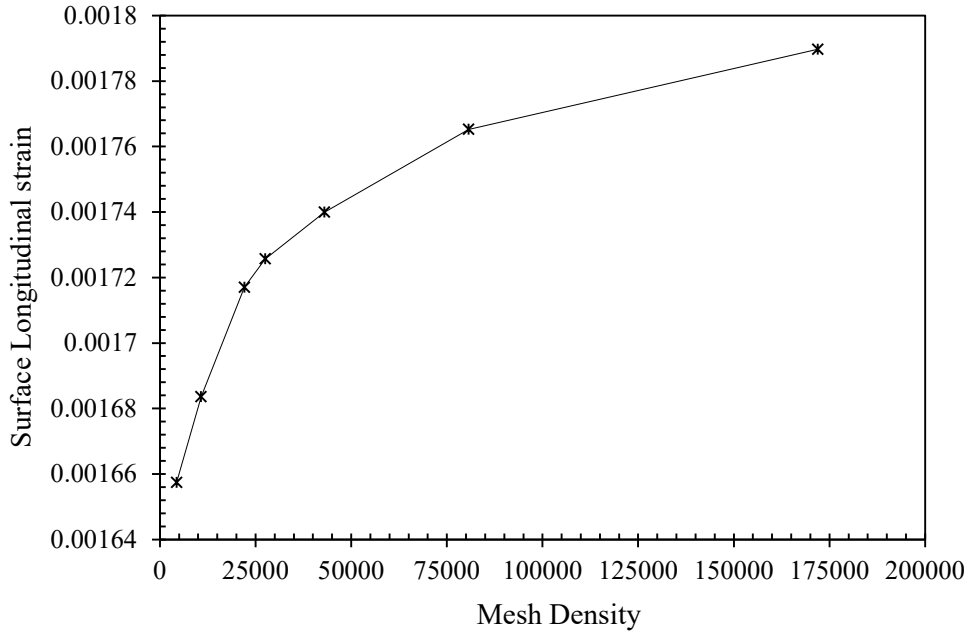

(b)

Figure 5.5 Longitudinal surface strain plotted as a function of mesh density (a) minimum strain around region (1), (b) maximum strain around region (2) in Figure 5.3(b).

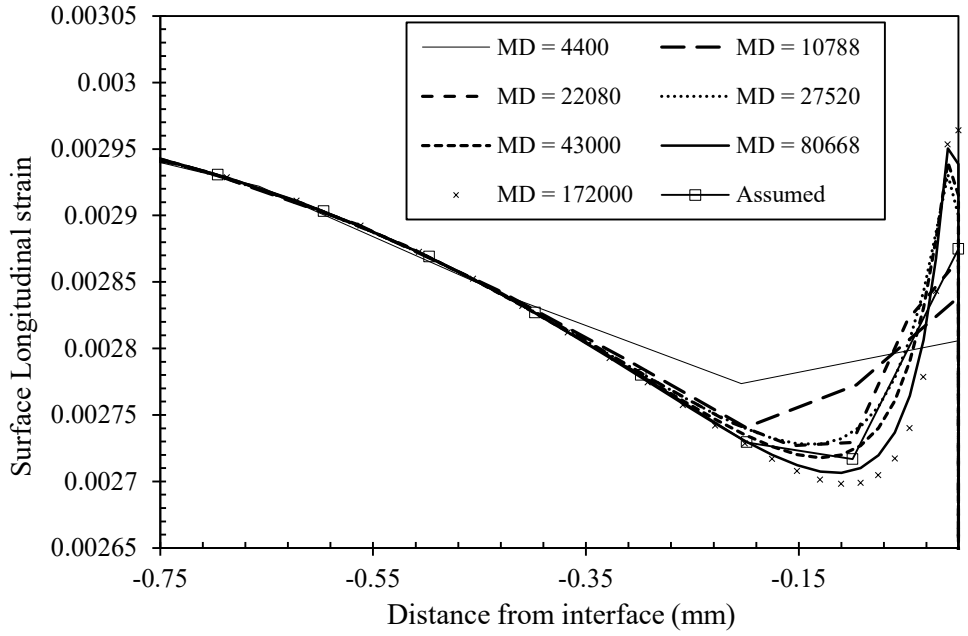

Figure 5.6 Comparison between the chosen mesh size (smallest element size of 0.1mm) and the mesh sensitivity results given in Figure 5.3(b).

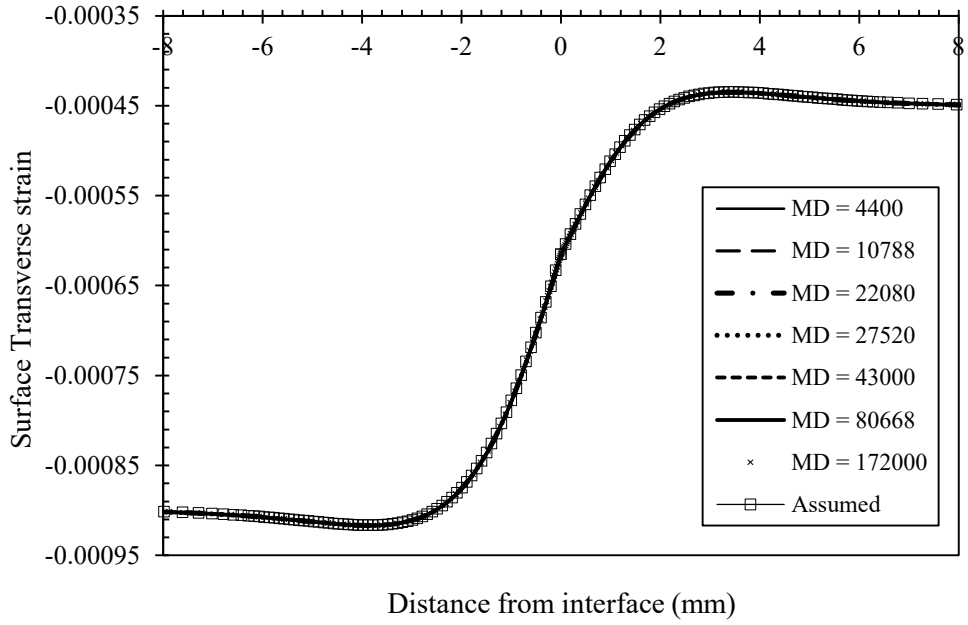

Figure 5.7 Comparison between the surface transverse strains obtained from the chosen mesh size of 0.1mm and the one obtained from a finer mesh near the interface.

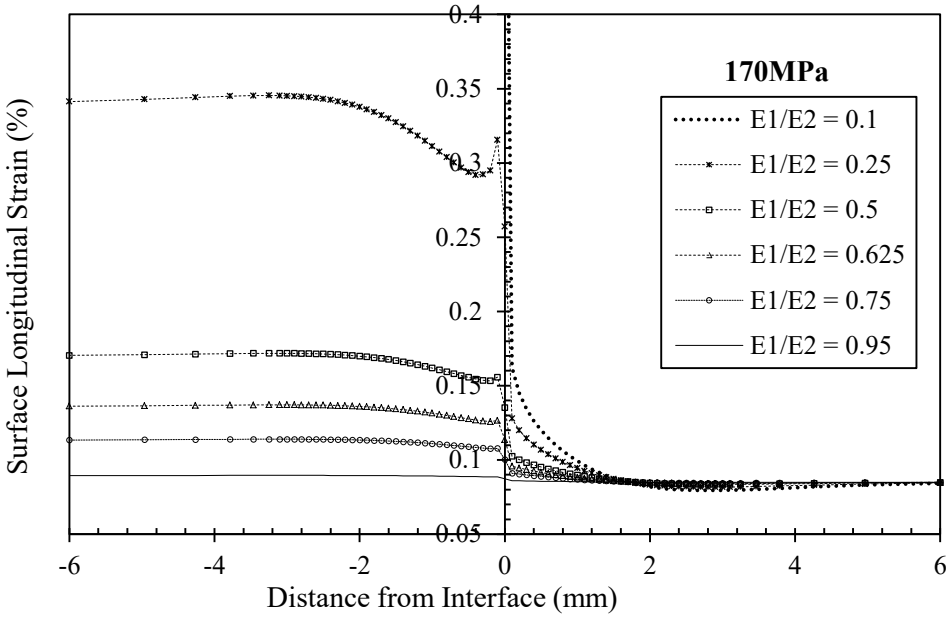

Figure 5.8 Surface longitudinal elastic strain distributions as a function of distance from the interface at different E_1/E_2 ratios, from a 3mm thick model subjected to a stress of 170MPa.

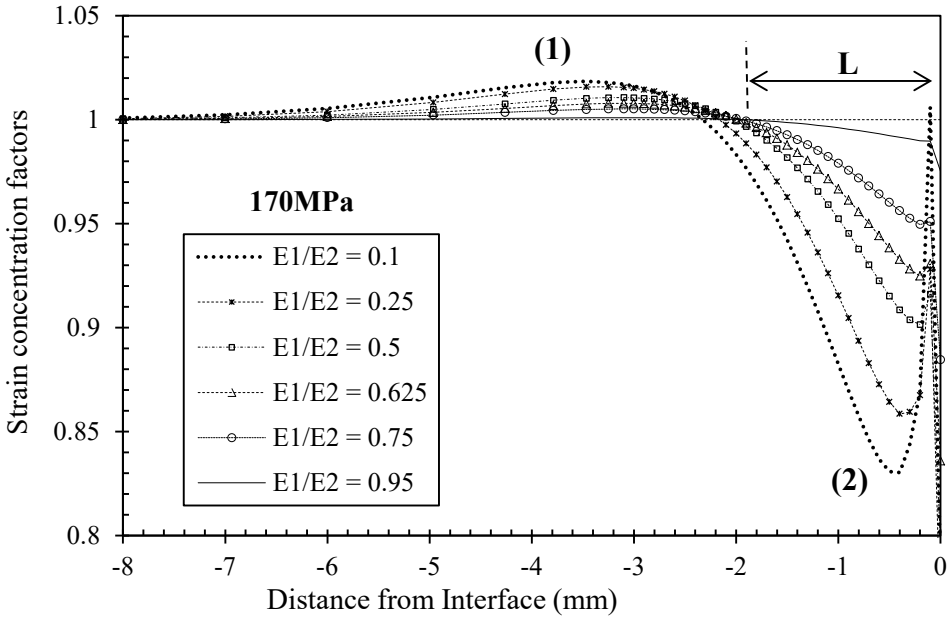

Figure 5.9 Surface longitudinal elastic strain distributions as a function of distance from the interface at different E_1/E_2 ratios, from a 3mm thick model.

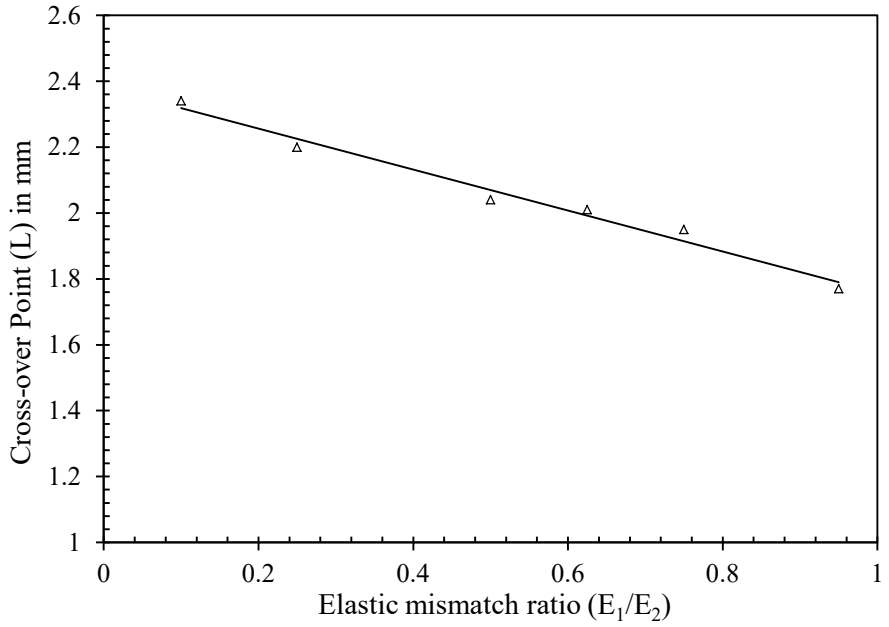

Figure 5.10 Plot of cross-over point (L) in Figure 5.9 as a function of the elastic mismatch ratio.

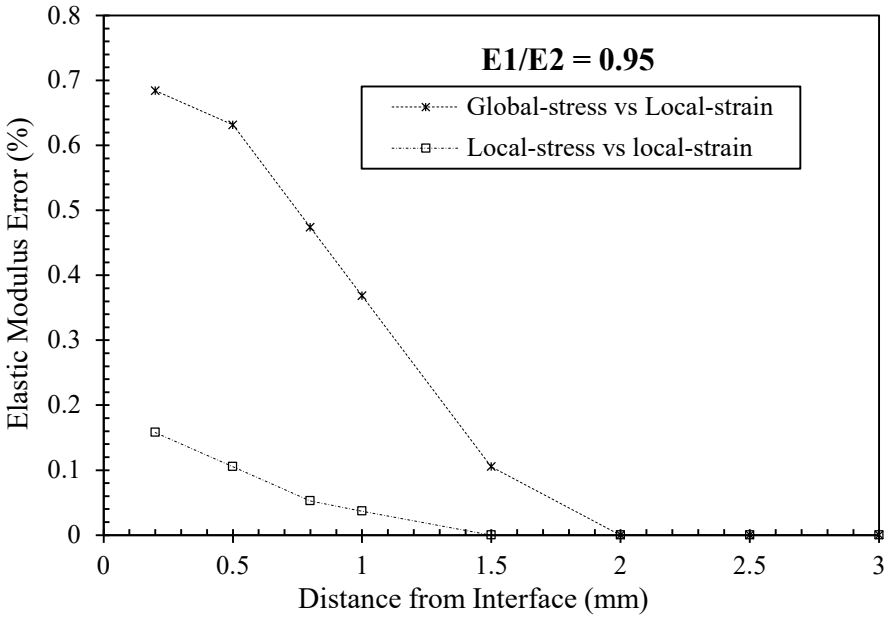

Figure 5.11 Comparison between the errors obtained when the local elastic modulus is determined from the linear fit to the plot of the global-stress against the local-strain, and when its determined from the linear fit to the plot of the local-stress against the local-strain, for a case of elastic mismatch ratio of E1/E2 = 0.95 for a 3mm thick model.

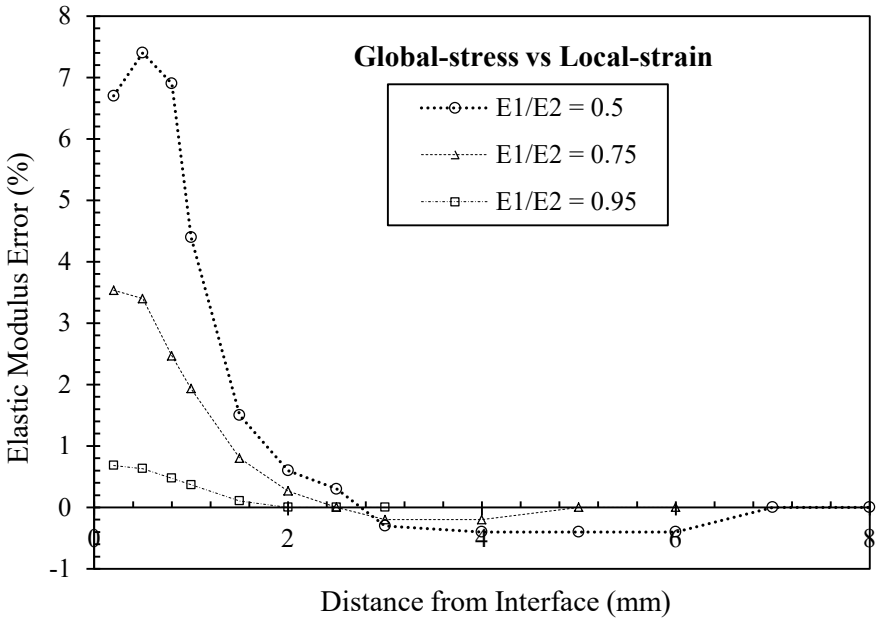

Figure 5.12 Effect of change in elastic mismatch on the errors in the determined 'local elastic moduli' from linear fit to the plot of the global-stress as a function of local-strain for a 3mm thick model.

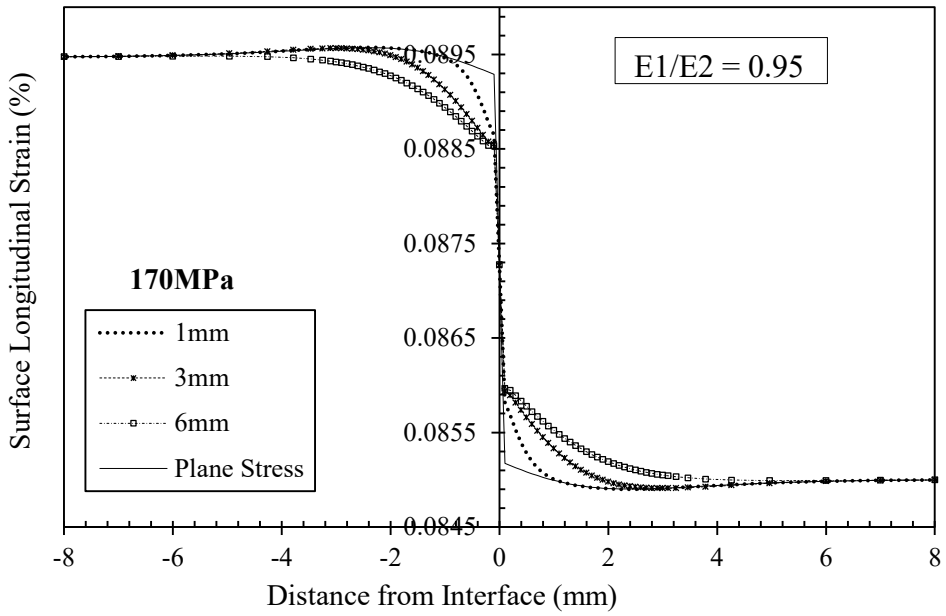

Figure 5.13 Strain distribution as function of distance from the interface, extracted from the 1mm, 3mm and 6mm thick models with elastic mismatch ratio of 0.95 at 170MPa applied stress

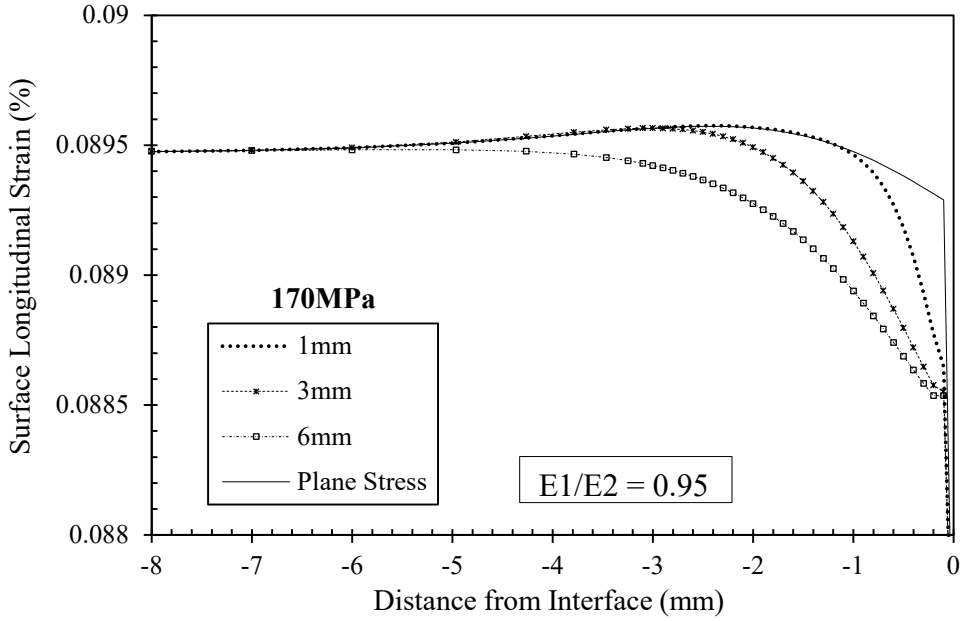

(a)

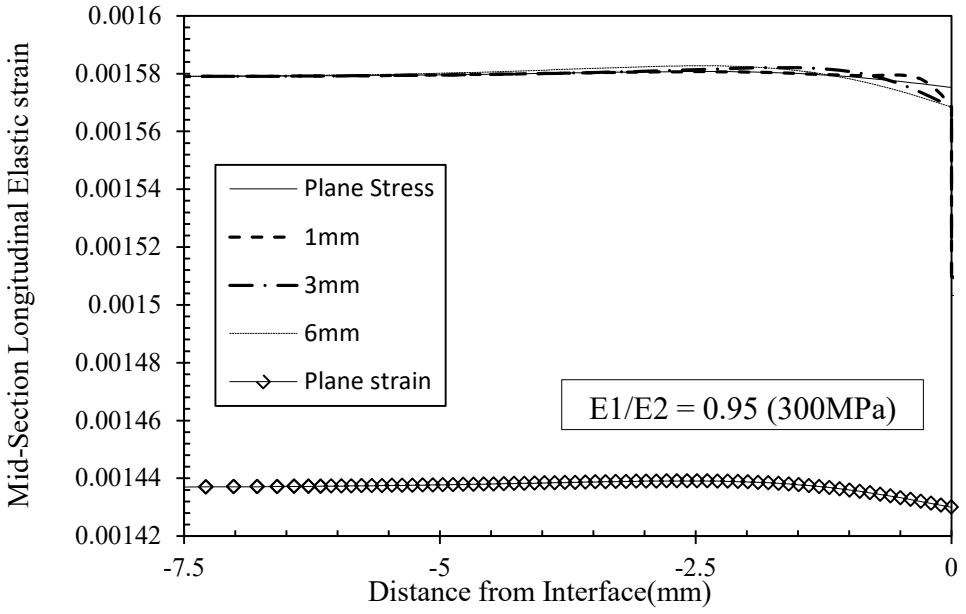

(b)

Figure 5.14 (a) Surface, and (b) mid-section strain distributions in the weaker material plotted as a function of distance from the interface at a $E_1/E_2 = 0.95$ and an applied stress of 170MPa

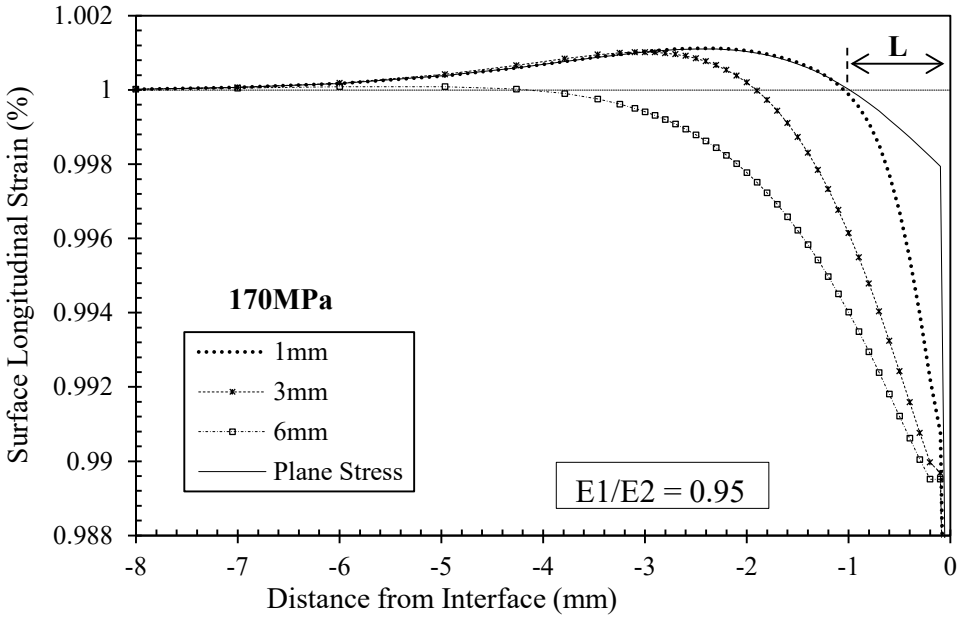

Figure 5.15 Normalised strain distributions in the weaker material plotted as a function of distance from the interface at 170MPa applied stress for E1/E2 = 0.95.

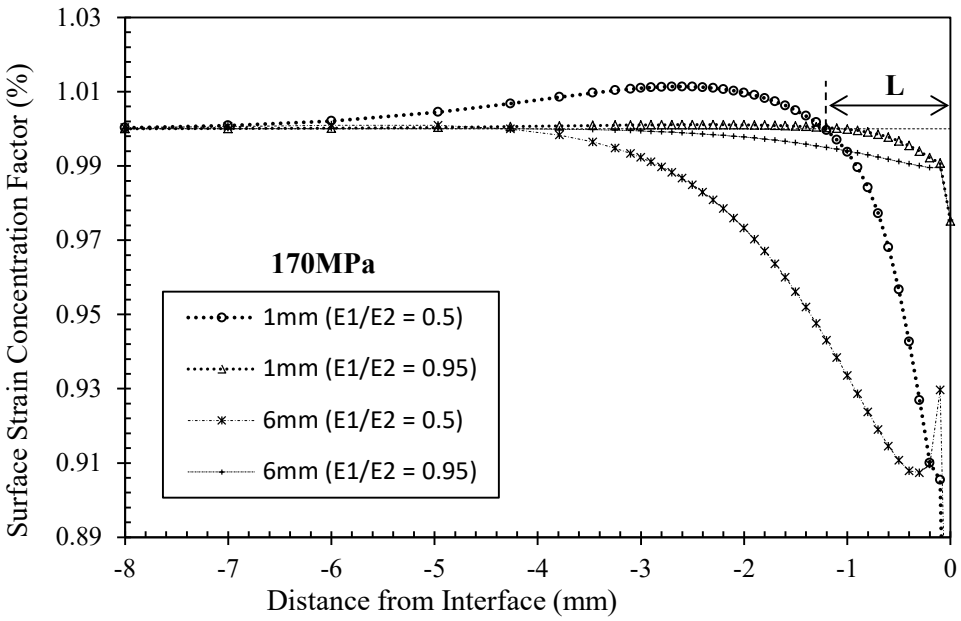

Figure 5.16 Comparison of the normalised strain distributions for material mismatches E1/E2 = 0.5 and E1/E2 = 0.9,5 for 1mm and 6mm model thicknesses at a stress of 170MPa.

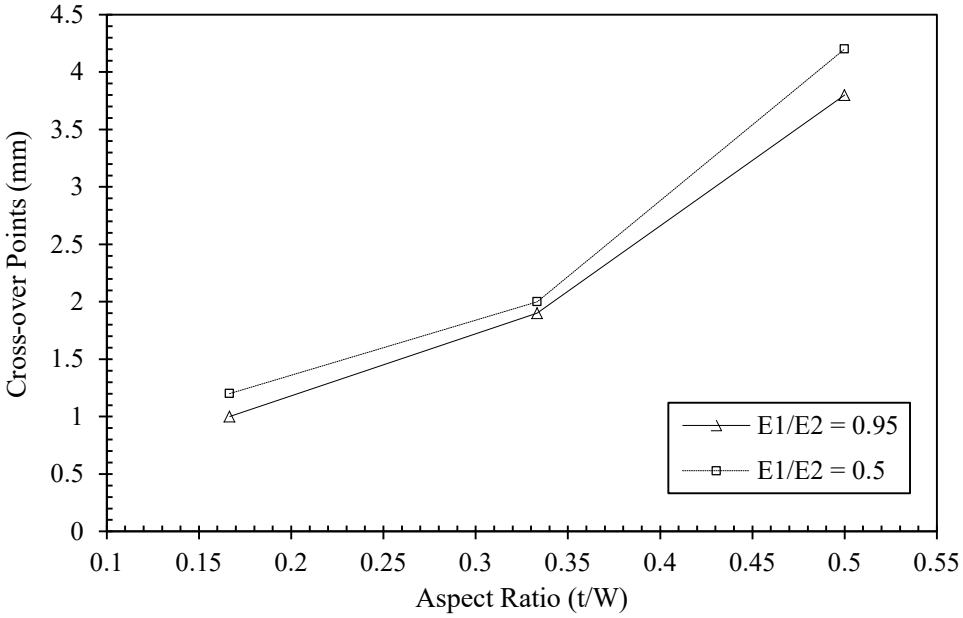

Figure 5.17 Effects of change in constraint on the cross-over points in the region near the interface.

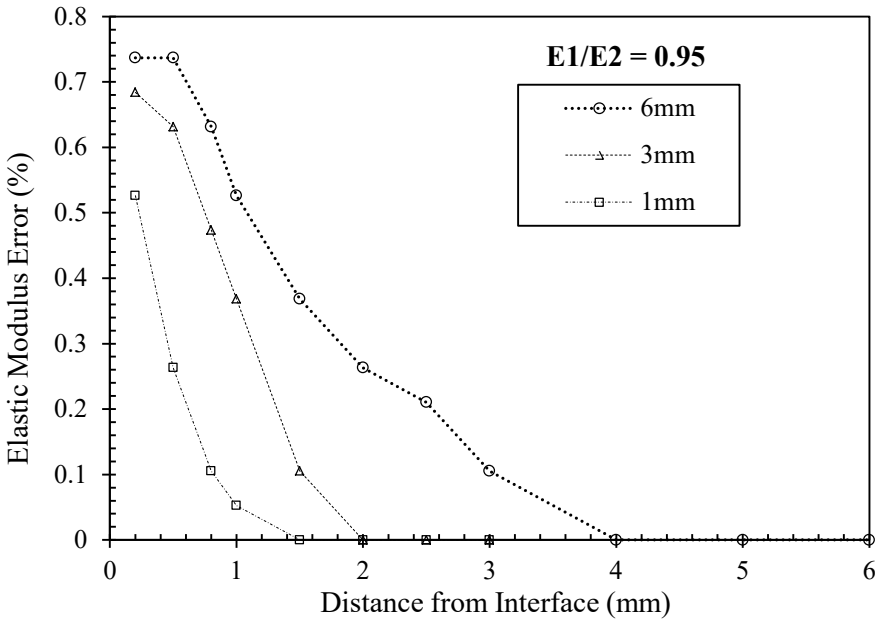

(a)

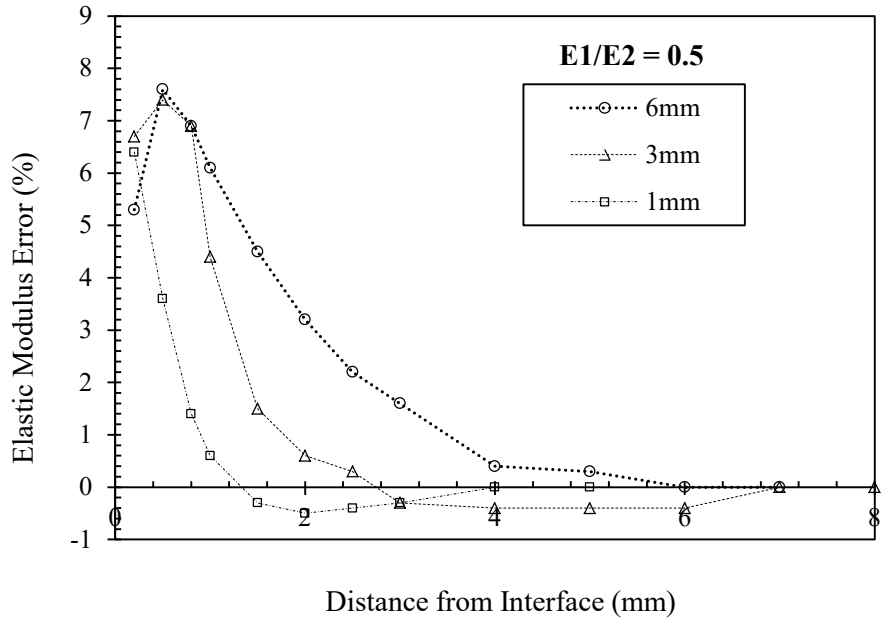

(b)

Figure 5.18 Effects of change in specimen geometry on the errors in the determined 'local elastic moduli' from linear fit to the plot of the global-stress as a function of local-strain for elastic mismatch ratios of (a) E1/E2 = 0.95 and (b) E1/E2 = 0.5.

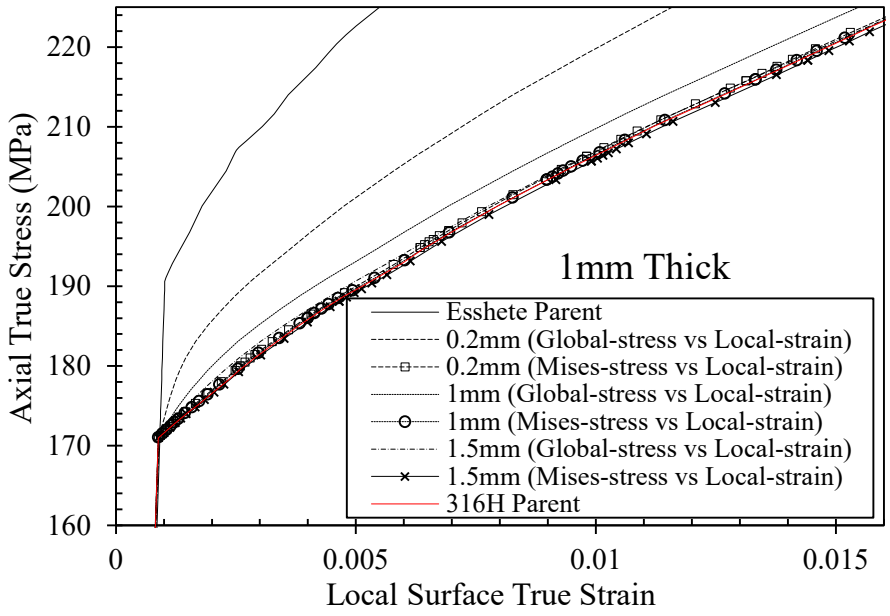

(a)

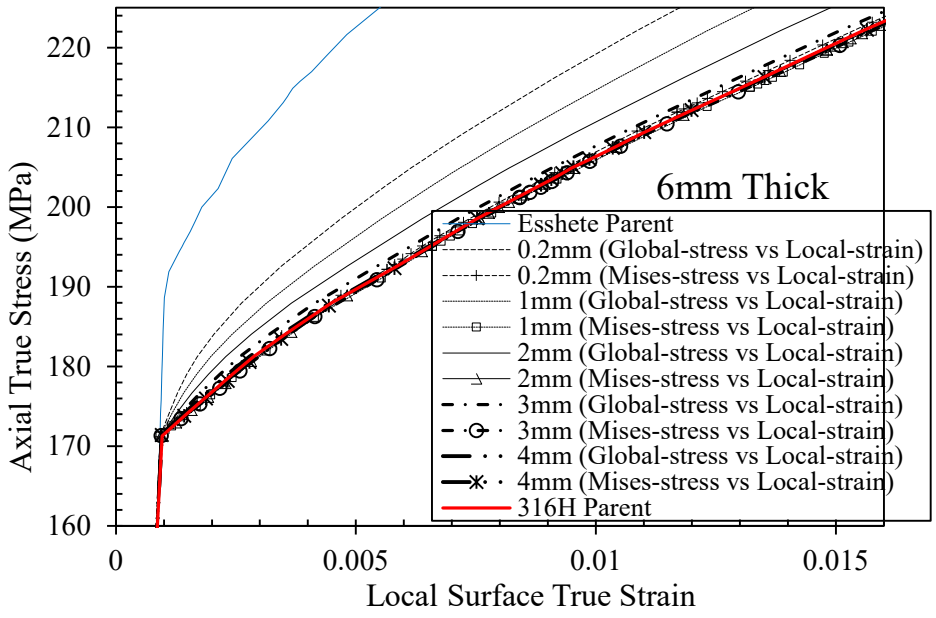

(b)

Figure 5.19 Comparison of the global-stress/local-strain curves to the local von Mises stress plotted against the local strain at varying distance from the interface for the (a) 1mm thick model, and (b) 6mm thick model.

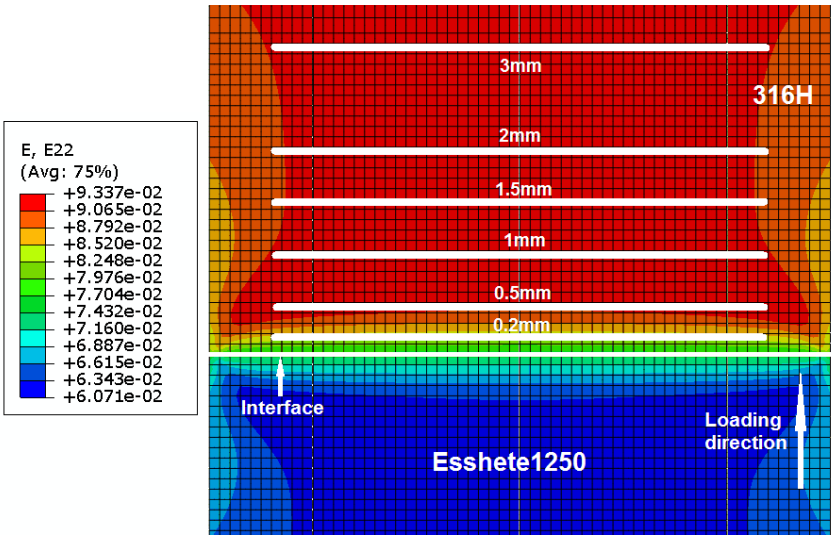

Figure 5.20 1mm thick model surface strain map showing regions from the interface where surface local strain were extracted. The white lines highlight elements which were used for computing the local axial strain.

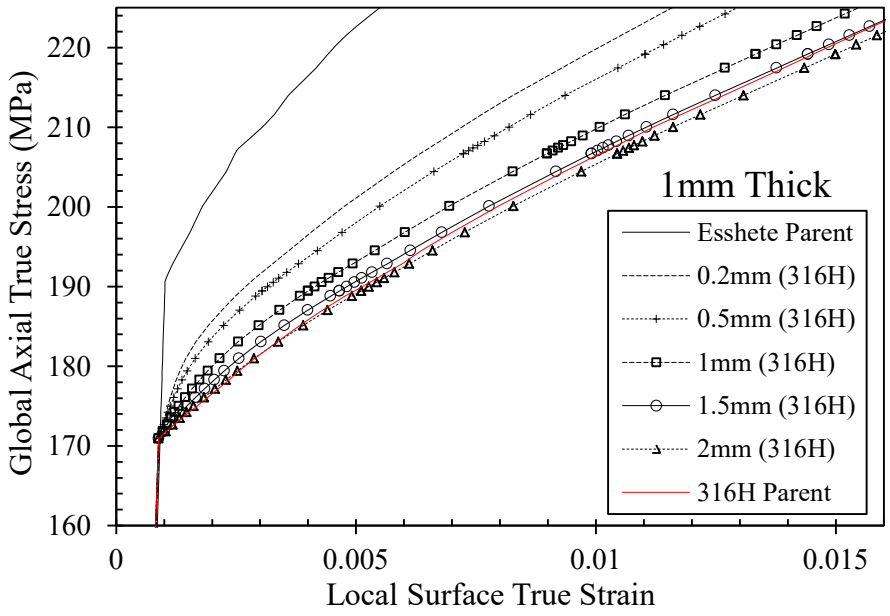
1mm Thick
Esshete Parent
0.2mm (316H)
0.5mm (316H)
1mm (316H)
1.5mm (316H)
2mm (316H)
316H Parent
Global Axial True Stress (MPa)
Local Surface True Strain
160
170
180
190
200
210
220
0
0.005
0.01
0.015

(a)

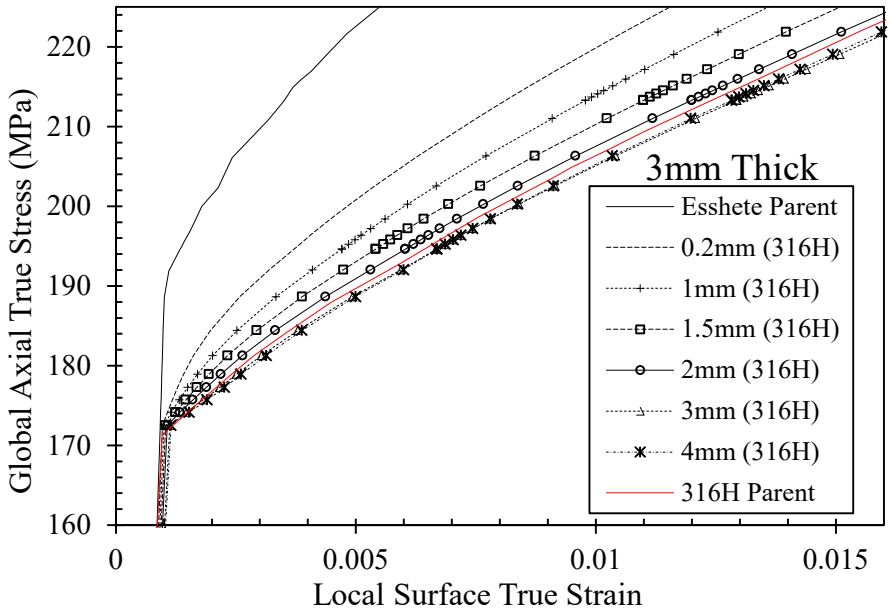
3mm Thick
Esshete Parent
0.2mm (316H)
1mm (316H)
1.5mm (316H)
2mm (316H)
3mm (316H)
4mm (316H)
316H Parent
Global Axial True Stress (MPa)
Local Surface True Strain
160
170
180
190
200
210
220
0
0.005
0.01
0.015

(b)

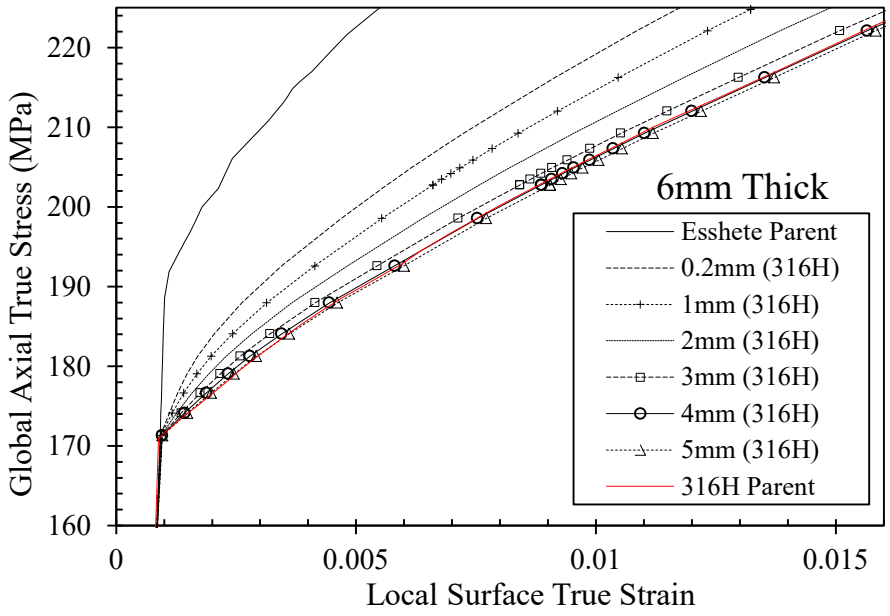

(c)

Figure 5.21 Comparison of the global-stress/local-strain curves extracted at varying distance from the interface to the FE model input stress-strain curves (a) 1mm thick model (b) 3mm thick model, and (c) 6mm thick model.

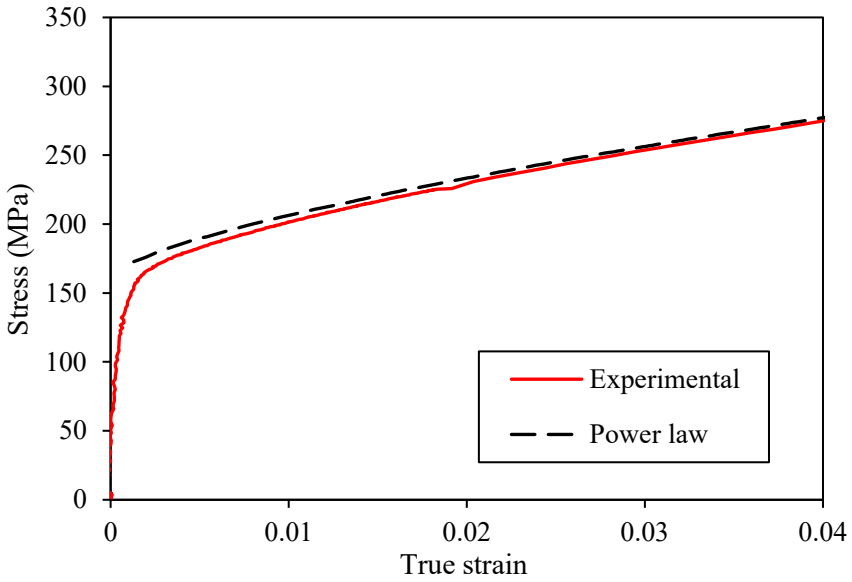

Figure 5.22 Comparison between the experimentally determined stress-strain curve for 316H and the one predicted by the power law given in Equation 5.2.

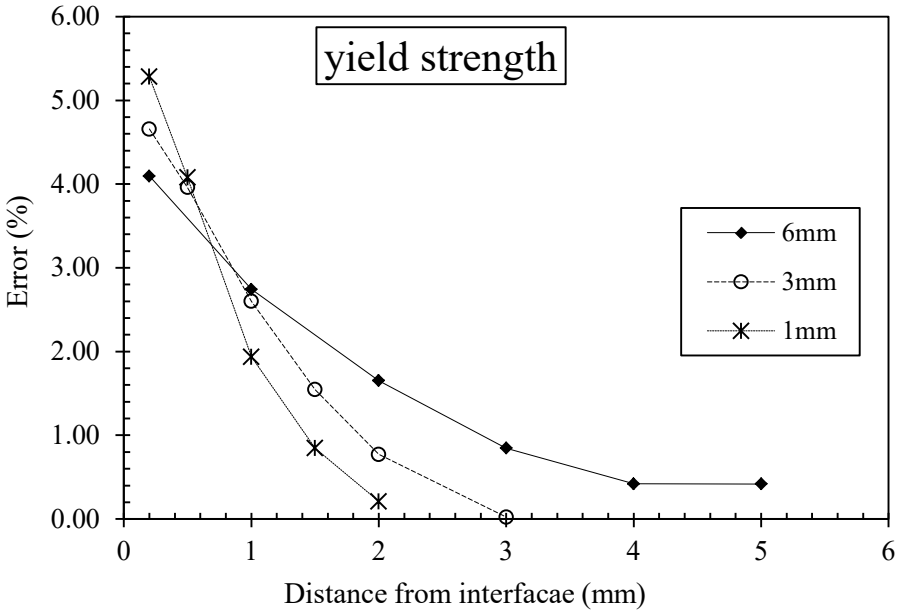

(a)

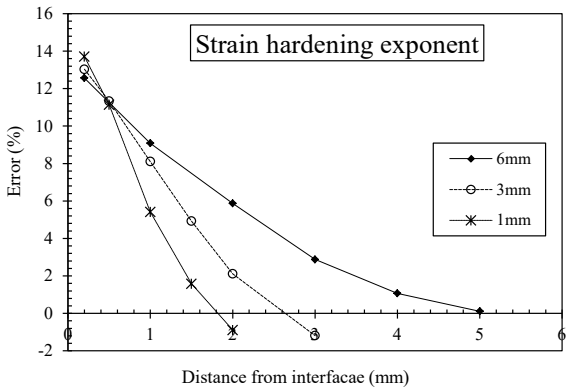

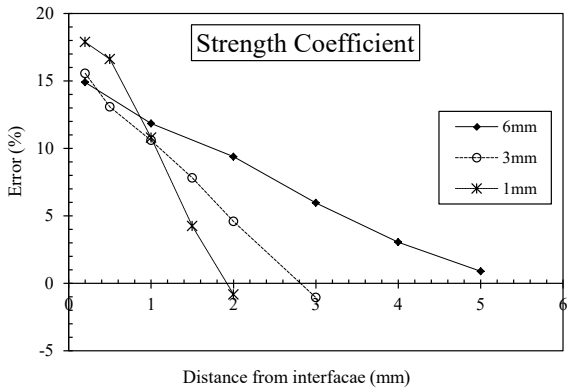

(b) (c)

Figure 5.23 Errors in the measured local mechanical properties plotted as function of distance from the interface (a) 0.1% yield stress (b) strain hardening exponent, and (c) strength coefficient.

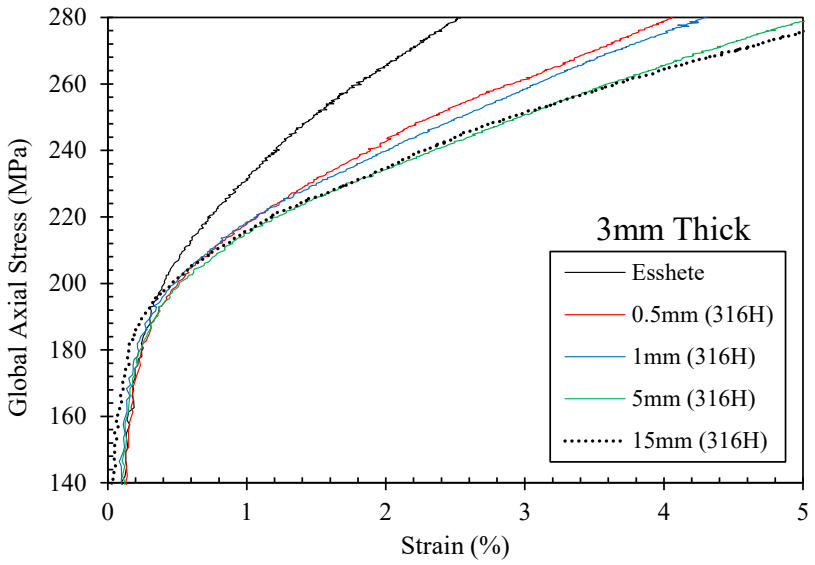

(a)

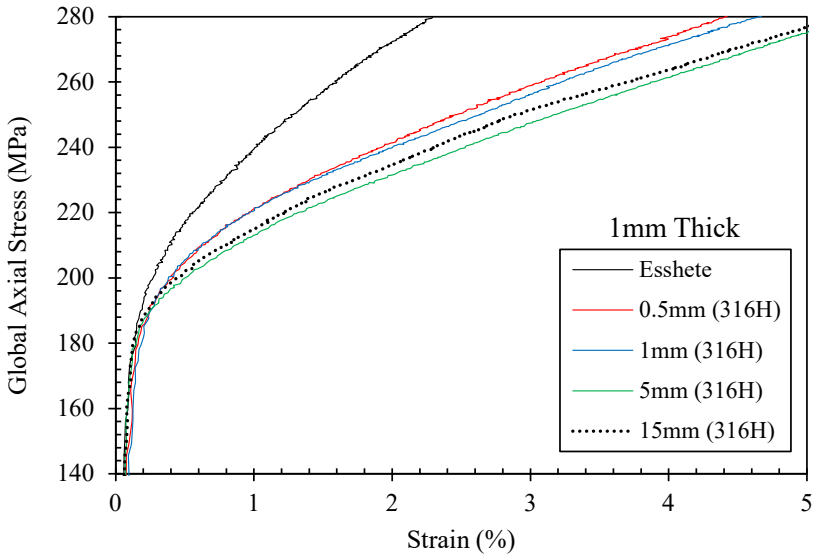

(b)

Figure 5.24 Local stress-strain curves obtained by plotting the global axial stress as a function of DIC measured local axial strain obtained at varying distance from the interface of a diffusion bond between 316H and Esshete1250 (a) 3mm thick (b) 1mm thick specimen.

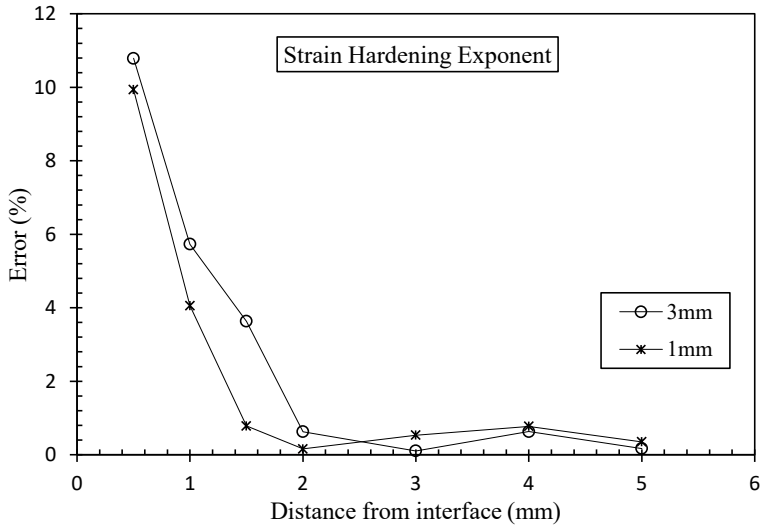

(a)

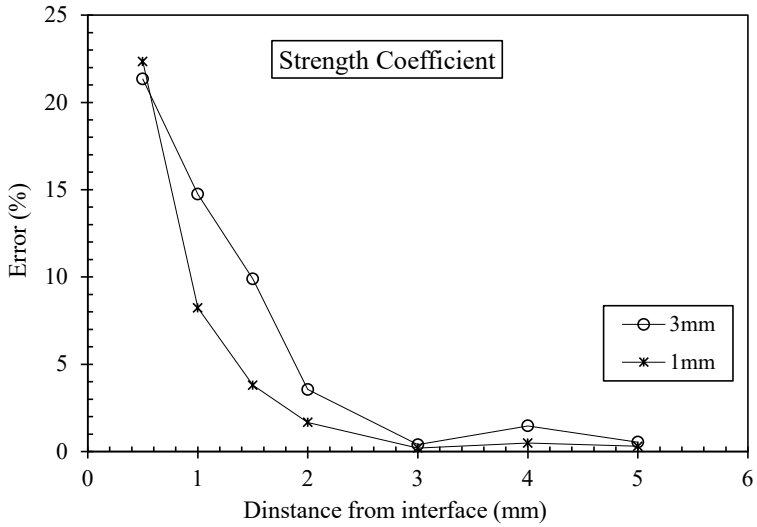

(b)

Figure 5.25 Errors in the measured local mechanical properties plotted as function of distance from the interface, from DIC tensile test results (a) strain hardening exponent (b) strength coefficient.

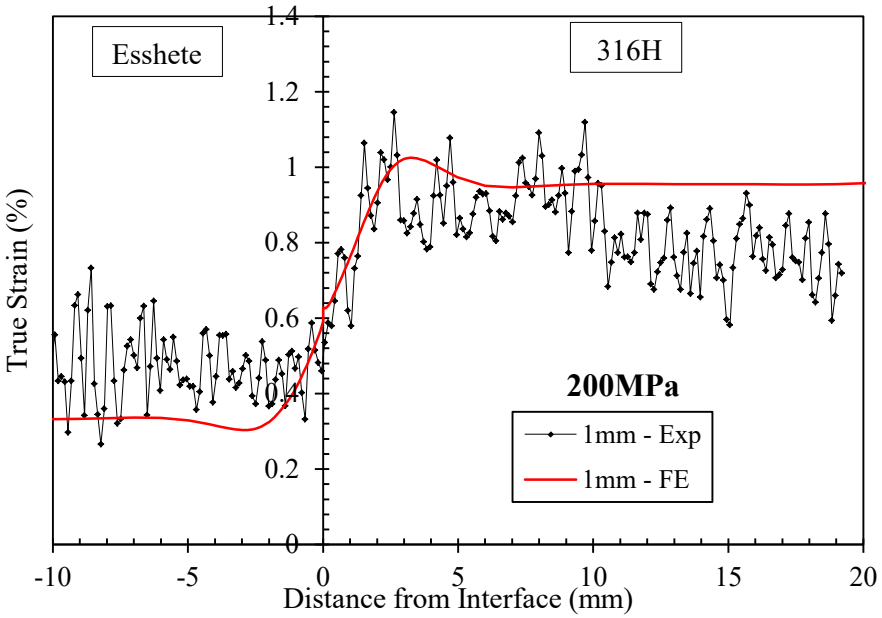

(a)

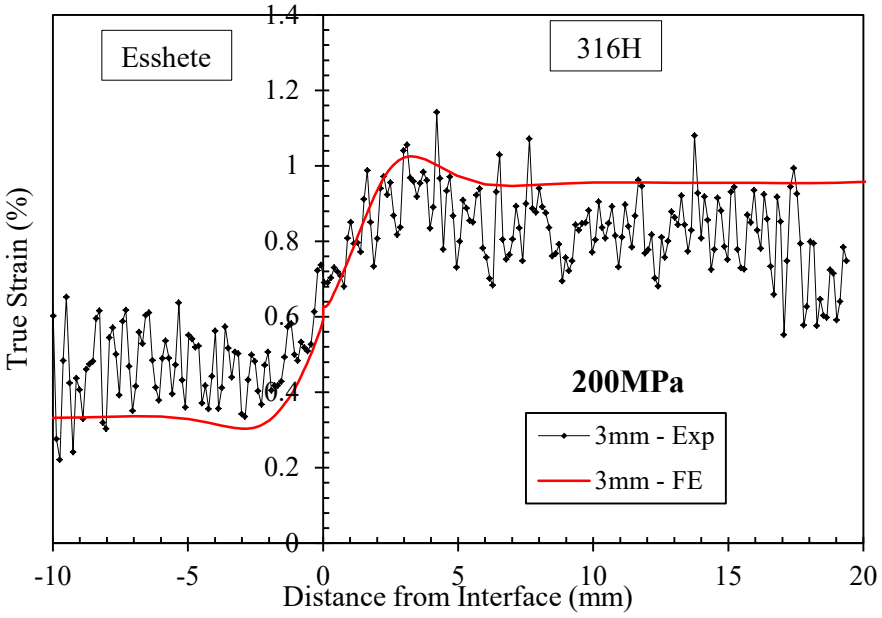

(b)

Figure 5.26 Comparison between FE and measured DIC tensile strain distribution from specimens with a small speckle size pattern (a) 1mm and (b) 3mm thick specimens at 200MPa.

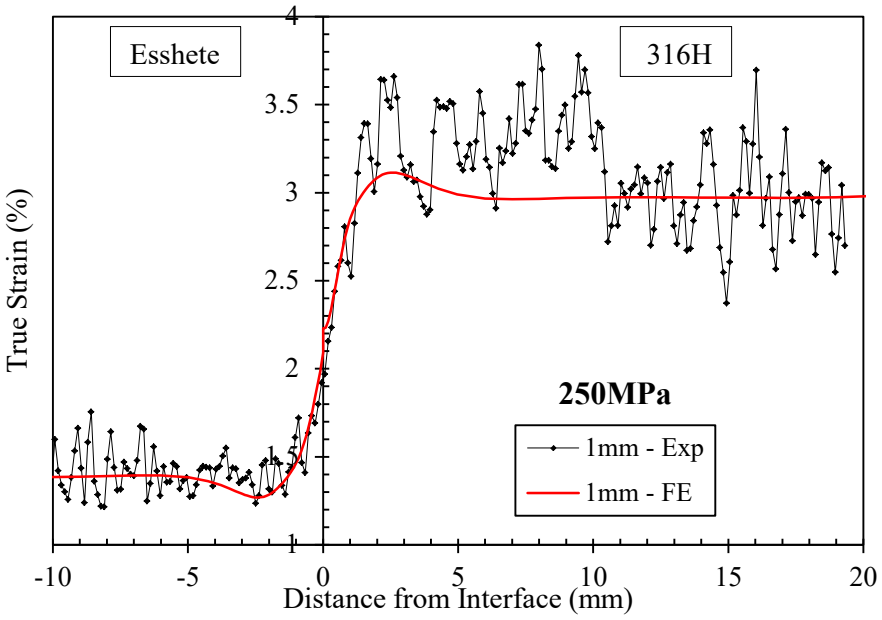

(a)

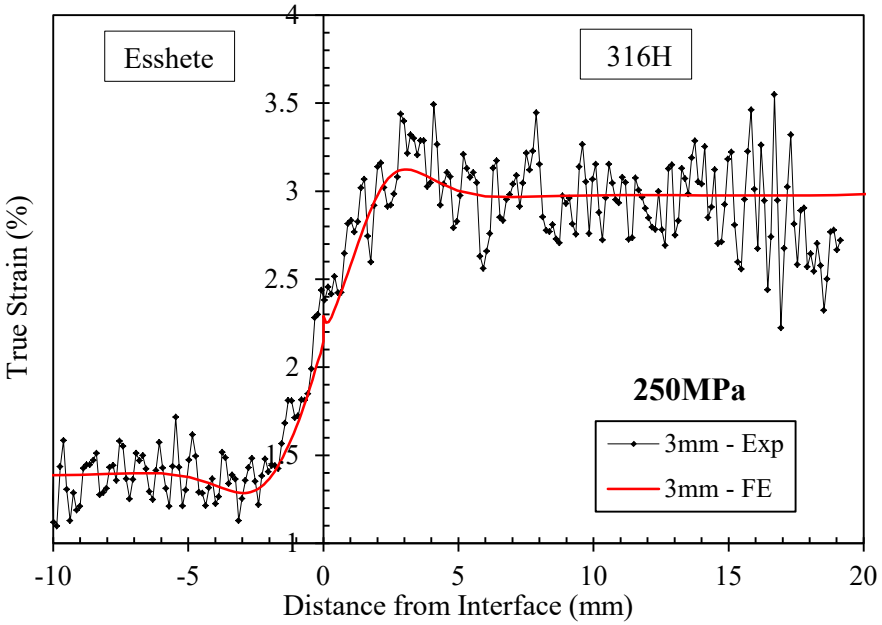

(b)

Figure 5.27 Comparison between FE and measured DIC tensile strain distribution from specimens with a small speckle size pattern (a) 1mm and (b) 3mm thick specimens at 250MPa.

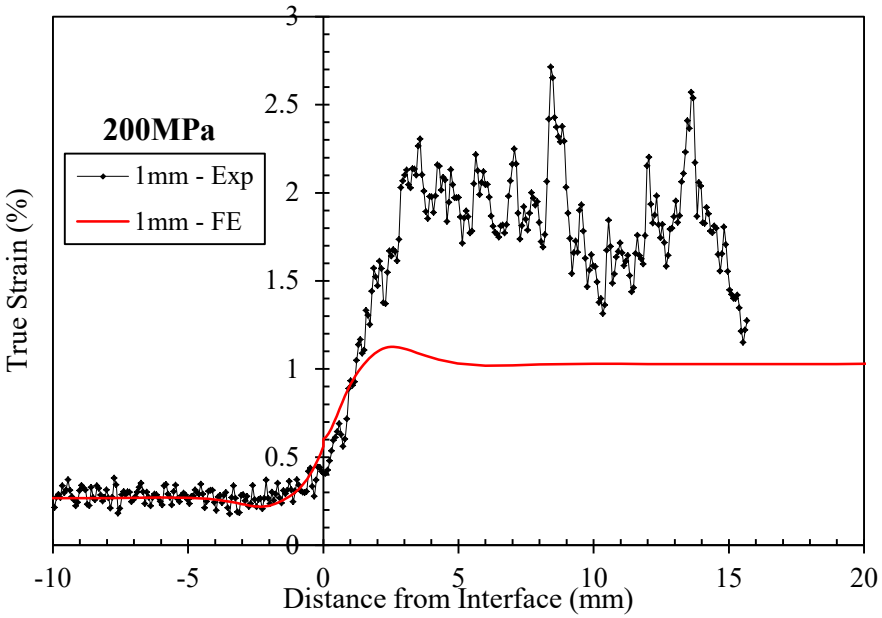

(a)

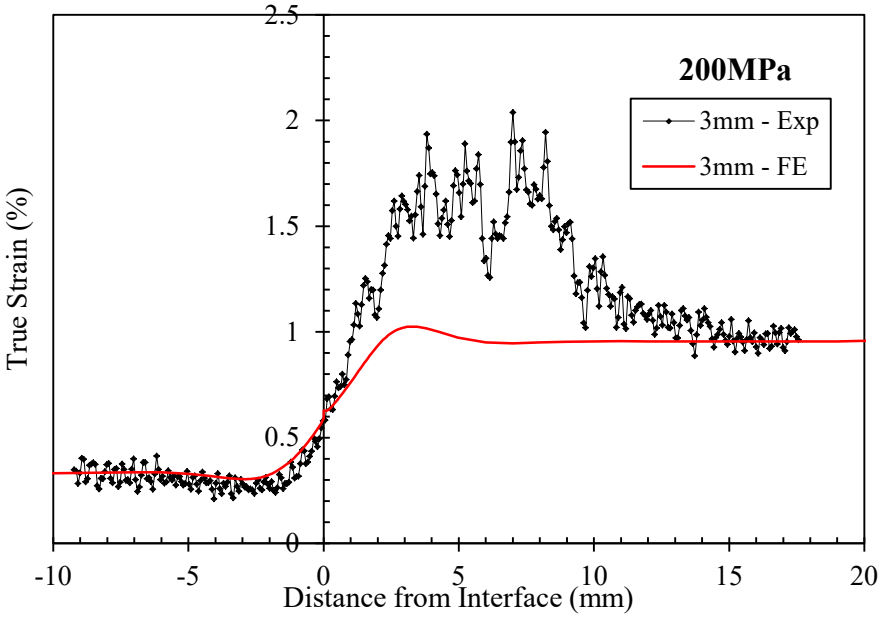

(b)

Figure 5.28 Comparison between FE and measured DIC tensile strain distribution from specimens with a large speckle size pattern (a) 1mm and (b) 3mm thick specimens at 200MPa.

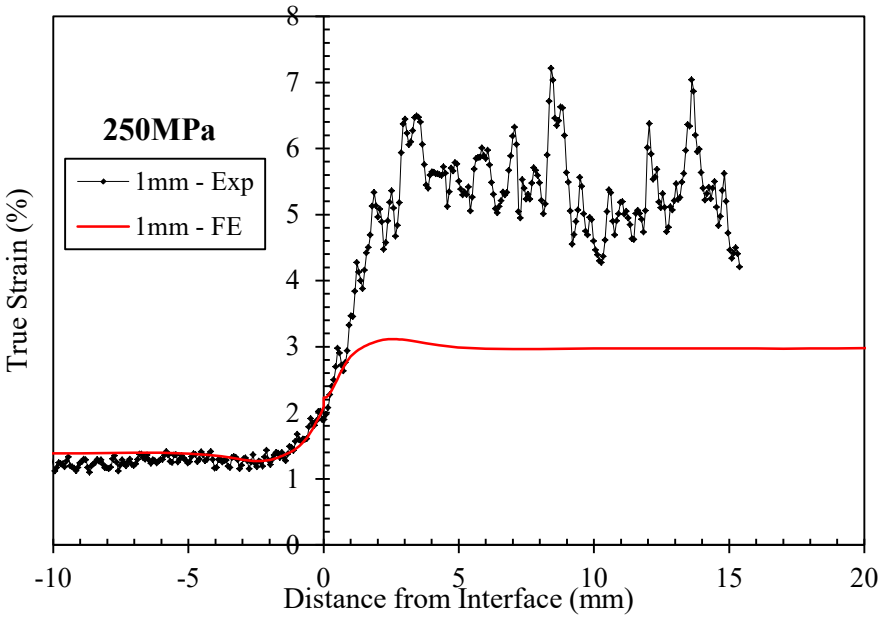

(a)

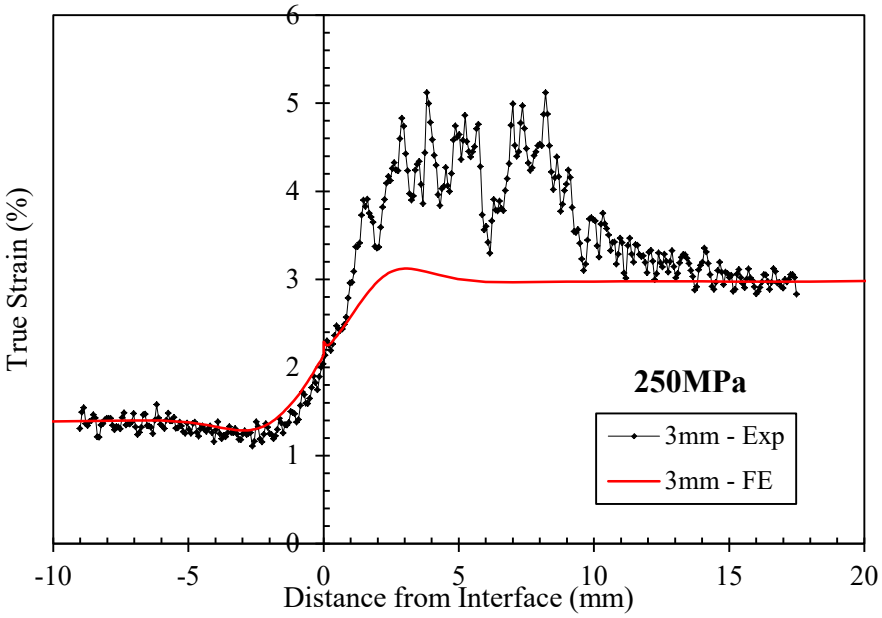

(b)

Figure 5.29 Comparison between FE and measured DIC tensile strain distribution from specimens with a small speckle size pattern (a) 1mm and (b) 3mm thick specimens at 250MPa.

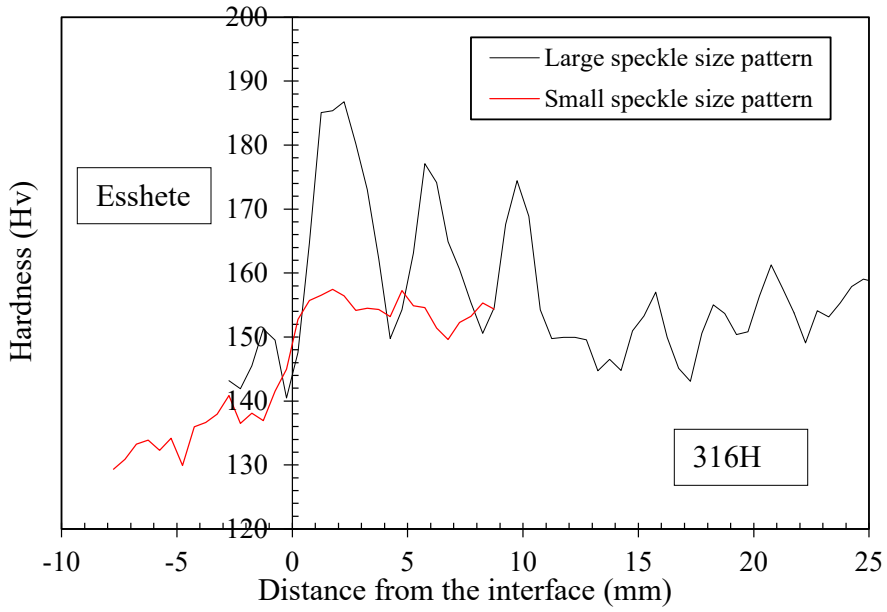

Figure 5.30 Macro-hardness distributions in the region near the interface for diffusion bonded billets from which DIC tensile test specimens with a large and small speckle size patterns were extracted.

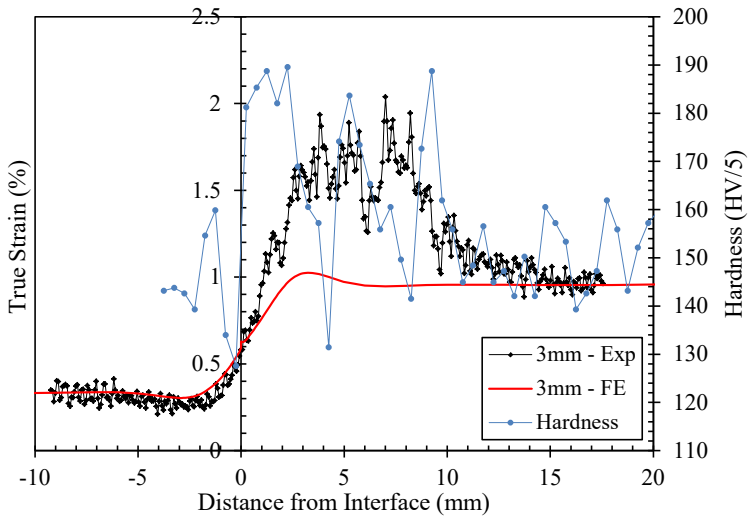

Figure 5.31 Comparison of the DIC measured strain at 200MPa from a specimen with a large speckle size pattern and elastic-plastic FE predicted strain to the measured hardness of the billet from which these specimens were extracted.

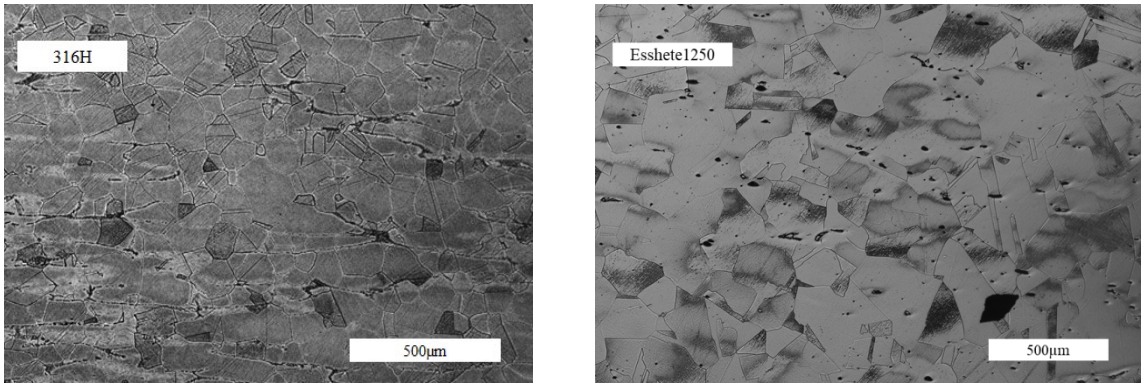

Figure 5.32 Microstructure of 316H and Esshete1250 extracted from regions further away from the interface of the diffusion bonded billet (from which DIC tensile test specimens with a large speckle pattern were extracted).

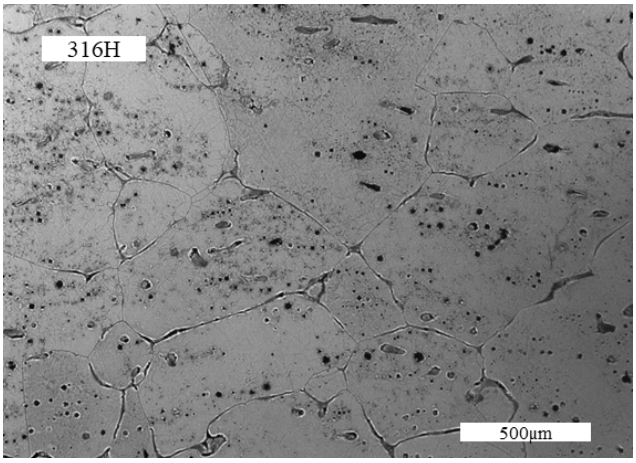

Figure 5.33 Microstructure of 316H in the region near the bond interface of the diffusion bonded billet from which DIC tensile test specimens with a large speckle pattern were extracted.

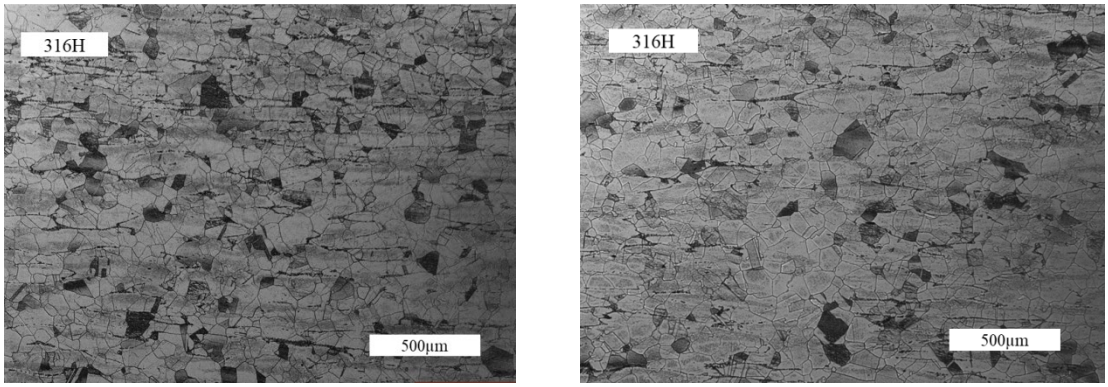

(a) (b)

Figure 5.34 316H microstructure of a diffusion bonded billet where DIC tensile test specimens with a small speckle pattern were extracted. (a) Microstructure from a region near the bond interface, (b) from a region further away the bond interface.

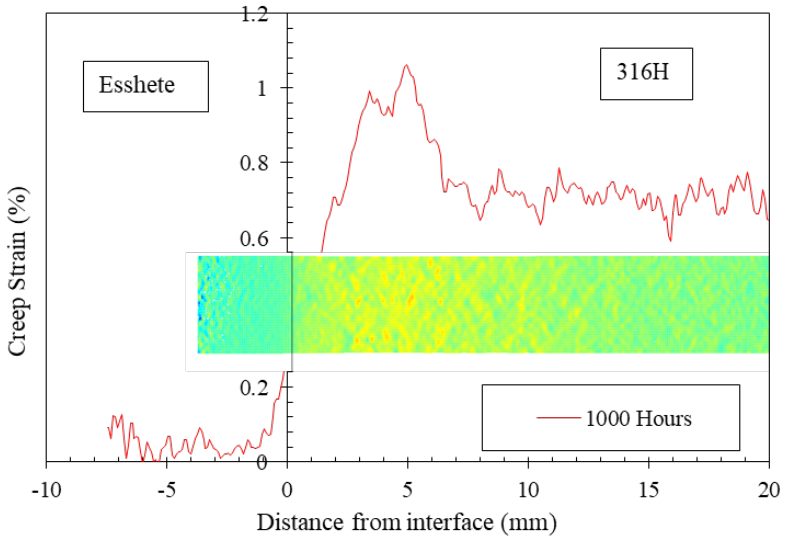

Figure 5.35, Creep DIC strain map and line plot extracted at 1000 hours from the 3mm thick specimen (tested at 575°C and applied stress of 180MPa), showing the strain distribution along the gauge length.

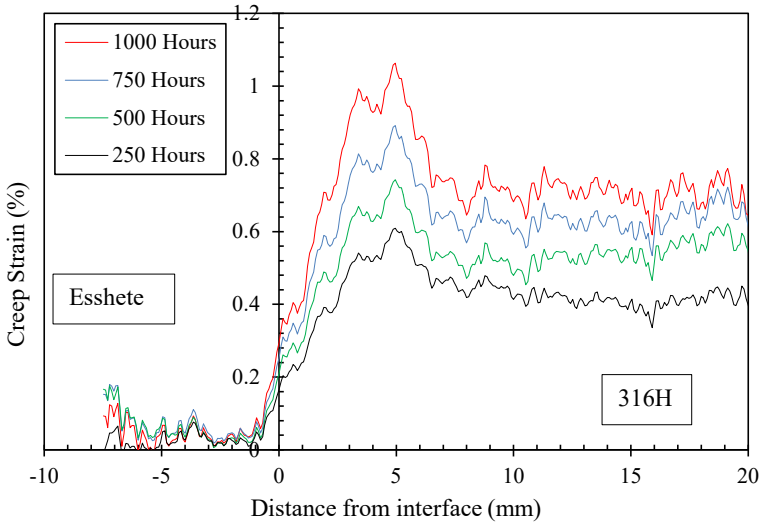

(a)

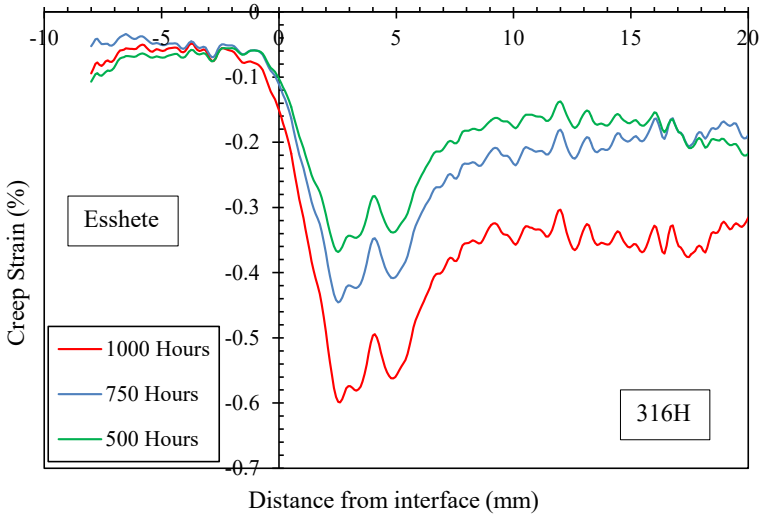

(b)

Figure 5.36 Change in local creep strain along the gauge length of a 3mm thick specimen with time, the applied stress was 180MPa (a) Longitudinal (b) Transverse

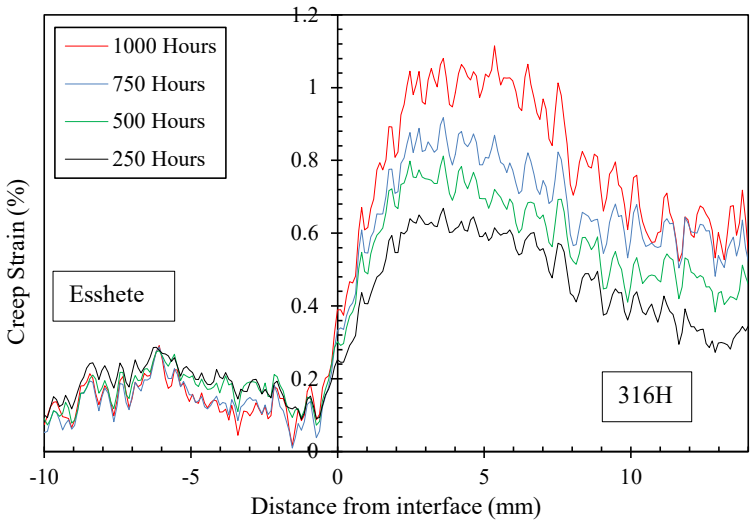

Figure 5.37 Change in longitudinal local creep strain along the gauge length of a 1mm thick specimen with time and applied stress of 180MPa.

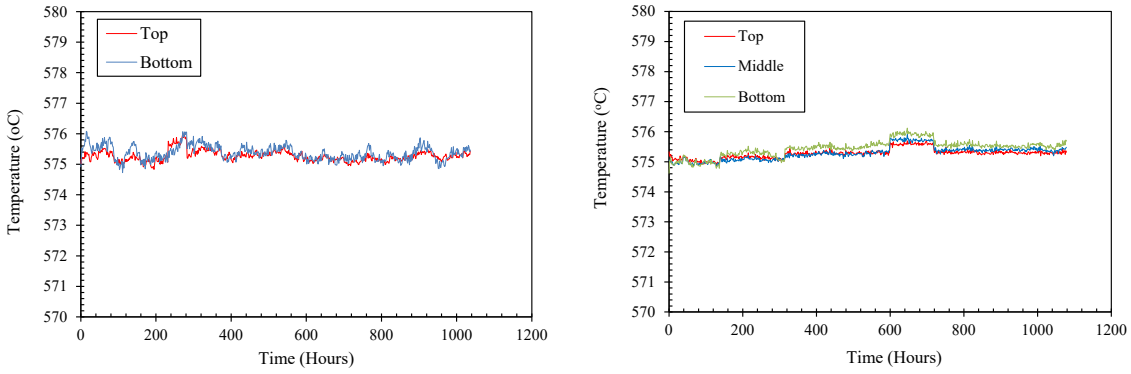

(a) (b)

Figure 5.38 Plot of creep test temperature distribution as a function of time for (a) 3mm (b) 1mm thick specimens tested at 180MPa applied stress.

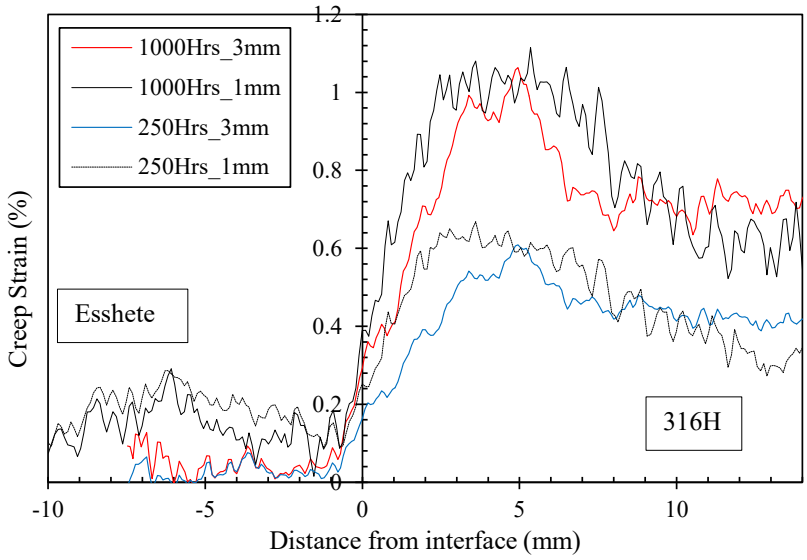

Figure 5.39 Comparison of longitudinal creep strain distribution across the specimen gauge section between the 1mm and 3mm thick specimens tested at 575°C and applied nominal stress of 180MPa.

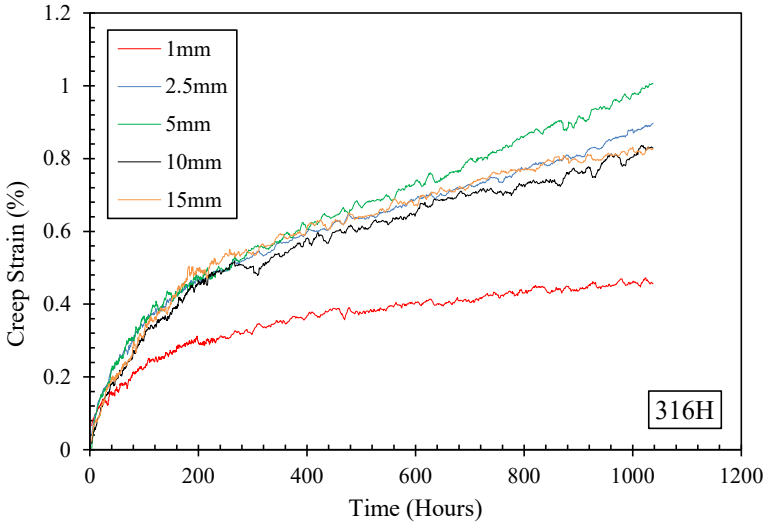

(a)

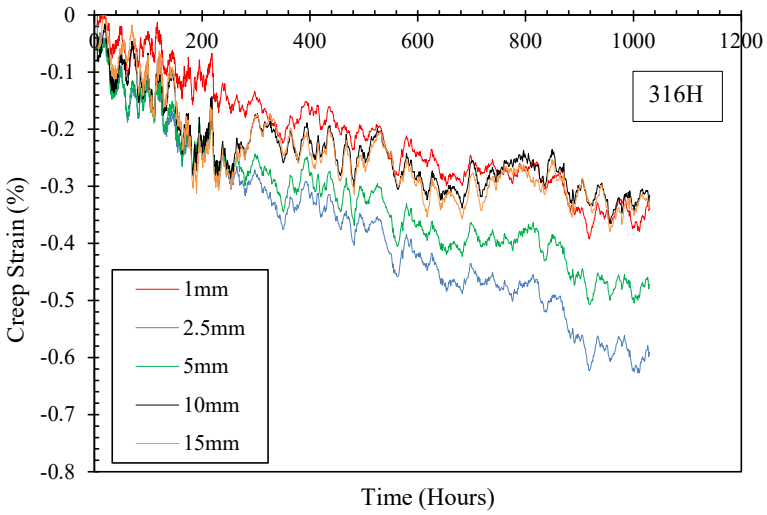

(b)

Figure 5.40 Local creep strain curves in 316H extracted at varying distance from the interface of the 3mm thick specimen tested at 575°C and applied nominal stress of 180MPa (a) Longitudinal and, (b) transverse creep strain curves.

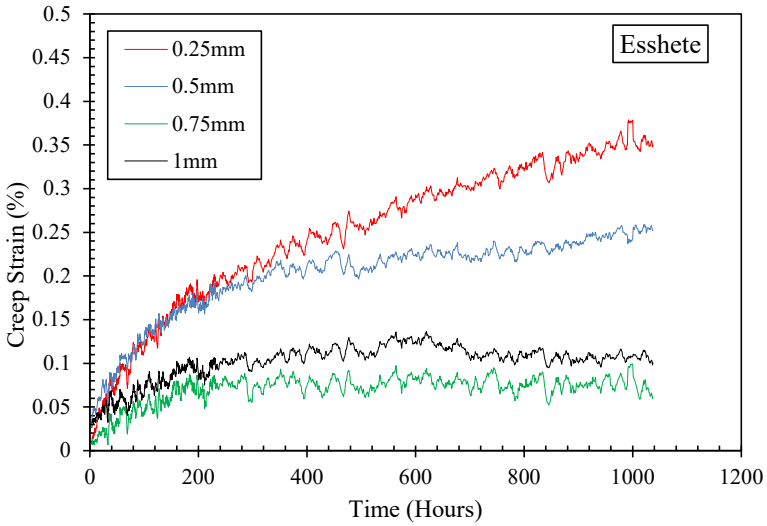

(a)

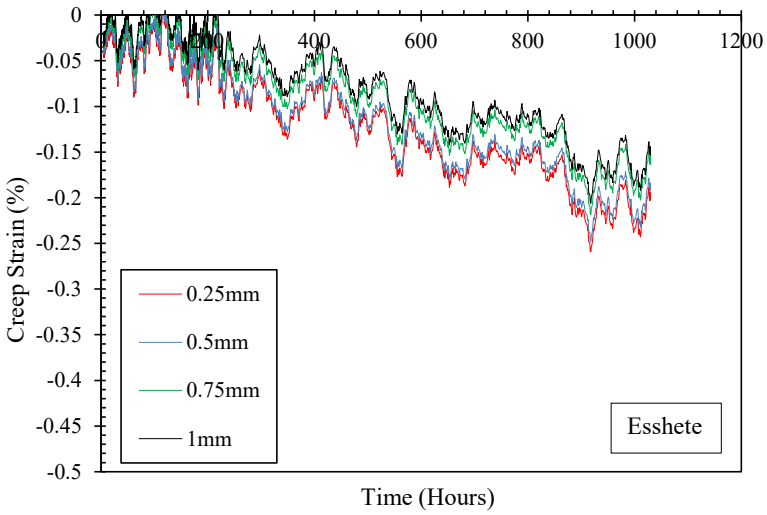

(b)

Figure 5.41 Local creep strain curves in Esshete1250 extracted at varying distance from the interface of the 3mm thick specimen tested at 575°C and applied nominal stress of 180MPa (a) Longitudinal and, (b) transverse creep strain curves.

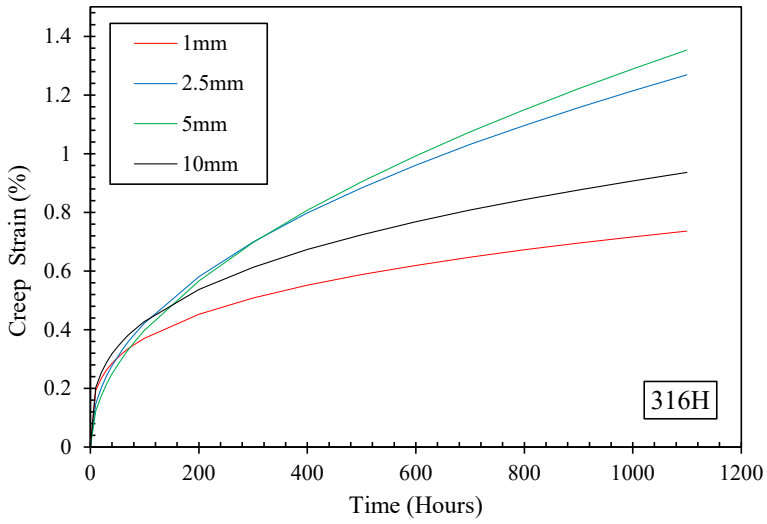

Figure 5.42 Local longitudinal creep strains extracted from 316H at varying distance from the interface of a 1mm thick specimen 575°C and applied nominal stress of 180MPa.

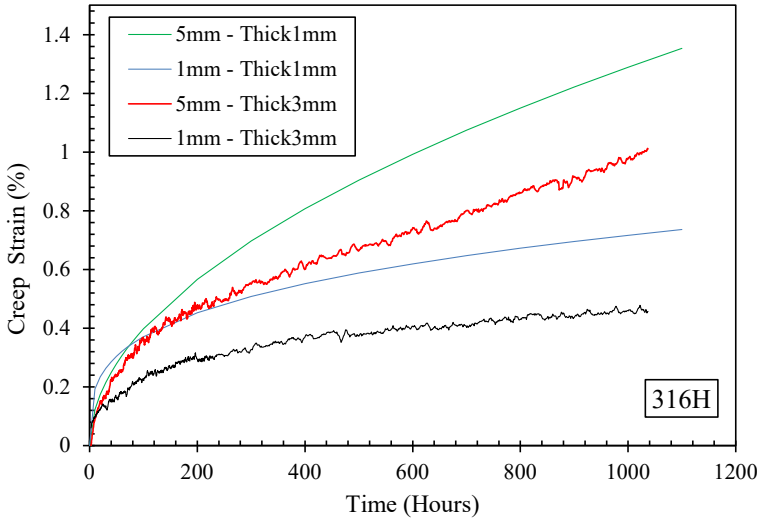

Figure 5.43 Comparison of local creep strain curves extracted from a 3mm and 1mm thick specimens at similar distance from the interface (both tests were carried out at 575°C and an applied nominal stress of 180MPa).

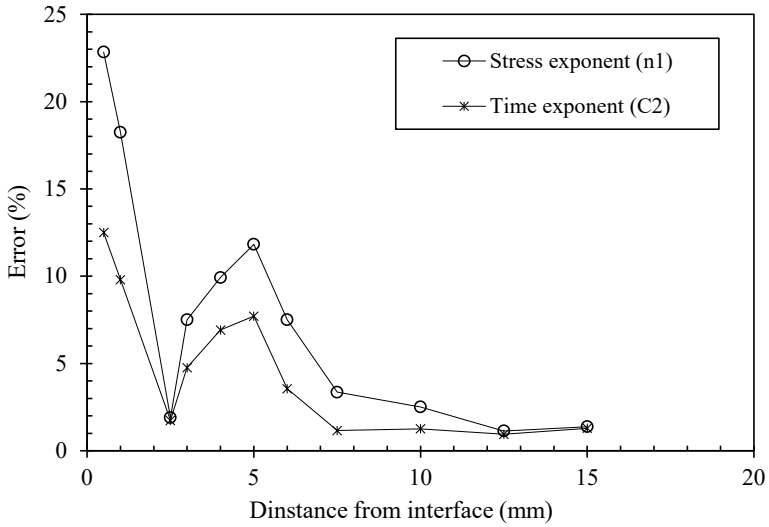

Figure 5.44 Errors in the DIC measured local creep properties plotted as function of distance from the interface from a 3mm thick specimen (with an aspect ratio of 0.5) tested at 575°C and applied nominal stress of 180MPa.

Table 5.1 Summary of element sizes near the interface used for mesh sensitivity study.

No:	Mesh density	Smallest element dimensions (mm)		
		x	y	z
1	4400	0.25	0.25	0.2
2	10788	0.175	0.175	0.1
3	22080	0.125	0.125	0.05
4	27520	0.125	0.125	0.01
5	43000	0.1	0.1	0.01
6	80668	0.075	0.075	0.01
7	172000	0.05	0.05	0.01
8	32000 (Assumed)	0.1	0.1	0.1

5.9 REFERENCES

1. Davis, J.R., *Tensile testing*. 2004: ASM international.
2. Rodrigues, D.M., et al., *Numerical study of the plastic behaviour in tension of welds in high strength steels.* International Journal of Plasticity, 2004. **20**(1): p. 1-18.
3. Satoh, K. and M. Toyada, *Joint Strength of Heavy Plates With Lower Strength Weld Metals.* Welding journal, 1975. **54**(9): p. 311.
4. Kim, Y.-J. and C.-S. Oh, *Finite element limit analyses of under-matched tensile specimens.* Engineering Fracture Mechanics, 2006. **73**(10): p. 1362-1378.
5. Cam, G., et al., *Determination of mechanical and fracture properties of laser beam welded steel joints.* WELDING JOURNAL-NEW YORK-, 1999. **78**: p. 193-s.
6. LaVision, *StrainMaster DaVis 8.1 Digital Image Correlation Software*. 2013.

7. Reynolds, A. and F. Duvall, *Digital image correlation for determination of weld and base metal constitutive behavior.* WELDING JOURNAL-NEW YORK-, 1999. **78**: p. 355-s.
8. Lockwood, W.D., B. Tomaz, and A. Reynolds, *Mechanical response of friction stir welded AA2024: experiment and modeling.* Materials Science and Engineering: A, 2002. **323**(1): p. 348-353.
9. Lockwood, W. and A. Reynolds, *Simulation of the global response of a friction stir weld using local constitutive behavior.* Materials Science and Engineering: A, 2003. **339**(1): p. 35-42.
10. Genevois, C., A. Deschamps, and P. Vacher, *Comparative study on local and global mechanical properties of 2024 T351, 2024 T6 and 5251 O friction stir welds.* Materials Science and Engineering: A, 2006. **415**(1-2): p. 162-170.
11. Acar, M., et al., *Effect of prior cold work on the mechanical properties of weldments*, in *Proceedings of the 2010 SEM Annual Conference and Exposition on Experimental and Applied Mechanics*. 2010: Indianapolis, Indiana, USA.
12. Acar, M., et al., *Variation of mechanical properties in a multi-pass weld measured using digital image correlation*, in *Society of Experimental Mechanics Annual Conference on Experimental and Applied Mechanics 2009*, K.B. Zimmerman, Editor. 2009, Society for Experimental Mechanics Inc.: Albuquerque, New Mexico, USA. p. 288-293.
13. Molak, R.M., et al., *Use of micro tensile test samples in determining the remnant life of pressure vessel steels.* Applied Mechanics and Materials, 2007. **7-8**: p. 187-194.
14. Rodrigues, D., et al., *Numerical study of the plastic behaviour in tension of welds in high strength steels.* International Journal of Plasticity, 2004. **20**(1): p. 1-18.
15. ABAQUS, *'Version 6.14', Dassault Systemes Simulia Corporation.* 2014.
16. Kurt, B. and A. Çalik, *Interface structure of diffusion bonded duplex stainless steel and medium carbon steel couple.* Materials Characterization, 2009. **60**(9): p. 1035-1040.
17. Shirzadi, A., *Diffusion bonding.* Science and Technology of Welding and Joining, 2004. **9**.
18. Satoh, K. and M. Toyoda, *Static strength of welded plates including soft interlayer under tension across a weld line.* Transactions of the Japan Welding Society, 1970. **1**(2): p. 10-17.
19. Hollomon, J.H., Tensile Deformation, 1945: p. 268-290.

20. ASTM-E8/E8M, *13a Standard Test Methods for Tension Testing of Metallic Materials*. 2013.
21. Lecompte, D., et al., *Quality assessment of speckle patterns for digital image correlation.* Optics and lasers in Engineering, 2006. **44**(11): p. 1132-1145.
22. Yılmaz, O., *Effect of welding parameters on diffusion bonding of type 304 stainless steel–copper bimetal.* Materials science and technology, 2001. **17**(8): p. 989-994.
23. Humphreys, F.J. and M. Hatherly, *Recrystallization and Related Annealing Phenomena (Second Edition)*, M. Hatherly, Editor. 2004, Elsevier: Oxford.
24. Sakanashi, Y., *Measurement of Creep Deformation in Weldments.* PhD Thesis, The Open University, 2013.
25. Sakanashi, Y., et al., *Measurement of Creep Deformation across Welds in 316H Stainless Steel Using Digital Image Correlation.* Experimental Mechanics, 2017. **57**(2): p. 231-244.
26. Parker, J.D., *The effect of specimen size on creep behaviour.* Welding in the World/Le Soudage dans le Monde, 1996. **5**(37): p. 233-241.
27. ASTM-E139, *Standard Test Methods for Conducting Creep, Creep-Rupture, and Stress-Rupture Tests of Metallic Materials.* ASTM International, West Conshohocken, PA, 2011.

CHAPTER SIX

6. Discussion

6.1 Introduction

In the current study, measurement of deformation in varying stress fields was carried out. Two distinct methods of varying stress fields were employed: in the first case, the stress field was varied by designing an hour-glass shaped specimen with the specimen width varying as a function of the gauge length. In the second case, stress fields were varied due to a change in the specimen thickness in mismatched dissimilar metal joints. To reduce the complexity in the developed stress fields in the region near the interface, a simple plane interface and a diffusion bonded interface, which gives a sharp change in the material properties, were studied by FE modelling and experimental tests. In both the cases, the local deformation was measured using DIC. The results obtained demonstrate the capability of DIC as a measurement technique for characterising the local deformation of specimens with varying stress fields. The findings also highlight some aspects of the technique which need to be considered when interpreting data from DIC measurements of local deformation from specimens with varying stress fields.

6.1 Measurement of local deformation from a single hour-glass shaped specimen

In the hour-glass shaped specimen, the stress field was varied by designing the specimen with its width varying as a function of position along the gauge section, with the minimum width at the centre of the specimen. To limit the effects of stress concentration at the centre of the specimen, the width curvature was optimised using elastic FE. The results obtained show that although the highest stresses are at the centre of the specimen, there is a gradual increase in the stresses as the specimen centre is approached. The stress distribution in the specimens can be obtained from elastic FE results if the initial loading of the specimen is elastic. In the case where the initial loading is elastic and partly plastic, true stresses at the end of initial loading can be calculated from the measured loading strains when the final initial load is applied, as outlined in section 4.6.1. The nominal stress distribution from the hour-glass shaped specimen shown in figure 4.12 shows a stress range of about 70MPa and this can be used in characterising the multiple creep curves extracted from a single specimen.

The results seen in figures 4.17, 4.18, 4.19 and 4.21 show multiple creep curves from both the longitudinal and transverse strains extracted from a single hour-glass shaped specimen at different stress levels. From these figures, it is clear that the creep strain rates within the specimen increase with increasing stress such that the creep strain rates at the centre of the specimen (nominal stress ≈ 320MPa) are higher than the ones extracted near the end of the gauge section (nominal stress ≈ 250MPa). Figure 4.21 shows a 3D plot of the creep strain as a function of stress and time from a single specimen. Although figure 4.21 only shows a surface plot of longitudinal creep strains, a similar 3D plot can be constructed for transverse strains from a single hour-glass-shaped specimen. This highlights the vast amount of data that can be extracted from single specimen with vary stress fields is characterised using strain.

There have been previous attempts to extract multiple creep curves from a single specimen. For instance, Levy *et al* [1] carried out trial tests to extract multiple creep curves from a single specimen using a tapered specimen. In their work, the strains were measured using replicas and the test had to be interrupted to allow strain measurement. The use of replicas limited the amount of data that could be extracted and only three creep curves were extracted. The creep measurements carried out by Levy *et al* [1] were restricted by their strain measurement technique and it is possible that the by interrupting the test, unloading and re-loading, could have affected of the mechanical properties of the material. Further trial tests to extract multiple creep curves from a single tapered specimen were carried out by Cloud *et al* [2]. In these tests, the whole field deformation of the specimen was captured using photoelasticity. Although using photoelasticity has an advantage over replicas, that technique cannot accommodate long creep test times and the tests were limited to only a few hours. Recently, an hour-glass shaped specimen was used to characterise the fracture behaviour of titanium alloys [3]. The technique employed focused on obtaining the fracture parameters of the material and so only the initial and final specimen shapes were measured to characterise the overall deformation of the specimen. Local deformation rates were not measured since the deformation rate was measured using an extensometer attached to the specimen, which gave strain values averaged over the entire curved region of the hour-glass shaped specimen. The work presented in the current study, using DIC, reports the only successful extraction of local creep deformation from a single specimen.

6.1.1 Characterisation of creep properties from a single hour-glass shaped specimen

The novelty of using DIC to characterise local creep deformation from a single specimen is that not only can longitudinal and transverse local strains be measured but also that these can be measured for an extended period of time suitable for characterising the creep properties of a material from a single specimen. The multiple creep curves at different stress level obtained from a single hour-glass shaped specimen where fitted with the RCC-MR creep model to characterise the creep properties of 316H. Tables 4.2 and 4.3 shows the primary and secondary creep properties obtained. Experimentally measured local creep curves were compared to the ones obtained from the fit parameters. A good correlation between the two data sets is obtained when local creep curves plotted as a function of true stress at the end of initial loading, figure 4.36. The RCC-MR model parameters given in Table 4.3 are similar to the ones obtained from ex-service 316H reported in the R66 materials handbook [4]. However, the RCC-MR model parameters obtained in the current study cannot be directly compared to those reported in the literature as the ex-service 316H materials used were extracted from different components with different service exposures. It should be noted that differences in the creep properties measured from specimens extracted from different positions from the same 316H ex-service component have been reported [5].

A further advantage of DIC in characterising creep properties from a single specimen is that the creep properties can be obtained by fitting a surface to the 3D creep data given in figure 4.21. Table 4.4 gives the RCC-MR model parameters obtained when a surface is fitted to the 3D creep data. Model parameters obtained from 3D fitting are expected to give improved correlation between the measured and the predicted creep curves. However, the results in Table 4.4 showed that the results from 3D fitting did not give a good correlation compared to the results given in Figure 4.36. The reason for the difference is that the 3D fit used the entire data set, including the erratic values obtained in the regions near the specimen gauge centre and the data was not smoothed. The fitting data can be improved by smoothing and by removal of any erratic creep curves, such as the ones near the specimen centre.

Considering Figure 4.36(b), although a good fit between the two data sets can be found, the correlation is poor for the data extracted near the centre of the specimen. The measured creep rates at the centre of the specimen are higher than the predicated from the fitted parameters. The difference could be because the fitting of the RCC-MR model is based on the true stress after initial loading of the specimen. This could have evolved with time, resulting in

increased creep rates at the centre of the specimen. Since the temperature measurements were based on the thermocouples attached to the top and bottom part of the specimen and the temperature at the centre of the specimen was not monitored, it is also likely that the actual temperature at the centre of the specimen could have been slightly higher than the ones recorded by the thermocouples, which would account for the observed effect.

6.1.2 Validity of DIC creep strain measurements from a single specimen

To validate the multiple creep curves at different stresses extracted from a single hour-glass shaped specimen, the creep strains extracted at 320MPa from the hour-glass shaped specimen were compared to the ones obtained from conventional creep specimens tested at the same temperature and stress level, Figure 4.29. The results from Figure 4.29, show that, at both stress levels, the creep strains measured from the hour-glass specimen compares very well to the ones obtained from conventional specimens, validating the multiple creep strain curves extracted from a single specimen. The creep strains from the conventional specimen at 320MPa were measured using both DIC and LVDT extensometer. Although strain measurements by DIC only went up to about 800 hours, due to a malfunction in the DIC camera used, the correlation between the data from conventional creep specimen and the one from the hour-glass shaped specimen extracted at 320MPa demonstrates the validity of the creep strains measured from a single hour-glass shaped specimen.

6.2 Considerations when extracting local creep properties from a single specimen

6.2.1 DIC-Creep experimental set-up

In the current study, the curved width of the specimen was measured using a coordinate measurement machine (CMM). The specimen's centre was ascertained from these measurements and marked as a reference point for strain measurement. The marked centre point was also used for positioning the specimen for DIC measurement. As described earlier, the specimen was positioned so that only half the gauge section of the hour-glass shape was imaged. The imaged section was magnified to fill the field of view of the camera. However, future tests would be carried out imaging the entire gauge section of the hour-glass shaped specimen. Although imaging half the specimen gauge section offers the advantage of a magnified view of the specimen, capturing the entire gauge section would provide more information, and initial validation of the measured creep strains at any given stress can be carried out by comparing the strains extracted from the two opposite sides of the hour-glass

gauge section at the same stress. In this case, validation of the measured creep strains at a given stress level would be provided by comparing these measured strains from the same specimen to the ones obtained from conventional creep specimens.

6.2.2 Temperature Control

Although the creep test temperatures reported in the current study was well controlled, the measured temperature was obtained from the ends of the gauge section. Since the cross-section of the specimen is small at its centre, it is important that the temperature at the centre as well as the ends of the gauge section should be monitored. For example, in Figure 4.33 higher creep rates are obtained in the regions near the centre of the gauge than in the other regions. The higher creep rates in these regions resulted in poor correlation between the measured and the predicted creep curves. Although Figure 4.20 shows that the creep test temperature was well controlled, the temperature recorded from regions near the two ends of the hour-glass shaped gauge section does not give the accurate temperature at the centre of the cross-section. Figure 6.1 shows the sensitivity of creep to change in temperature valuated from RCC-MR parameters provided in the R66 materials handbook [4]. Considering the high sensitivity of creep rates to temperature shown in Figure 6.1, it is important that the temperature at the centre of the hour-glass shaped specimen should be measured. The use of optical temperature measurement techniques would be advantageous as this would provide the whole field temperature distribution across the specimen gauge section.

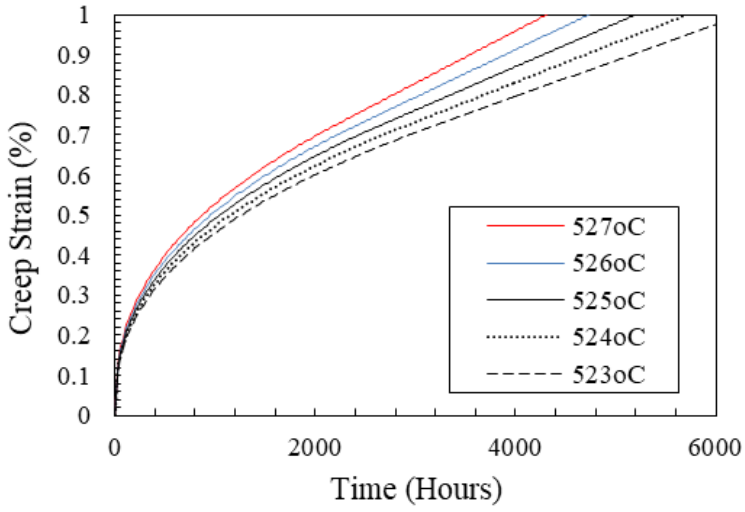

Figure 6.1 Sensitivity of creep strain to change in temperature evaluated using RCC-MR model parameters for an applied stress of 300MPa

6.3 Significance of the Experimental Technique

The application of DIC to extract multiple creep curves at different stress levels from a single specimen yields a vast amount of data characterising the creep behaviour of the material. This data can be used to assess any change in Poisson's ratio, and to study the evolution of the true stress during the creep test. The information revealed can be used in modelling the creep behaviour of the material.

The ability to extract multiple creep deformation curves from a single specimen at different stress levels implies that the number of creep tests, and the time required, for characterising the creep behaviour of any given material can be reduced several folds making the process more economical. The design criteria for high temperature materials should guarantee that neither excessive creep distortion nor creep rupture of a component used under stress at high temperature will occur within the component's planned service life [6, 7]. To ensure this, extensive creep strength and rupture data are required for high temperature materials. For instance, for a material with a design life of 100,000 hours, the ASME design code requires tests lasting more than 30,000 hours repeated at 50^{o}C intervals within the operating temperature [6]. The entire creep testing programme for the material would include at least 3 casts, with a minimum of 2 tests at each given temperature and stress, and at least 4 different stress levels at any given temperature. Similarly, the European code of practice for creep strength and rupture assessment requires test durations of about one third of a planned life of 250,000 hours, from at least 3 casts, at temperature intervals of 25^{o}C and including 50^{o}C higher than the application temperature [7]. For any given temperature a minimum of 5 tests at different stress levels are required. The creep testing programmes required by design codes entails a very high cost of developing new high temperature materials and the 'development cycle' for new high performance power plant steels is currently over 10 years [8]. To reduce the astronomical cost of acquiring material data for new high temperature steels, the current focus is on development of creep data extrapolation techniques [9-11]. The ultimate goal is to use creep data acquired from short term tests and extrapolate it to forecast the long term behaviour of the material, thus cutting down the cost of data acquisition. However, the extrapolation of creep data from short term tests is hampered by the facts that (a) the mechanisms controlling creep and creep fracture change as the test conditions change, and (b) during long term creep tests the microstructure varies with time, a characteristic not exhibited in short term tests [12].

Using DIC to extract multiple creep deformation curves from a single specimen at different stress levels would reduce the number of creep tests required thus reducing the cost of data acquisition. For instance, as stated above, a minimum of 4 tests at different stresses at any given temperature are required by the European code of practice for creep strength and rupture assessment, however using the technique developed in this study, only one test would be required at each temperature; the data acquired from this single test cover a wide range of stress levels. The technique developed in this study, would not only reduce the cost of data acquisition but also provide a wealth of information that can be used in modelling the creep behaviour of the materials at any given temperature.

The technique developed in this study would also be useful in the acquisition of creep strength data for component life assessment, especially in cases where the component's design life is based on a maximum strain allowable for the planned life of the component. This technique is not only applicable to steel or metallic materials; it can be applied to characterisation of the creep behaviour of a wide range of materials including cross-welds and in various testing atmospheres.

The technique can also be used to study the effects of elastic and plastic loading on the creep behaviour of high temperature materials (especially newly developed ones) using a single specimen. In such studies, a single specimen can be loaded in such a way that the middle section of the waisted specimen undergoes plastic loading whilst the rest of the gauge length undergo elastic deformation on initial loading. Apart from obtaining spatially resolved multiple creep curves from a single specimen, microstructural study of samples extracted from different regions of the specimen gauge length, where the stress and strain experienced could be determined, would reveal the microstructural evolution of the material during creep deformation in relation to the initial applied stress being either elastic or plastic. Similarly, creep damage of the material could be studied using a single specimen.

Considering the advantages of the technique developed in this study, it can be seen that it has the capability of transforming the way creep testing is carried out, saving cost and producing vast amounts of data that can be used in various ways such as modelling. Further development of this technique would lead to developing the capability of not only extracting multiple creep curves at different stress levels, but also at different temperatures from a single specimen.

6.4 Future work

6.4.1 Materials

The use of virgin material with known material properties (rather than ex-service material) would enable direct comparison of these with the properties determined from a single hour-glass shaped specimen. Further validation measurements could be carried out by comparing the measured creep strains and creep properties from conventional creep specimens (with strain measured using both DIC and extensometers) with the ones obtained from a single hour-glass specimen. These validation techniques can also be backed up with elastic-creep and elastic-plastic-creep FE modelling to consider the effect of the initial plastic strain on the local creep strains measured.

6.4.2 Characterisation of creep properties from a single hour-glass shaped specimen using 3D DIC

The success of using DIC to characterise creep properties of a material from a single hour-glass shaped specimen can be extended to 3D DIC. With 3D DIC, an hour-glass shaped specimen with a circular cross-section area can be used to characterise creep properties of any given material. Using a single hour-glass shaped specimen (with a circular cross-section area) tested to failure, the multiple creep curves extracted can be used to study the creep damage of the material. Therefore, the data obtained can be fitted with creep damage models to characterise the creep damage parameters [13, 14]. In this case, the data obtained can be used to characterise not only the creep deformation but also creep damage properties.

6.4.3 Extraction of multiple creep curves at varying stress and temperature from a single specimen

Given the success of using DIC to characterise creep properties from a single specimen presented in the current study, this can change the way creep tests are carried out. For instance, with an hour-glass shaped specimen (varying stress field) and the specimen subjected to varying temperature (from the centre to the ends of the gauge section), local creep curves at different stress and temperature can be obtained from a single specimen, The temperature gradients in the hour-glass shaped specimen can be monitored using optical methods.

6.5 Measurement of local deformation from the mismatched materials with sharp interface

The capability of DIC to measure whole field local strain of a specimen gauge length coupled with its being an easy technique to set up (only requiring a camera, lighting and a displacement/strain computation algorithm to apply to the images) makes it an attractive technique which is now widely applied. It is capable of resolving displacements as small as 0.02mm [15, 16] and the application of high resolution cameras allows improved resolution of the measured local displacement/strain [17]. Due to these advantages, DIC is now widely applied to characterising the local mechanical properties of welds at both room and high temperatures. As described earlier, a welded joint is composed of materials of varying microstructure due to the different thermal cycles that the different parts of the weld and the surrounding regions experience during the welding process. The inhomogeneous microstructures of welds give rise to varying local mechanical properties so that when a weld is subjected to uniaxial loading, the interactions of its different constituent parts (weld metal, HAZ and parent metals) result in local constraints. This results in multiaxial loading in the regions near the interfaces between the different constituent. Whereas conventional strain measurement techniques cannot capture the local deformation of the weld's various constituents, DIC is an outstanding technique for measuring this. Although local deformation is easily measured using 2D DIC, determining a weld's local mechanical properties from such measurements is a nontrivial problem. During mechanical testing, only the specimen's global stress is measured and to determine the local mechanical properties, it must be assumed that the stress is uniform (uniaxial) throughout the gauge section, (iso-stress) [18-20]. To determine the local mechanical properties, therefore, the global stress is plotted as a function of the local strain. The correctness of this assumption was investigated using FE [19, 21]. Although there was a measure of correlation between the FE model results and the measured DIC, full correlation between the two was never attained; highlighting the unavoidable errors in DIC measured local mechanical properties. The discrepancy between the FE and DIC measured local stress-strain curves was ascribed to the fact that, for under-matched welds, the DIC measured strain in the weld and HAZ is constrained by the adjacent stronger material. Using this local constrained deformation as input data for FE analysis of the welds would lead to further constrained deformation and so the FE results would differ from DIC measured ones [21]. On the other hand, the DIC measured local mechanical properties, obtained from a plot of the global stress as a function of the local strain in the

different constituents of the welds have been compared to the properties measured from micro tensile test specimens extracted from different sections of the welds. A measure of correlation between the DIC local stress-strain curves and the ones determined from micro specimens has been found [21, 22]. However, the extent to which the extracted local mechanical properties differ and how the specimen size influences the results have not been evaluated [21, 22].

Although there seems to be a measure of correlation between the DIC measured local stress-strain curves (under the iso-stress assumption) and the FE results obtained from different regions of cross-welds, the effects of the specimen aspect ratio on the DIC measured local mechanical properties has not been established. Because the iso-stress assumption gives rise to errors in the local mechanical properties in the regions near the interface, it is important to evaluate the extent of these errors. These outstanding questions concerning DIC measured local mechanical properties require answers before the technique can be applied in real industrial problems.

In the current study, DIC is used to measure the local mechanical properties of mismatched materials assuming the iso-stress loading. A simplified planar interface between the adjacent materials is used to reduce the complexity of the real stress fields which arise in cross-welds. The use of a simple planar interface makes it easier to evaluate the errors in the measured local mechanical properties (under the iso-stress assumption) as a function of distance from the interface. For instance, the local mechanical properties of a given material in the regions near the interface can be compared to the ones obtained further from the interface. For FE analyses, the simplified interface was achieved by plane partition of two materials whereas for experimental analysis this was achieved by diffusion bonding dissimilar materials, 316H to Esshete1250. The stress fields in the regions near the interface were varied by changing the specimen aspect ratio.

6.5.1 Effect of material mismatch and specimen geometry on the local elastic properties

The effect of material mismatch on the local mechanical properties in the regions near the interface was studied using elastic FE analysis, with a model having an aspect ratio of 0.5. Figure 5.11, shows that the errors in the measured local elastic properties in the region near the interface, obtained from the global stress plotted as a function of the local strain, are

higher than the ones obtained from plotting the local stress as a function of the local strain. This is as expected because the deformation of the weaker material in the regions near the interface is constrained. Figure 5.12 shows that for a given specimen aspect ratio, the errors in the measured local mechanical properties near the interface, obtained from a plot of the global stress as a function of the local strain, increase as the mismatch ratio is reduced. For instance, for an elastic mismatch ratio of 0.95 the maximum error in the region near the interface was about 0.7% whereas for a mismatch ratio of 0.5 the maximum error is about 7% which is 10 times more. Because the maximum error in the measured local elastic modulus for a mismatch ratio of 0.95 is about 0.7%, it can be concluded that it is valid to use the iso-stress assumption in obtaining the local elastic properties of mismatched materials using DIC measurements, since the resulting errors are small. Generally, most welds have closely matched elastic properties with elastic mismatch ratios higher than 0.95.

Figure 5.18 compares the error distributions in the region near the interface, at two elastic mismatch ratios, for three distinct specimen aspect ratios. The measured maximum error in the region near the interface does not change significantly with specimen thickness for a given elastic mismatch ratio. However, for a given elastic mismatch, the size of the region around the interface within which there are errors in the measured local mechanical properties changes with the specimen aspect ratio. In both, Figure 5.18(a) and (b), the region giving errors in the measured local elastic properties extends to about 1mm, 2mm or 4mm from the interface for specimen aspect ratios of 0.167, 0.5 or 1, respectively. It can therefore be concluded that distance from the interface within which there are errors in the measured local mechanical properties depends on the specimen aspect ratio.

Comparing Figures 5.15, 5.16, 5.17 to Figure 5.18, it is interesting to note the correlation, for a given specimen aspect ratio, between the cross-over distance L (the distance from the interface to the point at which the normalised longitudinal strain intercept the horizontal line drawn through 1, at a given stress) and the distance within which there are errors in the measured local mechanical properties. Therefore, it can be concluded that for mismatched elastic material, the cross-over distance L from the normalised longitudinal strain for a given stress provides an estimate of the size of the region within which there would be errors in the measured local mechanical properties when iso-stress loading is assumed.

6.5.2 Effect of specimen geometry on local plastic properties

The effect of specimen geometry on local mechanical properties in the regions near the interface was studied using both elastic-plastic FE analysis and DIC experimental measurements. Since the deformation of the weaker material in the regions near the interface would be constrained, Figure 5.19 compares local stress-strain curves constructed by plotting the global stress as a function of local strain and the ones constructed from plotting the von Mises stress as a function of local strain from specimens with varying aspect ratios. Plots of the von Mises stress as a function of local strain extracted at different distances from the interface do not deviate from the input stress-strain curve of 316H used. This is expected because deformation of the weaker material in these regions is constrained by the adjacent material. On the other hand, plots of the global stress as a function of local strain extracted at different distances from the interface show significant deviations from the input stress-strain curve of 316H used, signifying errors in the measured local mechanical properties. The variation in the plots of global stress as a function of local strain with distance from the interface for both FE and DIC experimental measurements can be seen in Figure 5.21 and Figure 5.24.

Figures 5.23 and 5.25 show the distributions of measured errors in the measured local mechanical properties (yield strength, strain hardening exponent and the strength coefficient) plotted as a function of distance from the interface from both FE and DIC experimentally measured results. Similarly, to the elastic properties, the results indicate that the size of the region within which errors in the measured local plastic properties would occur depends on the specimen aspect ratio. The measured errors are larger in the regions near the interface and decrease with increasing distance from the interface. This is as expected because constraint effects reduce with increasing distance from the interface. The region within which errors occur in the measured local plastic properties is slightly larger than for errors in the measured local elastic properties. From FE results, errors are expected in the measured local plastic properties up to about 1.4mm, 2.3mm or 3.5mm from the interface for specimens with aspect ratios of 0.167, 0.5 or 1, respectively, Figure 5.23. Similar trends in the error distribution can be seen from experimental results, Figure 5.25, although, for the 3mm thick specimen the size of the region within which there are errors in the measured local mechanical properties only extends to about 2mm, which is slightly less than the distance obtained by FE. However, this difference is within the range explicable by experimental factors.

The magnitudes of the errors in the measured local mechanical properties in the regions closer to the interface are similar for the all the different specimen aspect ratios, Figure 5.23 and Figure 5.25. For instance, comparing Figure 5.23(b) and (c) to results in Figure 5.25, the errors in the hardening exponent and the strength coefficient in the regions near the interface are about 10% and 20%, respectively. This demonstrates the magnitude of the errors in the measured local mechanical properties obtained with an assumption of iso-stress.

6.5.3 Effect of specimen geometry on local creep properties

The effect of specimen geometry on local creep properties was studied using DIC creep tests of specimens with different aspect ratio. Both changes in the local creep strain along the specimen gauge section with time and the local creep curves extracted at different distance from the interface were considered. Figure 5.40 shows that there is considerable difference between the local creep curves extracted in the regions near the interface and the ones extracted further from the interface. The creep curve extracted at 1mm from the interface exhibits lower creep rates compared to the ones extracted from regions further away from the interface. The creep strain curve extracted at 5mm from the interface has the highest creep rates. Local creep strain concentration can be observed at regions about 5mm from the interface in Figure 5.36. The observed local creep strain concentration in the regions between 3mm to 6mm from the interface, in a 3mm thick specimen, is consistent with the effects of constrained deformation in the regions near the interface. As observed in both FE and DIC tensile testing, deformation of the weaker material in the regions near the interface is constrained, thus giving low local deformation, whereas in the region just beyond the highly constrained region, there is a local stress/strain concentration, Figures 5.9, 5.15 and 5.27. For room temperature tensile testing, the mechanical properties obtained from regions between 3mm and 6mm away were like the ones obtained from regions further from the interface, Figure 5.23 and Figure 5.25. This indicates that the local stress/strain concentration in the vicinity of the interface had no significant effect on the measured local mechanical properties. On the other hand, the observed high creep rates in the regions between 3mm and 6mm from the interface in a 3mm thick specimen shows the high sensitivity of creep to changes in local stress [23].

Figure 5.44 shows the plot of errors in the measured local creep properties as a function of distance from the interface. Similar trends can be observed in the distribution of errors in both the measured time exponent (C_2) and the stress exponent (n_1). The maximum errors in the

measured creep properties occur in the region near the interface and reduce with distance to a minimum at about 2.5mm from the interface. Beyond 2.5mm from the interface, the measured errors increased, peaking at about 5mm, and then reduce to a minimum at about 6mm. The error distribution in the measured local creep properties indicates the complexity of the local creep deformation in the regions near the interface of mismatched materials.

The distribution of errors in the local creep properties as function of distance from the interface from a 1mm thick specimen were not analysed as the mechanical behaviour of the material was influenced by the diffusion bonding process. Although the error distributions presented in Figure 5.44 were only extracted from a 3mm thick specimen with aspect ratio of 0.5, the magnitude and length scale within which errors in measured local creep properties would occur will reduce when a specimen with low aspect ratio is used. This is supported by the elastic-plastic FE tensile test analysis and DIC experimental results. Similar conclusions have been made in the literature [19, 24].

It should be noted that the errors in the measured local creep properties are due to constraint effects in the regions near the interface which is the true reflection of local deformation of the weaker material adjacent to a stronger one. Whereas the errors obtained in measured local tensile properties at room at room temperature are influenced by not only local constraint in the weaker material but also by the assumption of iso-stress loading.

6.5.4 Significance of the results

As seen from elastic and elastic-plastic FE results and DIC experimental measurements, when iso-stress loading assumed, the magnitude of the errors in the regions near the interface for mismatched materials is dependent on the mismatch ratio between the materials, whereas the distance from the interface within which there are errors in the measured local mechanical properties depends on the specimen aspect ratio. The effect of the aspect ratio on the distance within which there are errors in the measured local mechanical properties when iso-stress is assumed is given in Figure 6.2. Both the FE and experimental results show a similar trend although experimental measurements are reported from only the 1mm and 3mm thick specimens.

Although the size of the region within which there are errors in the measured local mechanical properties would be influenced by the level of mismatch between adjacent materials, the results of Figure 5.18 show this influence to be minimal. The results of Figure

6.2 can therefore be generalised to sharp interfaces such as diffusion bonded joints and, to some extent, to welds with sharp changes in material properties, such as laser and electron beam welds. Therefore, when the local tensile properties of adjacent mismatched materials with a sharp change in the materials properties are measured using DIC, with the iso-stress assumption, the use of a specimen geometry with a smaller aspect ratio is recommended. If a specimen geometry with aspect ratio of 0.167 is used for DIC measurement of local mechanical properties (under the iso-stress assumption), there would be errors in any measured local mechanical properties within 1.4mm of the interface and the errors would increase as the interface is approached. When specimens with larger aspect ratios are used, the trends in Figure 6.2 can be used as guide to determine regions within which accurate results would be obtained.

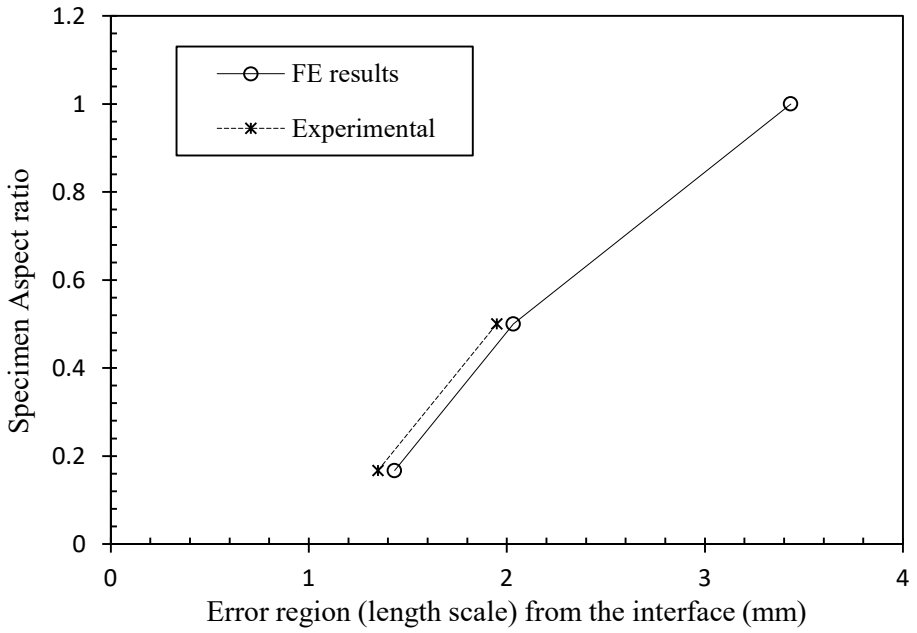

Figure 6.2 Plot of specimen aspect ratio as a function of region size from the interface within which errors in measured local mechanical properties occur when local properties are measured using DIC (assuming iso-stress).

However, for most joints, such as fusion welds, the interface between mismatched materials is not sharp; rather there is a gradient of the material properties from the weld fusion line to the parent materials. In ferritic steel welds, localised deformation has been observed in the

heat affected zone adjacent to the parent material [25-27]. In austenitic steel welds, higher strengths have been reported in the HAZ and the weld metal so that failure mostly occurs in the parent material. In all these cases, the level of constraint developing between the adjacent materials would be complex. Both the results of numerical analysis and experimental measurements show that the level of constraint in the weaker material surrounded by a stronger one increases with increasing aspect ratio [28-31]. In most cases, higher constraint is obtained from FE results since the weld interfaces are modelled as sharp [25, 30-32]. For a narrow weaker material surrounded by stronger material, DIC measurement of local mechanical properties and using iso-stress assumption, would result in higher errors in the measured properties due to high local constraint. Therefore, the results in Figure 6.2 can only be applied to sharp interfaces between mismatched materials, in the case of a weld with a narrow weaker material surrounded by stronger material, further DIC experimental work evaluating welds using specimens with varying aspect ratio needs to be carried out. However, from the results obtained in the current study, the general rule is to use a specimen with smaller aspect ratio as this reduce the size of the region within which errors occur when local mechanical properties are determined using DIC (assuming iso-stress loading).

6.6 REFERENCES

1. Levy, J. and I. Bàròdy, *A Set of Creep Curves from a Single Test using a Tapered Specimen.* Journal of Mechanical Engineering Science, 1964. **6**(3): p. 236-239.
2. Cloud, G., *Optical methods of engineering analysis*. 1998: Cambridge University Press.
3. Rist, M. and R. Reed, *Inverse method for parameter optimisation in superalloy tertiary creep equations.* Materials science and technology, 2002. **18**(2): p. 179-186.
4. *AGR Materials Data Handbook, R66, Issue 5.* British Energy Generation Ltd, 1999.
5. Githinji, D.N., *Characterisation of Plastic and Creep Strains From Lattice Orientation Measurements.* PhD Thesis, The Open University, 2013.
6. ASME, *Boiler and Pressure Vessel Code - Section II, Part D - Material Properties*. 2010.
7. ECCC-Recommendations, *High temperature component analysis overview of assessment and design procedures - Volume 9, Part II [Issue 1]*. 2005.

8. Garwood, D.A.S., *Energy material - strategic research agenda. .* 2007, Materials UK Energy Review.
9. Wilshire, B. and M. Bache. *Cost effective prediction of creep design data for power plant steels*. in *ECCC Creep Conference*. 2009.
10. Wilshire, B. and H. Burt, *Creep strain analysis for steel.* Creep resistant steels. Cambridge: Woodhead Publ, 2008: p. 421-45.
11. Wilshire, B. and P. Scharning, *Rationalization and extrapolation of creep and creep fracture data for Grade 91 steel.* Materials at High Temperatures, 2014.
12. Abe, F., T.-U. Kern, and R. Viswanathan, *Creep-resistant steels*. 2008: Elsevier.
13. Hayhurst, D.R., P. Dimmer, and C. Morrison, *Development of continuum damage in the creep rupture of notched bars.* Philosophical Transactions of the Royal Society of London. Series A, Mathematical and Physical Sciences, 1984. **311**(1516): p. 103-129.
14. Hayhurst, D.R., J. Lin, and R.J. Hayhurst, *Failure in notched tension bars due to high-temperature creep: Interaction between nucleation controlled cavity growth and continuum cavity growth.* International Journal of Solids and Structures, 2008. **45**(7–8): p. 2233-2250.
15. Vendroux, G. and W. Knauss, *Submicron deformation field measurements: Part 2. Improved digital image correlation.* Experimental Mechanics, 1998. **38**(2): p. 86-92.
16. LaVision, *StrainMaster DaVis 8.1 Digital Image Correlation Software*. 2013.
17. Forsey, A. and S. Gungor, *Demosaicing images from colour cameras for digital image correlation.* Optics and lasers in engineering, 2016. **86**: p. 20-28.
18. Reynolds, A. and F. Duvall, *Digital image correlation for determination of weld and base metal constitutive behavior.* WELDING JOURNAL-NEW YORK-, 1999. **78**: p. 355-s.
19. Lockwood, W. and A. Reynolds, *Simulation of the global response of a friction stir weld using local constitutive behavior.* Materials Science and Engineering: A, 2003. **339**(1): p. 35-42.
20. Lockwood, W.D., B. Tomaz, and A. Reynolds, *Mechanical response of friction stir welded AA2024: experiment and modeling.* Materials Science and Engineering: A, 2002. **323**(1): p. 348-353.
21. Genevois, C., A. Deschamps, and P. Vacher, *Comparative study on local and global mechanical properties of 2024 T351, 2024 T6 and 5251 O friction stir welds.* Materials Science and Engineering: A, 2006. **415**(1-2): p. 162-170.

22. Kartal, M., et al., *Determination of Weld Metal Mechanical Properties Utilising Novel Tensile Testing Methods.* Applied Mechanics and Materials, 2007. **7-8**: p. 127-132.
23. Evans, W.R. and B. Wilshire, *Introduction to Creep*. 1993, Institute of Materials: London.
24. Leitão, C., et al., *Determination of local constitutive properties of aluminium friction stir welds using digital image correlation.* Materials & Design, 2012. **33**: p. 69-74.
25. Storesund, J. and S.T. Tu, *Geometrical effect on creep in cross weld specimens.* International Journal of Pressure Vessels and Piping, 1995. **62**(2): p. 179-193.
26. Denys, R., *Strength and performance characteristics of welded joints.* International Symposium on Mis-Matching of Welds, ESIS (Ed. Schwalbe and Kocak), Mechanical Engineering Publications London, 1994: p. 59 - 102.
27. Dexter, R.J., *Significance of strength undermatching of welds in structural behaviour.* in: K.H. Schwalbe, M. Koçak (Eds.), Mismatching of Interfaces and Welds, GKSS Research Center Publications, 1997: p. 55–73.
28. Satoh, K. and M. Toyada, *Joint Strength of Heavy Plates With Lower Strength Weld Metals.* Welding journal, 1975. **54**(9): p. 311.
29. Satoh, K. and M. Toyoda, *Static strength of welded plates including soft interlayer under tension across a weld line.* Transactions of the Japan Welding Society, 1970. **1**(2): p. 10-17.
30. Kim, Y.-J. and C.-S. Oh, *Finite element limit analyses of under-matched tensile specimens.* Engineering Fracture Mechanics, 2006. **73**(10): p. 1362-1378.
31. Rodrigues, D.M., et al., *Numerical study of the plastic behaviour in tension of welds in high strength steels.* International Journal of Plasticity, 2004. **20**(1): p. 1-18.
32. Acar, M.O., et al., *Numerical study of strength mismatch in cross-weld tensile testing*, in *International Congress on Advances in Welding Science and Technology for Construction, Energy and Transportation Systems (AWST 2011)*. 2011: Antalya, Turkey.

CHAPTER SEVEN

7. CONCLUSIONS AND SUGGESTIONS FOR FUTURE WORK

7.1 Overall Conclusions

The main objective of this work was to characterise deformation in varying stress fields using DIC. The condition of varying stress in the specimens tested was, in one case, attained by designing an hour-glass shaped specimen from which multiple creep curves at different stress levels can be extracted from different positions along the gauge length, using DIC. The hour-glass shaped specimen was designed using FE to create a gently varying stress along the specimen gauge section. A stress difference between the centre and the ends of the gauge section of about 70MPa was attained. The local deformation at different stress levels along the gauge length was measured on one half of the hour-glass shaped specimen using DIC.

In the second case, specimens with mismatched materials joined by diffusion bonding were tested to evaluate the errors in the local mechanical properties obtained from DIC measured local stress-strain curves in the regions near the interface (derived using an iso-stress assumption). In these specimens, the triaxiality of concentrated stress fields in the regions near the bond interface were changed by varying the specimen thickness. To evaluate the errors in the measured local mechanical properties in the regions near the interface, elastic and elastic-plastic FE modelling, and experimental tests using DIC were carried out at room temperature. Errors in the creep properties measured near the interface were studied using DIC only.

7.2 Multiple creep deformation curves from a single hour-glass shaped specimen

i. Using DIC and a single hour-glass shaped specimen, multiple creep curves at different stress levels along the specimen gauge length have been successfully extracted for a test temperature of 525^{o}C.

ii. The validity of extracting multiple creep curves from a single specimen has been shown by comparing the local creep curve extracted from an hour-glass shaped specimen at a stress of 320MPa with creep data measured using a conventional creep specimen tested at the same stress level and temperature.

iii. Creep data at 525^{o}C from the hour-glass specimen test have been fitted to RCC-MR, Garofalo and Graham-Walles creep deformation models. A better correlation is achieved between the experimental data and the RCC-MR model predicted values when the local deformations from the single specimen are plotted as a function of time and true stress at the end of the specimen's initial loading.

iv. A poor correlation between the experimental data and the data obtained from the RCC-MR model fit was observed in the creep curves extracted from the central region of the specimen. This could be attributed to the onset of tertiary behaviour (which is not represented in the RCC-MR model) or potentially to subtle differences between the recorded temperature (from the ends of the specimen gauge section) and the actual temperature at the centre of the specimen.

v. Of the three models used in characterising the creep properties from the hour-glass specimen test, the RCC-MR gives the best fit to the measured data.

vi. An attempt to fit RCC-MR primary creep model to the multiple stress creep deformation curves using a 3D surface was unsuccessful owing to large scatter in the data. It is expected that the results from 3D surface fitting can be improved by smoothing the data.

7.3 Measurement of deformation properties in heterogeneous material

i. The local strain distribution in the regions near the interface between two mismatched materials is non-uniform under uniaxial tensile load. The size of the strain concentration region can be characterised by the distance at which the axial strain drops below the mean value (i.e. the cross-over point) for any specimen thickness.

ii. Results from elastic FE modelling show that changes in specimen geometry (thickness) only affects the size of the strain concentration region close to the interface. It is within this zone that errors in the measured local mechanical properties can occur because the inferred net section stress is correlated with the measured local strain. The magnitude of these errors depends on the level of mismatch between the adjacent materials.

iii. From both elastic-plastic FE models and local stress-strain curves measured by DIC, it can be concluded that a thin (1mm thick or less) 6mm wide test specimen should be used to extract the local mechanical properties from tensile specimens that have varying material properties along the gauge length, such as found in cross-weld test specimens. This is because the thinner specimen reduces the size of the strain concentration region adjacent to the interface where errors in measured local mechanical properties can occur. As a 'rule of thumb', the intrinsic stress-strain properties of the material should not be inferred from regions within 1mm of the interface for these 1mm thick samples because of concentration errors.

iv. Experimental study of the effects of specimen geometry on the measured local mechanical properties extracted from a plot of the global stress as function of local DIC measured strain, using diffusion bonded specimens, shows that the diffusion bonding process had an effect on the local microstructure and hence on the local mechanical properties. However, a good correlation was found between the elastic-plastic FE predicted response and low magnification DIC monitored test results of samples not unduly influenced by the diffusion bonding process.

v. The error distribution in the creep properties extracted from the regions near the interface shows the sensitivity of the creep process to changes in the local stress due to the constraining effects of the adjacent creep hard material. Although the errors were measured from a 3mm thick specimen (aspect ratio of 0.5), the use of a 1mm or less thick specimen would reduce the distance from the interface within which errors in the measured local properties would occur. This would require further investigation, especially in cross-weld specimens.

7.4 Suggestions for future work

i. In future, the experimental setup for DIC monitored creep tests should be designed to capture images of the entire length of the hour-glass gauge section of the specimen as this will allow pairs of curves to be extracted from the opposite sides of the specimen waist thus allowing validation comparisons.

ii. To consolidate the capability of the technique developed in the current study, further tests using virgin material with known creep properties should be carried out.

iii. Full scale elastic-plastic-creep FE modelling work should be carried out to investigate the effect of initial plastic loading on the creep properties of the material and local distribution of stress at initial loading

iv. 3D DIC could be applied to characterise the creep properties of a material from a single hour-glass shaped specimen with a circular cross-section.

v. Creep damage models can be fitted to the data obtained to evaluate not only the creep deformation but also the creep damage properties of the material.

vi. The DIC monitoring technique could be extended to extract multiple creep curves from a single specimen at different temperatures along the gauge section.

vii. Further tests would be required to evaluate the magnitude of the errors and the distance from the interface within which they would occur when the local tensile properties of cross-welds with varying thickness are determined using DIC based on the iso-stress assumption.

viii. Further DIC creep tests of heterogeneous material diffusion bonded specimens with varying thickness are required to fully evaluate the magnitude of the errors and size of the region around the interface within which errors in the measured creep properties can exist. But first the diffusion bonding process needs to be optimised and controlled to avoid the joining conditions altering the microstructure and stress-strain properties adjacent to the interface.

ix. Further FE studies and DIC monitored creep tests would be required to evaluate the magnitude of errors and their zone of influence when determining local creep properties from cross-weld samples, taking due account of specimen thickness (aspect ratio).